

東京工科大学
博士学位論文

Establishment of Method for Measuring
the Surface Area of Metal Oxides

Using Organic Molecule Adsorption and Application
on the Development of Supported Metal Oxide Catalysts

2025年3月

商 磊

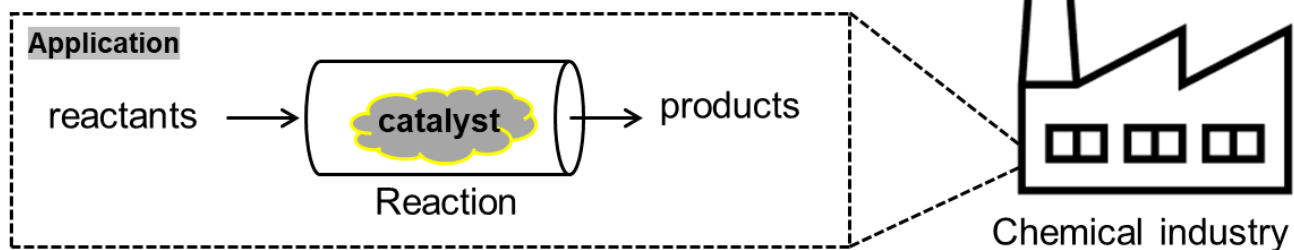
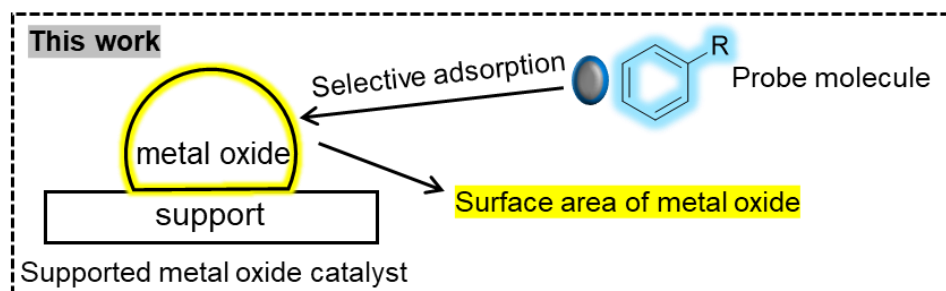
Table of Contents

Chapter 1.	Introduction	1
1.1.	Introduction: from scientific revolution to sustainable development–the role of catalyst in chemical industry.....	2
1.2.	Fundamentals and classifications of catalyst	4
1.3.	Supported metal and metal oxide catalysts	6
1.4.	Methodology for surface area measurement	9
1.4.1.	Surface area measurement by adsorption methods	9
1.4.2.	Surface area measurement by non-adsorption methods	13
1.5.	The aim of this thesis	14
1.6.	Reference.....	16
1.7.	Materials and instruments	20
1.8.	Abbreviation.....	26
Chapter 2.	Surface Area Measurement of Metal Oxide by Selective Adsorption of Organic Molecules 27	
2.1	Introduction: adsorption of molecules on metal oxide.....	28
2.2	Experimental	29
2.3	Results and discussion.....	30
2.3.1.	Investigation of organic molecules selectively adsorbed on titanium oxide.....	30
2.3.2.	Effect of experimental conditions on adsorption of probe molecules.....	39
2.3.3.	Adsorption amounts and structures of various organic molecules on TiO ₂ and carbon... 43	
2.3.4.	Adsorption models of probe molecules on TiO ₂	48
2.3.5.	Adsorption of probe molecules on various metal oxides and SiO ₂	51
2.4	Conclusions	54
2.5	Reference.....	54
2.6	Appendix	58
Chapter 3.	TiO ₂ /carbon Catalysts for Hydrogen Fuel Cell	62
3.1.	Introduction: TiO ₂ /carbon catalysts and hydrogen fuel cell.....	63
3.1.1.	Introduction: Hydrogen fuel cell and catalysts.....	63
3.1.2.	Nb-TiO ₂ /CSCNT catalysts	65
3.1.3.	N-TiO ₂ /MWCNT catalysts prepared with different annealing times	66
3.1.4.	N-Fe-TiO ₂ /carbon catalysts	68
3.1.5.	N-TiO ₂ /MWCNT catalysts prepared with different oxygen contents	69
3.2.	Experimental	70
3.3.	Results and discussion.....	70

3.3.1.	Surface area analysis of Nb-TiO ₂ /CSCNT catalysts	70
3.3.2.	Surface area analysis of N-TiO ₂ /MWCNT catalysts prepared with different annealing times	72
3.3.3.	Surface area analysis of N-Fe-TiO ₂ /carbon catalysts	73
3.3.4.	XRD and surface area analyses of N-TiO ₂ /MWCNT catalysts prepared with different oxygen contents	75
3.4.	Conclusions	76
3.5.	Reference	78
3.6.	Appendix	80
Chapter 4.	Fe ₂ O ₃ /graphene Catalysts for Imine Synthesis	83
4.1.	Introduction: Iron oxide catalysts and imine synthesis	84
4.2.	Experimental	86
4.2.1.	Preparation of supported Fe ₂ O ₃ catalysts	86
4.2.2.	Catalyst characterization	88
4.2.3.	Catalytic performance for imine synthesis	89
4.2.4.	Measurement of Fe ₂ O ₃ surface area	90
4.3.	Results and discussion	90
4.3.1.	Characterization of supported Fe ₂ O ₃ catalysts	90
4.3.2.	Catalytic performance for imine synthesis	94
4.3.3.	Fe ₂ O ₃ surface area and catalytic activity	96
4.3.4.	Substrate scope and reusability of Fe ₂ O ₃ /graphene catalyst	100
4.4.	Conclusions	104
4.5.	Reference	104
4.6.	Appendix	109
Chapter 5.	Fe ₂ O ₃ /Activated Carbon Catalysts for Oxidation of Benzene	112
5.1.	Introduction: Carbon-supported Fe ₂ O ₃ catalysts and direct oxidation of benzene to phenol	113
5.2.	Experimental	114
5.2.1.	Preparation of Fe ₂ O ₃ /activated carbon catalysts	114
5.2.2.	Catalyst characterization and measurement of Fe ₂ O ₃ surface area	115
5.2.3.	Catalytic performance for oxidation of benzene	115
5.3.	Results and Discussion	116
5.3.1.	Characterization of Fe ₂ O ₃ /activated carbon catalysts	116
5.3.2.	Catalytic performance and Fe ₂ O ₃ surface area	119
5.3.3.	Reusability and comparison with literature	123
5.4.	Conclusions	124
5.5.	Reference	125

5.6. Appendix	129
Chapter 6. CuO/graphene Catalysts for Oxidative Dehydrogenation of Alcohols	130
6.1. Introduction: Copper oxide catalysts and oxidative dehydrogenation of alcohols	131
6.2. Experimental	132
6.2.1. Preparation of CuO/graphene catalysts	132
6.2.2. Catalyst characterization and measurement of CuO surface area	133
6.2.3. Catalytic performance for oxidation of benzyl alcohols	133
6.3. Results and discussion.....	134
6.3.1. Characterization of CuO/graphene catalysts	134
6.3.2. Catalytic performance and CuO surface area.....	136
6.3.3. Substrate scope and reusability of CuO/graphene catalyst	139
6.4. Conclusions	141
6.5. Reference.....	142
6.6. Appendix	144
Chapter 7. Conclusions and Challenges.....	146
Publications	150
Papers	150
Presentations	151
Acknowledgements	153

Chapter 1. Introduction



1.1. Introduction: from scientific revolution to sustainable development—the role of catalyst in chemical industry

The progress of science and technology has long served as the cornerstone of human civilization. The Renaissance, which emerged in 14th-century Europe, ignited an unprecedented wave of intellectual and scientific awakening, laying the groundwork for modern industrial society. In the realm of theoretical science, pivotal breakthroughs—from Copernicus’s heliocentric model (1543) and Newton’s laws of motion (1687) to Lavoisier’s combustion theory (1777–1783) and the formulation of cell theory by Schleiden and Schwann (mid-19th century)—collectively forged the conceptual bedrock of contemporary scientific thought. Parallel advancements in applied technology—such as Newcomen’s steam engine (1712), Barber’s gas turbine prototype (1791), Gramme’s electrical generator (1871), and Turing’s foundational work in computation (1936)—dramatically increased productive capacity and redefined the trajectory of technological evolution.

As the 21st century progresses, humanity faces critical challenges spanning energy security, public health, educational equity, and ecological resilience. Addressing these issues while maintaining global stability has become a paramount imperative. The 2030 Agenda for Sustainable Development (2015), ratified by all UN (United Nations) member states, outlines 17 Sustainable Development Goals (SDGs) as a comprehensive blueprint for equitable growth, environmental stewardship, and societal well-being (Figure 1.1) [1a]. Crucially, the realization of these ambitions depends on sustained scientific and technological innovation—a driving force that not only propels sustainable development initiatives but also enhances their effectiveness and scalability.



Figure 1.1. The sustainable Development Goals (SDGs) logo [1a].

The chemical industry serves as a cornerstone of numerous scientific disciplines and economic sectors. By 2027, it is projected to rank as the fifth-largest global manufacturing sector in terms of direct annual

GDP contribution, accounting for 8.3% of the total economic output of global manufacturing (Figure 1.2) [1b]. Furthermore, the industry is deeply interconnected with key sectors such as rubber, metal, and food production. It directly employs approximately 15 million people worldwide, with each job in the chemical industry estimated to generate an additional seven jobs across the global economy [1b].

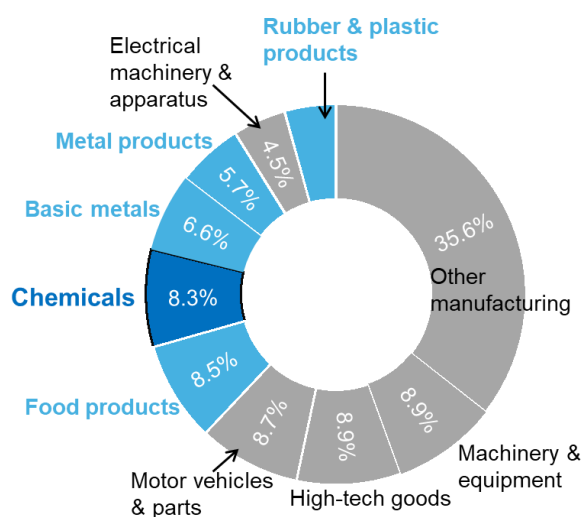


Figure 1.2. Direct contributions to GDP as percentages of total global manufacturing, 2017 [1b, Source: Oxford Economics].

Historically, nitrogen fertilizers—particularly those derived from synthetic ammonia—have been instrumental in increasing food production and sustaining the global population. Without ammonia, the availability of inorganic fertilizers would be drastically reduced, potentially placing nearly half of the world’s population at risk of hunger [1c]. In medicine, synthetic drugs have profoundly shaped human health. For example, aspirin, widely recognized for its analgesic, antipyretic, anti-inflammatory, and antithrombotic properties, played a pivotal role in the research that led to the 1982 Nobel Prize in Physiology or Medicine for elucidating its mechanism of inhibiting prostaglandin and thromboxane synthesis. Similarly, nitroglycerin has been essential in treating conditions such as heart failure, angina, and hypertension—while also historically serving as an explosive, as pioneered by Alfred Nobel. In addition to these emblematic products, the petrochemical industry—which experienced significant growth in the 20th century—has provided essential fuels such as gasoline, as well as large quantities of basic chemical raw materials, including synthetic rubber [1d].

In the 21st century, the chemical industry is undergoing a profound transformation, driven by advances in novel materials (e.g., superconducting graphene), sustainable energy solutions (e.g., hydrogen technologies), and breakthrough pharmaceuticals (e.g., the anti-HIV combination therapy Atripla, which integrates efavirenz, emtricitabine, and tenofovir). These innovations mark a new era of scientific

progress and industrial evolution.

Catalysts are indispensable in facilitating chemical transformations [1e, f]. For example, iron-based catalysts underpin the Haber–Bosch process for ammonia synthesis—a breakthrough that earned Fritz Haber the 1918 Nobel Prize in Chemistry. Acid catalysts, such as sulfuric acid (H_2SO_4), play a pivotal role in industrial organic synthesis, including the production of aspirin and nitroglycerin. Additionally, catalysts such as zeolites in fluid catalytic cracking and platinum in isomerization processes are central to the operation of the petrochemical industry.

As the chemical industry continues to evolve, catalysts remain at the forefront of innovation, driving advances across material science, energy, and medicine. Notable examples include the low-temperature growth of graphene at 150°C via indium-catalyzed ion-induced assembly [2a]; hydrogen production through water splitting facilitated by SrTiO_3 -based photocatalysts [2b]; and the chiral ruthenium-catalyzed synthesis of pharmaceuticals such as the anti-HIV drug efavirenz [2c].

Catalyst development also plays a critical role in advancing several of the 17 Sustainable Development Goals (SDGs), including Goal 6: Clean Water and Sanitation; Goal 7: Affordable and Clean Energy; Goal 9: Industry, Innovation, and Infrastructure; and Goal 13: Climate Action. For instance, photocatalytic water purification technologies (e.g., TiO_2 -based materials for sterilization [3a]), catalytic energy conversion processes (e.g., Fischer–Tropsch synthesis using iron-based catalysts [3b]), and electrochemical CO_2 reduction (e.g., copper-based catalysts for CO_2 conversion [3c]) all exemplify how catalysis underpins sustainable development. Moreover, innovations in catalysis generate significant spillover benefits, enhancing productivity and improving quality of life beyond the chemical sector. Continued progress in catalyst technology will therefore be instrumental in shaping a more sustainable and prosperous future.

1.2. Fundamentals and classifications of catalyst

In general, a catalyst is defined as a substance that increases the rate of a chemical reaction without affecting the overall standard Gibbs free energy change. It can also be described as a substance that accelerates a reaction without shifting the reaction equilibrium and remains chemically and physically unchanged in both composition and quantity before and after the process. Catalysts function by lowering the activation energy required for a reaction, thereby facilitating otherwise unfavorable reactions and enhancing reaction efficiency (Figure 1.3).

For instance, in ammonia synthesis, an iron oxide-based catalyst is widely employed to reduce the

activation energy and facilitate the reaction. In the absence of a catalyst, the activation energy for this reaction is approximately 335 kJ mol^{-1} [4a]. However, when an iron catalyst is introduced, the reaction pathway is modified, dividing the process into two steps and significantly decreasing the activation energy. Specifically, during the first step (nitridation), the activation energy is reduced to approximately $126\text{--}167 \text{ kJ mol}^{-1}$, while in the second step (nitrogen hydride formation), it decreases further to around 13 kJ mol^{-1} [4a]. In this catalytic cycle, nitrogen molecules are initially adsorbed onto the surface of the iron oxide catalyst, weakening the $\text{N}\equiv\text{N}$ triple bond. Subsequently, hydrogen atoms react stepwise with the adsorbed nitrogen species, forming intermediate compounds. Finally, ammonia molecules are generated and desorbed from the catalyst surface, completing the reaction cycle [4b].

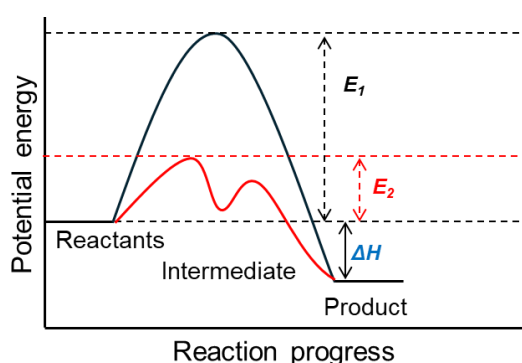


Figure 1.3. Potential energy diagram with and without catalyst.
 E_1 , E_2 : Activation energy without and with catalyst; ΔH : heat of reaction.

Catalysts can be classified into various types based on their reaction systems and physical states. In terms of reaction systems, they are categorized as homogeneous catalysts, heterogeneous catalysts, and biocatalysts (enzymes). Based on their physical state, catalysts are further divided into liquid and solid catalysts [1e, f].

Homogeneous catalysis occurs when the catalyst and reactants exist in the same phase, typically in the liquid state, with no phase interface. Common examples include liquid acid-base catalysts and soluble transition metal complexes. A well-known case is the palladium-catalyzed Suzuki coupling reaction, which was recognized with the 2010 Nobel Prize in Chemistry [4c]. Since the active sites in homogeneous catalysts are molecularly dispersed, these systems often exhibit high selectivity and activity.

In contrast, heterogeneous catalysis involves catalysts and reactants in different phases, most commonly solid catalysts interacting with gaseous or liquid-phase reactants. Due to this phase separation, heterogeneous catalysts are generally easier to recover and reuse after the reaction. Beyond iron-based catalysts used in ammonia synthesis, a notable example is molybdenum(VI)- and tungsten(VI)-based catalysts supported by alkoxide and imido ligands, which are widely employed in olefin metathesis [4d].

Given their reusability and efficiency, heterogeneous catalysts are of immense industrial significance.

Biocatalysts, a distinct category of catalysts, refer to enzymes that drive biochemical reactions in living organisms. Enzymes play crucial roles in various biological processes across humans, animals, and plants. For instance, chloroplast enzymes facilitate photosynthesis in plants, a process essential for sustaining life on Earth [4e]. As natural catalysts, enzymes are indispensable in biochemical transformations.

1.3. Supported metal and metal oxide catalysts

Heterogeneous catalysts are highly valued in industrial applications for their recyclability, whereas homogeneous molecular catalysts often present challenges in reuse. To overcome this, various solid-state strategies—such as ion exchange, adsorption, encapsulation, and covalent grafting—have been explored to enhance the reusability of homogeneous systems. However, these methods face notable limitations. For example, although covalent attachment of ligands to solid supports is widely used, supported molecular catalysts often suffer from reduced stability, activity loss due to surface interactions, leaching, and thermal/chemical degradation. Moreover, their high synthesis cost remains a key drawback [5a].

Similarly, enzymes (biocatalysts) offer excellent activity and selectivity but are limited by strict reaction conditions, rapid inactivation, and short lifespans. These constraints highlight the need to prioritize the development of heterogeneous catalysts.

Heterogeneous catalysts are typically solid materials, with active components composed of metals, metal oxides and sulfides etc. However, single-metal catalysts exhibit inherent drawbacks, including high costs (e.g., platinum or gold), poor dispersion, and limited thermal or chemical stability. To mitigate these issues, catalyst supports (or carriers) are commonly employed to improve the activity, stability, and dispersion of active sites. Table 1.1 summarizes representative supported catalysts used in industrial processes, featuring common supports such as activated carbon, SiO₂, Al₂O₃, and zeolites.

Table 1.1. Examples of supported metal or metal oxide catalysts in chemical industry.

Catalyst	Application	Reference
CrO _x /SiO ₂	polymerization	[5b]
FeO _x -K ₂ O/Al ₂ O ₃	ammonia synthesis	[5c]
Pt/carbon	hydrogenations in organic synthesis, hydrogen fuel cell	[5d, e]
V ₂ O ₅ /SiO ₂	oxidation in organic synthesis	[5f-h]
Pt-Re/zeolite	naphtha reforming	[5i]

In recent years, supported metal and metal oxide catalysts have garnered considerable attention. As summarized in Table 1.2, these catalysts demonstrate significant potential across diverse applications, including water splitting, organic synthesis, photocatalysis, and electrocatalysis. Their broad applicability highlights their critical role in advancing future technologies and industrial processes.

Table 1.2. Examples of supported metal or metal oxide catalysts in recent research.

Catalyst	Application	Reference
TiO ₂ /carbon	hydrogen fuel cell, H ₂ O ₂ photo-synthesis	[6a, b]
Fe ₂ O ₃ /carbon	synthesis of amine, Fischer–Tropsch synthesis, photo-decomposition	[6c-e]
CuO/SiO ₂	AsH ₃ oxidation, alkylation of indole	[6f, g]
Au/TiO ₂	water photo-splitting	[6h]
Cu/carbon	CO ₂ electro-reduction	[6i]

Typically, metals or metal oxides serve as active components, while supports function as inert matrices or, in some cases, act as promoters by participating in catalytic reactions (Figure 1.4). For example, in ammonia synthesis, iron oxide acts as the primary catalytic component, aluminum oxide serves as a structural stabilizer, and potassium oxide functions as an electronic promoter, all working synergistically to enhance catalytic performance [1e, 4a]. Another notable example is the CrO_x/SiO₂ system, commonly known as the Phillips catalyst. Although some debate persists regarding the precise nature of the active site, it is generally accepted that chromium species (on CrO_x) facilitate the catalytic reaction, while SiO₂ provides structural stability and a high surface area [5g, h]. In electro- and photocatalysis, carbon supports play a crucial role, exhibiting key properties such as high porosity, electronic conductivity, thermal stability, optical absorption, and an extended active surface area [6a, b, e, l].

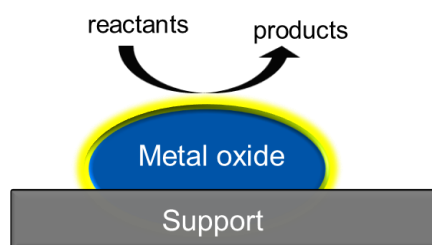


Figure 1.4. Supported metal or metal oxide catalyst.

In heterogeneous catalysis, catalytic reactions typically proceed via one or more adsorption processes (Figure 1.5, a representative reaction model via adsorption). The fundamental mechanism can be summarized as follows: (i) reactants adsorb onto the catalyst's surface, (ii) their existing chemical bonds are weakened, facilitating the formation of new bonds, and (iii) the products eventually desorb, regenerating the active sites. These adsorption processes are critical for transforming reactants into products. However, adsorption does not occur uniformly across the catalyst surface but is localized to specific regions known as active sites, assuming that all adsorption sites contribute to catalytic activity. In certain cases, adsorption may not take place on cocatalysts, supports, or inert crystal facets, further emphasizing the need to focus on the study of active surfaces when investigating catalysts.

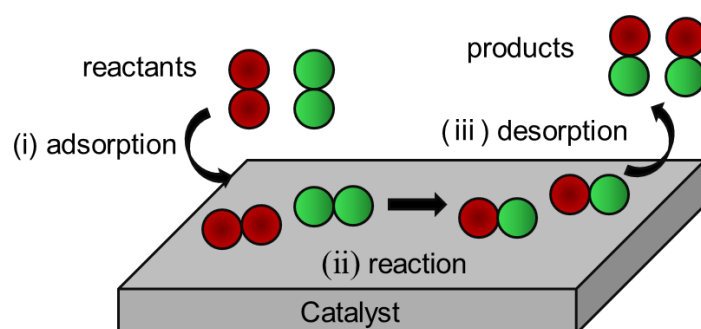


Figure 1.5. Simplified reaction model via surface adsorption.

For supported metal or metal oxide catalysts, analyzing the surfaces of the primary catalytic components—metals or oxides—is essential for advancing the understanding and development of heterogeneous catalysts. Over the years, numerous analytical techniques have been developed and widely applied to characterize these catalysts (Figure 1.6, characterization of supported catalysts by analytical tools) [1e]. Spectroscopic techniques such as X-ray photoelectron spectroscopy (XPS) provide insights into the chemical states of metal elements, while X-ray diffraction (XRD) is used to determine crystal structures and crystallite sizes. Electron microscopy techniques, including scanning and transmission electron microscopy (SEM/TEM), enable direct visualization of surface morphology. Additional methods, such as extended X-ray absorption fine structure (EXAFS), Auger electron spectroscopy (AES), and infrared spectroscopy (IR), further contribute to comprehensive catalyst characterization. Adsorption-based techniques also play a pivotal role in catalyst analysis. For instance, ammonia adsorption is widely employed to probe surface acid sites, while nitrogen adsorption via the Brunauer-Emmett-Teller (BET) method is commonly used to measure the total surface area of solid catalysts. However, despite its widespread application, the BET method presents limitations in quantifying the surface areas of supported metal or metal oxide on supported catalysts. Thus, continued research and innovation in surface area analysis remain crucial for advancing catalytic science.

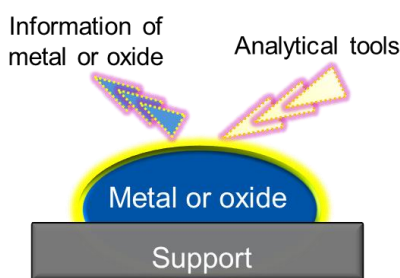


Figure 1.6. Characterization of supported metal or metal oxide catalysts.

1.4. Methodology for surface area measurement

To advance catalyst development, various quantitative methods have been established to evaluate both the total surface area (e.g., the BET method), and the surface area of specific materials on supported catalysts [1e, 7a, b, c]. In this section, these surface area evaluation techniques are divided into two main groups: adsorption-based methods, non-adsorption-based methods.

1.4.1. Surface area measurement by adsorption methods

Adsorption can be categorized into two types: physical adsorption and chemical adsorption [7a, b]. Physical adsorption typically involves multiple layers, has low adsorption heat, and is easily reversible. In contrast, chemical adsorption usually forms a monolayer, is associated with high adsorption heat, and is difficult to reverse due to the formation of chemical bonds. The key characteristics of physical and chemical adsorption are summarized in Table 1.3.

Table 1.3. Comparison of physical and chemical adsorption [7a, b].

Type	Physical adsorption	Chemical adsorption
Adsorption force	Van der Waals force	chemical bonding force
Adsorption heat	close to heat of vaporization	close to heat of reaction
Selectivity	No selectivity	selectivity
Stability	unstable, reversible	stable
Molecular layer	single or multilayer	single
Adsorption rate	fast, not affected by temperature	slow, affected by temperature
Adsorption temperature	low, below boiling point	unlimited

The BET method, which determines the total surface area of solid catalysts via the physical adsorption of nitrogen, is the most widely used technique for surface area analysis. Developed by Brunauer, Emmett, and Teller, this method is based on the principle of multilayer adsorption and is frequently applied in the

evaluation of surface area [1e, 7a-c]. The underlying assumption is that molecular adsorption occurs at specific sites on the material's surface and progresses through multiple layers (Figure 1.8). In the first layer, the adsorption rate of gas molecules is equal to the desorption rate, achieving equilibrium. Similarly, in the second layer, adsorption and desorption rates are balanced. Beyond the second layer, it is assumed that the heat of adsorption equals the heat of condensation, remaining constant due to molecular interactions that are independent of the material's adsorption forces. Based on these principles, the BET isotherm (Formula 1.1) is derived as follows:

$$v = \frac{v_m C p}{(p_0 - p) [1 + (C - 1) (\frac{p}{p_0})]} \dots \dots \dots \text{(Formula 1.1)}$$

v : total adsorption amount; v_m : monolayer adsorption amount; C : parameters related to heat of adsorption; p : pressure; p_0 : saturated vapor pressure of molecule.

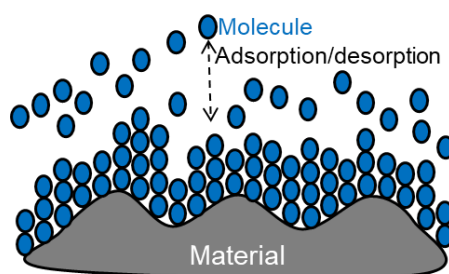


Figure 1.7. BET theory: adsorption of molecules on surface by multiple layer.

For conventional solid catalysts, it is generally postulated that the catalytically active sites are homogeneously distributed over the available surface area. Under this assumption, the catalytic performance of a material is often directly proportional to its total surface area. For instance, unsupported Co_3O_4 catalysts prepared at calcination temperatures ranging from 300 to 600 °C have been investigated for applications such as water electrolysis [7d] and hydrogen peroxide (H_2O_2) decomposition [7e]. In the case of water electrolysis, the catalytic activity—typically expressed as the current density per macroscopic unit area of a disk-shaped working electrode—has been shown to exhibit a clear positive correlation with the BET surface area of the Co_3O_4 catalyst [7d]. Similarly, for H_2O_2 decomposition reactions, the activity per unit mass of catalyst, measured by the rate of oxygen evolution from H_2O_2 , decreases as the calcination temperature increases. This trend is attributed to a reduction in BET surface area with increasing temperature. However, when the activity is normalized to the unit surface area, the catalytic performance remains essentially constant [7e], suggesting that the intrinsic activity per surface site does not change significantly. Taken together, these two examples demonstrate that, under the assumption of uniform active site distribution, the total surface area of a catalyst can serve as a reliable parameter for evaluating and comparing its catalytic efficiency across different reaction systems and preparation conditions.

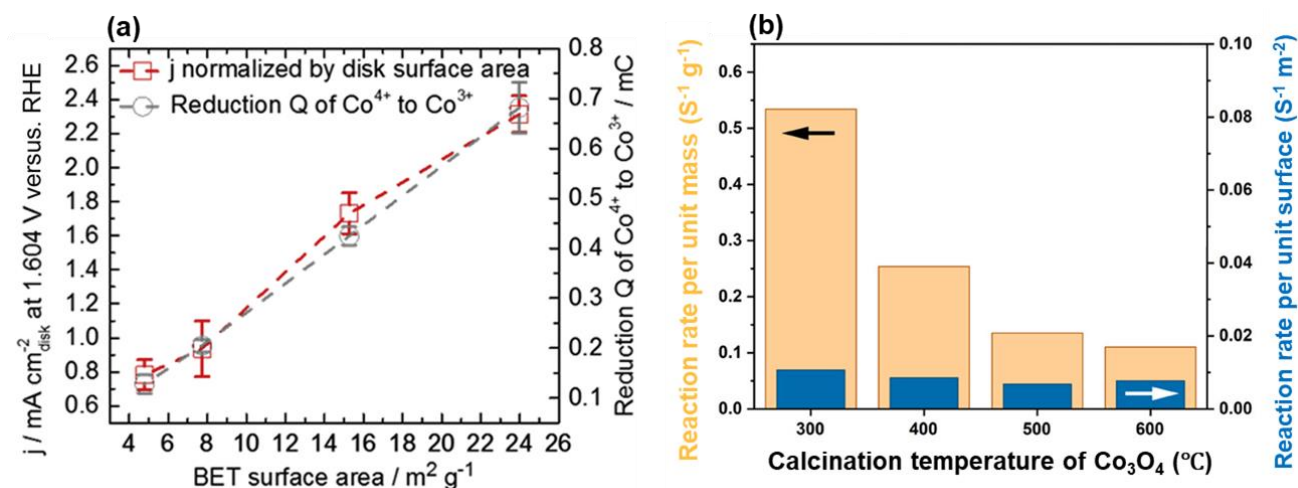


Figure 1.8. (a) Relationship between BET surface area, Oxygen evolution reaction (OER) currents by geometric surface area, and the charge associated with the reduction of Co^{4+} to Co^{3+} at the potential range of 1.25–1.55 V versus hydrogen electrode (RHE) [7e], reuse by permission; Copyright {2018} Elsevier; (b) Reaction rate determined per unit mass (orange) and per unit surface area (blue) of the calcined Co_3O_4 catalysts [7e], reuse by license under CC-BY; Copyright {2021} American Chemical Society.

Liquid fatty acids, dyes, iodine, and ethylene glycol are commonly used to estimate the surface area of materials such as activated carbon, metals, and metal oxides [7a, b, f]. This method calculates the total surface area of the adsorbent based on the cross-sectional area of the organic molecules. Additionally, some less commonly used methods for determining the total surface area of materials exist but are not elaborated here [7g-l]; these methods are summarized in Table 1.4.

However, in most cases, the distribution of active catalytic sites on the surface of solid materials is not uniform. This is particularly true for supported metal or metal oxide catalysts, where the catalytic activity largely depends on the state and distribution of the active material—either metal or metal oxide. Factors such as the dispersion and accessibility of the active material, the interaction between the active material and the support, as well as the shape and porosity of the support, all play a crucial role in influencing or determining catalytic performance [1e].

Quantitative determination of the metal surface area on the support is an effective method for characterizing supported catalysts. Hydrogen or carbon monoxide selectively adsorbs onto the metal surface with minimal adsorption on the support, enabling the calculation of the metal surface area (Figure 1.9). This selective adsorption method is widely recognized as one of the most commonly used techniques alongside the BET method and is extensively introduced in textbooks and literature [1e, 7a, b, 8a, b]. In practice, this method is often combined with voltametric measurements to determine the metal surface area of electrocatalysts (H adsorption/desorption and CO stripping,) [8c, d]. For example, a study

demonstrated that the catalytic activities (current) of Pt/macroporous carbon electrodes for methanol oxidation were positively correlated with the Pt surface areas measured by hydrogen adsorption (Figure 1.10) [8e]. This highlights the significance of quantitatively determining the metal surface area on the support in understanding and optimizing catalytic activity.

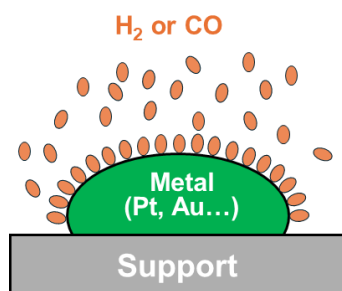


Figure 1.9. Selective adsorption of H₂ or CO molecules on metal surface for supported catalysts.

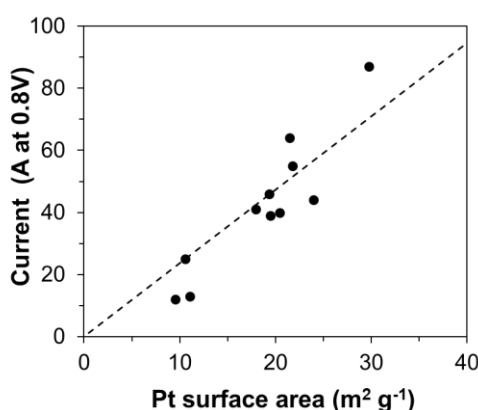


Figure 1.10. Pt surface area and catalytic activity towards methanol oxidation obtained for Pt/macroporous carbon catalysts [8e].

Some less commonly used and special methods for surface area determination are briefly discussed here. The surface area of metals on supports can be measured using the chemical reaction: $\text{N}_2\text{O} + 2 \text{Cu} \rightarrow \text{N}_2 + \text{Cu}_2\text{O}$ [8b, f]. In this reaction, the amount of N₂O consumed and the N₂ produced are used to quantitatively determine the surface area of exposed copper. In another study, benzoic acid was selectively adsorbed onto alumina and titania supports at 523 K, but not onto V₂O₅. This selective adsorption allowed the calculation of the surface area of these supports based on the amount of benzoic acid adsorbed [8g]. Benzoic acid adsorbed onto reduced V₂O₃ was oxidized to CO₂ at 623 K, enabling the determination of the support's surface area based on the quantity of CO₂ produced [8g]. Additionally, determining the hydrophilic surface area of non-supported materials through the hydrophilicity or hydrophobicity of water molecules represents a relatively novel approach [8h, i].

Table 1.4 provides a summary of various methods for determining surface area via adsorption, including the techniques described above.

Table 1.4. Approaches for determining the surface area by adsorption.

Application	Method
Total surface area	BET method (common method) [1e, 7a-c]
	molecule adsorption in liquid phase, I ₂ (for activated carbon) [7a, b, f]
	ethylene glycol monoethyl ether (EGME) (for fine-grained soil) [7g]
	electrokinetic analysis of complex-ion (for aqueous particulate matter e.g., Al ₂ O ₃) [7h]
	protein Retention (PR) (for clay) [7i]
Metal surface area	CO (for without surface reaction to form carbonyl) and H ₂ (not for Pd) [1e, 7a, b, 8a-e] N ₂ O for Cu or Ag [8a, f]
Metal oxide surface area	Benzoate for TiO ₂ or Al ₂ O ₃ (VO _x /TiO ₂ or Al ₂ O ₃ catalysts) [8g]
Hydrophilic surface area	Adsorption of H ₂ O for activated carbon, Al ₂ O ₃ and SiO ₂ [9h, i]

1.4.2. Surface area measurement by non-adsorption methods

In addition to adsorption-based approaches, various non-adsorption techniques have also been developed for surface area determination. Among them, small-angle X-ray scattering (SAXS) is widely employed as a rapid and effective method to estimate the total surface area of porous or nanostructured materials, serving as a common alternative to the conventional BET method [9a].

For unsupported electrocatalysts, the surface area of the active metal or metal oxide can be quantitatively evaluated through several electrochemical techniques. These include underpotential deposition (UPD), surface redox reaction analysis, and measurements of double-layer capacitance, all of which provide insights into the accessible electrochemically active surface area [9d-f].

In the case of supported catalysts, the surface area of exposed metal or metal oxide species can be approximately estimated via electron microscopy techniques [9f]. This approach involves visualizing nanoparticles on the support surface and assuming that they are fully exposed and ideally spherical. The surface area is then calculated using standard geometric formulas. However, this method introduces considerable uncertainties due to its idealized assumptions. Furthermore, the high operational cost and limited accessibility of advanced electron microscopy instruments restrict the routine use of this technique in surface area determination.

A comparison of representative non-adsorption methods for evaluating catalyst surface area is summarized in Table 1.5.

Table 1.5. Approaches for determining the surface area by non-adsorption.

Application	Method
Total surface area	small-angle X-ray scattering method (fast) [9a]
	heat of wetting [7a, 9b]
	air permeability [7a, 9c]
Metal surface area in electrocatalysts (unsupported)	underpotential deposition [9d]
	surface redox reaction [9e]
Metal oxide surface area in electrocatalysts (unsupported)	surface redox reaction, and double layer capacitance [9f]
Metal (or oxide) surface area on support	rough evolution by TEM telescope [9f]

1.5. The aim of this thesis

Supported metal oxide catalysts constitute a crucial class of catalysts with significant industrial value, contributing to advancements in productivity and societal development [10a-c]. Section 1.4 introduced various techniques for determining the surface area of solid materials, including adsorption-based and non-adsorption-based methods. While most of these techniques effectively estimate total surface area or, more generally, metal surface area in supported catalysts, methods specifically tailored for measuring the surface area of supported metal oxide catalysts remain underdeveloped or have limited applicability. For example, although transmission electron microscopy (TEM) can provide an estimate of the surface area of metals or oxides [9f], its considerable margin of error restricts its widespread use.

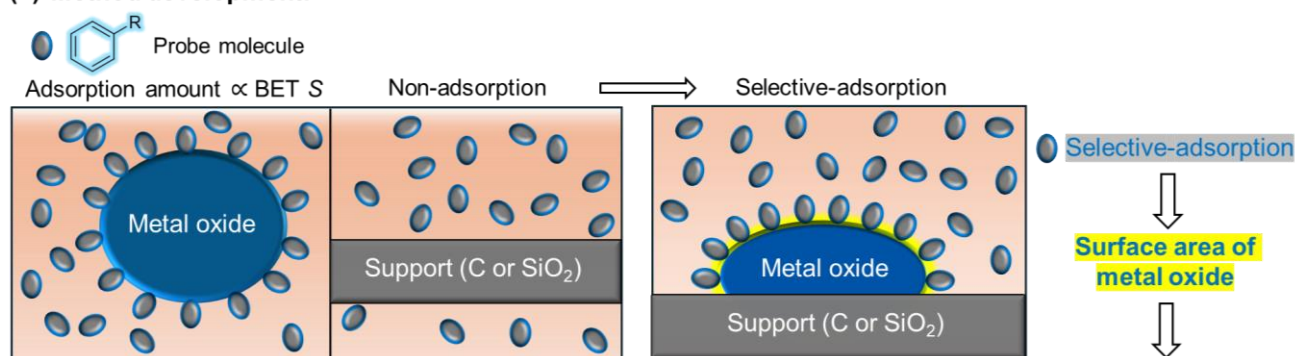
Surface area measurements are typically performed using gas-phase adsorption techniques that require pressure-based instruments or costly spectroscopic equipment. Developing cost-effective and user-friendly methodologies would significantly benefit scientific research and industrial applications. For instance, adsorption in liquid-phase systems offers advantages such as lower costs and operational simplicity. Some existing methods, such as iodine adsorption, have been applied to measure the surface area of activated carbon [7f]; however, these methods lack selectivity in adsorption.

Selective adsorption of probe molecules at surface acidic sites, such as pyridine [1e, 7a, b, 8b], has proven to be an effective approach for catalyst surface analysis. Inspired by pyridine's selective adsorption on acidic sites, this work aims to employ organic molecules that selectively adsorb onto metal oxide surfaces in supported catalysts while minimizing adsorption on the support itself. These organic probe molecules are introduced in liquid solutions, and their adsorption quantities can be rapidly and accurately determined using UV-visible spectroscopy (UV-Vis, as used in this thesis), gas chromatography (GC), or liquid chromatography (LC). Compared to gas-phase adsorption techniques,

these methods offer significant cost and convenience advantages.

Chapter 2 focuses on developing methodologies to quantify the exposed surface area of metal oxides on supports. The work examines widely used metal oxides, including titanium dioxide (TiO_2), iron oxide (Fe_2O_3), and copper oxide (CuO), as well as various support materials, such as carbon-based materials (e.g., activated carbon, graphene, and carbon nanotubes) and silica (both spherical and mesoporous SiO_2). By systematically varying experimental conditions, such as solvent type, temperature, adsorption time, and agitation methods (stirring or shaking), this work aims to identify organic molecules that preferentially adsorb onto metal oxides while exhibiting minimal interaction with carbon or SiO_2 supports. Furthermore, the adsorption quantities of these selected probe molecules must correlate with the BET surface area of the metal oxides, thereby fulfilling the requirements for accurate surface area measurement. As a result, the selective adsorption of probe molecules enables the determination of the exposed metal oxide surface area in supported catalysts (Figure 1.11a). The adsorption structures were further analyzed using FT-IR, adsorption behavior was investigated under various conditions, and surface adsorption models were established.

(a) Method development:



(b) Method application:

- TiO_2 /carbon for hydrogen fuel cell
- Fe_2O_3 /graphene for imine synthesis
- Fe_2O_3 /activated carbon for benzene oxidation
- CuO /graphene for alcohol oxidation

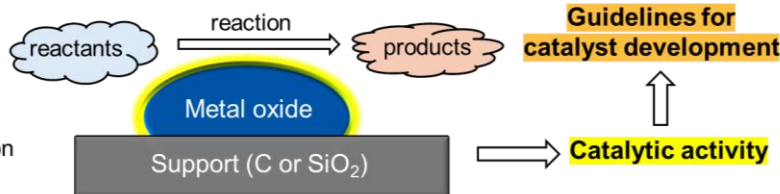


Figure 1.11. The scheme of this thesis is for development of supported metal oxide catalysts.

This established method was applied to measure the surface area of metal oxides in TiO_2 /carbon catalysts for hydrogen fuel cells (Chapter 3, collaborative research), Fe_2O_3 /graphene catalysts for imine synthesis (Chapter 4), Fe_2O_3 /activated carbon for oxidation of benzene (Chapter 5), and CuO /graphene catalysts for alcohol oxidation (Chapter 6). In addition to conventional solid surface characterization methods (e.g., XRD, TEM, BET surface area), the selective adsorption of probe molecules was employed

to measure the surface area of metal oxides in the catalysts. By integrating these results with standard solid surface characterization techniques, the relationship between catalytic activity and the metal oxide surface area was further investigated (Figure 1.11b).

The primary significance of this work resides in its systematic investigation of the correlation between catalytic activity and metal oxide surface area. This comprehensive analysis substantially deepens our understanding of the critical role that metal oxide surface area plays in determining catalytic efficiency within conventional catalyst systems. The derived insights establish a theoretical framework for the rational engineering of advanced catalysts, enabling performance enhancement through precise structural modifications and compositional tuning. Furthermore, in addition to developing an innovative surface area characterization methodology, this work incorporates novel discussions on organic molecule adsorption across diverse materials, alongside thorough examinations of catalyst synthesis, characterization techniques, and practical applications, thereby making multifaceted contributions to catalytic science.

1.6. Reference

- [1] (a) *The United Nations Home Page*. <https://sdgs.un.org/2030agenda/> (accessed 2024-08-29). (b) *CHEManager Home Page*. <https://www.chemanager-online.com/en> (accessed 2024-09-4). (c) Smil, V. Detonator of the population explosion. *Nat.* **1999**, 400 (6743), 415-415. DOI: 10.1038/22672. (d) Clew, R. J. *Project Finance for the International Petroleum Industry*. The Petrochemicals Industry. Academic Press, 2016; pp 187-203. DOI: 10.1016/B978-0-12-800158-5.00011-6. (e) Kikuti, e. *et al. New catalysis*; Sankyo print, **1997** (book in Japanese). (f) Yansaneh, O. Y.; Zein, S. H. Contemporary Perspectives on Waste Plastic Catalysis. In: VSR Rajasekhar Pullabhotla, editor. Prime Archives in Chemistry: 2nd Edition. Hyderabad, India: Vide Leaf. **2022**.
- [2] (a) Araby, M. I.; Rosmi, M. S.; Vishwakarma, R.; Sharma, S.; Wakamatsu, Y.; Takahashi, K.; Kalita, G.; Kitazawa, M.; Tanemura, M. Graphene formation at 150°C using indium as catalyst. *RSC adv.* **2017**, 7 (75), 47353-47356. DOI: 10.1039/C7RA07892G. (b) Takata, T.; Jiang, J.; Sakata, Y.; Nakabayashi, M.; Shibata, N.; Nandal, V.; Seki, K.; Hisatomi, T.; Domen, K. Photocatalytic water splitting with a quantum efficiency of almost unity. *Nat.* **2020**, 581 (7809), 411-414. DOI: 10.1038/s41586-020-2278-9. (c) Zheng, Y.; Zhang, L.; Meggers, E. Catalytic enantioselective synthesis of key propargylic alcohol intermediates of the anti-HIV drug efavirenz. *Org. Process Res. Dev.* **2018**, 22 (1), 103-107. DOI: 10.1021/acs.oprd.7b00376.
- [3] (a) Wei, Y.; Meng, H.; Wu, Q.; Bai, X.; Zhang, Y. TiO₂-Based Photocatalytic Building Material for Air Purification in Sustainable and Low-Carbon Cities: A Review. *Catalysts.* **2023**, 13 (12), 1466. DOI: 10.3390/catal13121466. (b) Gao, Y.; Shao, L.; Yang, S.; Hu, J.; Zhao, S.; Dang, J.; Wang, W.; Yan, X.; Yang, P. Recent advances in iron-based catalysts for Fischer–Tropsch to olefins reaction. *Catal. Commun.* **2023**, 181,

106720. DOI: 10.1016/j.catcom.2023.106720. (c) Ji, Y.; Guan, A.; Zheng, G. Copper-based catalysts for electrochemical carbon monoxide reduction. *Cell Rep. Phys. Sci.* **2022**, 3 (10). DOI: 10.1016/j.xcrp.2022.101072.

[4] (a) *Shandong Avant New Material Technology Co., Ltd. Home Page*. <https://www.sd-avant.com/news/how-to-synthesize-ammonia.html> (accessed 2024-08-29). (b) Li, C.; Wang, T.; Gong, J. Alternative Strategies Toward Sustainable Ammonia Synthesis. *Trans. Tianjin Univ.* **2020**, 26 (2), 67-91. DOI: 10.1007/s12209-020-00243-x. (c) Miyaura, N.; Yamada, K.; Suzuki, A. A new stereospecific cross-coupling by the palladium-catalyzed reaction of 1-alkenylboranes with 1-alkenyl or 1-alkynyl halides. *Tetrahedron Lett.* **1979**, 20 (36), 3437-3440. DOI: 10.1016/S0040-4039(01)95429-2. (d) Schrock, R. R.; Murdzek, J. S.; Bazan, G. C.; Robbins, J.; DiMare, M.; O'Regan, M. Synthesis of molybdenum imido alkylidene complexes and some reactions involving acyclic olefins. *J. Am. Chem. Soc.* **1990**, 112 (10), 3875-3886. DOI: 10.1021/ja00166a023. (e) Arnon, D. I.; Whatley, F. R.; Allen, M. B. Photosynthesis by Isolated Chloroplasts. II. Photosynthetic Phosphorylation, the Conversion of Light into Phosphate Bond Energy. *J. Am. Chem. Soc.* **1954**, 76 (24), 6324-6329. DOI: 10.1021/ja01653a025.

[5] (a) Zaera, F. Molecular approaches to heterogeneous catalysis. *Coord. Chem. Rev.* **2021**, 448, 214179. DOI: 10.1016/j.ccr.2021.214179. (b) Hogan, J. P.; Banks, R. L. U.S. Patent 2,825,721, **1958**. (c) Haber, F.; Le Rossignol, R. Über die technische Darstellung von Ammoniak aus den Elementen. *Zeitschrift für Elektrochemie und angewandte physikalische Chemie* **1913**, 19 (2), 53-72. DOI: 10.1002/bbpc.19130190201. (d) Shriner, R. L.; Adams, R. THE PREPARATION OF PALLADOUS OXIDE AND ITS USE AS A CATALYST IN THE REDUCTION OF ORGANIC COMPOUNDS.1 VI. *J. Am. Chem. Soc.* **1924**, 46 (7), 1683-1693. DOI: 10.1021/ja01672a018. (e) Grubb, W. T.; Niedrach, L. W. U.S. Patent 2,928,771, **1960**. (f) Kerr, G. T.; McCain, J. H. U.S. Patent 3,156,705, **1964**. (g) McDaniel, M. P. Chapter 3 - A Review of the Phillips Supported Chromium Catalyst and Its Commercial Use for Ethylene Polymerization. In *Advances in Catalysis*, Gates, B. C., Knözinger, H. Eds.; Vol. 53; Academic Press, 2010; pp 123-606. DOI: 10.1016/S0360-0564(10)53003-7. (h) Wang, S.; Liu, B.; Jin, Y. Why could the $\text{CrO}_x/\text{SiO}_2$ and VO_x/SiO_2 catalysts show so different behaviors in ethylene polymerization? A theoretical approach. *Mol. Catal.* **2020**, 493, 111090. DOI: 10.1016/j.mcat.2020.111090. (i) Haensel, V.; Kloucek, F. Patent 3,415,737, **1968**.

[6] (a) Abdullah, N.; Kamarudin, S. K. Titanium dioxide in fuel cell technology: An overview. *J. Power Sources* **2015**, 278, 109-118. DOI: 10.1016/j.jpowsour.2014.12.014. (b) Zhang, H.; Wang, S.; Tian, J.; Bai, X. Photocatalytic hydrogen peroxide production from seawater over graphitic carbon nitride supported titanium dioxide quantum dots. *J. Environ. Chem. Eng.* **2024**, 12 (2), 112290. DOI: 10.1016/j.jece.2024.112290. (c) Jagadeesh, R. V.; Stemmler, T.; Surkus, A.-E.; Junge, H.; Junge, K.; Beller, M. Hydrogenation using iron oxide-based nanocatalysts for the synthesis of amines. *Nat. Protoc.* **2015**, 10 (4), 548-557. DOI: 10.1038/nprot.2015.025. (d) Chen, Y.; Wei, J.; Duyar, M. S.; Ordonsky, V. V.; Khodakov, A. Y.; Liu, J. Carbon-based catalysts for Fischer-Tropsch synthesis. *Chem. Soc. Rev.* **2021**, 50 (4), 2337-2366. (e) Moreira, R.; B. Esfahani, E.; A. Zeidabadi, F.; Rostami, P.; Thuo, M.; Mohseni, M.; Foster, E. J. Hybrid graphenic and iron oxide photocatalysts for the decomposition of synthetic chemicals. *Commun. Eng.* **2024**, 3 (1), 114. DOI: 10.1038/s44172-024-00267-4. (f) Li, K.; Hao, X.; Yang, X.; Wang, C.; Ning, P.; Li, K. Optimization of $\text{CuO}@/\text{SiO}_2$ core-shell catalysts for catalytic AsH_3

oxidation. *Environ. Chem. Eng.* **2023**, *11* (3), 110273. DOI: 10.1016/j.jece.2023.110273. (g) Fraile, J. M.; Le Jeune, K.; Mayoral, J. A.; Ravasio, N.; Zaccheria, F. CuO/SiO₂ as a simple, effective and recoverable catalyst for alkylation of indole derivatives with diazo compounds. *Org. Biomol. Chem.* **2013**, *11* (26), 4327-4332. DOI: 10.1039/C3OB40264A. (h) Tanaka, A.; Teramura, K.; Hosokawa, S.; Kominami, H.; Tanaka, T. Visible light-induced water splitting in an aqueous suspension of a plasmonic Au/TiO₂ photocatalyst with metal co-catalysts. *Chem. Sci.* **2017**, *8* (4), 2574-2580. DOI: 10.1039/C6SC05135A. (i) Lum, Y.; Kwon, Y.; Lobaccaro, P.; Chen, L.; Clark, E. L.; Bell, A. T.; Ager, J. W. Trace Levels of Copper in Carbon Materials Show Significant Electrochemical CO₂ Reduction Activity. *ACS Catal.* **2016**, *6* (1), 202-209. DOI: 10.1021/acscatal.5b02399.

[7] (a) Keiichi, T. *et al. Adsorption*; Sankyo Print, **1965** (book in Japanese). (b) Kondo, S. *et al. Adsorption Science*; Maruzen Print, **1991** (book in Japanese). (c) Brunauer, S.; Emmett, P. H.; Teller, E. Adsorption of Gases in Multimolecular Layers. *J. Am. Chem. Soc.* **1938**, *60* (2), 309-319. DOI: 10.1021/ja01269a023. (d) Sun, S.; Li, H.; Xu, Z. J. Impact of Surface Area in Evaluation of Catalyst Activity. *Joule* **2018**, *2* (6), 1024-1027. DOI: 10.1016/j.joule.2018.05.003. (e) Bernard, P.; Stelmachowski, P.; Broś, P.; Makowski, W.; Kotarba, A. Demonstration of the Influence of Specific Surface Area on Reaction Rate in Heterogeneous Catalysis. *J. Chem. Educ.* **2021**, *98* (3), 935-940. DOI: 10.1021/acs.jchemed.0c01101. (f) Mianowski, A.; Owczarek, M.; Marecka, A. Surface area of activated carbon determined by the iodine adsorption number. *Energy sources, part A* **2007**, *29* (9), 839-850. DOI: 10.1080/00908310500430901. (g) Cerato, A. B.; Lutenecker, A. J. Determination of Surface Area of Fine-Grained Soils by the Ethylene Glycol Monoethyl Ether (EGME) Method. *Geotech. Test. J.* **2002**, *25* (3), 315-321. DOI: 10.1520/GTJ11087J. (h) Hanaor, D. A. H.; Ghadiri, M.; Chrzanowski, W.; Gan, Y. Scalable Surface Area Characterization by Electrokinetic Analysis of Complex Anion Adsorption. *Langmuir* **2014**, *30* (50), 15143-15152. DOI: 10.1021/la503581e. (i) Paykov, O.; Hawley, H. A Protein-Retention Method for Specific Surface Area Determination in Swelling Clays. *Geotech. Test. J.* **2013**, *36* (4), 606-611. DOI: 10.1520/GTJ20120197.

[8] (a) Komai, S. i.; Hattori, T.; Murakami, Y. CO H₂ titration for the determination of super small metal surface area. *J. Catal.* **1989**, *120* (2), 370-376. DOI: 10.1016/0021-9517(89)90276-5. (b) Gil, A. Classical and new insights into the methodology for characterizing adsorbents and metal catalysts by chemical adsorption. *Catal. Today* **2023**, *423*, 114016. DOI: 10.1016/j.cattod.2023.01.023. (c) Doña Rodríguez, J. M.; Herrera Melián, J. A.; Pérez Peña, J. Determination of the Real Surface Area of Pt Electrodes by Hydrogen Adsorption Using Cyclic Voltammetry. *J. Chem. Educ.* **2000**, *77* (9), 1195. DOI: 10.1021/ed077p1195. (d) Garrick, T. R.; Moylan, T. E.; Carpenter, M. K.; Kongkanand, A. Editors' Choice—Electrochemically Active Surface Area Measurement of Aged Pt Alloy Catalysts in PEM Fuel Cells by CO Stripping. *J. Electrochem. Soc.* **2017**, *164* (2), F55. DOI: 10.1149/2.0381702jes. (e) Domínguez-Domínguez, S.; Arias-Pardilla, J.; Berenguer-Murcia, Á.; Morallón, E.; Cazorla-Amorós, D. Electrochemical deposition of platinum nanoparticles on different carbon supports and conducting polymers. *J. Appl. Electrochem.* **2008**, *38* (2), 259-268. DOI: 10.1007/s10800-007-9435-9. (f) Osinga, T. J.; Linsen, B. G.; van Beek, W. P. The determination of the specific copper surface area in catalysts. *J. Catal.* **1967**, *7* (3), 277-279. DOI: 10.1016/0021-9517(67)90106-6. (g) Niwa, M.; Inagaki, S.; Murakami, Y. Measurement of exposed surface area of supports on supported metal oxide catalysts. *J. Phys. Chem.* **1985**, *89* (18), 3869-3872. DOI: 10.1021/j100264a020.

(h) Nguyen, V. T.; Horikawa, T.; Do, D. D.; Nicholson, D. Water as a potential molecular probe for functional groups on carbon surfaces. *Carbon* **2014**, *67*, 72-78. DOI: 10.1016/j.carbon.2013.09.057. I) SHIMADZU Home Page. <https://www.shimadzu-techno.co.jp/> (accessed 2024-12-24).

[9] (a) Schlumberger, C.; Scherdel, C.; Kriesten, M.; Leicht, P.; Keilbach, A.; Ehmann, H.; Kotnik, P.; Reichenauer, G.; Thommes, M. Reliable surface area determination of powders and meso/macroporous materials: Small-angle X-ray scattering and gas physisorption. *Micropor. Mesopor. Mat.* **2022**, *329*, 111554. DOI: 10.1016/j.micromeso.2021.111554. (b) Razouk, R. I.; Nashed, S.; Mourad, W. E. The heats of wetting of carbons in relation to their specific surface areas. *Carbon* **1965**, *2* (4), 359-364. DOI: 10.1016/0008-6223(65)90006-0. (c) Suganuma, A.; Matsumoto, Y.; Murata, E.; Hamada, T. Specific Surface Area Measurement by Air Permeability with Consideration for the Molecular Flow Effect. *KONA Powder Part. J.* **2000**, *18*, 230-235. DOI: 10.14356/kona.2000030. (d) Green, C. L.; Kucernak, A. Determination of the Platinum and Ruthenium Surface Areas in Platinum–Ruthenium Alloy Electrocatalysts by Underpotential Deposition of Copper. I. Unsupported Catalysts. *J. Phys. Chem. B* **2002**, *106* (5), 1036-1047. DOI: 10.1021/jp0131931. (e) Sheng, W.; Myint, M.; Chen, J. G.; Yan, Y. Correlating the hydrogen evolution reaction activity in alkaline electrolytes with the hydrogen binding energy on monometallic surfaces. *Energy Environ. Sci.* **2013**, *6* (5), 1509-1512. DOI: 10.1039/C3EE00045A. (f) Wei, C.; Sun, S.; Mandler, D.; Wang, X.; Qiao, S. Z.; Xu, Z. J. Approaches for measuring the surface areas of metal oxide electrocatalysts for determining their intrinsic electrocatalytic activity. *Chem. Soc. Rev.* **2019**, *48* (9), 2518-2534. DOI: 10.1039/C8CS00848E.

[10] (a) Lee, D. W.; Yoo, B. R. Advanced metal oxide (supported) catalysts: Synthesis and applications. *J. Ind. Eng. Chem.* **2014**, *20* (6), 3947-3959. DOI: 10.1016/j.jiec.2014.08.004. (b) Biswas, S.; Pal, A.; Pal, T. Supported metal and metal oxide particles with proximity effect for catalysis. *RSC adv.* **2020**, *10* (58), 35449-35472. DOI: 10.1039/D0RA06168A. (c) Tomishige, K.; Nakagawa, Y.; Tamura, M. Design of supported metal catalysts modified with metal oxides for hydrodeoxygenation of biomass-related molecules. *Curr. Opin. Green Sustain. Chem.* **2020**, *22*, 13-21. DOI: 10.1016/j.cogsc.2019.11.003.

1.7. Materials and instruments

The commercially available materials used in this thesis, along with their specific surface areas (S), are summarized in Tables 1.6–1.10. Crystallite sizes and crystal phases were determined by XRD analysis, while BET surface areas were measured by N_2 adsorption. Other relevant data were obtained directly from the manufacturers' product information or Ishihara group at Yokohama National University.

Table 1.6. Carbon materials.

Carbon (detailes)	BET S ($m^2 g^{-1}$)
MWCNT (40~60 nm diam., 5~15 μm length)	200
MWCNT (15 nm diam., 3 μm length)	293
MWCNT (15 nm diam., 3 μm length) ^[a]	345
CSCNT (70~100 nm diam., 5 μm length)	50
CSCNT (70~100 nm diam., 5 μm length) ^[b]	–
graphene (nanoplatelets aggregates sub-micron particles)	750
activated carbon (RB3)	975
activated carbon (RB4)	598
activated carbon (PK1-3)	557
activated carbon (GAC, 1240W)	916
carbon black (denka black Li-100)	64
carbon black (cabot vulcan VC72R)	328

Calcination was performed at ^[a]900°C, ^[b]700°C for 1 h in air. Details are based on commercial information (except for BET surface area by N_2 adsorption analysis).

Table 1.7. Silicas.

SiO ₂ (details)	BET S (m ² g ⁻¹)
JRC-SIO-10 (spherical, 70~150 μm, pore size: 10 nm)	300
60N (spherical neutral, particle size 40~50 μm)	738
TMPS-1.5 (mesoporous, pore size: 1.7 nm)	800
TMPS-2 (mesoporous, pore size: 2.4 nm)	845
TMPS-4 (mesoporous, pore size: 3.9 nm)	900

TMPS: Taiyokagaku (a company) mesoporous silica. Details are based on commercial information (except for BET surface area by N₂ adsorption analysis).

Table 1.8. Titanium oxides.

TiO _x (crystal phase, particle size/nm)	BET S (m ² g ⁻¹)
TiO ₂ (anatase, 5)	265
TiO ₂ (anatase, 5) ^[a]	120
TiO ₂ (anatase, 5) ^[b]	93
TiO ₂ (amorphous, 5)	215
TiO ₂ (anatase, 6)	290
TiO ₂ (anatase, 8)	215
TiO ₂ (anatase, 30)	49
TiO ₂ (rutile, 30)	27
TiO ₂ (anatase, 100)	18
TiO ₂ (rutile, 100)	14
TiO ₂ (brookite, 100)	37
TiO ₂ (anatase and rutile, 100) P25	53
Ti ₄ O ₇	13
Ti ₄ O ₇	9
TiO	39
TiO _{1.7}	3
Ti ₂ O ₃	6
5 at% Nb-TiO ₂	151
10 at% Nb-TiO ₂	124

Calcination was performed at ^[a]500°C, ^[b]380°C for 1 h in air. Details are based on commercial information (except for BET surface area by N₂ adsorption analysis).

Table 1.9. Iron oxides.

FeO _x (crystal phase, particle size)	BET S (m ² g ⁻¹)
Fe ₂ O ₃ (γ, 30~50 nm)	41
Fe ₂ O ₃ (γ, < 50 nm)	59
Fe ₂ O ₃ (α, 0.3 μm)	17
Fe ₂ O ₃ (α, < 5 μm)	10
Fe ₂ O ₃ (α, γ)	10
Fe ₃ O ₄ (50~100 nm)	13
Fe ₃ O ₄ (1 μm)	9

Crystalline phase and BET surface area were determined by XRD and N₂ adsorption analysis, respectively. Particle size is based on commercial information.

Table 1.10. Copper oxides.

CuO (particle and crystalline size)	BET S (m ² g ⁻¹)
CuO (10~50, 14 nm)	26
CuO (30, 28 nm)	24
CuO (< 50, 22 nm)	24
CuO (< 1 μm, 22 nm)	14
CuO (–, 39 nm)	5

Crystalline size and BET surface area were determined by XRD and N₂ adsorption analysis, respectively. Particle size is based on commercial information.

Table 1.11. Zirconium oxides.

ZrO ₂ (crystal phase)	BET S (m ² g ⁻¹)
Teragonal	74
Monoclinic	25
Monoclinic	67
Teragonal	59
Monoclinic	8
Monoclinic-Tetragonal	65
Monoclinic	87
Monoclinic	19
Monoclinic	58
Monoclinic-Tetragonal	55
Monoclinic	21
Monoclinic	6

Details were obtained either from the Ishihara group at Yokohama National University or based on commercial information.

All reagents used in this work were commercially available and employed without further purification or treatment; therefore, no additional details are provided here.

The analytical instruments used in this thesis are introduced below.

According to the Lambert-Beer law, incident light and transmitted light have a specific relationship (Formula 1.2). The concentration of an unknown solution can be measured using the absorbance of a solution of known concentration and the absorbance of an unknown solution.

$$A = -\log \frac{I}{I_0} = \varepsilon cL \dots \dots \dots \textbf{(Formula 1.2)}$$

T: Transmittance, *A*: Absorbance, *I*₀: Intensity of incident light, *I*: Intensity of transmitted light, *ε*: Constant, *c*: Concentration, *L*: Light path length.

The absorbance of the solution before and after the adsorption experiments were measured on UV-Vis spectrometer UV2600 (SHIMADZU, optical path length 1 cm).

Infrared spectroscopy (IR) is a powerful tool for analyzing chemical bonds and functional groups. By utilizing the principle that molecular bonds absorb specific infrared vibration wavenumbers, this technique allows for both qualitative and quantitative analysis of specific compounds. The mid-infrared region, ranging from approximately 4,000–400 cm⁻¹, is typically employed to study fundamental

molecular vibrations. The FT-IR spectra of metal oxide powder before and after the adsorption, and the catalyst were measured on IR Affinity-1S (SHIMADZU) by KBr method.

The BET method was introduced in Section 1.4.1. In order to remove the effects of impurities absorbed on the sample, the sample is pretreated by evacuation while increasing the temperature (room temperature \rightarrow 100 or 120°C). After pretreatment, the sample is subjected to nitrogen adsorption at the temperature of liquid nitrogen. The total surface area of the material can be obtained from the BET method. The Barrett-Joyner-Halenda method (BJH method), which is also widely used as pore size distribution analysis method, is an analysis method that assumes that mesopores are cylindrical in shape based on Kelvin's capillary condensation theory. Using this method, pore size and volume can be obtained. BET surface area, pore size and pore volume were analyzed by N₂ adsorption on Micromeritics TriStar, Surface Area and Porosity Analyzer (SHIMADZU).

X-ray diffraction (XRD) leverages the wave-like properties of X-rays, which possess wavelengths comparable to interatomic distances. When a beam of monochromatic X-rays is directed at a crystalline sample, the X-rays are scattered by the electrons of the atoms within the crystal. This scattering results in wave interference, which can be either constructive or destructive, depending on the relative positions of the atoms in the crystal lattice.

The diffraction pattern is based on Bragg's Law:

$$n\lambda = 2d\sin\theta \dots\dots\dots \textbf{(Formula 1.3)}$$

The Scherrer equation can be used to calculate the grain size as follows.

$$\tau = \frac{K\lambda}{\beta\cos\theta} \dots\dots\dots \textbf{(Formula 1.4)}$$

In formulas 1.3 and 1.4, n is an integer representing the order of the diffraction, λ is the wavelength of the incident X-rays, d is the spacing between atomic planes in the crystal, θ is the angle of incidence (or diffraction angle), τ is the mean crystallite size, K is a dimensionless shape factor, β is the line broadening at half the maximum intensity.

The all-prepared catalysts were analyzed by XRD (Smartlab III, Rigaku), CuK α (1.5405 Å), scanning speed: 2° min⁻¹, prefocusing method. The crystalline sizes of metal oxide in catalyst were, according to Scherrer Equation.

Transmission electron microscope (TEM) is a specialized type of electron microscope. It operates by directing an electron beam onto the specimen under observation, analyzing the spatial distribution of electron transmittance based on the intensity of the transmitted electrons. The wave-like properties of electrons can be harnessed to visualize the structure of the specimen through interference patterns

produced by electron diffraction within the sample. The transmission electron microscope TEM (JEM-3200FS, 300 kV) was used for observing Fe₂O₃/graphene and CuO/graphene catalysts.

Scanning Electron Microscopy (SEM) is a powerful imaging technique used to examine the fine structure and morphology of sample surfaces. SEM images provide excellent three-dimensional effects, facilitating a deeper understanding of the sample's morphology and structural characteristics. The surface morphology of TiO₂ after adsorption experiments and Fe₂O₃/activated carbon catalyst were analyzed using JSM-7700F scanning electron microscope (JEOL).

The thermogravimetry-differential thermal simultaneous measurement instrument (TG-DTA) is a device that concurrently conducts thermogravimetry (TG) and differential thermal analysis (DTA). Thermogravimetry involves measuring the weight of a sample as its temperature changes, while differential thermal analysis measures the temperature difference between the sample and a reference as the temperature changes. By monitoring these temperature differences, it is possible to identify endothermic and exothermic peaks associated with various reactions. TG-DTA was used for analysis of metal oxide catalysts by Thermos plus EVO2 series (Rigaku Corporation). Analytical conditions of TG-DTA: from 40°C, 10°C min⁻¹, at 800°C for 0.5 h, air.

Nuclear magnetic resonance (NMR) was considered an experimental technique for investigating the internal structure of atomic nuclei. However, it was later found that the Larmor frequency of a nucleus varies slightly depending on the atom's chemical bonding state, a phenomenon known as chemical shift. This discovery paved the way for using NMR as a tool for substance analysis and identification. The spectroscopic technique that utilizes NMR to obtain spectra is known as nuclear magnetic resonance spectroscopy.

Gas chromatography (GC) is a widely used analytical technique in chemistry for separating and analyzing compounds that can be vaporized without decomposition. Common applications of GC include assessing the purity of a molecule and separating the components of a mixture. The process involves injecting a gas or liquid sample into a mobile phase, often referred to as a carrier gas, which then passes through a stationary phase. The mobile phase is typically an inert gas, such as argon or nitrogen. The stationary phase can be either solid or liquid, though modern GC systems predominantly use polymeric liquid stationary phases.

Organic products were analyzed by GC and ¹H-NMR; GC-2010 plus (Shimadzu, Japan), column: DB-1, length 15 m, inner diameter 0.15 mm, thickness 0.15 μm; NMR (Bruker, 400 MHz).

1.8. Abbreviation

S (specific) Surface area.

Probe molecule Some measurable property of the molecule changes upon interaction with the analyte, using this interaction to indirectly reflect the nature of the analyte. In this thesis, the author refer to organic molecules that selectively adsorb onto the surface of metal oxides while exhibiting minimal adsorption on the support.

MWCNT Multi-walled carbon nanotube.

CSCNT Cup stacked carbon nanotube.

RB3 or 1240W 2 types of activated carbon.

SiO₂ Silicon oxide or silica.

SIO Silicon oxide or silica.

TMPS Taiyokagaku meso porous silica.

DMF *N, N*-dimethylformamide

EtOH Ethanol

MeCN Acetonitrile

θ Adsorption ratio.

W Adsorption amount.

W_S Adsorption amount per unit surface area.

ORR Catalytic activity in oxygen reduction reaction for hydrogen fuel cell.

Double layer capacitance (C_{dl}) The double layer in a hydrogen fuel cell refers to the electric double layer formed at the interface between the electrode (such as platinum) and the electrolyte.

XRD X-ray diffraction.

N₂ (nitrogen) adsorption a method to characterize the solid materials (in formation of the surface areas or pores) at low temperature.

TG-DTA Thermogravimetry and differential thermal analysis.

TEM Transmission electron microscope.

SEM Scanning electron microscope.

FT-IR Fourier transforms infrared spectroscopy.

UV-Vis Ultraviolet-Visible absorption spectroscopy.


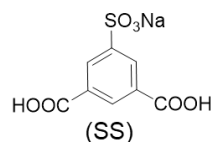
GC Gas chromatography.

NMR Nuclear magnetic resonance.

Crystal facet Flat faces on geometric shapes of this crystal phases.

Chapter 2. Surface Area Measurement of Metal Oxide by Selective Adsorption of Organic Molecules

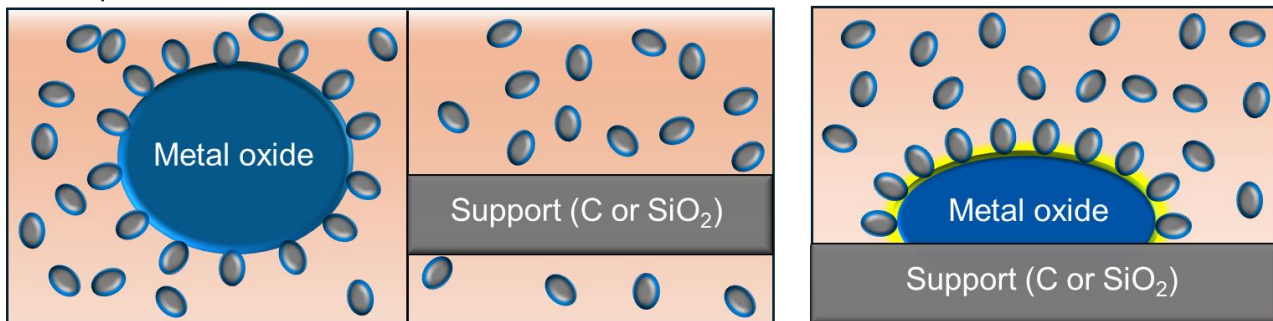
(a) Selective adsorption

 Probe molecule

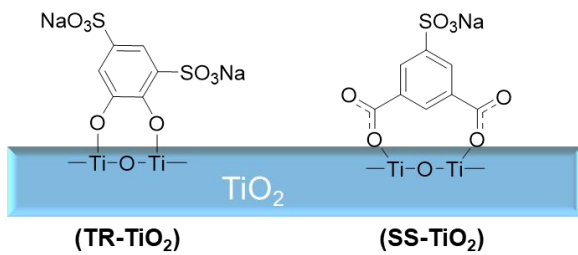
Adsorption amount \propto BET S

Non-adsorption

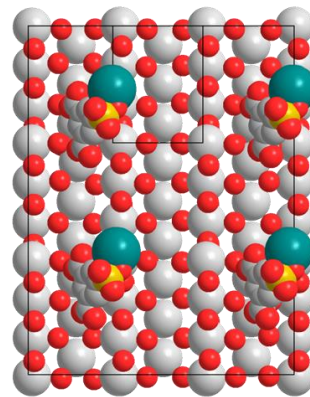
Selective-adsorption



(b) Adsorption structure



**An example of SS
on TiO₂ rutile {110}**



2.1 Introduction: adsorption of molecules on metal oxide

Over the past century, metal oxides, particularly titanium dioxide (TiO_2), have been widely recognized as photosensitive catalysts [11a-c]. However, due to their wide band gap (e.g., 3.2 eV for the anatase phase), the photocatalytic efficiency of bare TiO_2 is limited. To overcome this, TiO_2 has been modified, primarily through chemical adsorption with organic compounds such as hydroquinone and salicylic acid, resulting in significantly enhanced catalytic activity [11a-c, 12a, f, g, l]. To further optimize and better understand the catalytic performance of TiO_2 modified by organic compounds, derivatives such as phenol and benzoic acid have been extensively studied for their adsorption behavior on TiO_2 surfaces and their influence on catalytic processes [12a-d, f-l].

Surface atomic defects on metal oxides facilitate the adsorption of water molecules, leading to the formation of hydroxyl groups on the surface. These hydroxyl groups contribute to the strong hydrophilicity of metal oxide surfaces, particularly TiO_2 , as demonstrated in previous studies [7a, b, 12a, c]. In contrast, carbon-based materials are commonly used as supports typically exhibit hydrophobic properties [7a, b]. Hydrophilic functional groups on activated carbon surfaces have been characterized using water molecules as probe molecules [8g, h]. Consequently, the exposed surface area of metal oxides can be quantified by selectively adsorbing hydrophilic organic molecules onto the metal oxide surfaces, while avoiding adsorption onto the hydrophobic carbon supports.

Previous studies have shown that various organic molecules form chemisorbed structures on TiO_2 surfaces via carboxyl or hydroxyl groups [12a, c]. The chemisorption mechanism involves the removal of protons from the organic molecules and hydroxyl groups from the metal oxide surface, resulting in the formation of covalent bonds and water molecules. An example of this adsorption mechanism, salicylic acid (SA) on TiO_2 , is illustrated in Figure 2.1a. The deprotonated organic molecules replace surface hydroxyl groups, forming stable chemisorbed structures. In this process, metal oxides serve as basic surfaces, whereas the organic molecules act as acidic adsorbates [12a, c]. In contrast, SiO_2 surfaces are characterized by acidic properties [12n], which facilitate adsorption of basic organic molecules such as ammonia or pyridine [1e, 7a, b, 8b]. Conversely, acidic molecules such as catechol or salicylic acid are expected to exhibit minimal adsorption on SiO_2 surfaces due to their acidity. Consequently, some hydrophilic and acidic molecules are expected to adsorb selectively onto several metal oxides over SiO_2 supports.

In this work, various hydrophilic and acidic aromatic compounds were extensively studied for their adsorption behaviors on metal oxides such as TiO_2 . These compounds and their derivatives have demonstrated selective adsorption on metal oxides, which makes them serve as promising candidate

molecules for accurate determination of surface areas (see Figure 2.1b). The adsorption amounts of the aromatic probe molecules were quantified using UV-Vis spectroscopy due to its high accuracy at low concentrations.

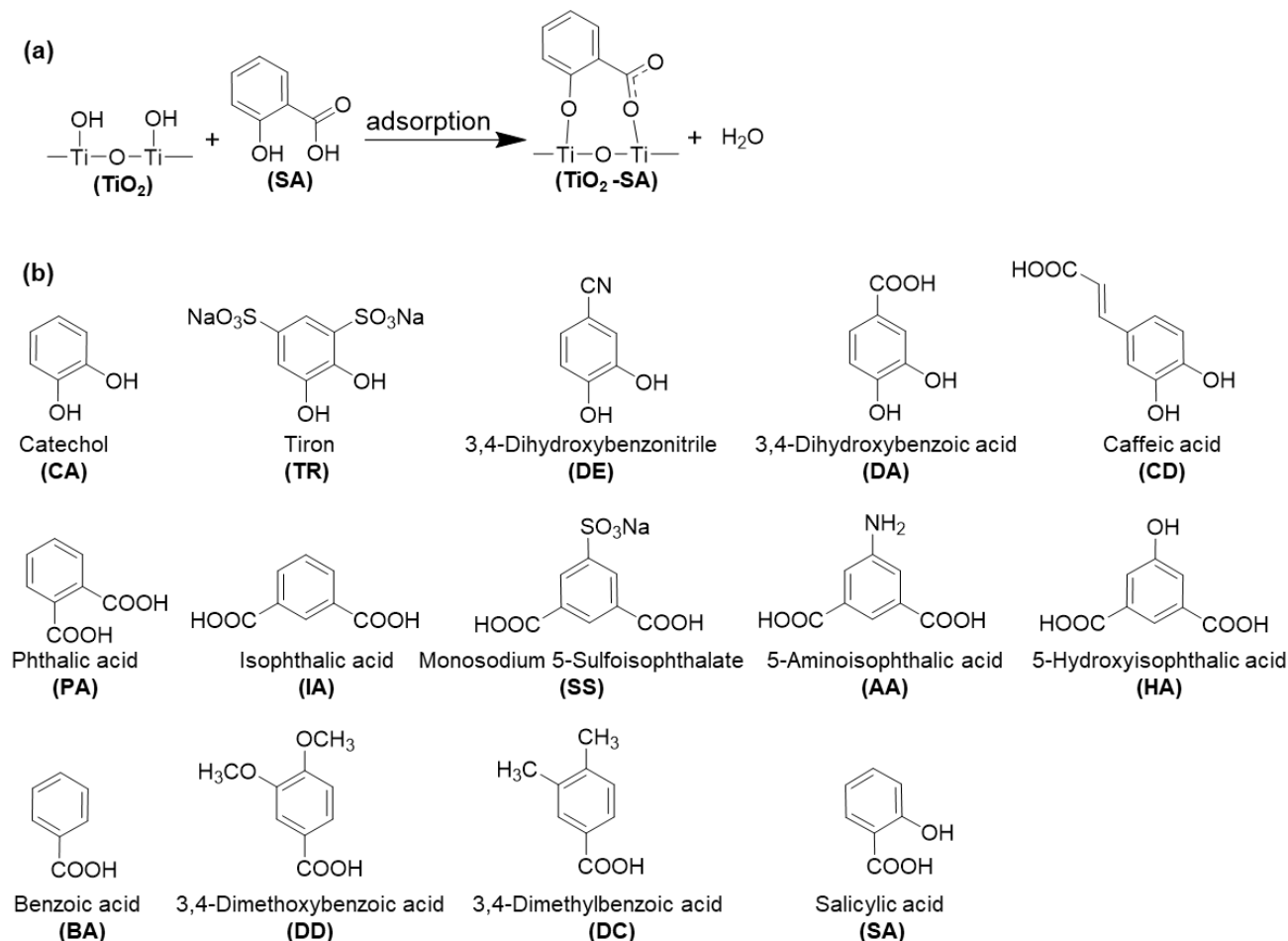


Figure 2.1. (a) Proposed chemisorption of salicylic acid (SA) on TiO₂ [12a-c, f]. (b) Organic compounds investigated in the adsorption experiments in this study.

Experimental

In the typical procedure, powdered materials such as TiO₂ or carbon (10 mg) were added to a 5 mL solution of the organic molecule (0.2 mM) in *N,N*-dimethylformamide (DMF) in a brown vial. The mixture was stirred or shaken at 110°C for 1 h in air. The organic molecules employed in the adsorption experiments are summarized in Figure 2.1b.

The adsorption ratio and amount were calculated by UV-Vis spectroscopy of the supernatant after centrifugation, based on the following equations:

$$\theta = \frac{A_1 - A_2}{A_1} \dots \dots \dots \text{(Formula 2.1)}$$

$$W = C V \frac{A_1 - A_2}{A_1} \dots \dots \dots \text{(Formula 2.2)}$$

$$W_s = \frac{W}{S} \dots \dots \dots \text{(Formula 2.3)}$$

In these formulas, θ and W represent the adsorption ratio (%) and the adsorption amount (mol), respectively; C and V are the concentration (mol L⁻¹) and volume (L) of solution, respectively; A_1 and A_2 are the absorbance values before and after adsorption, W_s is adsorption amounts per unit surface area (mol m⁻²), S is BET surface area (m² g⁻¹).

The adsorption structures on TiO₂ were characterized by FT-IR, after washing by DMF and drying under reduced pressure. Additionally, TiO₂ samples (30 nm rutile and 100 nm anatase) after adsorption experiments were observed using SEM, and the results are summarized in Appendix (Figure 2.24).

2.3 Results and discussion

2.3.1. Investigation of organic molecules selectively adsorbed on titanium oxide

The author focused on investigating the selective adsorption of probe molecules on metal oxides and further designed the following experiments. Titanium dioxide (TiO₂, particle size: 30 nm, crystalline structure: anatase, BET surface area $S = 49 \text{ m}^2 \text{ g}^{-1}$), multi-walled carbon nanotubes (MWCNTs, diameter: 40–60 nm, length: 5–15 μm , $S = 200 \text{ m}^2 \text{ g}^{-1}$), and activated carbon (RB3 type, $S = 975 \text{ m}^2 \text{ g}^{-1}$) were selected as representative adsorbents. A variety of organic molecules, as shown in Figure 2.1b, were used as adsorbates, and their adsorption behaviors were evaluated under different solvent and temperature conditions. The adsorption ratios (θ , %) for each molecule are summarized in Table 2.1.

Catechol (CA) was observed to adsorb onto both TiO₂ and carbon materials under various conditions including water, DMF, EtOH, and MeCN at various temperatures, indicating its unsuitability as a selective probe molecule (entries 1–8). Nevertheless, in DMF, CA exhibited markedly lower adsorption on carbon materials, particularly activated carbon (entries 7 and 8). After multiple trials, tiron (TR) was identified as a promising probe candidate due to its selective adsorption onto TiO₂ in DMF, accompanied by negligible adsorption on carbon materials (entries 11 and 12). Owing to TR's limited solubility in ethanol and MeCN (<0.02 mM), these solvents were excluded from further adsorption studies. Temperature was also found to significantly influence adsorption behavior [7a, b], with noticeable variation in adsorption ratios across different conditions (entries 1–12).

Table 2.1. Adsorption ratios of various compound on TiO₂ and carbon.

Entry	Adsorbate	Solvent	T (°C)	θ (%)		
				TiO ₂	MWCNT	Activated carbon
1	CA	H ₂ O	25	40	21	98
2	CA	H ₂ O	80	39	17	99
3	CA	EtOH	25	48	1	49
4	CA	EtOH	70	53	< 1	72
5	CA	MeCN	25	83	2	49
6	CA	MeCN	70	88	2	72
7	CA	DMF	25	52	< 1	16
8	CA	DMF	110	58	4	54
9	TR	H ₂ O	25	29	9	86
10	TR	H ₂ O	80	27	8	96
11	TR	DMF	25	37	1	3
12	TR	DMF	110	50	2	4
13	DA	DMF	110	91	13	62
14	CD	DMF	110	93	15	86
15	IA	DMF	110	60	<1	12
16	SS	DMF	110	47	<1	3
17	AA	DMF	110	59	4	25
18	SA	DMF	110	41	5	8

Adsorption condition: adsorbent (10 mg) in solution (5 mL) of organic molecule (0.2 mM), stirring, 1 h. Adsorption ratio was quantified by UV-Vis analysis.

Furthermore, comparative analyses were conducted using other organic molecules: 3,4-dihydroxybenzoic acid (DA), caffeic acid (CD), isophthalic acid (IA), sodium 5-sulfoisophthalate (SS), 5-aminoisophthalic acid (AA), and salicylic acid (SA), which revealed that SS, having structural similarities with TR, exhibited comparable adsorption behavior with TR (entries 13–18). SS selectively adsorbed onto TiO₂ in DMF at 110°C. The selective adsorption of TR and SS found here is likely attributed to their molecular structures having sulfonate groups and proximal two hydroxyl or carboxyl functionalities. In summary, both TR and SS preferentially adsorb onto TiO₂ to carbon materials in DMF, underscoring their potential as probe molecules for selective surface analyses of TiO₂.

Unlike gas-phase adsorption, which typically involves interactions simply between single molecules and the adsorbent, liquid-phase adsorption in solution is inherently more complex due to the simultaneous involvement of interactions among solute, solvent, and adsorbent [7a, b]. In general, molecules with lower solubility tend to exhibit stronger adsorption affinities with adsorbent [7a, b].

The space-filling models of the two molecules, TR and SS, were analyzed to elucidate their structural characteristics. Both molecules possess sodium sulfonate groups with hydroxyl or carboxyl groups around the benzene ring, forming a distinct three-dimensional hydrophilic shell (Figure 2.2). Although the benzene ring itself is hydrophobic, the presence of these polar functional groups results in a predominantly hydrophilic molecular surface. The minimal adsorption of TR and SS onto hydrophobic carbon materials can be attributed to significant repulsive interactions between these hydrophilic molecular surface and hydrophobic carbon surface.

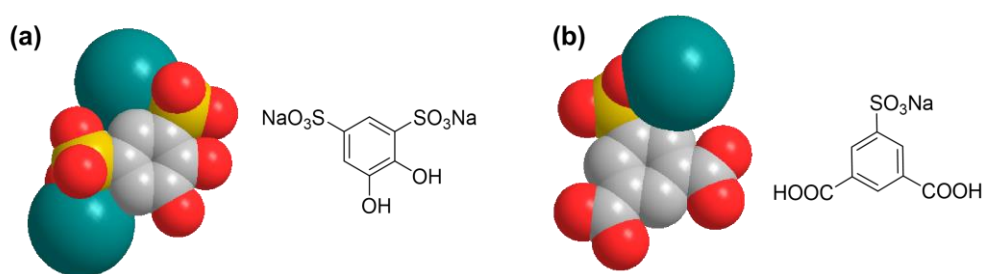


Figure 2.2. Space-filling models of (a) TR and (b) SS.

C: gray, O: red, S: yellow, Na: blue.

To gain deeper insight into the nature of TR adsorption on TiO_2 , desorption experiments were carried out. In the desorption procedure, DMF solvent (4 mL) was added to the mixture after adsorption experiment using TiO_2 (30 nm anatase, 10 mg) and the TR solution in DMF (1 mL). After stirring for 1 h at room temperature, centrifugation was conducted to measure the TR concentration in the supernatant. This process was repeated at 70°C and 110°C for the second and third desorption cycles, respectively, and the corresponding remaining adsorption rates were calculated. At all the tested temperatures, the desorption of TR from the TiO_2 surface remained minimal compared to its initial adsorption (Table 2.2). As physical adsorption typically results in substantial desorption, this observation indicates that TR adsorption on TiO_2 is predominantly chemical adsorption. Notably, the adsorption amount increased with rising temperature (Table 2.1, entries 11 and 12). The temperature-dependent increase in adsorption can be attributed to two main factors: (1) the acceleration of adsorption kinetics at higher temperatures, leading to faster adsorption rates, and (2) the possible removal of pre-adsorbed water or water produced during the adsorption process, which exposes additional adsorption sites on the TiO_2 surface. These factors collectively account for the enhanced adsorption observed at elevated temperatures, which will be discussed in detail in Section 2.3.2.

Table 2.2. Adsorption ratios of TR on TiO₂ by desorption.

Run (<i>T</i> /°C)	0 (110)	1 (25)	2 (70)	3 (110)
Residual ratio (%)	50	47	44	40

Desorption condition: After the adsorption of TR (as described in Table 2.1, entry 12), DMF (4 mL) was added to the remaining mixture of TiO₂ (30 nm anatase) and solution. The suspension was stirred for 1 h, and the residual TR concentration was quantified by UV-Vis analysis.

The adsorption experiments summarized in Table 2.1 demonstrates that TR and SS exhibit considerable potential as probe molecules for surface analysis. A fundamental requirement for employing such molecules to estimate surface area of metal oxides is the existence of a positive correlation between the adsorption amount and the surface area. Accordingly, subsequent experiments were conducted to evaluate whether the adsorption amounts of TR and SS on TiO₂ correlate with the surface area of TiO₂. In parallel, the adsorption amounts of TR and SS to various carbon materials were also assessed.

To address these objectives, adsorption experiments were performed using various TiO₂ and carbon-based adsorbents. The TiO₂ samples included four types with particle sizes of 30 nm and 100 nm and crystal phases such as anatase, rutile, and brookite (as listed in Table 1.8, Chapter 1). The carbon-based adsorbents comprised carbon nanotubes, graphene, carbon black, and activated carbon (Table 1.6, Chapter 1). All adsorption experiments were conducted in DMF solution at 110°C for 1 h. The relationship between the adsorption amount (W , mol) of TR and SS and the BET surface area (m² g⁻¹) of the adsorbents is illustrated in Figure 2.3 (examples of UV spectra are provided in Appendix, Figure 21a-c). The results show that the adsorption amounts of TR and SS on TiO₂ are directly proportional to the BET surface area of TiO₂, regardless of its particle size (e.g., 30 nm or 100 nm) and crystal structure (e.g., anatase or rutile). A similar trend was observed for TiO_x samples with different Ti/O atomic ratios (e.g., TiO_{1.7} and Ti₂O₃) under shaking conditions (Figure 2.4). Notably, the adsorption on carbon materials was found to be negligible.

Except for minor deviations observed for TiO_x samples, adsorption amounts on titanium oxides consistently remained proportional to their BET surface areas under both stirring and shaking conditions (Figures 2.3 and 2.4). The adsorption on carbon materials slightly decreased under shaking, leading to higher adsorption selectivity on titanium oxides over carbon materials.

Diffusion and mass transfer also play a critical role in determining the adsorption amount within a fixed timeframe. Given the short adsorption duration of 1 h, significant stirring enhances the mass transfer. This is particularly important for porous materials such as multi-walled carbon nanotubes (MWCNTs) and

activated carbon, where molecules may enter ultra-small pores and undergo physical adsorption. Furthermore, magnetic stirring may lead to mechanical fragmentation of carbon materials and/or adsorption on newly exposed surfaces. These effects can markedly increase the apparent adsorption amounts for carbon materials.

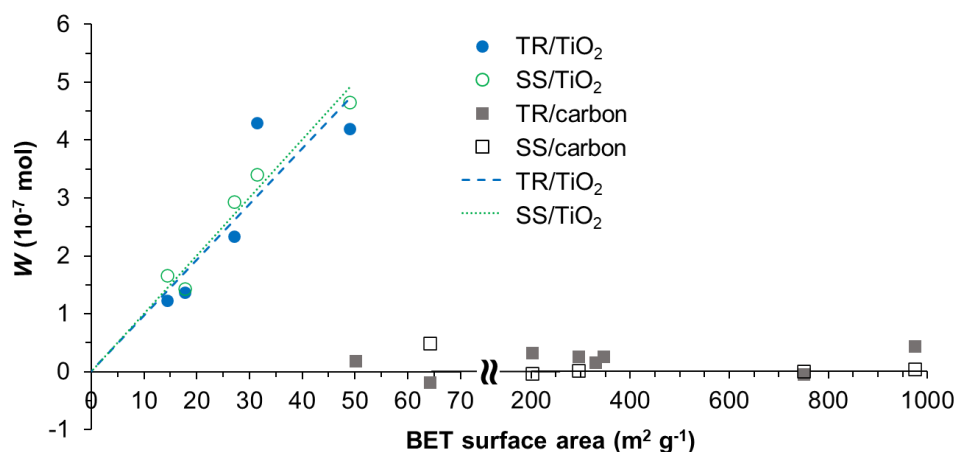


Figure 2.3. Adsorption amounts of TR and SS on TiO₂ and carbon under stirring.

Adsorption condition: adsorbent (10 mg) in solution (5 mL) of organic molecule (DMF, 0.2 mM), 110°C, stirring, 1 h.

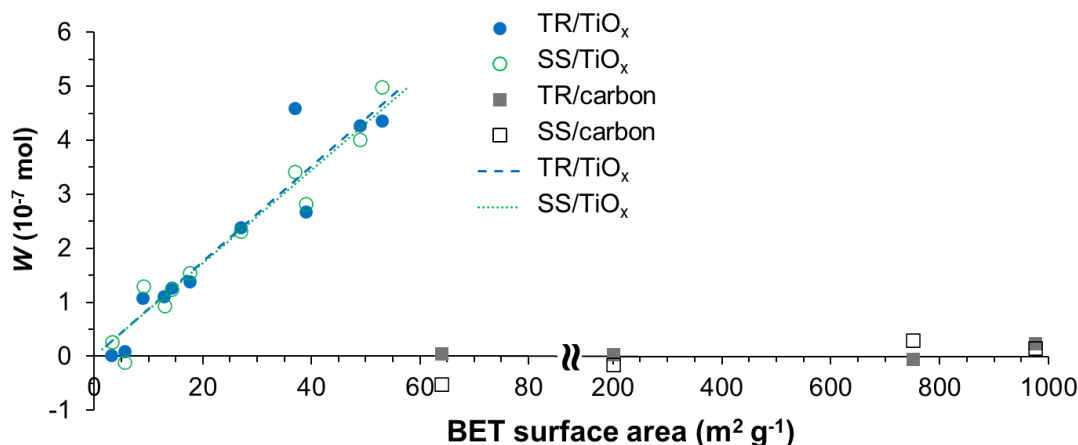


Figure 2.4. Adsorption amounts of TR and SS on TiO_x and carbon under shaking.

Adsorption was conducted under shaking. The other adsorption condition was identical to that used in Figure 2.3.

The adsorption amounts per unit surface area (W_s , mol m^{-2}) of CD, DA, TR, and SA on four types of TiO₂ were further evaluated under stirring conditions at 110°C for 1 h. The results indicated that the adsorption amounts of SA, CA, and TR were proportional to the BET surface area of TiO₂, whereas CD

deviated from this trend (Figure 2.5). This deviation might be due to the presence of its compact aliphatic carboxyl group, which acts as an adsorbing functional group on TiO₂.

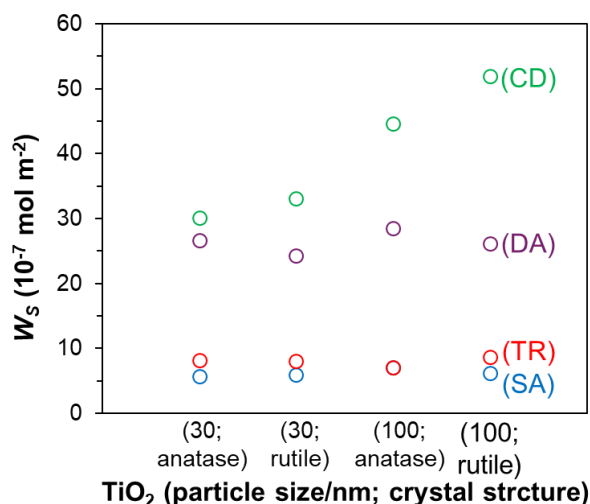


Figure 2.5. Adsorption amounts of CD, DA, TR, and SA on TiO₂.

The adsorption experiments were conducted using CD (0.5 mM), DA (0.5 mM), TR (0.2 mM), and SA (0.2 mM) under the same conditions as those described in Figure 2.3.

Previous experiments have demonstrated that TR and SS selectively adsorb onto titanium oxide rather than carbon materials (Table 2.1, Figures 2.3 and 2.4), and their adsorption amounts were proportional to the BET surface area of titanium oxide. To further assess the accuracy and applicability of this selective adsorption approach for measuring the surface area of titanium oxide in composite systems, an additional experiment was designed. Titanium oxide and carbon materials with known specific surface areas were physically mixed at defined ratios (Table 2.3). Based on these ratios, the theoretical surface area of titanium oxide in the mixture was calculated. If the surface area determined using the molecular adsorption method corresponds closely to the calculated value, it would provide indirect validation of the present method.

The adsorption of TR and SS on the mixtures of TiO₂ and carbon materials, blended in specific ratios, was carried out by shaking at 110°C in DMF (Table 2.3). The results showed that the TiO₂ surface area calculated via the selective adsorption of TR closely matched the value estimated from the blending ratios. The presence of carbon nanotubes and activated carbon exerted minimal influence on the adsorption behavior of TiO₂. This result supports the feasibility of using the selective adsorption of TR or SS as a method for determining the surface area of TiO₂ in carbon-based composite/supported materials.

Table 2.3. Adsorption of TR and SS on TiO₂-carbon (blended materials)

TiO₂ (30 nm anatase) 25 or 50 wt% + carbon (MWCNT or activated carbon RB3) $\xrightarrow{\text{mixing}}$ TiO₂/carbon

Entry	TiO ₂ /carbon	TiO ₂ surface area (m ² g ⁻¹)	
		by mixing ratio	by adsorption of TR
1	25 wt% TiO ₂ /CNT	12	13
2	50 wt% TiO ₂ /CNT	25	24
3	25 wt% TiO ₂ /RB3	12	15
4	50 wt% TiO ₂ /RB3	25	27

TiO₂-carbon materials were made by mixing TiO₂ (30 nm anatase, $S = 49 \text{ m}^2 \text{ g}^{-1}$) and carbon (MWCNT, $S = 200 \text{ m}^2 \text{ g}^{-1}$; activated carbon RB3, $S = 871 \text{ m}^2 \text{ g}^{-1}$). TiO₂ surface area was calculated by ratios of blending, or the selective adsorption of TR. Experimental condition and TiO₂ surface area based on Figure 2.4.

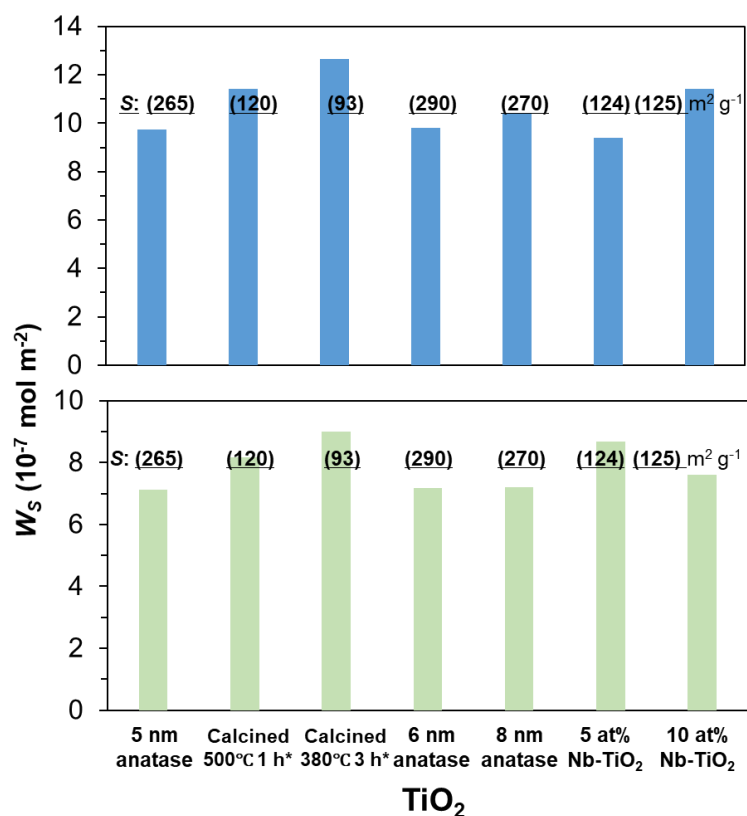


Figure 2.6. Adsorption amounts of (a) TR and (b) SS on high surface area or Nb-doped TiO₂.

Adsorption condition: adsorbent (10 mg) in solution (5 mL) of organic molecule (DMF, 1.25 mM), 110°C, stirring, 1 h. *Calcined TiO₂ (5 nm, anatase).

On the other hand, specific surface areas of supported TiO₂ catalysts can be higher than those investigated here. Moreover, the TiO_x/carbon catalysts discussed in the next chapter (Chapter 3) include Nb doping. Therefore, the adsorption amounts per unit surface area (W_s , mol m⁻²) were evaluated for several high-surface-area TiO₂ materials (with particle sizes of 5, 6, or 8 nm and anatase crystal structure), together with three commercial anatase TiO₂ samples, 5 nm anatase calcined at 500°C for 1 h or at 380°C for 3 h in air, and Nb-doped TiO₂ with 5 or 10 at% Nb ($S = 93\text{--}270 \text{ m}^2 \text{ g}^{-1}$; see Table 1.8 in Chapter 1). In high-concentration DMF solutions of TR and SS, comparable W_s values were obtained among these TiO₂ materials as shown in Figure 2.6. This result further demonstrates that the selective adsorption of TR or SS in DMF solution is applicable for evaluating the surface area of high-surface-area or Nb-doped TiO₂ supported on carbon.

Previous experiment (in Table 2.2) revealed that TR primarily undergoes chemical adsorption on the TiO₂ surface. Several studies reported that FT-IR spectrum can be utilized to analyze the chemical adsorption structure of organic molecules on titanium oxide materials [12a-d, f-l]. TiO₂ (6 nm anatase) with a high specific surface area demonstrated significantly high adsorption amounts of TR or SS as shown in Figure 2.6. The FT-IR spectra measured by KBr method are shown in Figures 2.7a and c.

In Figure 2.7a, the peaks at 1631 and 1402 cm⁻¹ were assigned to bending vibrations of the hydroxylic group $\delta(\text{O-H})$ and adsorbed water $\delta(\text{HO-H})$ on surface of TiO₂, respectively [13a]. The main characteristic bands for free TR include: stretching vibrations of the aromatic ring $\nu(\text{C=C, C-C})$ at 1635, 1589, 1467 and 1436 cm⁻¹ [12f, g], bending vibration of the hydroxylic groups $\delta(\text{C-OH})$ at 1379 cm⁻¹ [12f, g], stretching vibrations of the hydroxylic groups $\nu(\text{C-OH})$ at 1292 and 1232 cm⁻¹ [12f, g], stretching vibrations of the sodium sulfate $\nu(\text{O-S(=O)}_2)$ at 1190, 1105 and 1045 cm⁻¹ [12e, l, m]. For TR-TiO₂, bending vibrations of the hydroxylic groups $\delta(\text{C-OH})$ at 1379 cm⁻¹ disappeared, and a new band at 1276 cm⁻¹ corresponding to stretching vibrations $\nu(\text{C-O-Ti})$ appeared. This suggests a possible adsorption structure for TR involving the two adjacent phenolic groups as shown in Figure 2.7 b [12f, g]. The bands of TR-TiO₂ at 1190, 1093 and 1033 cm⁻¹ were assigned to stretching vibrations of the sodium sulfate $\nu(\text{O-S(=O)}_2)$, as compared with the literature on adsorption of CA-TiO₂ [12f, g]. These bands should not be associated with the C-H or O-H groups of the benzene ring, as these stronger bands show almost no change before and after adsorption. The absorption band of the benzene ring also shifted under the influence of the new environment, indicating that chemisorption on TiO₂ alters the electronic distribution, which propagates across the entire aromatic ring [12f].

Similarly, in Figure 2.7c, the primary bands of assignment for free SS are as follows: stretching vibrations of the carboxylic groups $\nu(\text{C=O})$ at 1737 and 1712 cm⁻¹ [12b, d, h], stretching vibrations of the aromatic ring $\nu(\text{C=C, C-C})$ at 1676, 1612, 1473 and 1433 cm⁻¹ [12f, g], asymmetric and symmetric

stretching vibrations of the carboxylic groups $\nu_{as}(\text{CO}_2^-)$ and $\nu_s(\text{CO}_2^-)$ at 1676/1612 and 1373 cm^{-1} [12b, d, h], stretching and bending vibrations of the carboxylic groups (C–OH) at the region of 1300–1166 cm^{-1} [12b, d, h], stretching vibrations of the sodium sulfate $\nu(\text{O–S(=O)}_2)$ at 1215, 1112 and 1047 cm^{-1} [12e, l, m]. For SS-TiO₂, the bands at 1737 and 1712 cm^{-1} corresponding to the carboxylic groups $\nu(\text{C=O})$ disappeared, while new bands appeared at 1565 and 1365 cm^{-1} , which were assigned to the asymmetric and symmetric stretching vibrations of the carboxylic groups $\nu_{as}(\text{CO}_2^-)$ and $\nu_s(\text{CO}_2^-)$. These results suggest that the two carboxylic groups might be adsorbed on TiO₂, as illustrated in Figure 2.7d [12b, d, h]. Accordingly, the bands of SS-TiO₂ at 1201, 1110 and 1045 cm^{-1} were assigned to stretching vibrations of the sodium sulfate $\nu(\text{O–S(=O)}_2)$, based on the same analysis used for TR comparison with the literature [12b].

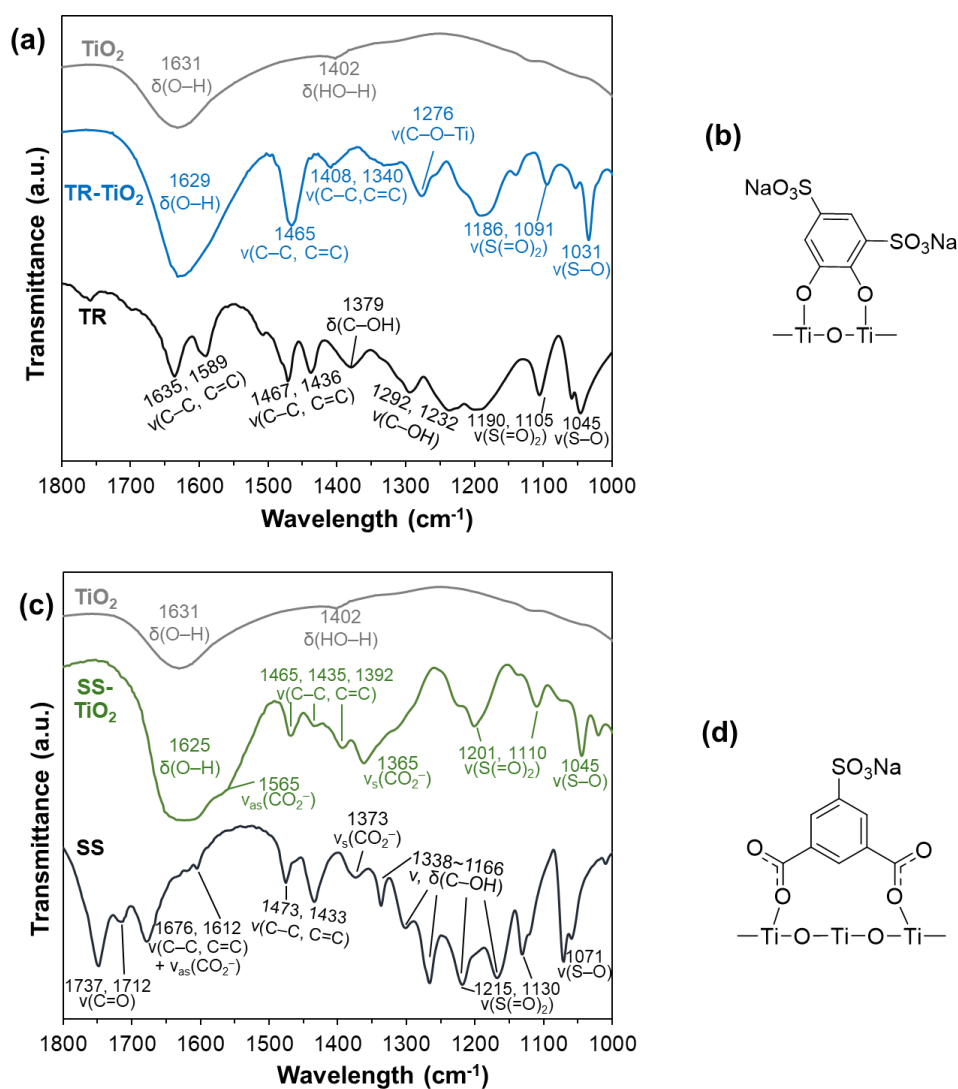


Figure 2.7. FT-IR (KBr) of (a) TR and (c) SS-TiO₂ (6 nm anatase) and the predicted adsorption structures of (b) TR and (d) SS-TiO₂.

TiO₂ (6 nm anatase) after adsorption, as described in Figure 2.6, was analyzed by FT-IR following washing with DMF and drying under reduced pressure.

In addition, a significant blue shift was observed in the $\nu(\text{O}-\text{S}(=\text{O})_2)$ vibration of sodium sulfate from TR-TiO₂ to SS-TiO₂, which may be attributed to the influence of the strong electron-withdrawing carboxyl (-COOH) group [12o].

2.3.2. Effect of experimental conditions on adsorption of probe molecules

Section 2.3.1 confirmed that TR and SS can serve as probe molecules for determining the surface area of carbon-supported titanium oxide through selective adsorption. However, their adsorption behavior under varying conditions remains unclear. This lack of clarity impedes the development of a comprehensive adsorption model and limits a deeper understanding of the adsorption process. Additionally, while the adsorption of organic molecules in aqueous solutions or gas phases has been extensively studied, the adsorption in organic solutions remains rare. In order to analyze how experimental conditions influence adsorption in DMF solutions, various comparative experiments were conducted using TR and SS as adsorbents. The relationships between W_S (adsorption amounts per unit surface area) and different conditions are summarized in Figures 2.8 and 2.11 (TiO₂: particle size of 30 and 100 nm, crystal structure of anatase and rutile; carbon: multi-walled carbon nanotube CNT and activated carbon RB3).

The time dependence of W_S exhibited obviously different trends between TR and SS. The W_S of TR increases progressively over time, whereas the adsorption of SS rapidly reaches equilibrium within 0.5 h (Figures 2.8a and b, conditions: 0.2 mM, 110°C). The plots based on quasi-second-order adsorption kinetics model (Formula 2.4) of TR at a concentration of 0.2 mM and 110°C are shown in Figure 2.9a [7a, b, 14a-c]. The R^2 values exceeded 0.9, indicating a strong correlation and a good fit. This suggests that the adsorption rate of TR on the TiO₂ surface is governed by a chemical adsorption mechanism [14a-c]. The equilibrium adsorption amounts (W_e) were found to be in an inverse proportionality to the surface areas of TiO₂ (Figure 2.9b).

The dependencies of W_S on the concentration (C) are shown in Figures 2.8c and d (conditions: 110°C, 1 h). The maximum adsorption amount per unit area of rutile TiO₂ appears slightly higher than that of anatase TiO₂. The plots based on Langmuir adsorption model (Formula 2.5) [14d] for SS at 110°C for 1 h are presented in Figure 2.10. The R^2 values exceeded 0.93, indicating a high fit. The maximum adsorption amount per unit area was calculated using the Langmuir adsorption model to be $13.3 \times 10^{-7} \text{ mol m}^{-2}$ (an average value of the four TiO₂ samples). Quantitative discussion will be described later in the context of the adsorption model.

By increasing temperature, the W_S of TR showed significant increase, while the W_S of SS remains nearly constant or slightly decreases (Figures 2.7e and f, conditions: 0.2 mM, 1 h). The increase in W_S of

TR can be explained by the fact that the condition at 110°C for 1 h is insufficient to reach an adsorption equilibrium. In addition, the higher temperature may enhance the evaporation of water absorbed on the surface and/or chemisorption on less reactive absorption sites.

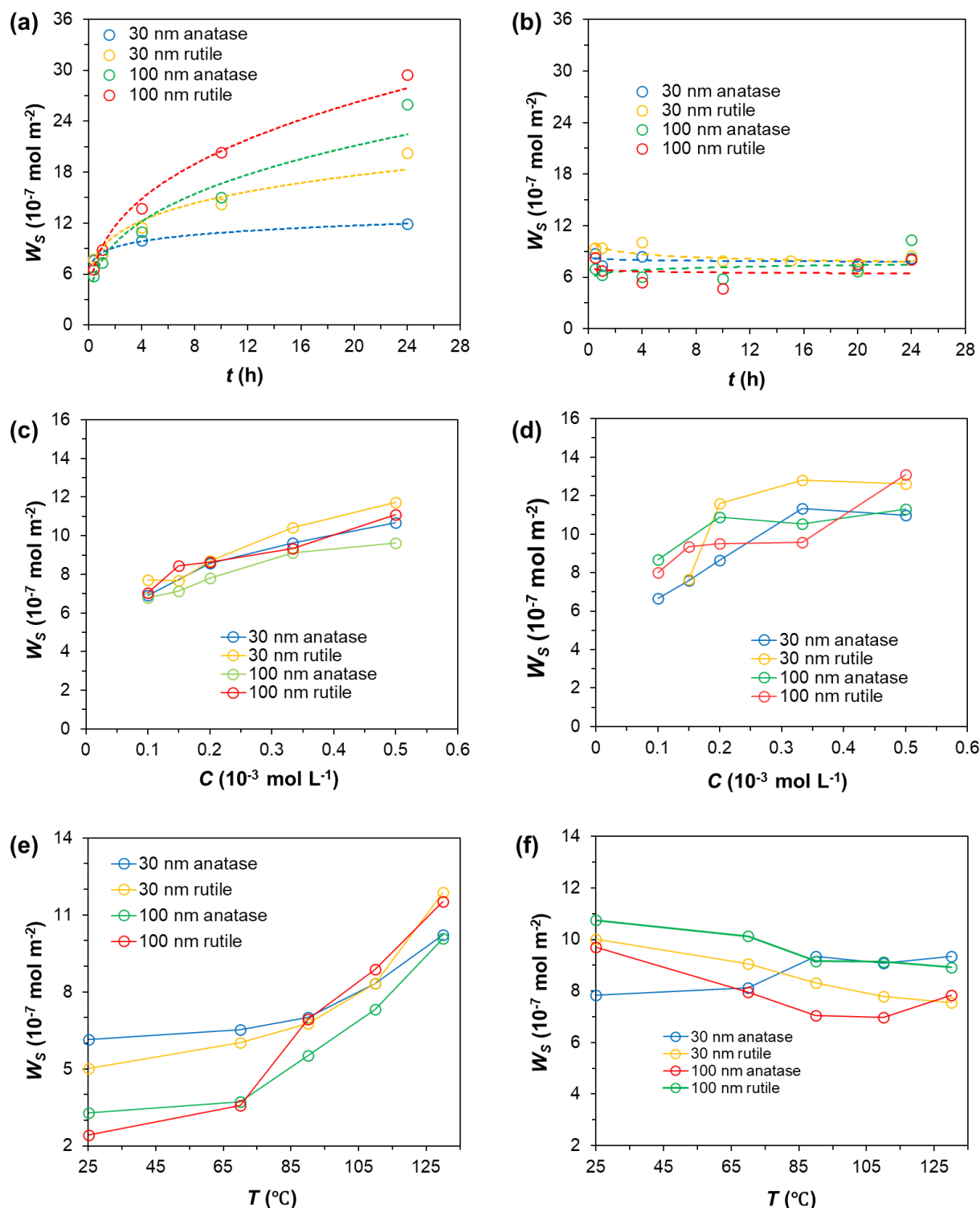


Figure 2.8. Adsorption amounts (W_s) of (a, c, e) TR and (b, d, f) SS per unit surface area on TiO₂ (10 mg) in DMF solution with different (a, b) time (0.2 mM, 110°C) ; (c, d) concentrations (110°C, 1 h); and (e, f) temperatures (0.2 mM, 1 h).

$$\frac{t}{W_s} = \frac{1}{KW_e} + \frac{t}{W_e} \dots\dots\dots \text{(Formula 2.4)}$$

$$\frac{C_e}{W_e} = \frac{C_e}{W_m} + \frac{1}{(K_L W_m)} \dots\dots\dots \text{(Formula 2.5)}$$

In these formulas, W_s , W_e , and W_m represent the adsorption amount under specific conditions, the equilibrium adsorption amount, and the maximum adsorption amount per unit surface area (mol m^{-2}), respectively. C_e and t are the equilibrium concentration ($\text{mol m}^{-2} \text{L}^{-1}$) and time (h). K and K_L are the diffusion rate constants of quasi-second-order kinetics ($\text{m}^2 \text{mol}^{-1} \text{h}^{-1}$) and Langmuir isotherm adsorption constant ($\text{L m}^2 \text{mol}^{-1}$), respectively. Since the adsorption in this work is expressed as adsorption amount per unit surface area, the units of the physical quantities in the formulas mentioned above were modified accordingly.

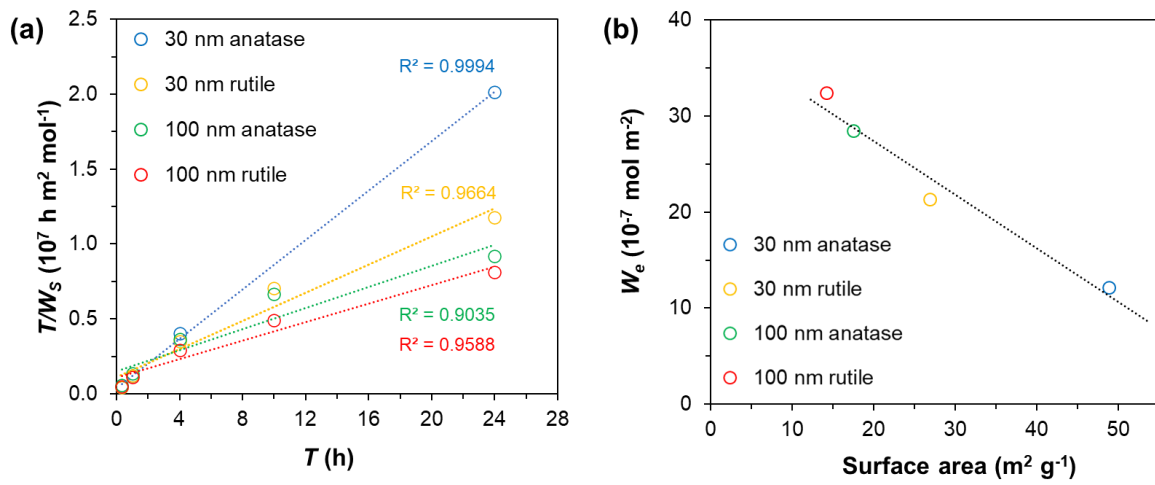


Figure 2.9. (a) Plots based on quasi-second-order kinetics adsorption model for TR on TiO₂ (based on Figure 2.8a); (b) TiO₂ surface area and the equilibrium adsorption amount of TR per unit area (W_e) on TiO₂ (based on Figure 2.9a).

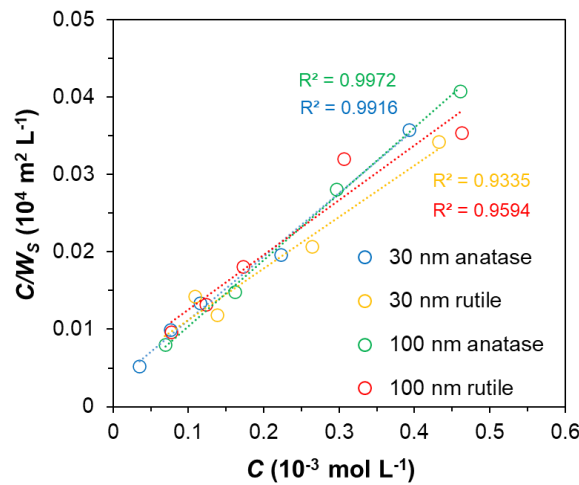
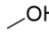
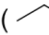

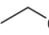
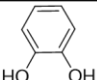
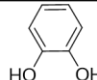


Figure 2.10. Plots based on Langmuir adsorption model of SS on TiO₂ (based on Figure 2.8d).

The author did not find specific reports on the adsorption energies of TR and SS in DMF solutions. However, as TR and SS adsorb primarily through two hydroxyl and carboxyl groups, respectively, their adsorption behaviors can be inferred by examining the adsorption of molecules with similar functional groups. Table 2.4 summarizes the reported adsorption energies of several alcohols and carboxylic acids on the most stable anatase and rutile crystal facets of TiO₂ under vacuum conditions [14e-l]. Notably, the adsorption energies of methanol and ethanol are significantly lower than those of acetic acid and propionic acid. Both the literature [14e-l] and the adsorption structures identified via FT-IR analysis (Figure 2.7) indicate that carboxylic acids form conjugated adsorption bonds, whereas alcohols form only simple single adsorption bonds. This difference likely explains the higher adsorption energies observed for carboxylic acids. Additionally, the adsorption energy of catechol is 2 to 3 times higher than that of methanol and ethanol, which may be attributed to structural differences (e.g., the presence of a benzene ring versus a linear alkane) and the number of functional groups involved in adsorption. Based on these facts, it can be inferred that the adsorption energy of SS on the titanium oxide surface is higher than that of TR.

Table 2.4. Adsorption energies (eV) of several alcohols and acids on TiO₂ in vacuum. [14e-l]

Molecules on TiO ₂	Crystal phase (TiO ₂)	
	anatase {101}	rutile {110}
R-OH	-0.73 () [14e]	-0.76 or -0.85 () [14f]
R-COOH	-1.00 () [14e]	-1.48 or -1.50 () [14g]
Ph-OH	-1.24 () [14h]	-2.25 or -2.27 () [14i]

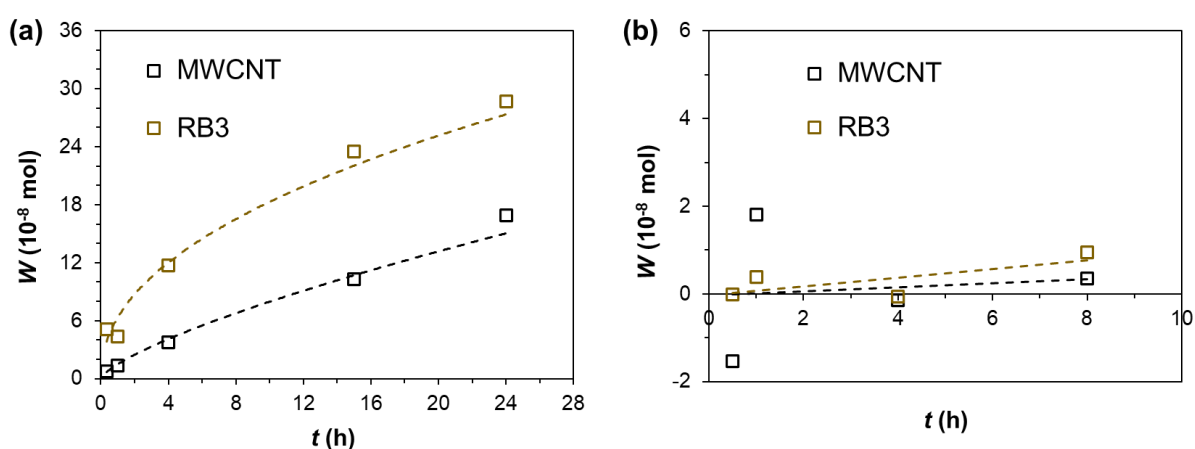


Figure 2.11. Adsorption amounts (W) of (a) TR and (b) SS on carbon nanotubes MWCNT and activated carbon RB3 under different times.

Figure 2.11 shows the adsorption amounts (W) of TR and SS on carbon nanotubes MWCNT and activated carbon RB3 over different time intervals. The adsorption of TR on carbon increases gradually with time, whereas no obvious adsorption of SS was observed on the carbon materials.

The adsorption rate of TR on activated carbon RB3 is well described by the quasi-second-order kinetics model as shown in Figure 2.12. This suggests that the adsorption of TR on the activated carbon RB3 primarily involves chemical adsorption. In contrast, the adsorption of TR on MWCNT seems to proceed mainly by physical adsorption [14a-c, m, n]. The abundant functional groups on the surface of activated carbon [7a, b] likely interact chemically with the phenolic hydroxyl groups of TR. The adsorption capabilities of CA and IA on carbon, as listed in entries 7, 8, and 15 in Table 2.1, further support these conclusions.

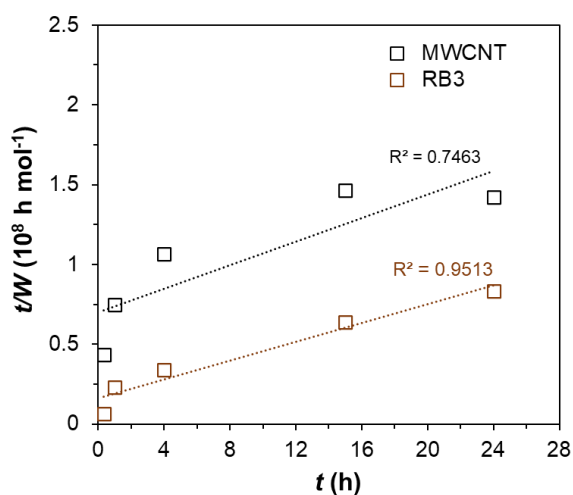


Figure 2.12. Plots based on quasi-second-order kinetics adsorption model of TR on carbon materials (based on Figure 2.11a).

2.3.3. Adsorption amounts and structures of various organic molecules on TiO₂ and carbon

The adsorption behaviors of TR and SS under various conditions are shown in Section 2.3.2. The adsorption amounts of various organic molecules were investigated to understand the adsorption mechanism. Since certain molecules such as DD may be unstable at elevated temperatures, adsorption experiments here were conducted at room temperature using high-surface-area TiO₂ (6 nm, anatase) and activated carbon (RB3) at 1.25 mM for 1 h in DMF solution.

Figure 2.13a shows the adsorption amounts of various organic compounds on TiO₂ in DMF, indicating that adsorption favors the following order: catechol derivatives > phthalic acid derivatives > benzoic acid

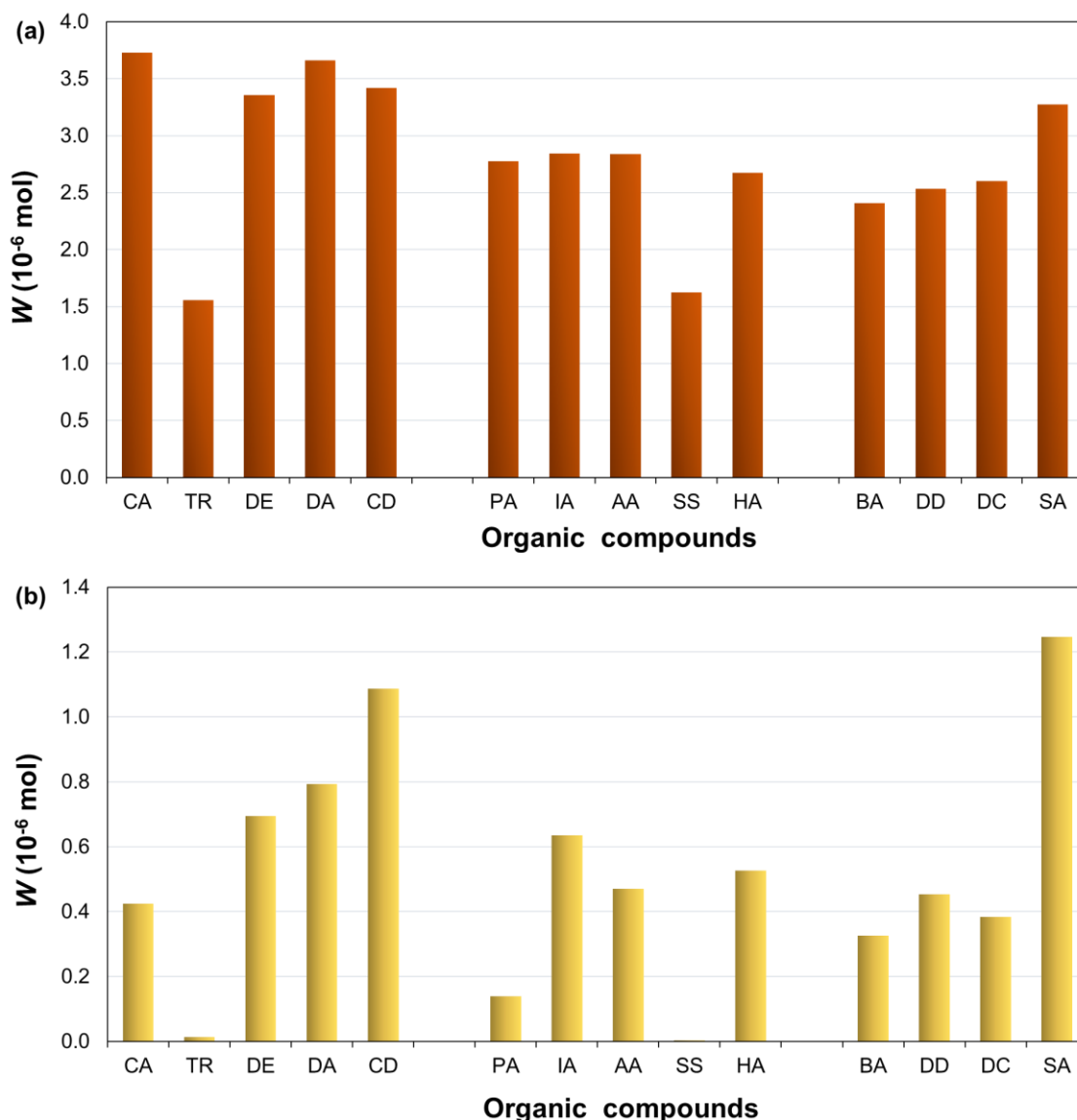


Figure 2.13. Adsorption amounts (W) of various organic compounds on (a) TiO_2 (6 nm anatase) and (b) activated carbon (RB3) in DMF.

Adsorption condition: adsorbent (10 mg) in DMF solution (5 mL) of organic molecule (1.25 mM), 25°C, stirring, 1 h.

derivatives. The adsorption behaviors of these molecules can be influenced by the following three factors:

i. Adsorption site availability: Catechol derivatives, having closely positioned hydroxyl groups, can interact with more adsorption sites compared to phthalic acid derivatives, whose carboxyl groups are more widely spaced. Similarly, the bifunctional SA exhibits much higher adsorption than the monofunctional BA, and its adsorption level is comparable to CA.

ii. Solubility and bond strength: While benzoic acid derivatives are soluble in DMF, their single-carboxyl

adsorption bond could be less stable, resulting in easier desorption and consequently lower adsorption amounts than molecules possessing dual functional groups.

iii. Steric and/or electronic effects of functional group: Exceptionally low adsorption amounts were observed for TR among the catechol derivatives and SS among the phthalic acid derivatives. Since both TR and SS contain sulfonate functional groups, it is speculated that steric hindrance and/or electronic repulsion from these groups suppresses adsorption.

Figure 2.13b shows the adsorption amounts of various organic molecules on activated carbon in DMF solution. In general, the adsorption amounts of hydrophobic organic molecules such as DA, CD, and SA were relatively high. In contrast, the adsorption of TR and SS is nearly negligible. As previously discussed, this is likely due to strong repulsion between the hydrophilic functional groups of these molecules and the activated carbon surface.

The adsorption amounts of various compounds on TiO_2 in aqueous solution are shown in Figure 2.14a. The adsorption behavior is generally similar to that observed in DMF solution, suggesting a comparable adsorption mechanism. However, the overall trend appears somewhat irregular and does not show a clear correlation with the molecular structures. This variability is likely influenced by factors such as water ionization and hydrolysis. For example, the adsorption amounts of DA and CD, both having carboxyl groups, are significantly higher than those of other catechol derivatives. This may be attributed to intermolecular hydrogen bonding and/or multilayer physical adsorption in water. Aromatic compounds with multiple carboxyl and hydroxyl groups have been reported to more readily form intermolecular hydrogen bonds or molecular associations in aqueous environments [15a].

Similarly, the adsorption amounts of various compounds on activated carbon in aqueous solution are shown in Figure 2.14b. Most molecules, except for TR and SS, exhibited high adsorption rates, mostly exceeding 80%. This highlights the effectiveness of activated carbon as a strong adsorbent in aqueous solutions [7a, b, 14a, m, n, 15b]. Activated carbon is widely recognized as an effective adsorbent in aqueous solutions and is frequently used for water purification and filtration in everyday applications. This efficiency arises due to the low affinity between water and activated carbon, which allows dissolved molecule in water to be easily adsorbed onto the carbon surface. Additionally, the high specific surface area and various functional groups on the surface of activated carbon contribute to its strong adsorption capacity. Since IA, AA, DD, and DC are insoluble in water, their adsorption experiments were not carried out.

These experiments generally showed that the adsorption amounts of organic compounds on hydrophobic activated carbon are higher in water, while the adsorption amounts on hydrophilic TiO_2 are

higher in DMF solution.

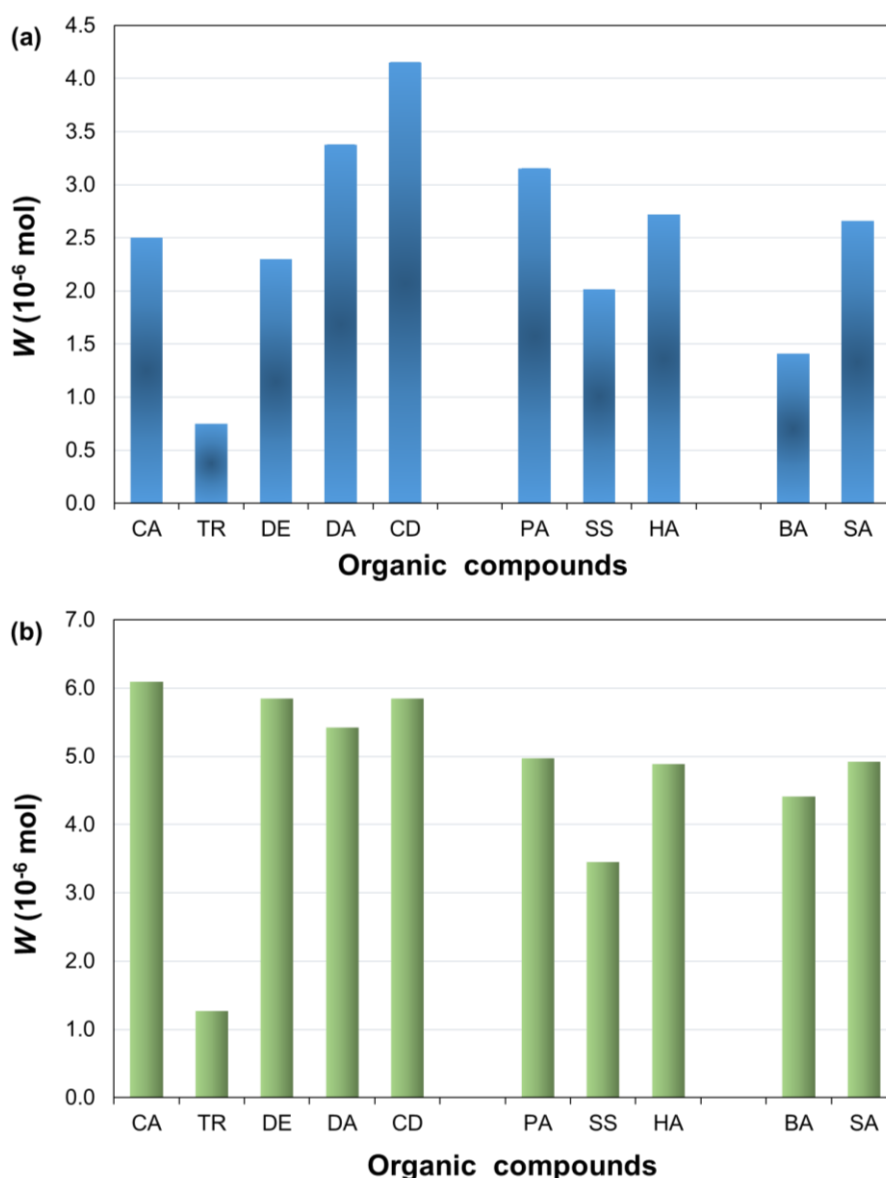


Figure 2.14. Adsorption amounts (W) of various organic compounds on (a) TiO₂ (6 nm anatase) and (b) activated carbon (RB3) in water.

Experimental condition: adsorbent (10 mg) in aqueous solution (1.25 mM, 5 mL) of organic molecule, 25°C, stirring, 1 h.

Some typical organic compounds, CA, IA, and BA, were analyzed by FT-IR to examine their adsorption structures in DMF and aqueous solutions (FT-IR analysis of other compounds can be found in published result 1) to help establish the adsorption models of TR and SS on TiO₂. FT-IR analysis was not performed with the activated carbon due to the low transmittance. The peak assignments of the FT-IR spectra were conducted according to reference [12b, d, f, g, h], in Figure 2.15.

In the spectra of CA on TiO_2 (CA- TiO_2 in Figure 2.15a), the peaks observed for free CA at 1359 and 1186 cm^{-1} , assigned to phenolic group $\delta(\text{C-OH})$, were observed while the new peak at 1259 cm^{-1} in the region of the adsorbed species of $\nu(\text{C-O-Ti})$ appeared. Moreover, the FT-IR spectra of TiO_2 after adsorption in DMF and aqueous solution were similar. The adsorption structures of CA- TiO_2 in both DMF and water are presumed to be bidentate binuclear bridging of the two adjacent phenolic groups with two Ti atoms as shown in Figure 2.15d (CA- TiO_2) [12f, g]. Furthermore, since CA- TiO_2 has a different electronic distribution from that of free CA, the peaks of stretching vibrations of the aromatic ring were observed at shifted wavenumbers [12f, g].

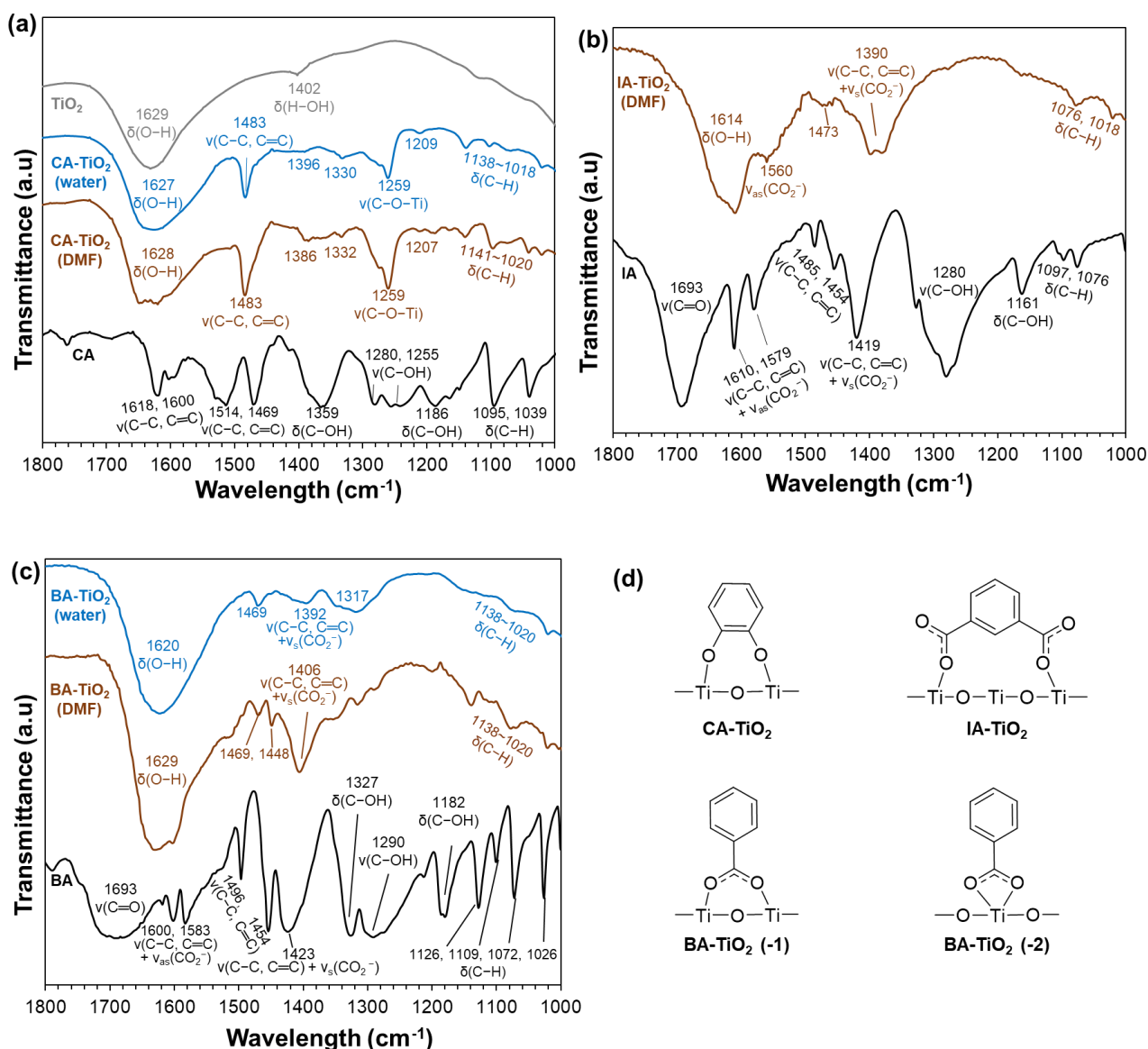


Figure 2.15. FT-IR spectra (KBr) of (a) CA, (b) IA and (c) BA adsorbed on TiO_2 (6 nm anatase), along with (d) their proposed adsorption structures in DMF and aqueous solutions.

The spectra were obtained after the materials were subjected to adsorption (as shown in Figures 2.13a and 2.14a), followed by washing and drying.

For IA-TiO₂ in Figure 2.15b, the peaks of stretching vibrations $\nu(\text{C-OH})$ and bending vibrations $\delta(\text{C-OH})$, and $\nu(\text{C=O})$ carboxylic group disappeared. In addition, the spectrum IA-TiO₂ was analogous structure that has two strong peaks in regions of hydroxylic groups $\delta(\text{O-H})$ of TiO₂, $\nu(\text{C-C}, \text{C=C})$ and/or $\nu_s(\text{CO}_2^-)$. Therefore, IA-TiO₂ could be in the structure in Figure 2.15d (IA-TiO₂) [12b, d, h].

In the spectra of BA-TiO₂ in Figure 2.15c, by contrast with IA-TiO₂, the peaks of stretching vibrations $\nu(\text{C-OH})$ and bending vibrations $\delta(\text{C-OH})$, and $\nu(\text{C=O})$ carboxylic group disappeared both in DMF and aqueous solution. Therefore, it is presumed that BA is adsorbed on the surface of TiO₂ through a single carboxylic group as shown in Figure 2.15d (BA-TiO₂-1 and 2) [12f, h]. Another report stated that the adsorption structure with binuclear and bidentate form shown in Figure 2.15d (BA-TiO₂-1) is more reasonable according to DFT studies [15d].

By comparing all the FT-IR spectra of the TiO₂ after adsorption with these aromatic organic compounds (including TR and SS) having different hydroxylic and carboxylic substituents, it was found that these molecules adsorb on the TiO₂ surface via both phenolic and carboxylic groups. Furthermore, most of the adsorption structures were found to be not dependent on the difference of the solvent and to be via chemical adsorption.

2.3.4. Adsorption models of probe molecules on TiO₂

In the previous adsorption experiments, the adsorption behaviors of TR and SS under various conditions, involving different TiO₂ and carbon materials, were investigated (in Sections 2.3.1-2.3.3). The adsorption of molecules with structures similar to TR and SS was also examined. Based on these fundamental findings, and in conjunction with titanium oxide surface structure data from the literature, the next step is to establish adsorption models for TR and SS on the TiO₂ surface to facilitate analysis at the atomic level.

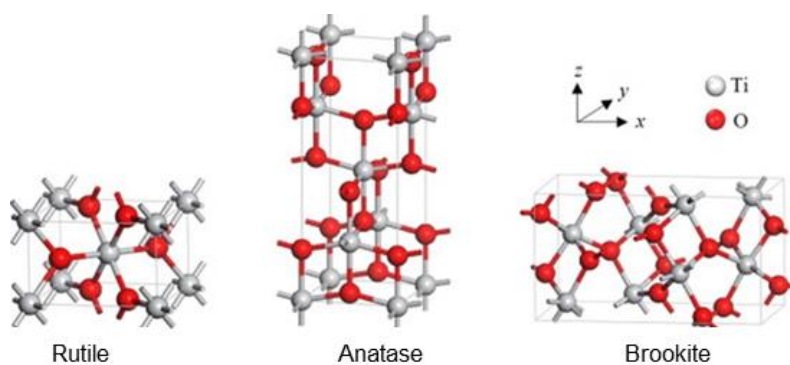


Figure 2.16. Crystal (ball-and-stick) structure of anatase, rutile and brookite [16a], reuse by license under CC-BY; Copyright {2024} Encyclopedia.

TiO₂ exists mainly in three crystal structures: anatase, rutile, and brookite (Figure 2.16) [16a]. Anatase and rutile are the most common and extensively studied forms. It has been reported that the {101} surface is the predominant exposed crystal plane in anatase, while the {110} surface is most common in rutile [15c, d, 16b-f]. In this work, the selective adsorption of TR and SS on TiO₂ is assumed to occur primarily on these two surface structures.

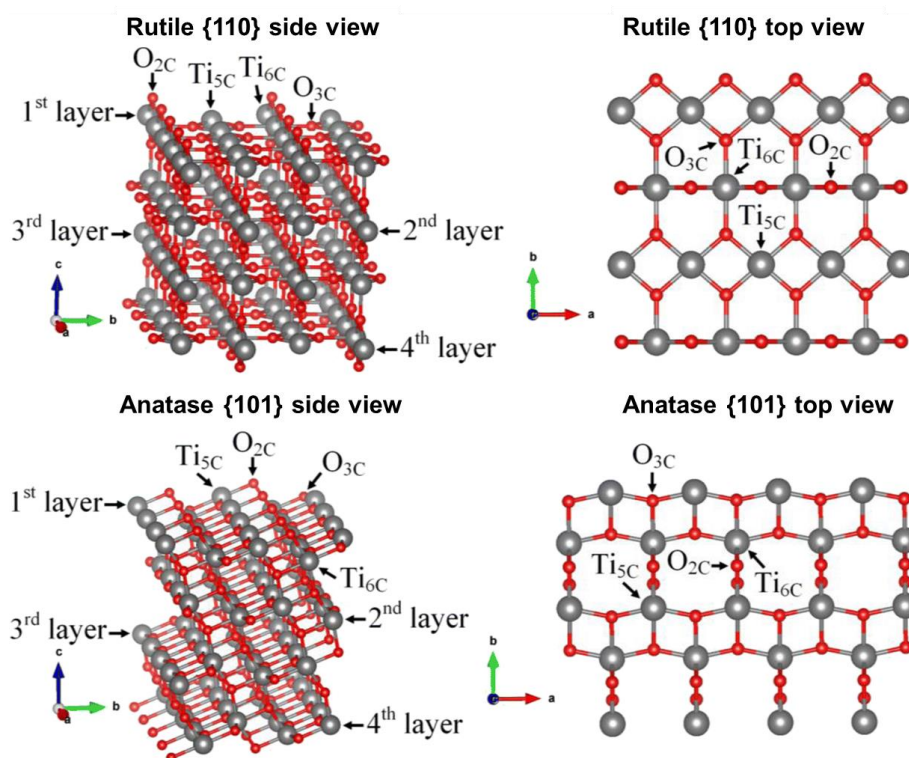


Figure 2.17. Structure (ball-and-stick) of TiO₂ surfaces: rutile {110} and anatase {101} facet surfaces [16l], Gray and red spheres represent Ti and O atoms, respectively; reuse by permission from Springer Nature; Copyright {2019} Springer Nature.

Through the analysis in Section 3.3.2, SS exhibits a stable single adsorption site on the TiO₂ surface, allowing for the development of a corresponding surface adsorption model. Based on adsorption energy and site preferences, Ti_{5C} and Ti_{6C} atoms were identified as favorable adsorption sites on the anatase {101} and rutile {110} surfaces (Figure 2.17) [16b, d, e]. Previous studies on pyrocatechol and benzoate adsorption [15c, d] suggest that the SS molecule aligns at approximately 75° with the TiO₂ crystal plane. Considering the interaction forces between SS molecules: Na⁺ electrostatic interaction (0 to -0.2 eV in 0 to 0.2 nm intermolecular distance, calculated by Coulomb mechanics formula), van der Waals forces between benzene rings (0 to -0.1 eV), and π - π interactions (0 to -0.02 eV) [7a, b], all these are significantly lower than the adsorption energy of SS on TiO₂ (around -2.0 to -4.5 eV, based on Table 2.4). This suggests that intermolecular interactions between adsorbed SS molecules have minimal impact on adsorption. On

the other hand, SS could accept coordination of DMF solvent molecules to its sodium ion further positively charged by the electron-withdrawing of the two carboxyl groups (as analyzed in Figure 2.7) [16h]. This coordination can lead to have a larger apparent molecular volume. Adsorption at $\text{Ti}_{5\text{C}}$ sites, which are separated by vacancies, is more stable, thereby minimizing intermolecular steric interactions.

Using structural data from the literature [16e, g, l] and molecular models of SS and TR constructed with ChemDraw 3D, monolayer saturation adsorption models are proposed for the anatase $\{101\}$ and rutile $\{110\}$ facet surfaces as shown in Figure 2.18. Coordination of DMF molecules to SS was considered to make the adsorption models proposed here, whereas no consideration was given to the models for TR.

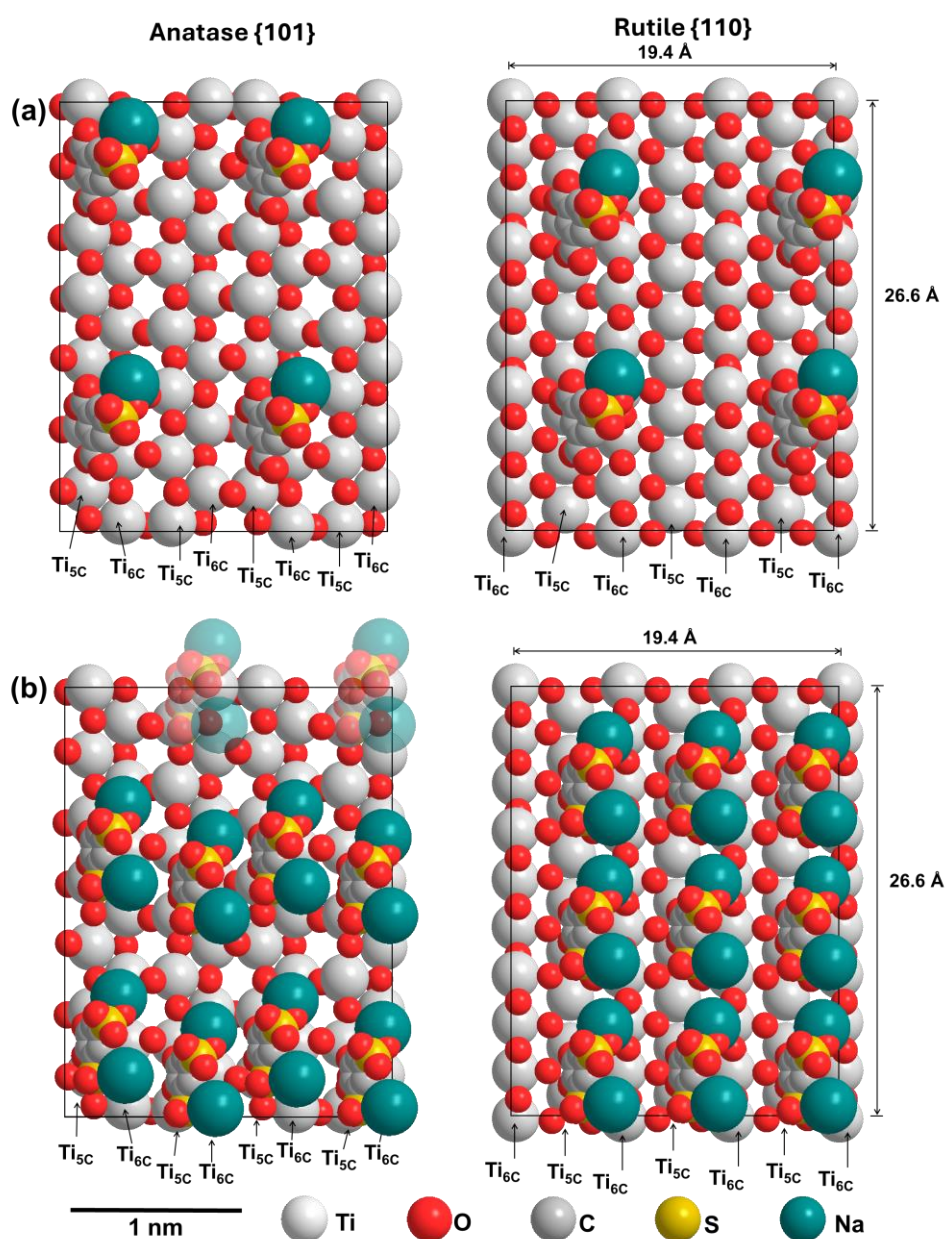


Figure 2.18. Adsorption models (top view) of (a) SS (b) TR on TiO_2 anatase $\{101\}$ and rutile $\{110\}$ surfaces (covalent radius).

Based on the proposed adsorption models, the adsorption densities of SS on TiO₂ are estimated to be 0.60 molecules/nm² for anatase and 0.58 molecules/nm² for rutile (Figure 2.18a). In comparison, the experimentally determined adsorption densities were 0.59 molecules/nm² under the standard adsorption conditions in this study (based on Figures 2.3 and 2.4) and 0.77 molecules/nm² at maximum estimated by the Langmuir adsorption model (based on Figure 2.10).

Similarly, the adsorption densities of TR on TiO₂ are estimated to be 1.63 molecules/nm² for anatase and 1.74 molecules/nm² for rutile based on the proposed adsorption models (Figure 2.18b). The experimentally determined values were 0.73 and 1.71 molecules/nm² for anatase and 1.28 and 1.95 molecules/nm² for rutile at an equilibrium estimated by a quasi-second-order kinetics adsorption model from Figure 2.9 on TiO₂ of particle sizes 10 nm and 30 nm, respectively. The saturated adsorption amount of TR on rutile is slightly higher than that on anatase, which aligns with the results obtained from the pseudo-second-order adsorption kinetics model (Figure 2.9).

2.3.5. Adsorption of probe molecules on various metal oxides and SiO₂

The results in Section 3.3.1 will show that the surface areas of titanium oxide in carbon-supported catalysts can be determined through the selective adsorption of TR and SS. Additionally, this work explored other catalysts, including Fe₂O₃, Fe₃O₄, CuO, ZrO₂ supported on carbon and SiO₂ materials (Tables 1.7 and 1.9–1.11 in Chapter 1). The adsorption amounts of TR and SS on various metal oxides under the same conditions as Figure 2.4 are shown in Figure 2.19. Similar to titanium dioxide, the adsorption amounts of TR and/or SS on these metal oxides were proportional to their surface areas. Since TiO₂, Fe₂O₃, CuO and ZrO₂ have both Lewis acidic sites (metal cations) and Lewis basic sites (hydroxyl groups bonded to metal cations via adsorbed water) [7a, b, 12n], chemisorption at the surface basic sites could enable adsorption of TR and SS.

The correlation between the adsorption amount of ZrO₂ and its surface area was relatively low. However, since the work did not proceed with the application of supported ZrO₂ catalysts, further discussion will not be pursued. Nevertheless, within a specific range of error, it remains feasible to estimate the surface area of ZrO₂ using adsorption of SS molecule. Adsorption models for SS on γ and α -Fe₂O₃ surfaces are also proposed (Appendix, Figure 2.22) [16o–r]. In contrast, silica-based materials exhibited negligible adsorption (Figure 2.19). This can be attributed to a lack of basic sites of the SiO₂ surface, dominated by isolated silanol (Si–OH) groups, which render it largely neutral or weakly acidic.

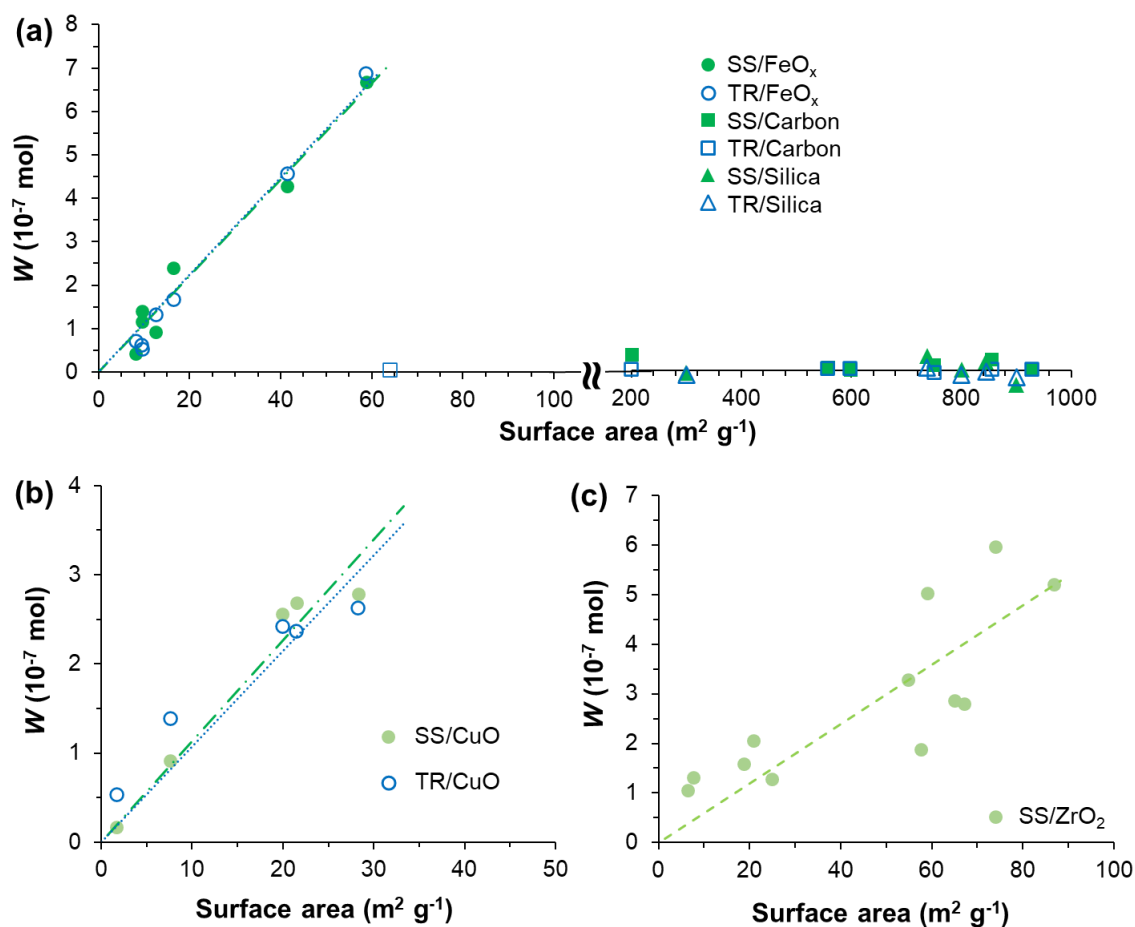


Figure 2.19. Adsorption amounts of SS and TR on (a) FeO_x , carbon and SiO_2 ; (b) CuO ; (c) ZrO_2 .

Adsorption condition: adsorbent (10 mg) in DMF solution (5 mL) of organic molecule (0.2 mM), 110°C , shaking, 1 h.

FT-IR analyses of the adsorption structures of SS and TR on Fe_2O_3 are summarized in Figures 20a and c. The peak assignments were conducted according to literature [12b, d-m, 13b, c]. The peaks at 1631 and 1384 cm^{-1} of Fe_2O_3 are assigned to bending and stretching vibrations of the hydroxylic groups $\delta(\text{FeO-H})$ and $\nu(\text{Fe-OH})$, respectively [13b, c]. Since similar spectra were obtained between SS- TiO_2 and SS- Fe_2O_3 , and also between TR- TiO_2 and SS- Fe_2O_3 , the same adsorption structures of SS and TR on Fe_2O_3 surface as those on TiO_2 surface are proposed as shown in Figures 20b and d, respectively. Similar FT-IR analyses and proposal of the adsorption structures are possible for TR and SS on CuO and ZrO_2 surfaces (Appendix, Figure 2.23).

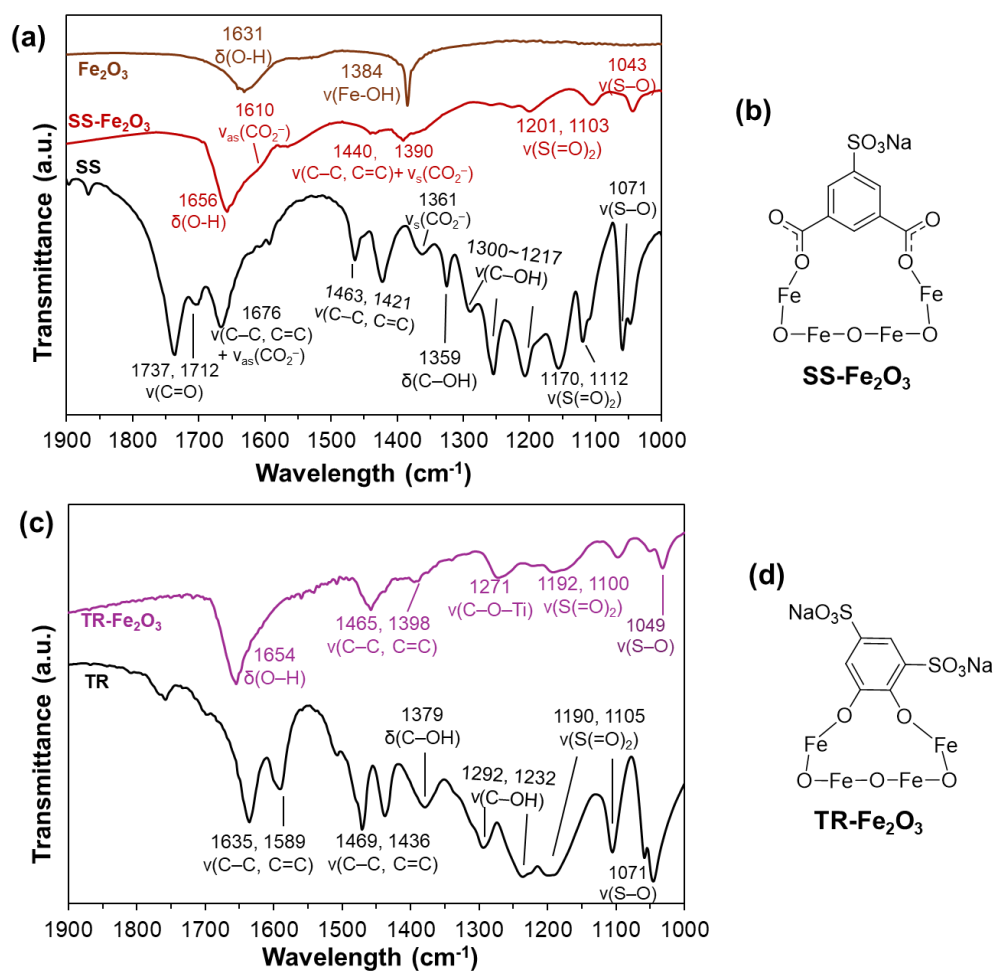


Figure 2.20. FT-IR spectra (KBr) of (a) SS and (c) TR on Fe_2O_3 (γ , 20–40 nm, $S = 42 \text{ m}^2 \text{ g}^{-1}$), and expected absorption structures of (b) SS and (d) TR on Fe_2O_3 .

2.4 Conclusions

This chapter demonstrates that the organic molecules TR and SS exhibit selective adsorption on metal oxide surfaces such as titanium oxide, iron oxide, and copper oxide under specific adsorption conditions, while their adsorption on carbon and silicon oxide materials is negligible. The adsorption amounts on metal oxides correlate with the BET surface areas of the metal oxides, indicating that this method can be applied to measure the surface area of metal oxides in catalysts supported on carbon or silicon oxide substrates.

The adsorption behaviors of TR and SS under various conditions and those of structurally related compounds were examined. TR and SS show minimal adsorption on hydrophobic carbon and silicon oxide surfaces due to their hydrophilic and acidic nature. SS exhibited stronger adsorption on TiO₂ compared to TR. In addition, comparative analysis suggests that the primary driving forces for adsorption of TR and SS are the hydroxyl and carboxyl functional groups, respectively. The adsorption models of TR and SS on TiO₂ were proposed, and the estimated adsorption amounts were compared with the experimental values.

This chapter establishes a novel surface evaluation method in organic media. The chapter includes comparisons of the adsorption amounts estimated by the proposed hypothesis and those obtained by experiments. The findings are expected to contribute to advancements in catalysis and surface chemistry. The results also offer valuable insights into macromolecular adsorption, purification processes, photocatalysis, and related areas of research.

2.5 Reference

- [11] (a) Cheng, H.; Xu, W. Recent advances in modified TiO₂ for photo-induced organic synthesis. *Org. Biomol. Chem.* **2019**, *17* (47), 9977-9989. DOI: 10.1039/c9ob01739a. (b) Wang, J.; Guo, R.-t.; Bi, Z.-x.; Chen, X.; Hu, X.; Pan, W.-g. A review on TiO₂-x-based materials for photocatalytic CO₂ reduction. *Nanoscale* **2022**, *14* (32), 11512-11528. (c) Sari, Y.; Gareso, P. L.; Armynah, B.; Tahir, D. A review of TiO₂ photocatalyst for organic degradation and sustainable hydrogen energy production. *Int. J. Hydrog. Energy* **2024**, *55*, 984-996. DOI: 10.1016/j.ijhydene.2023.11.126.
- [12] (a) Regazzoni, A. E.; Mandelbaum, P.; Matsuyoshi, M.; Schiller, S.; Bilmes, S.; Blesa, M. A. Adsorption and Photooxidation of Salicylic Acid on Titanium Dioxide: A Surface Complexation Description. *Langmuir* **1998**, *14* (4), 868-874. DOI: 10.1021/la970665n. (b) Dobson, K. D.; McQuillan, A. J. In situ infrared spectroscopic analysis of the adsorption of aromatic carboxylic acids to TiO₂, ZrO₂, Al₂O₃, and Ta₂O₅ from aqueous solutions.

Spectrochim. Acta. Part A **2000**, 56 (3), 557–565. DOI: 10.1016/S1386-1425(99)00154-7. (c) Araujo, P. Z.; Morando, P. J.; Blesa, M. A. Interaction of Catechol and Gallic Acid with Titanium Dioxide in Aqueous Suspensions. 1. Equilibrium Studies. *Langmuir* **2005**, 21 (8), 3470–3474. DOI: 10.1021/la0476985. (d) Nagayasu, T.; Imamura, K.; Nakanishi, K. Adsorption characteristics of various organic substances on the surfaces of tantalum, titanium, and zirconium. *J. Colloid Interface Sci.* **2005**, 286 (2), 462–470. DOI: 10.1016/j.jcis.2005.01.023. (e) Guedes, M.; Ferreira, J. M.F.; Ferro, A. C. A study on the aqueous dispersion mechanism of CuO powders using Tiron. *J. Coll. Interf. Sci.* **2009**, 330 (1), 119–124. DOI: 10.1016/j.jcis.2008.10.057. (f) Janković, I. A.; Šaponjić, Z. V.; Čomor, M. I.; Nedeljković, J. M. Surface Modification of Colloidal TiO₂ Nanoparticles with Bidentate Benzene Derivatives. *J. Phys. Chem. C* **2009**, 113 (29), 12645–12652. DOI: 10.1021/jp9013338. (g) Savić, T. D.; Čomor, M. I.; Nedeljković, J. M.; Veljković, D. Ž.; Zarić, S. D.; Rakić, V. M.; Janković, I. A. The effect of substituents on the surface modification of anatase nanoparticles with catecholate-type ligands: a combined DFT and experimental study. *Phys. Chem. Chem. Phys.* **2014**, 16, 20796–20805. DOI: 10.1039/C4CP02197E. (h) Yao, B.; Peng, C.; Lu, P.; He, Y.; Zhang, W. Fabrication of Tiron-TiO₂ charge-transfer complex with excellent visible-light photocatalytic performance. *Mater. Chem. Phys.* **2016**, 184, 298–305. DOI: 10.1016/j.matchemphys.2016.09.056. (i) Buchholz, M.; Xu, M.; Noei, H.; Weidler, P.; Nefedov, A.; Fink, K.; Wang, Y.; Wöll, C. Interaction of carboxylic acids with rutile TiO₂(110): IR-investigations of terephthalic and benzoic acid adsorbed on a single crystal substrate. *Surf. Sci.* **2016**, 643, 117–123. DOI: 10.1016/j.susc.2015.08.006. (m) Shishlov, N.; Khursan, S. Effect of ion interactions on the IR spectrum of benzenesulfonate ion. Restoration of sulfonate ion symmetry in sodium benzenesulfonate dimer. *J. Mol. Struct.* **2016**, 1123, 360–366. DOI: 10.1016/j.molstruc.2016.06.030. (n) Sahai, N. Is Silica Really an Anomalous Oxide? Surface Acidity and Aqueous Hydrolysis Revisited. *Environ. Sci. Technol.* **2002**, 36 (3), 445–452. DOI: 10.1021/es010850u. (o) Kabiri, K.; Zohuriaan-Mehr, M. J.; Mirzadeh, H.; Kheirabadi, M. Solvent-, ion- and pH-specific swelling of poly(2-acrylamido-2-methylpropane sulfonic acid) superabsorbing gels. *J. Polym. Res.* **2010**, 17 (2), 203–212. DOI: 10.1007/s10965-009-9306-7.

[13] (a) Barkul, R. P.; Sutar, R. S.; Patil, M. K.; Delekar, S. D. Photocatalytic Degradation of Organic Pollutants by Using Nanocrystalline Boron-doped TiO₂ Catalysts. *ChemistrySelect* **2021**, 6 (14), 3360–3369. DOI: 10.1002/slct.202003910. (b) Narayanan, K. B.; Han, S. S. One-Pot Green Synthesis of Hematite (α -Fe₂O₃) Nanoparticles by Ultrasonic Irradiation and Their In Vitro Cytotoxicity on Human Keratinocytes CRL-2310. *J. Clust. Sci.* **2016**, 27, 1763–1775. DOI: 10.1007/s10876-016-1040-9. (c) Lemine, O. M.; Madkhali, N.; Alshammari, M.; Algessair, S.; Gismelseed, A.; Mir, L. E.; Hjiri, M.; Yousif, A. A.; El-Boubbou, K. Maghemite (γ -Fe₂O₃) and γ -Fe₂O₃-TiO₂ Nanoparticles for Magnetic Hyperthermia Applications: Synthesis, Characterization and Heating Efficiency. *Mater.* **2021**, 14 (19), 5691. DOI: 10.3390/ma14195691.

[14] (a) Xie, B.; Qin, J.; Wang, S.; Li, X.; Sun, H.; Chen, W. Adsorption of Phenol on Commercial Activated Carbons: Modelling and Interpretation. *Int. J. Environ. Res. Public Health* **2020**, 17 (3), 789. (b) Abugazleh, M. K.; Rougeau, B.; Ali, H. Adsorption of catechol and hydroquinone on titanium oxide and iron (III) oxide. *J. Environ. Chem. Eng.* **2020**, 8 (5), 104180. DOI: 10.1016/j.jece.2020.104180. (c) Wu, Y.; Zhang, X.; Liu, C.; Tian, L.; Zhang, Y.; Zhu, M.; Qiao, W.; Wu, J.; Yan, S.; Zhang, H.; et al. Adsorption Behaviors and Mechanism of Phenol and

Catechol in Wastewater by Magnetic Graphene Oxides: A Comprehensive Study Based on Adsorption Experiments, Mathematical Models, and Molecular Simulations. *ACS Omega* **2024**, *9* (13), 15101-15113. DOI: 10.1021/acsomega.3c09346. (d) Langmuir, I. The adsorption of gases on plane surfaces of glass, mica and platinum. *J. Am. Chem. Soc.* **1918**, *40* (9), 1361-1403. DOI: 10.1021/ja02242a004. (e) Gong, X.-Q.; Selloni, A. Role of steps in the reactivity of the anatase TiO₂(101) surface. *J. Catal.* **2007**, *249* (2), 134-139. DOI: <https://doi.org/10.1016/j.jcat.2007.04.011>. (f) Muir, J. N.; Choi, Y.; Idriss, H. Computational study of EtOH adsorption and reaction over rutile TiO₂ (110) surfaces. *Phys. Chem. Chem. Phys.* **2012**, *14* (34), 11910-11919, 10.1039/C2CP40641A. DOI: 10.1039/C2CP40641A. (g) Nadeem, I. M.; Hargreaves, L.; Harrison, G. T.; Idriss, H.; Shluger, A. L.; Thornton, G. Carboxylate Adsorption on Rutile TiO₂(100): Role of Coulomb Repulsion, Relaxation, and Steric Hindrance. *J. Phys. Chem. C* **2021**, *125* (25), 13770-13779. DOI: 10.1021/acs.jpcc.1c00892. (h) Luo, J.-H.; Mo, Y.-F.; Li, Z.-S.; Du, F.-Y. Doping effects on catechol functionalized anatase TiO₂ (101) surface for dye-sensitized solar cells. *Mater. Res. Express* **2021**, *8* (1), 015906. DOI: 10.1088/2053-1591/abdc3c. (l) Kristoffersen, H. H.; Shea, J.-E.; Metiu, H. Catechol and HCl Adsorption on TiO₂(110) in Vacuum and at the Water–TiO₂ Interface. *J. Phys. Chem. Lett.* **2015**, *6* (12), 2277-2281. DOI: 10.1021/acs.jpcclett.5b00958. (m) Mojoudi, N.; Mirghaffari, N.; Soleimani, M.; Shariatmadari, H.; Belver, C.; Bedia, J. Phenol adsorption on high microporous activated carbons prepared from oily sludge: equilibrium, kinetic and thermodynamic studies. *Sci. Rep.* **2019**, *9* (1), 19352. DOI: 10.1038/s41598-019-55794-4. (n) Wahid, S. N.; Maharaj, R.; Boodlal, D.; Smith, J. V. The adsorption of phenol on granular activated carbon prepared from waste coconut shell in Trinidad. *Environ. Prog. Sustainable Energy* **2022**, *41* (1), e13729. DOI: 10.1002/ep.13729.

[15] (a) Xiao, C.; Wu, M.; Zhang, Y.; Zhao, X.; Yu, J.; Zheng, X. The structure-dependent self-association of five phenolic acids in aqueous solution. *Magn. Reson. Chem.* **2014**, *52* (8), 460-466. DOI: 10.1002/mrc.4089. (b) Schumann, P.; Muschket, M.; Dittmann, D.; Rabe, L.; Reemtsma, T.; Jekel, M.; Ruhl, A. S. Is adsorption onto activated carbon a feasible drinking water treatment option for persistent and mobile substances? *Water Res.* **2023**, *235*, 119861. DOI: 10.1016/j.watres.2023.119861. (c) Syres, K. L.; Thomas, A. G.; Flavell, W. R.; Spencer, B. F.; Bondino, F.; Malvestuto, M.; Preobrajenski, A.; Grätzel, M. Adsorbate-Induced Modification of Surface Electronic Structure: Pyrocatechol Adsorption on the Anatase TiO₂ (101) and Rutile TiO₂ (110) Surfaces. *J. Phys. Chem. C* **2012**, *116* (44), 23515-23525. DOI: 10.1021/jp308614k. (d) Busayaporn, W.; Duncan, D. A.; Allegretti, F.; Wander, A.; Bech, M.; Möller, P. J.; Doyle, B. P.; Harrison, N. M.; Thornton, G.; Lindsay, R. Structure of a Model Dye/Titania Interface: Geometry of Benzoate on Rutile-TiO₂ (110)(1 × 1). *J. Phys. Chem. C* **2016**, *120* (27), 14690-14698. DOI: 10.1021/acs.jpcc.6b03991.

[16] (a) Gackowski, M.; Osmalek, T.; Froelich, A.; Otto, F.; Schneider, R.; Lulek, J. Titanium (IV) Oxide in Dermal Formulations. *Encyclopedia*. Available online: <https://encyclopedia.pub/entry/44176> (accessed on 07 October 2024). (b) Tao, J.; Luttrell, T.; Bylsma, J.; Batzill, M. Adsorption of Acetic Acid on Rutile TiO₂(110) vs (011)-2 × 1 Surfaces. *J. Phys. Chem. C* **2011**, *115* (8), 3434-3442. DOI: 10.1021/jp111270x. (c) Xu, H.; Reunchan, P.; Ouyang, S.; Tong, H.; Umezawa, N.; Kako, T.; Ye, J. Anatase TiO₂ Single Crystals Exposed with High-Reactive {111} Facets Toward Efficient H₂ Evolution. *Chem. Mater.* **2013**, *25* (3), 405-411. DOI: 10.1021/cm303502b. (d)

Tian, F. H.; Wang, X.; Zhao, W.; Zhao, L.; Chu, T.; Yu, S. Adsorption of 2-propanol on anatase TiO₂ (101) and (001) surfaces: A density functional theory study. *Surf. Sci.* **2013**, *616*, 76-84. DOI: 10.1016/j.susc.2013.05.005.

(e) O'Rourke, C.; Bowler, D. R. DSSC anchoring groups: a surface dependent decision. *J. Phys.: Condens. Matter* **2014**, *26* (19), 195302. DOI: 10.1088/0953-8984/26/19/195302.

(f) Moses, P.; Janotti, A.; Franchini, C.; Kresse, G.; Van de Walle, C. Donor defects and small polarons on the TiO₂ (110) surface. *J. Appl. Phys.* **2016**, *119* (18). DOI: 10.1063/1.4948239.

(g) Zhao, S.; Tang, Y.; Yu, X.; Li, J. Superior reactivity of heterogeneous single-cluster catalysts for semi-hydrogenation of acetylene. *Sci. China Mater.* **2023**, *66* (10), 3912-3921. DOI: 10.1007/s40843-023-2558-7.

(h) Chen, X.; Lingam, H. K.; Meyers, E. A.; Shore, S. G. Structures of DMF solvated potassium and sodium salts of [Fe(CO)₄]²⁻ and [M₂(CO)₈]²⁻ (M = Fe, Ru). *J. Organomet. Chem.* **2012**, *721-722*, 137-143. DOI: 10.1016/j.jorganchem.2012.07.040.

(l) dos Reis Vargas, M.; de Castro, E. A. S.; Politi, J. R. d. S.; Gargano, R.; Martins, J. B. L. BTEX adsorption on TiO₂ anatase and rutile surfaces: DFT functionals. *J. Mol. Model* **2019**, *25* (5), 137. DOI: 10.1007/s00894-019-4027-2.

(m) Bagus, P. S.; Nelin, C. J. Covalent interactions in oxides. *J. electron spectros. relat. Phenomena* **2014**, *194*, 37-44. DOI: 10.1016/j.elspec.2013.11.004.

(n) Sousa, C.; Illas, F. Ionic-covalent transition in titanium oxides. *Phys. Rev. B* **1994**, *50* (19), 13974-13980. DOI: 10.1103/PhysRevB.50.13974.

(o) Baetzold, R. C.; Yang, H. Computational Study on Surface Structure and Crystal Morphology of γ -Fe₂O₃: Toward Deterministic Synthesis of Nanocrystals. *J. Phys. Chem. B* **2003**, *107* (51), 14357-14364. DOI: 10.1021/jp035785k.

(p) Geng, X.; Xie, C.; Zhu, B.; Chen, J.; Sun, Y.; Xu, M. Calcium poisoning mechanism on the selective catalytic reduction of NO_x by ammonia over the γ -Fe₂O₃ (001) surface. *Environ. Sci. Pollut. Res.* **2022**, *29* (58), 88256-88268. DOI: 10.1007/s11356-022-21912-5.

(q) Dzade, N. Y.; Roldan, A.; De Leeuw, N. H. A density functional theory study of the adsorption of benzene on hematite (α -Fe₂O₃) surfaces. *Minerals* **2014**, *4* (1), 89-115. DOI: 10.3390/min4010089.

(r) Pabisiak, T.; Kiejna, A. Incipient adsorption of water and hydroxyl on hematite (0001) surface. *J. Phys. Commun.* **2019**, *3* (3), 035023. DOI: 10.1088/2399-6528/ab0fa7.

2.6 Appendix

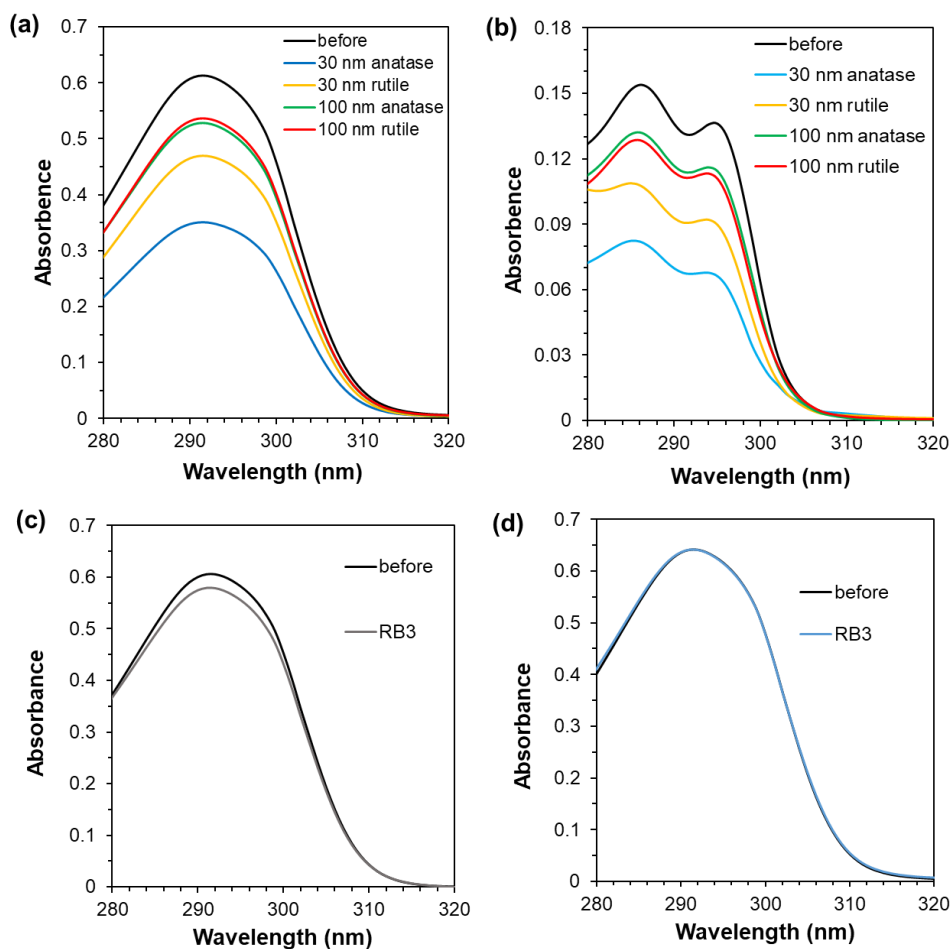


Figure 2.21. UV-Vis spectra before and after absorption of (a) TR and (b) SS on TiO₂ (particle size 30 and 100 nm, crystal phase anatase and rutile, $S = 49\text{--}14\text{ m}^2\text{ g}^{-1}$, data-based on Figure 2.3); TR on activated carbon (RB3, $S = 855\text{ m}^2\text{ g}^{-1}$) under (c) stirring (data for Figure 2.3) and (d) shaking (data for Figure 2.4).

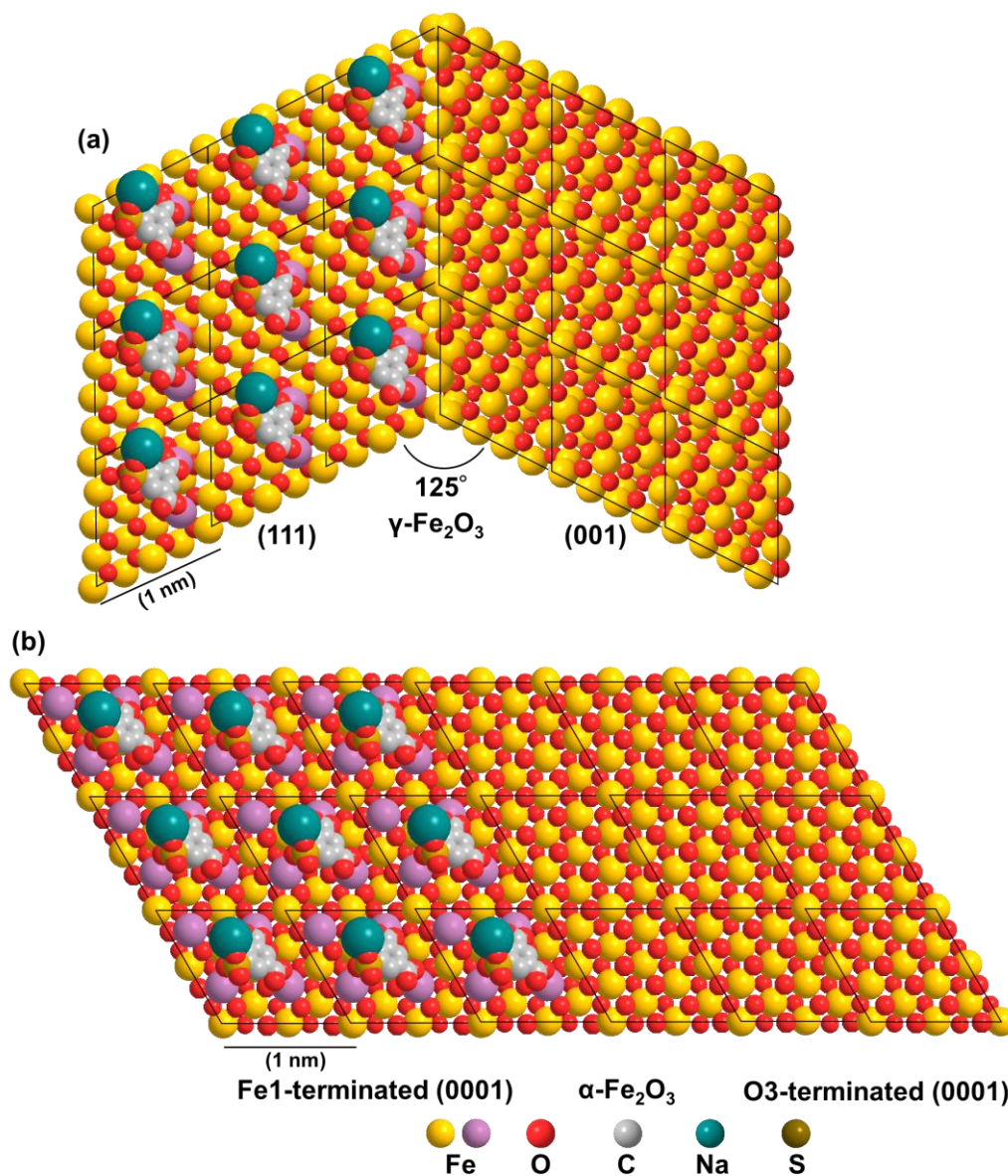


Figure 2.22. Adsorption models of SS on (a) $\gamma\text{-Fe}_2\text{O}_3$ (111) and (001) surfaces, (b) $\alpha\text{-Fe}_2\text{O}_3$ (0001) surface with Fe1 and O3-terminations. The structures of $\gamma\text{-Fe}_2\text{O}_3$ (111) [16n] and (001) [16o], $\alpha\text{-Fe}_2\text{O}_3$ (0001) surface with Fe1 and O3-terminations [16p, q] were prepared based on the reference. The Fe atom acting as an adsorption site was highlighted in purple.

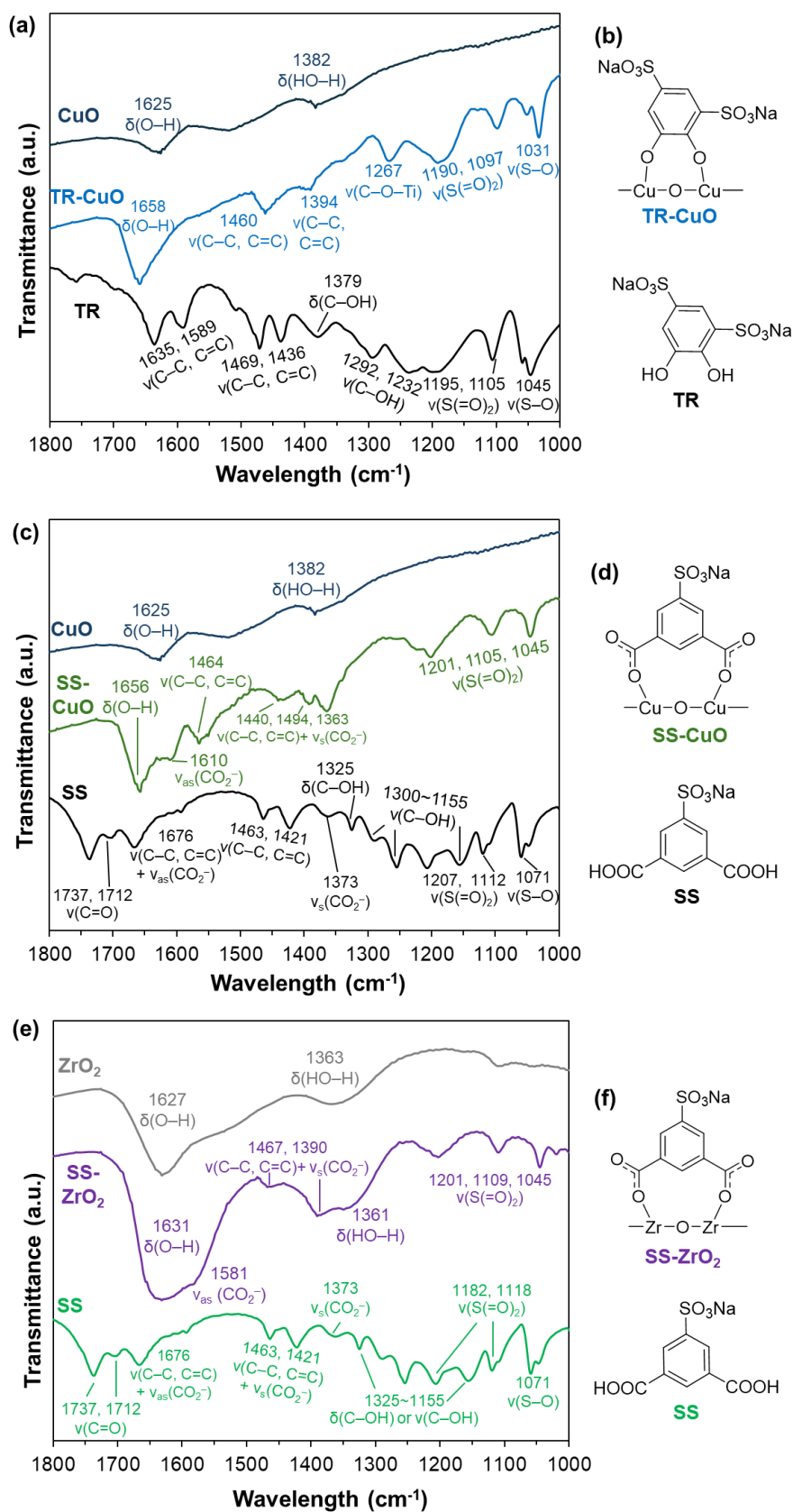


Figure 2.23. FT-IR (KBr) spectra of (a) TR, (c) SS-CuO (CuO, particle size < 50, crystallite size = 22 nm, $S = 24 \text{ m}^2 \text{ g}^{-1}$); (c) SS-ZrO₂ (ZrO₂, tetragonal, crystallite size = 10 nm, $S = 74 \text{ m}^2 \text{ g}^{-1}$) and (b, d, e) proposed adsorption structures. (based on Figure 2.19b, c).

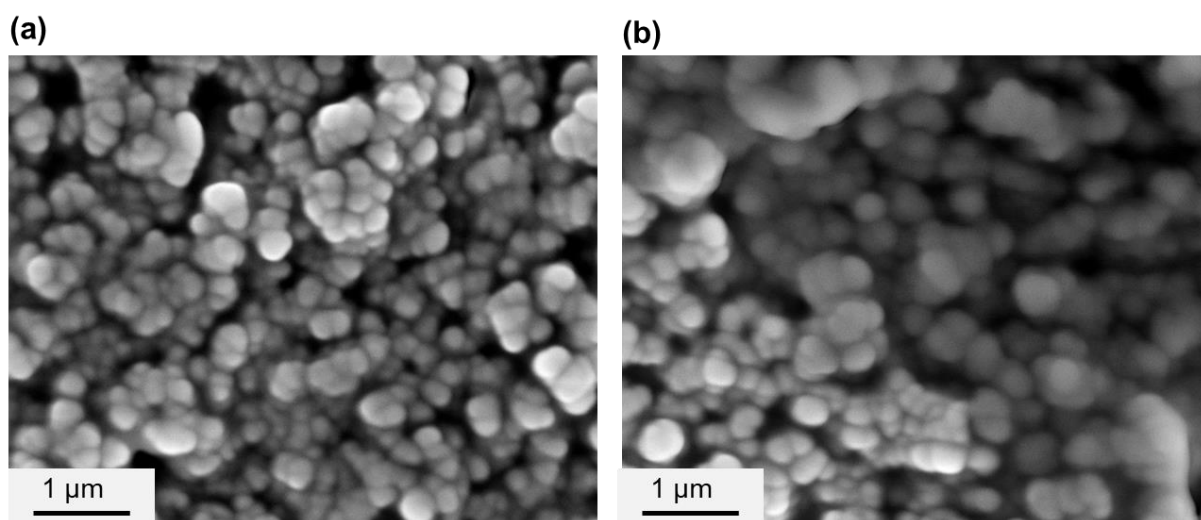
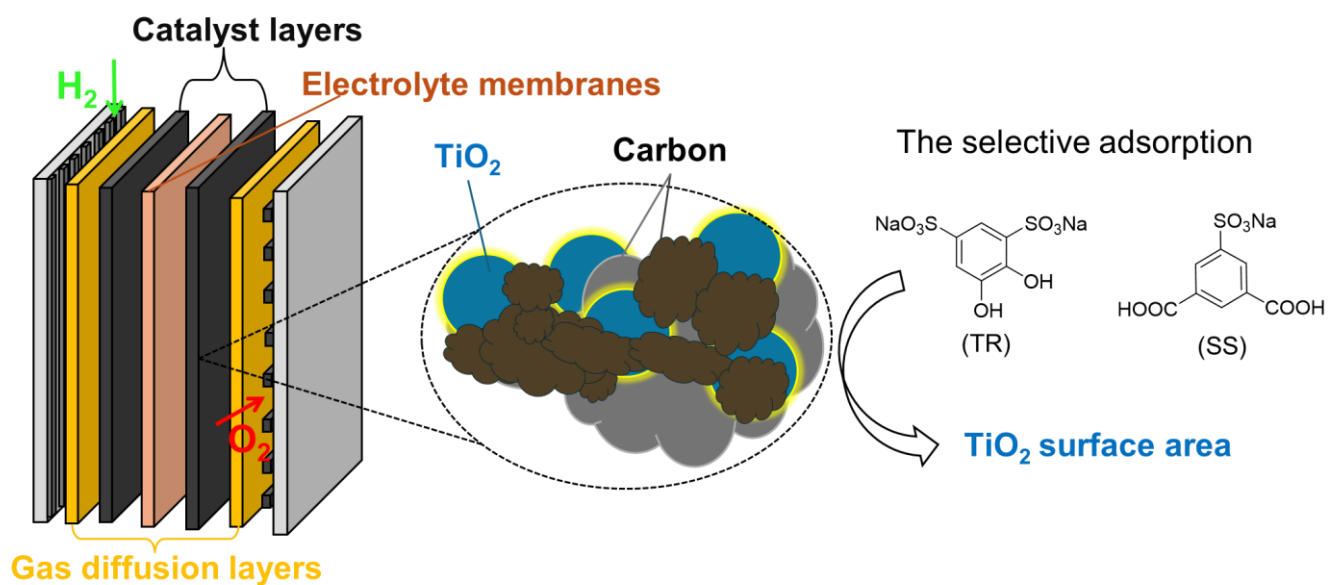


Figure 2.24. SEM images of TiO₂ (a) 30 nm rutile; (b) 100 nm anatase (after adsorption of TR based on Figure 2.3)

Chapter 3. TiO_2 /carbon Catalysts for Hydrogen Fuel Cell



3.1. Introduction: TiO₂/carbon catalysts and hydrogen fuel cell

3.1.1. Introduction: Hydrogen fuel cell and catalysts

As society advances into the 21st century, the depletion of traditional fossil fuel reserves (e.g., coal, oil, natural gas) has become increasingly evident, accompanied by rising levels of environmental pollution. Moreover, the global distribution of fossil fuels is highly uneven and vulnerable to geopolitical disruptions. Oil crises resulting from conflicts such as the Israeli-Palestinian tensions, the Iran-Iraq War, and natural gas shortages during the Russia-Ukraine conflict exemplify this fragility. These challenges underscore the urgent need for environmentally friendly, efficient, and sustainable alternative energy sources.

Nuclear energy, which is widespread throughout the universe (e.g., solar nuclear fusion), is considered abundant and has been widely adopted in power generation. However, its inherent risks—highlighted by catastrophic accidents such as Chernobyl and Fukushima—remain a significant concern.

Renewable energy sources, including solar, biomass, wind, and geothermal energy, are abundant and environmentally advantageous. However, to meet the demands of modern society, they must first be converted into electrical or chemical forms. For instance, solar panels and wind turbines generate electricity for the power grid, while biomass-derived fuels (e.g., methane, ethanol) and lithium-ion batteries serve as energy storage and transportation solutions. Among chemical energy sources, hydrogen stands out due to its high energy density and minimal environmental impact.

Hydrogen can be produced from solar energy, fossil fuels, or water electrolysis and then transported to hydrogen refueling stations or residential areas, where it is converted into electricity using fuel cells and other technologies [17a]. Despite its promising features, hydrogen energy faces substantial challenges. These include the need for environmentally benign and cost-effective production methods that do not rely on fossil fuels, the high costs and risks associated with hydrogen transport and storage infrastructure, and the relatively low efficiency and high expense of fuel cells. Nevertheless, hydrogen energy remains a vital avenue for developing future energy systems.

The Japanese government has identified hydrogen energy as a priority in its future energy strategy [17b, c], in alignment with similar initiatives in the United States, Europe, and China [17d]. This global momentum has accelerated the commercialization of hydrogen-powered technologies, including vehicles such as cars, trucks, trains, and buses. An example is Toyota's deployment of a hydrogen-powered bus (Figure 3.1).

At present, most hydrogen fuel cells employ platinum/carbon catalysts, where platinum facilitates the oxygen reduction to form water [17e, f]. While platinum is an exceptionally efficient catalyst, its scarcity,

high cost, and tendency to detach from carbon supports present significant obstacles. To address these issues, alternative catalysts—such as Fe-N-C materials [17f, g] and metal oxide/carbon composites [6a, 18], are being actively investigated as potential substitutes for the platinum-based systems.



Figure 3.1. Toyota SORA school bus in Tokyo University of Technology.

The Ishihara research group at Yokohama National University has made significant progress in developing oxide/carbon-based catalysts [18]. Their strategy involves depositing metal precursors—typically organometallic compounds—onto carbon supports, followed by pyrolysis in a mixed gas atmosphere of oxygen, hydrogen, and nitrogen (or argon). Various carbon materials, such as carbon nanotubes, graphene, and carbon black, are commonly employed as supports due to their excellent electrical conductivity. During pyrolysis, metal oxides are formed on the carbon surface and are partially reduced, resulting in the emergence of catalytic activity. These active sites are primarily located at the partially reduced regions of the metal oxides on the catalyst surface [18], as illustrated in Figure 3.2 for the Nb-TiO₂/carbon catalyst.

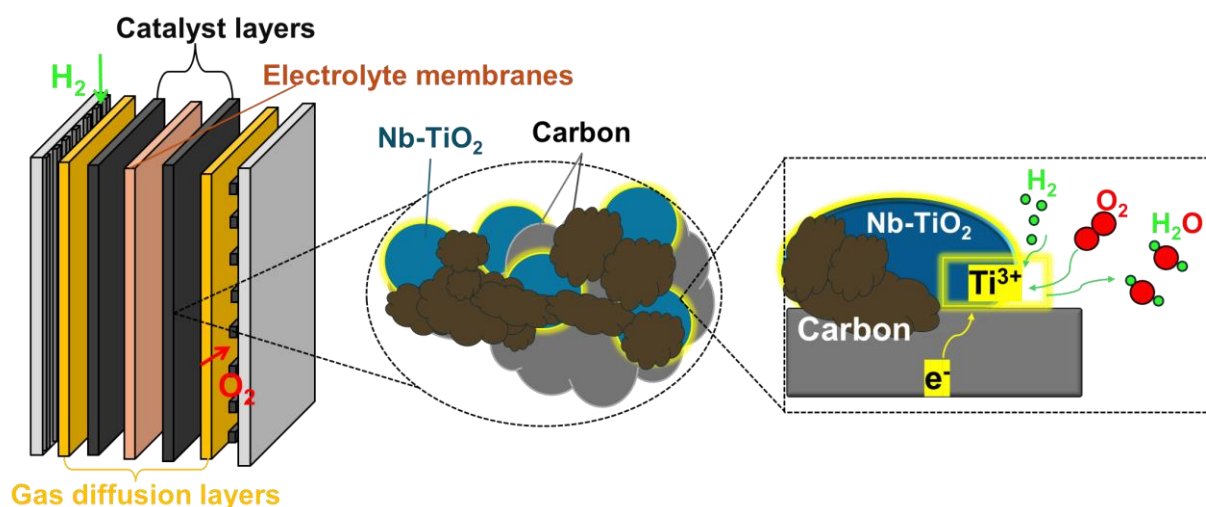


Figure 3.2. Nb-TiO₂/carbon catalyst for hydrogen fuel cell [18b, e-g].

To identify these active sites and evaluate the surface areas of catalytic materials, it is essential to quantitatively assess the surface area of metal oxides supported on carbon. In Chapter 2, a novel technique was introduced for determining the surface area of carbon-supported metal oxides via the selective adsorption of probe organic molecules. In the present chapter, this method is applied to TiO₂/carbon catalysts developed for hydrogen fuel cell applications. The goal here in this study is to investigate the correlation between the surface area of titanium oxide and its catalytic performance in fuel cell systems through the selective adsorption of probe molecules.

3.1.2. Nb-TiO₂/CSCNT catalysts

Although titanium oxide (TiO₂) inherently exhibits low catalytic activity, niobium (Nb) doping significantly enhances its catalytic properties. Nb incorporation promotes the generation of Ti³⁺ active sites, enhances the electrical conductivity of TiO₂, increases its specific surface area and durability, and introduces new catalytic sites associated with niobium oxides [18b, e-f]. Additionally, cup-stacked carbon nanotubes (CSCNTs) possess excellent conductivity and facilitate the formation of nanoscale oxides along their edges [18g]. Building on these advantages, the Ishihara group developed Nb-doped TiO₂ supported on CSCNTs (Nb-TiO₂/CSCNT) as an electrocatalyst.

The catalyst precursors were synthesized by mixing Ti (titanium(IV) tetraisopropoxide, C₁₂H₁₈O₄Ti) and Nb (niobium(V) ethoxide, C₁₀H₂₅O₅Nb) compounds with CSCNTs, followed by hydrolysis. The resulting precursors were heat-treated at 600–1000°C for 10 min in an Ar atmosphere containing 4% H₂, producing the Nb-TiO₂/CSCNT catalysts. The catalysts were characterized by field-emission scanning electron microscopy (FE-SEM), X-ray diffraction (XRD), and X-ray photoelectron spectroscopy (XPS), and their oxygen reduction reaction (ORR) activity was evaluated [18g].

The XRD patterns and mean particle sizes of the Nb-TiO₂/CSCNT catalysts are presented in Figure 3.3 [18g]. The crystal phase transformation of TiO₂ depends on various factors, including synthetic procedure, heat-treatment temperature, pressure, atmosphere, and dopants [19a-c]. Under ambient conditions, anatase begins to transform into rutile above 600°C [19a]. This transformation is governed by crystal size, as the surface Gibbs free energy determines the most stable crystal structure. Specifically, anatase is more stable for particle sizes below 11 nm, while rutile becomes more stable for sizes exceeding 35 nm [19b, c]. In line with these observations, the experimental results show the appearance of rutile (grain size 11.7 nm) at 800°C, and coexistence of anatase and rutile phases at 900°C with a grain size of 26.1 nm. The CSCNT support may contribute to stabilizing the anatase phase by limiting crystal growth, with rutile appearing only above 700°C. Notably, Nb diffraction peaks were not observed in XRD, likely due to their

low content or high dispersion.

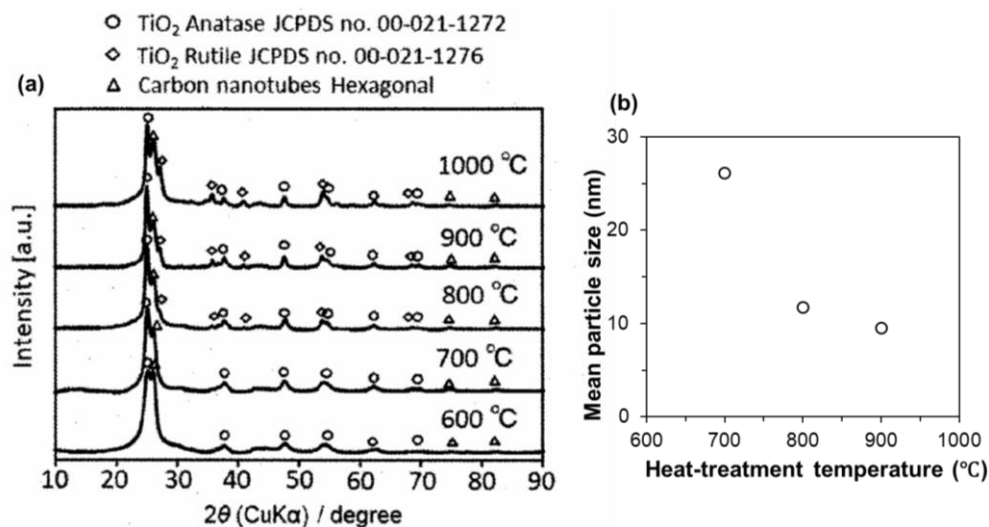


Figure 3.3. (a) XRD pattern and (b) mean particle size (by FE-SEM) of Nb-TiO₂/CSCNT catalysts [18g].

In this work, the exposed surface areas of Nb-TiO₂ on Nb-TiO₂/CSCNT catalysts were quantified using the selective adsorption of TR, and the correlation between surface areas of Nb-TiO and the ORR activity was investigated. The Brunauer–Emmett–Teller (BET) surface areas were also measured (Appendix, Figure 3.14).

3.1.3. N-TiO₂/MWCNT catalysts prepared with different annealing times

Nitrogen-doped TiO₂ (N-TiO₂) supported on multi-walled carbon nanotubes (MWCNTs), synthesized from Ti-, N-, and C-containing precursors. Nitrogen doping has been shown to stabilize specific crystalline phases of TiO₂ [18c, d]. MWCNTs, known for their high specific surface area and excellent conductivity, serve as effective support materials.

The Ishihara group synthesized and investigated the N-TiO₂/MWCNT catalysts [18d]. To prepare the catalysts, titanium-based organic compounds (oxytitanium(IV) tetrapyrazinoporphyrazine, C₂₄H₈N₁₆OTi) and MWCNTs were mixed, then heat-treated at 900 °C in Ar atmosphere containing 2% H₂ and 0.05% O₂, and subsequently annealed for 0–10 h. During this process, carbon deposition from C₂₄H₈N₁₆OTi occurred on the catalyst surface, improving electrical conductivity [18c]. The Ishihara group conducted characterization (XPS, TEM, and X-ray pair distribution function (PDF) structural analysis) and evaluated the catalytic activity for the oxygen reduction reaction (ORR) [18d].

The evolution of the titania crystal structure and particle size with annealing time (0–10 h) is

summarized in Figure 3.4 [18d]. Due to the extremely small crystal size (below the detection limit of XRD), direct analysis using XRD was not feasible. At annealing times of 0 and 1 h, a relatively rare lepidocrocite-type layered titanate structure was observed. Although reports on this structure are limited, lepidocrocite-like TiO_2 is recognized as a unique form of titanium oxide, featuring a layered arrangement similar to the mineral lepidocrocite (an iron oxide) [19d-f]. Nitrogen doping appears to stabilize this lepidocrocite structure [18d, 19c]. After 3 h of annealing, the brookite phase appeared. Brookite is generally considered a metastable intermediate phase during the transformation of anatase to rutile [19b, c]. Prolonged annealing (5 and 10 h) resulted in the formation of TiO_2 particles, most likely due to the reduction of brookite under the H_2 atmosphere, as indicated by changes in mass fractions (Figure 3.4). During this stage, the rutile phase also began to form, although its crystal size remained below the expected thermodynamic threshold for rutile formation (which typically occurs when particle sizes exceed 11 nm) [19b, c].

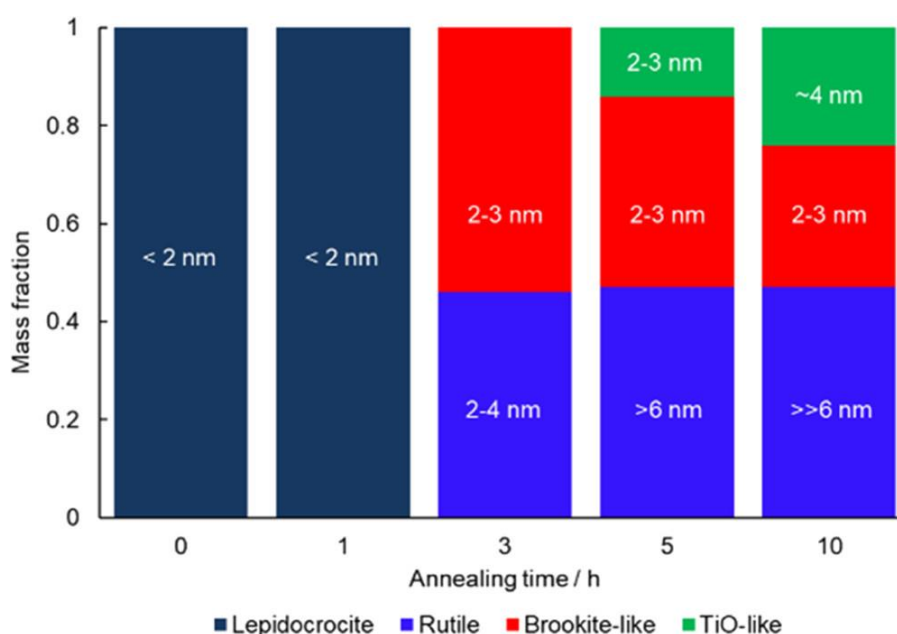


Figure 3.4. Summary of phase composition. Numbers above bars represent domain sizes obtained by PDF analysis or TEM for the N- TiO_2 /MWCNT catalysts [18d], reuse by license under CC-BY; Copyright {2017} American Chemical Society.

Phase transitions in TiO_2 are influenced by impurities and atmospheric conditions. Impurities such as Li, K, Na, Fe, Ce and Mn oxides promote phase transitions by increasing oxygen vacancies, while S, P, and W oxides inhibit transitions by stabilizing the existing structure [19c]. A reducing atmosphere (e.g., H_2) facilitates phase transitions by creating Ti interstitials, whereas oxidizing conditions tend to suppress them [19c]. The nitrogen doping may have further promoted rutile formation even below its thermodynamic particle size threshold [18d, 19c].

Although XPS analysis confirmed the presence of TiN and Ti^{3+} species in the catalyst, these were found to have only a minimal impact on catalytic activity, as demonstrated by comparisons of XPS spectra between HF-treated and untreated samples after removing oxide components [18d].

In this work, the TiO_2 surface areas were determined using the selective adsorption of SS, and the BET surface areas were also measured (Appendix, Figure 3.15a).

3.1.4. N-Fe- TiO_2 /carbon catalysts

The Ishihara group reported that carbon derived from the $\text{C}_{24}\text{H}_8\text{N}_{16}\text{OTi}$ precursor formed a conductive network on the catalyst surface. Notably, even without MWCNT support, the introduction of Fe and Zn enabled the formation of highly dispersed titanium oxide [18].

The Ishihara group employed a similar catalyst preparation method. A titanium-based organic complex, oxytitanium(IV) tetrapyrzine porphyrzine, $\text{C}_{24}\text{H}_8\text{N}_{16}\text{OTi}$, was mixed with trace amounts of Fe (ferric acetate) and Zn (zinc acetate) salts, without the use of any external support material. The atomic ratios of Fe or Zn to Ti were varied from 0 to 0.3 or 0.5. The resulting N-Fe- TiO_2 /carbon catalysts (with carbon derived from the organic precursor) were synthesized via pyrolysis and/or calcination at 900°C for 3 h under an Ar atmosphere containing 2% H_2 and 0.05% O_2 [18h]. During the pyrolysis process, the low boiling point of Zn led to its volatilization, resulting in negligible Zn content in the final catalyst [19m]. The catalysts were characterized by X-ray diffraction (XRD), field-emission scanning electron microscopy (FE-SEM), and Brunauer–Emmett–Teller (BET) surface area analysis. Their oxygen reduction reaction (ORR) current densities were evaluated in hydrogen fuel cell [19m].

Figure 3.5 shows the XRD patterns of two samples with Zn/Ti ratios of 0 and 0.3, each with varying Fe/Ti ratios (0 to 0.5). In the absence of Fe, no distinct TiO_2 diffraction peaks were detected, likely due to the titanium oxide nanocrystals being too small for XRD detection. As the Fe content increased (Fe/Ti = 0.05–0.3), diffraction peaks corresponding to rutile TiO_2 and Fe and/or Fe_3C phases gradually appeared, suggesting that Fe addition promoted the formation of stable rutile TiO_2 [19c]. Moreover, Fe may have competed with Ti in rutile formation by interacting with C and N, possibly resulting in the generation of Fe_3C species.

No significant differences in XRD-detected crystal phases were observed between the Zn/Ti = 0 and Zn/Ti = 0.3 samples. However, the diffraction peaks became sharper with increased Zn content (Zn/Ti = 0.3), indicating the formation of larger crystallites. This could be attributed to Zn volatilization during thermal treatment, which may have generated voids and facilitated crystal growth [18l].

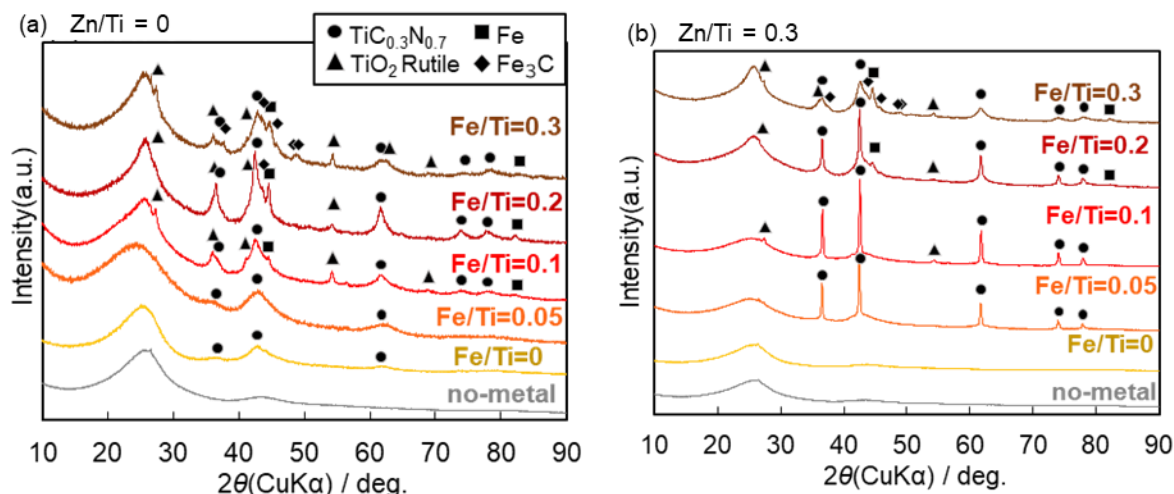


Figure 3.5. XRD patterns of the N-Fe-TiO₂/carbon catalysts with (a) Zn/Ti = 0 and (b) Zn/Ti = 0.3 [18].

In the present work, the TiO₂ surface areas of the catalysts were determined using the selective adsorption of SS.

3.1.5. N-TiO₂/MWCNT catalysts prepared with different oxygen contents

The previous section discussed the effects of Fe and Zn doping on catalyst activity. The Ishihara group next focused on the influence of oxygen concentration during thermal decomposition. To isolate the variable of oxygen content, the catalysts were prepared without Fe and Zn doping using multi-walled carbon nanotubes (MWCNTs) as the support. The N-TiO₂/MWCNT catalysts were synthesized following a procedure similar to that described in Section 3.1.3, with the primary difference being the calcination atmosphere. The catalysts were calcined at 900°C in a 2% H₂/Ar mixture, with oxygen concentrations ranging from 0 to 2%. The Ishihara group evaluated oxygen reduction reaction (ORR) activity by reaction in hydrogen fuel cells, as well as BET surface area and TiO₂ loading using N₂ adsorption and thermogravimetric (TG) analysis, respectively.

In this work, the structural properties of the catalysts were analyzed through XRD measurements and quantitative evaluation of the TiO₂ surface areas by the selective adsorption of SS.

3.2. Experimental

In the typical procedure (performed at half of the scale described in Chapter 2), TiO₂/carbon catalyst powder material (5.0 mg) was added into a solution (2.5 mL) of TR or SS in DMF in a vial. The mixture was stirred or shaken at 110°C for 1 h in air.

The adsorption ratios or amounts of TR or SS on the TiO₂/carbon catalysts were quantified by liquid UV-Vis analysis. The adsorption of TR and SS in DMF solution on the carbon support materials and deposited carbon (produced during catalyst preparation) was assumed to be neglected. The relationship between the adsorption amounts and the surface area of the metal oxide was referred to the data in Figures 2.3 and 2.4 and Formula 3.1 below:

$$S = \frac{W}{W_s} \dots \dots \dots (\text{Formula 3.1})$$

In this formula, S is the estimated surface area of metal oxide (m² g⁻¹), W is the adsorption amount (mol) of TR or SS, W_s is adsorption amounts per unit surface area (mol m⁻²).

This work was conducted in collaboration with the Ishihara group at Yokohama National University. Four series of catalysts, Nb-TiO₂/CSCNT [18g], N-TiO₂/MWCNT [18d], N-Fe-TiO₂/carbon [18l], and N-TiO₂/MWCNT, were prepared under various conditions by the Ishihara group. Most of the catalyst characterizations and all of the catalytic activity evaluations were performed by the Ishihara group. In this study, the exposed TiO₂ surface areas of these catalysts were determined to investigate the correlation between catalytic activity and TiO₂ surface area.

3.3. Results and discussion

3.3.1. Surface area analysis of Nb-TiO₂/CSCNT catalysts

The surface areas of Nb-TiO₂ on the Nb-TiO₂/CSCNT catalysts were evaluated using the selective adsorption of TR as shown in Figure 3.6a. The exposed surface area decreases from 600°C to 800°C, then increases from 800°C to 1000°C. This trend reflects the increasing Nb-TiO₂ particle size with heat-treatment temperature, which generally reduces surface area. However, partial decomposition of the CSCNT support and deposited carbon at elevated temperatures may increase metal oxide exposure, thereby offsetting the impact of particle growth. These competing processes contribute to the nonlinear variation (a basin-shaped plot) observed in the Nb-TiO₂ surface area as a function of heat-treatment temperature. Additionally, the BET surface area may influence the Nb-TiO₂ surface area to some extent (Appendix, Figure 3.14b).

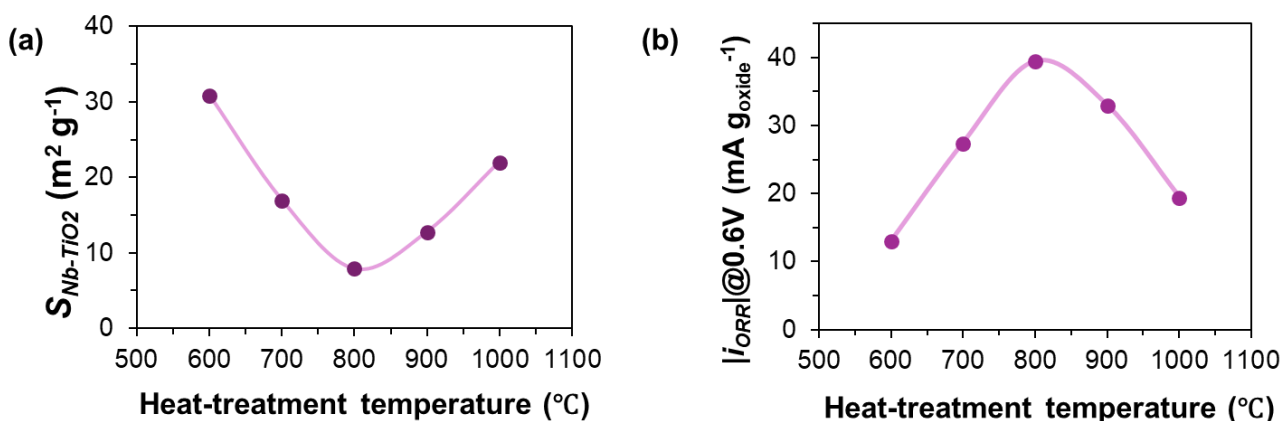


Figure 3.6. Dependence of a) the exposed Nb-TiO₂ surface area, and (b) the catalytic activity of ORR current at 0.6 V of Nb-TiO₂/CSCNT catalysts [18g] on heat-treatment temperature.

Figure 3.6b illustrates the relationship between the specific oxygen reduction reaction current density (i_{ORR}) and the heat treatment temperature of the Nb-TiO₂/CSCNT catalyst [18g]. The i_{ORR} increases from 600°C to 800°C, then decreases from 800°C to 1000°C, forming a volcano-shaped plot with heat-treatment temperature, which is inversely correlated with the surface area of Nb-TiO₂ (Appendix, Figure 3.14a). Since the carbon component contributes to electrical conductivity, active catalytic sites are likely to form at the interface between Nb-TiO₂ and the carbon support [18a, c, e, f, n]. Furthermore, the current density at 0.6V, an indicator of catalytic activity, exhibits a positive correlation with the $Ti^{3+}/(Ti^{3+} + Ti^{4+})$ ratio (Figure 3.7) [18h]. The presence of Ti^{3+} , owing to its lower oxidation state relative to Ti^{4+} , likely promotes oxygen adsorption and functions as an active site for the oxygen reduction reaction [18c, e, f, g].

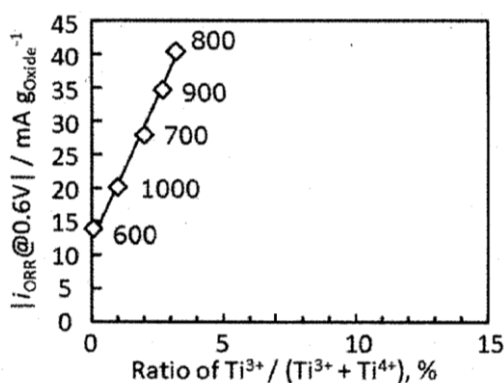


Figure 3.7. Relationship between the ratio of $Ti^{3+}/(Ti^{3+} + Ti^{4+})$ and the catalytic activity of ORR current of Nb-TiO₂/CSCNT catalysts. The oxide current represents the current density per unit Nb-TiO₂, calculated by subtracting the carbon-derived current from the total current density [18f].

3.3.2. Surface area analysis of N-TiO₂/MWCNT catalysts prepared with different annealing times

Since TiN was detected in the N-TiO₂/MWCNT catalyst by XPS, the adsorption characteristics of titanium carbonitride (TiCN) were first investigated, assuming that TiCN, a continuous solid solution of TiC and TiN, exhibits the surface properties of both components [19h, l]. Adsorption tests using TiCN (Aldrich, BET surface area: 172 m² g⁻¹) revealed only minor adsorption (adsorption rates: 3% for SS and 5% for TR), suggesting that these Ti–N compounds do not significantly interfere with the adsorption behavior on titanium oxides.

Attempts to measure the TiO₂ surface area on the N-TiO₂/MWCNT catalysts using the selective adsorption of TR were unsuccessful. A new UV peak appeared at approximately 520 nm (Appendix, Figure 3.13b), implying that TR may form complexes with trace Ti ions released from the catalysts because TR forms stable complexes with Ti and Fe ions [19h]. Interestingly, no such UV peaks were observed in the catalysts discussed in Section 3.3.1, suggesting that nitrogen doping in the N-TiO₂/MWCNT catalyst may be responsible for the observed spectral changes.

Fortunately, we could successfully quantify the surface area of titanium dioxide using the selective adsorption of SS. As shown in Figure 3.8a, the TiO₂ surface area initially increased and then decreased with prolonged annealing at 1000°C (0–10 h). This trend is attributed to TiO₂ particle growth and concurrent carbon decomposition. A moderate annealing time (e.g., 3 h) promoted slight TiO₂ growth and carbon loss, increasing the exposed TiO₂ surface. However, after 10 h, excessive sintering reduced the accessible surface area. Notably, this surface area trend differs from that observed in BET measurements (Appendix, Figure 3.15a).

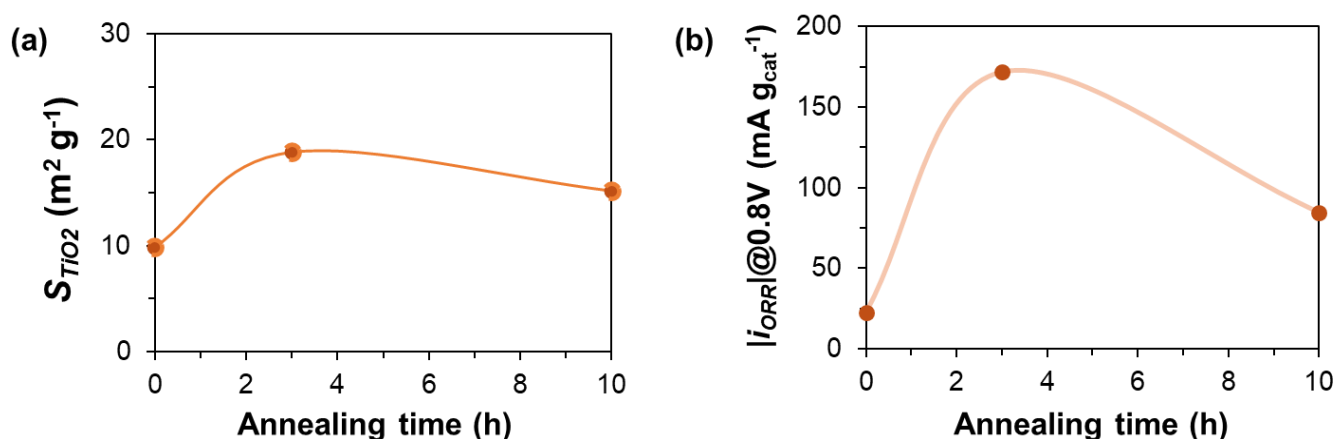


Figure 3.8. Dependence of (a) the exposed TiO₂ surface area; and (b) the catalytic activity of ORR current of N-TiO₂/MWCNT catalysts [18d] on annealing time.

Figure 3.8b [18d] illustrates the relationship between iORR catalytic activity and annealing time. Catalytic activity correlates positively with the surface area of TiO₂. The unannealed catalyst (0 h) shows the lowest activity, consistent with its relatively small TiO₂ surface area. The highest catalytic performance is observed after 3 h of annealing, corresponding to a moderate increase in surface area. However, despite only a slight decrease in surface area after 10 h of annealing, catalytic activity drops markedly. This decline may be attributed to a significant loss of nitrogen dopants [18d], which is key in enhancing conductivity.

Interestingly, the catalytic performance did not directly correlate with Ti³⁺ density [18d]. According to Ishihara et al., the active sites for the ORR are primarily located on the surface of brookite and/or rutile TiO₂ (Appendix, Figure 3.15b) [18d]. These results indicate that the electrocatalytic activity of N-TiO₂/MWCNT catalysts annealed for different durations is influenced by a combination of factors, including exposed surface area, crystalline phase composition, and conductive pathways within the composite TiO₂ catalysts.

3.3.3. Surface area analysis of N-Fe-TiO₂/carbon catalysts

The surface areas of titanium oxide on carbon were determined using the selective adsorption of SS, as shown in Figure 3.9a. As previously discussed, SS does not adsorb onto metal nitrides or carbides such as TiC_{0.3}N_{0.7} in the absence of a Fe precursor. It has been reported that adding Zn to the catalyst precursor, followed by its volatilization during pyrolysis, can enhance catalyst porosity [19m]. However, the present results show that while the oxide surface area initially increases with rising Zn content, it slightly decreases at higher Zn levels. This decrease may be attributed to excessive Zn volatilization, which could induce the formation of larger pores, promote crystal growth, or collapse fine pores, thereby reducing the exposed oxide surface area.

Interestingly, variations in the Fe content of the precursor appear to have minimal influence on the oxide surface area, likely because Fe is not significantly converted to its oxide form. Generally, the surface area of metal oxides tends to increase with increasing Zn content. Moreover, no clear correlation was observed between the TiO₂ surface area and the BET surface area of the catalysts (Appendix, Figure 3.16).

Figure 3.9b illustrates the catalytic activity for the ORR reaction. Although some fluctuations were observed, the overall trend indicates a positive correlation between catalytic activity and the surface area of metal oxide. This suggests that under similar calcination conditions, tuning the Fe/Ti and Zn/Ti ratios results in a uniform distribution of active sites on the oxide surface of the N-Fe-TiO₂/carbon catalyst. This uniformity likely contributes to the observed correlation between surface area and catalytic performance.

In addition, the increase in rutile XRD peak intensity (Figure 3.5) correlates with enhanced catalytic activity, further supporting the hypothesis that the rutile TiO_2 surface acts as an active site for catalysis.

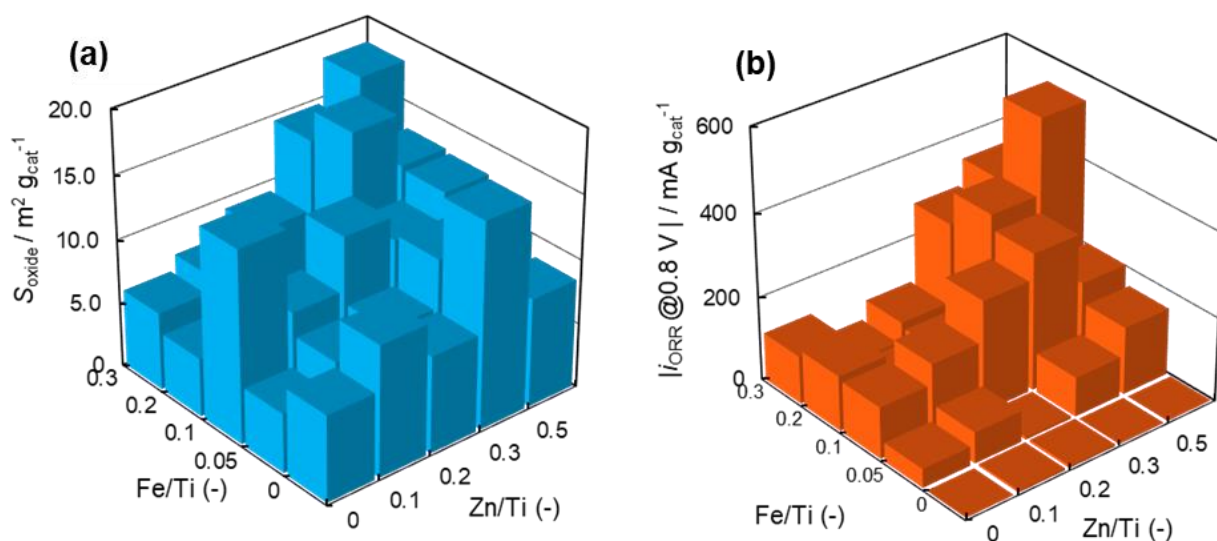


Figure 3.9. (a) Exposed TiO_2 surface area and (b) ORR catalytic activity of the N-Fe- TiO_2 /carbon catalysts [18].

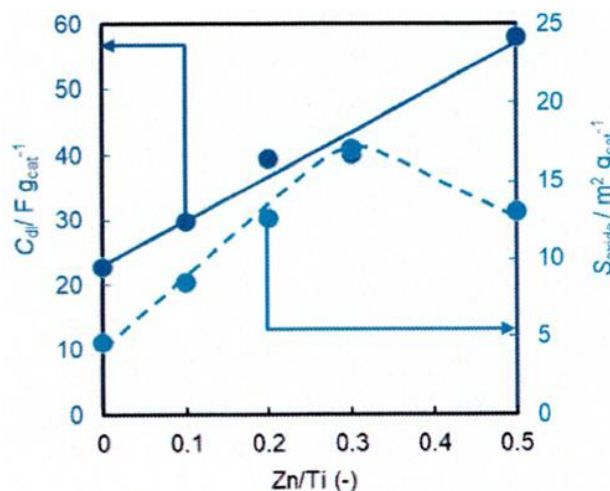


Figure 3.10. Dependence of double layer capacitance (C_{dl}) and Ti oxide surface area on Zn/Ti ratio of N-Fe- TiO_2 /carbon catalysts [18].

In hydrogen fuel cells, the electrical double layer refers to the charge separation that forms at the interface between the electrode (e.g., Pt) and the electrolyte. The capacitance of this double layer (C_{dl}) is influenced by factors such as electrode material, surface area, and electrolyte composition. Porous or nanostructured electrodes typically exhibit higher capacitance due to their large surface areas. Figure 3.10 illustrates the dependence of the Zn/Ti ratio on the double-layer capacitance and on the metal oxide surface area. For Zn/Ti ratios from 0 to 0.3, both C_{dl} and the oxide surface area increase with increasing

Zn content. However, at a Zn/Ti ratio of 0.5, the surface area decreases while the capacitance continues to increase. This discrepancy could be attributed to the growth of Ti oxide crystallites at higher Zn concentrations, which reduces the exposed surface area despite the increase in total electrical interface.

3.3.4. XRD and surface area analyses of N-TiO₂/MWCNT catalysts prepared with different oxygen contents

The XRD patterns of the N-TiO₂/MWCNT catalysts are shown in Figure 3.11. With increasing O₂ concentration in the pyrolysis atmosphere, the formation of TiO₂ crystals became more pronounced. At 0.05% O₂, no distinct diffraction peaks were observed besides those of the MWCNT support. In contrast, when the oxygen concentration was increased to 2%, pronounced peaks corresponding to anatase and rutile TiO₂ phases were observed, with crystallite sizes estimated at 9–10 nm. Notably, despite the presence of nitrogen in the catalyst precursor, no TiN or TiC phases were detected, unlike in the previous reports [18m, 1].

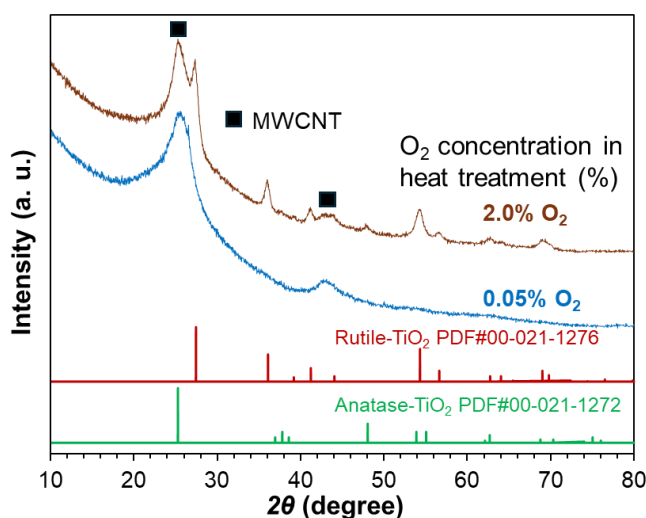


Figure 3.11. XRD patterns of the N-TiO₂/MWCNT catalysts synthesized under 0.05% and 2.0% O₂ atmospheres.

The titanium oxide surface area was determined using the selective adsorption of SS, as shown in Figure 3.12a. The results indicate that the TiO₂ surface area increased with oxygen concentration in the Ar atmosphere up to a certain point. This trend is attributed to enhanced decomposition of the carbon support, facilitating the formation of titanium oxide phases and exposing more surface area. However, at higher O₂ concentrations, sintering and agglomeration of TiO₂ occurred, leading to particle growth and a decrease in surface area. Moreover, no direct correlation was observed between the TiO₂ surface area and

either the BET surface area or TiO₂ loading (Appendix, Figure 3.17).

A similar trend was observed in ORR catalytic activity (Figure 3.12b), which increased initially and then declined. However, the peak positions in the volcano plots of surface area and catalytic activity did not coincide. This discrepancy could be due to the rapid loss of active sites caused by over-oxidation of titanium oxide, which precedes the decline in surface area resulting from sintering.

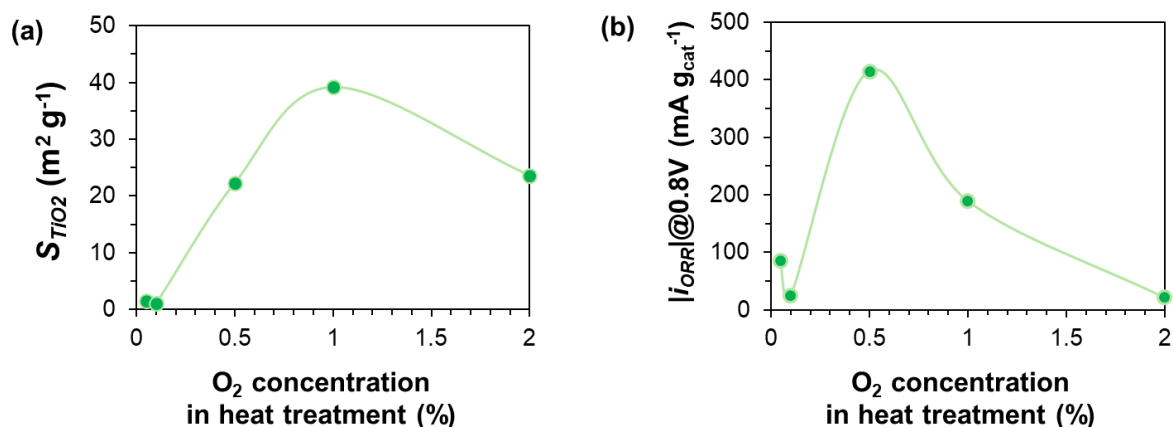


Figure 3.12. Dependence of (a) the exposed TiO₂ surface area and (b) the ORR current (provided by the Ishihara group) of N-TiO₂/MWCNT catalysts on O₂ concentration.

3.4. Conclusions

In this chapter, the selective adsorption method established in Chapter 2, the selective adsorption of TR and SS on titanium dioxide over the carbon support, was employed. Using this method, the TiO₂ surface areas on four different carbon-supported TiO₂ catalysts synthesized under inert atmospheres (Ar or N₂) containing H₂ and O₂ were evaluated. Furthermore, the relationships between the TiO₂ surface area on the support and the electrocatalytic activity toward hydrogen fuel cell reactions were investigated.

For Nb-TiO₂/CSCNT catalysts prepared at different heat-treatment temperatures, the TiO₂ surface area initially decreased and then increased with increasing heat-treatment temperature. An inverse correlation was observed between the TiO₂ surface area and the catalytic activity for Nb-TiO₂/CSCNT.

In contrast, for the N-TiO₂/MWCNT catalysts prepared with different annealing times, the TiO₂ surface area initially rose and then declined with increasing annealing time. Additionally, a positive correlation between surface area and catalytic activity was observed across these N-TiO₂/MWCNT catalysts.

When carbon-supported N-TiO₂ catalysts were synthesized with different Fe and Zn doping levels (i.e., N-Fe-TiO₂/C catalysts), and without the use of CNTs as a support, the TiO₂ surface area increased significantly with increasing the Fe and Zn doping levels. A noticeable positive correlation between TiO₂

surface area and catalytic activity was identified.

Moreover, for N-TiO₂/MWCNT catalysts prepared under atmospheres with different oxygen concentrations, the TiO₂ surface area initially increased and then decreased with rising oxygen concentration. A partial positive correlation between surface area and catalytic activity was also observed in this case.

The surface area, crystal structure, and particle size of TiO₂ are influenced by synthesis conditions and the nature of dopants. A weak but consistent positive correlation between TiO₂ surface area and catalytic activity was observed for N-TiO₂/MWCNT, N-Fe-TiO₂/C, and N-TiO₂/MWCNT catalysts across different annealing times, Fe doping levels, and oxygen concentrations. Assuming that the active sites are similar in nature and uniformly distributed across the TiO₂ surface, catalytic activity is expected to scale with surface area. An exception was noted for Nb-TiO₂/CSCNT catalysts, where an inverse correlation was observed with varying heat treatment temperatures. This deviation may be attributed to differences in nitrogen doping, which influences the formation of conductive pathways. In the N-doped TiO₂ catalysts with enhanced conductivity, catalytic activity generally correlates positively with surface area.

Although the findings presented here provide valuable insights, the relationship between the TiO₂ surface area and catalytic activity in these electrocatalysts remains inherently complex. Factors such as particle size, crystal phase, elemental doping, and electrical conductivity are also likely to play significant roles in determining catalytic performance. Understanding the interplay among these variables remains an important direction for future research.

It is hoped that these results will aid in the rational design of carbon-supported TiO₂ catalysts, not only for electrocatalytic applications in hydrogen fuel cells but also for broader applications such as photocatalysis, acid–base catalysis, and related catalytic processes.

3.5. Reference

- [17] (a) Le, T. T.; Sharma, P.; Bora, B. J.; Tran, V. D.; Truong, T. H.; Le, H. C.; Nguyen, P. Q. P. Fueling the future: A comprehensive review of hydrogen energy systems and their challenges. *Int. J. Hydrogen Energy* **2024**, *54*, 791-816. DOI: 10.1016/j.ijhydene.2023.08.044. (b) The Ministerial Council on Renewable Energy, Hydrogen and Related Issues. *Basic Hydrogen Strategy*, June 6, 2023. https://www.meti.go.jp/shingikai/enecho/shoene_shinene/ (accessed 2024-09-13). (c) *World Economic Forum Home Page*. <https://www.weforum.org/agenda/2024/04/hydrogen-japan/> (accessed 2024-09-13). (d) *International Energy Agency Home Page*. <https://www.iea.org/energy-system/low-emission-fuels/hydrogen> (accessed 2024-09-13). (e) Ren, X.; Wang, Y.; Liu, A.; Zhang, Z.; Lv, Q.; Liu, B. Current progress and performance improvement of Pt/C catalysts for fuel cells. *J. Mater. Chem. A* **2020**, *8* (46), 24284-24306. DOI: 10.1039/d0ta08312g. (f) Kodama, K.; Nagai, T.; Kuwaki, A.; Jinnouchi, R.; Morimoto, Y. Challenges in applying highly active Pt-based nanostructured catalysts for oxygen reduction reactions to fuel cell vehicles. *Nat. Nanotechnol.* **2021**, *16* (2), 140-147. DOI: 10.1038/s41565-020-00824-w. (g) Kumar, K.; Dubau, L.; Jaouen, F.; Maillard, F. Review on the Degradation Mechanisms of Metal-N-C Catalysts for the Oxygen Reduction Reaction in Acid Electrolyte: Current Understanding and Mitigation Approaches. *Chem. Rev.* **2023**, *123* (15), 9265-9326. DOI: 10.1021/acs.chemrev.2c00685.
- [18] (a) Ishihara, A.; Tamura, M.; Ohgi, Y.; Matsumoto, M.; Matsuzawa, K.; Mitsushima, S.; Imai, H.; Ota, K.-i. Emergence of Oxygen Reduction Activity in Partially Oxidized Tantalum Carbonitrides: Roles of Deposited Carbon for Oxygen-Reduction-Reaction-Site Creation and Surface Electron Conduction. *J. Phys. Chem. C* **2013**, *117* (37), 18837-18844. DOI: 10.1021/jp405247m. (b) Ishihara, A.; Tamura, Y.; Chisaka, M.; Ohgi, Y.; Kohno, Y.; Matsuzawa, K.; Mitsushima, S.; Ota, K.-i. Titanium-Niobium Oxides as Non-Noble Metal Cathodes for Polymer Electrolyte Fuel Cells. *Catalysts* **2015**, *5* (3), 1289-1303. (c) Hayashi, T.; Ishihara, A.; Nagai, T.; Arao, M.; Imai, H.; Kohno, Y.; Matsuzawa, K.; Mitsushima, S.; Ota, K.-i. Temperature dependence of oxygen reduction mechanism on a titanium oxide-based catalyst made from oxy-titanium tetra-pyrazino-porphyrine using carbon nano-tubes as support in acidic solution. *Electrochim. Acta* **2016**, *209*, 1-6. DOI: 10.1016/j.electacta.2016.05.068. (d) Tominaka, S.; Ishihara, A.; Nagai, T.; Ota, K.-i. Noncrystalline Titanium Oxide Catalysts for Electrochemical Oxygen Reduction Reactions. *ACS Omega* **2017**, *2* (8), 5209-5214. DOI: 10.1021/acsomega.7b00811. (e) Ishihara, A.; Wu, C.; Nagai, T.; Ohara, K.; Nakada, K.; Matsuzawa, K.; Napporn, T.; Arao, M.; Kuroda, Y.; Tominaka, S.; et al. Factors affecting oxygen reduction activity of Nb₂O₅-doped TiO₂ using carbon nanotubes as support in acidic solution. *Electrochimica Acta* **2018**, *283*, 1779-1788. DOI: 10.1016/j.electacta.2018.07.082. (f) Ishihara, A.; Arao, M.; Matsumoto, M.; Tokai, T.; Nagai, T.; Kuroda, Y.; Matsuzawa, K.; Imai, H.; Mitsushima, S.; Ota, K.-i. Niobium-added titanium oxides powders as non-noble metal cathodes for polymer electrolyte fuel cells – Electrochemical evaluation and effect of added amount of niobium. *Inter. J. Hydrogen Energy* **2020**, *45* (8), 5438-5448. DOI: 10.1016/j.ijhydene.2019.08.217. (g) Adachi, Y.; Nagai, T.; Ohgi, Y.; Kuroda, Y.; Matsuzawa, K.; Mitsushima, S.; Ishihara, A. Factors Affecting ORR Activity. Of Nb-added TiO_x Catalysts Supported on CNTs for PEFC. *J. Fuel Cell Tech.* **2021**, *21* (1), 80-86. (h) Takeuchi, Y.; Matsuzawa, K.; Matsuoka, Y.; Watanabe, K.; Nagai, T.; Monden,

R.; Ishihara, A. Improvement of ORR Activity of Monoclinic Zirconium Oxides by Fe and F Co-addition for PEFC Cathodes. *Electrochem.* **2023**, *91* (12), 127001-127001. DOI: 10.5796/electrochemistry.23-00103. (l) Obata, M.; Ma; Matsuzawa, K.; Takeuchi, Y.; Shang, L.; Hara, K.; Ishihara, S.; Izawa, K.; Nagai, T.; Monden, R.; Ishihara, A. Improvement of Oxygen Reduction Reaction Activity by Addition of Fe and Zn to Titanium Oxide-based Catalysts in Acid Electrolytes. *J. Fuel Cell Tech.* **2024**, *23* (3), 83-94. (m) Obata, M.; Matsuzawa, K.; Takeuchi, Y.; Nagai, T.; Monden, R.; Ishihara, A. Improvement of ORR Activity of TiO₂-Based Catalysts for PEFC Cathodes by Controlling Zn Addition Rate and Heat Treatment Atmosphere. *J. Fuel Cell Tech.* **2024**, *24* (1), 58-65. (n) Shinyoshi, N.; Seino, S.; Hasegawa, Y.; Uetake, Y.; Nagai, T.; Monden, R.; Ishihara, A.; Nakagawa, T. Effect of particle size on the oxygen reduction reaction activity of carbon-supported niobium-oxide-based nanoparticle catalysts. *J. Mater. Sci.* **2025**, *60* (7), 3275-3285. DOI: 10.1007/s10853-025-10632-z.

[19] (a) Hanaor, D. A. H.; Sorrell, C. C. Review of the anatase to rutile phase transformation. *J. Mater. Sci.* **2011**, *46* (4), 855-874. DOI: 10.1007/s10853-010-5113-0. (b) Di Paola, A.; Bellardita, M.; Palmisano, L. Brookite, the Least Known TiO₂ Photocatalyst. *Catalysts* **2013**, *3* (1), 36-73. DOI: 10.3390/catal3010036. (c) Gatou, M.-A.; Syrrakou, A.; Lagopati, N.; Pavlatou, E. A. Photocatalytic TiO₂-Based Nanostructures as a Promising Material for Diverse Environmental Applications: A Review. *Reactions* **2024**, *5* (1), 135-194. (d) Gateshki, M.; Yin, S.; Ren, Y.; Petkov, V. Titania Polymorphs by Soft Chemistry: Is There a Common Structural Pattern? *Chem. Mater.* **2007**, *19* (10), 2512-2518. DOI: 10.1021/cm0630587. (e) Reeves, K. G.; Ma, J.; Fukunishi, M.; Salanne, M.; Komaba, S.; Dambournet, D. Insights into Li⁺, Na⁺, and K⁺ Intercalation in Lepidocrocite-Type Layered TiO₂ Structures. *ACS Appl. Energy Mater.* **2018**, *1* (5), 2078-2086. DOI: 10.1021/acsaem.8b00170. (f) Sorrentino, A. L.; Serrano, G.; Poggini, L.; Cortigiani, B.; El-Kelany, K. E.; D'Amore, M.; Ferrari, A. M.; Atrei, A.; Caneschi, A.; Sessoli, R.; et al. Quasi-Hexagonal to Lepidocrocite-like Transition in TiO₂ Ultrathin Films on Cu(001). *J. Phys. Chem. C* **2021**, *125* (19), 10621-10630. DOI: 10.1021/acs.jpcc.1c01098. (g) Nucera, A.; Carniato, F.; Baranyai, Z.; Platas-Iglesias, C.; Botta, M. Characterization of the Fe(III)-Tiron System in Solution through an Integrated Approach Combining NMR Relaxometric, Thermodynamic, Kinetic, and Computational Data. *Inorg. Chem.* **2023**, *62* (10), 4272-4283. DOI: 10.1021/acs.inorgchem.2c04393. h) He, J.; He, Z.; Qin, Y.; Zhao, H.; Bi, Y. A Review of TiCN Coating Prepared by Reaction Plasma Spraying. *J. Therm. Spray Tech.* **2022**, *31* (8), 2280-2299. DOI: 10.1007/s11666-022-01454-5. (i) Xie, S.; Yan, J.; Alhassan, S. I.; Huang, L.; Sio, W. H.; Zeng, Z.; Zhang, H. Application of metal nitrides in catalysis and adsorption of pollutants in water. *J. Environ. Chem. Eng.* **2024**, *12* (2), 111961. DOI: 10.1016/j.jece.2024.111961. (m) Xin, W.; Song, Y. Mesoporous carbons: recent advances in synthesis and typical applications. *RSC Adv.* **2015**, *5* (101), 83239-83285. DOI: 10.1039/C5RA16864C.

3.6. Appendix

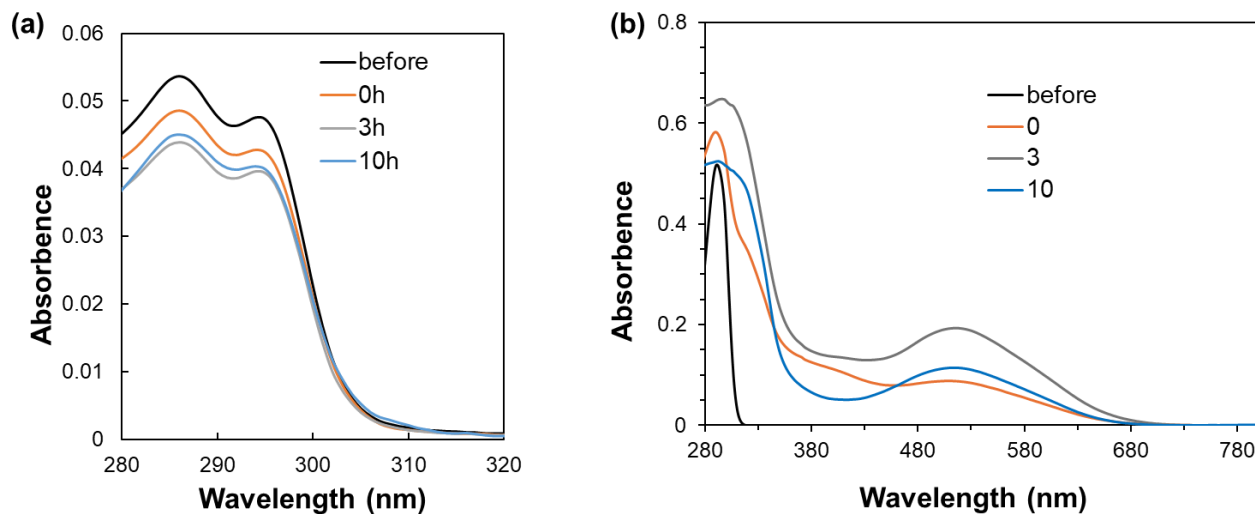


Figure 3.13. UV-Vis spectra (examples of before and after absorption) of (a) SS and (b) TR on N-TiO₂/MWCNT (different annealing time 0–10 h) catalysts. The all data is for Figure 3.7.

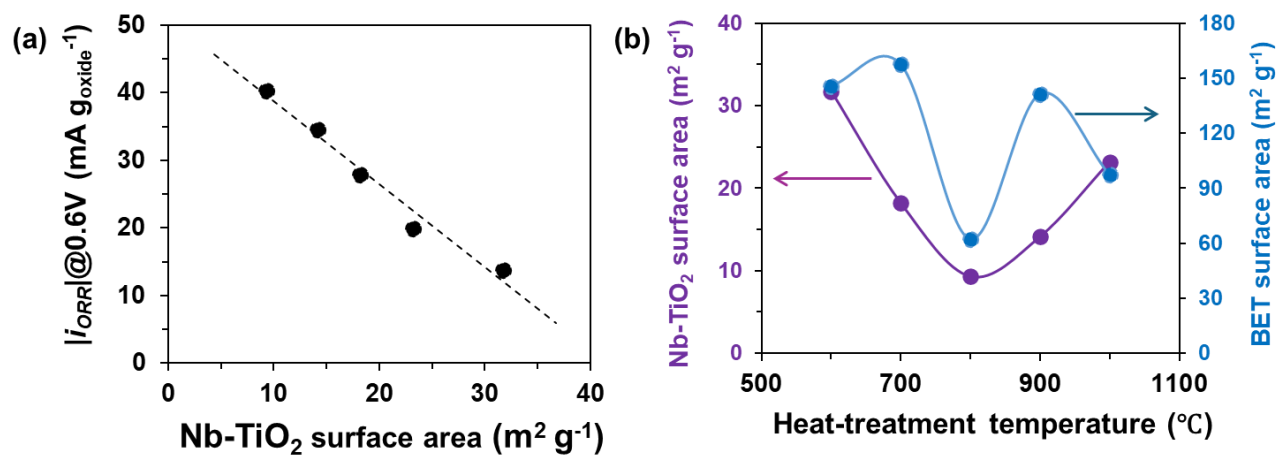


Figure 3.14. (a) Relationship between the Nb-TiO₂ surface area and ORR current [18g]; (b) Nb-TiO₂ surface area and BET surface area of Nb-TiO₂/CSCNT catalysts.

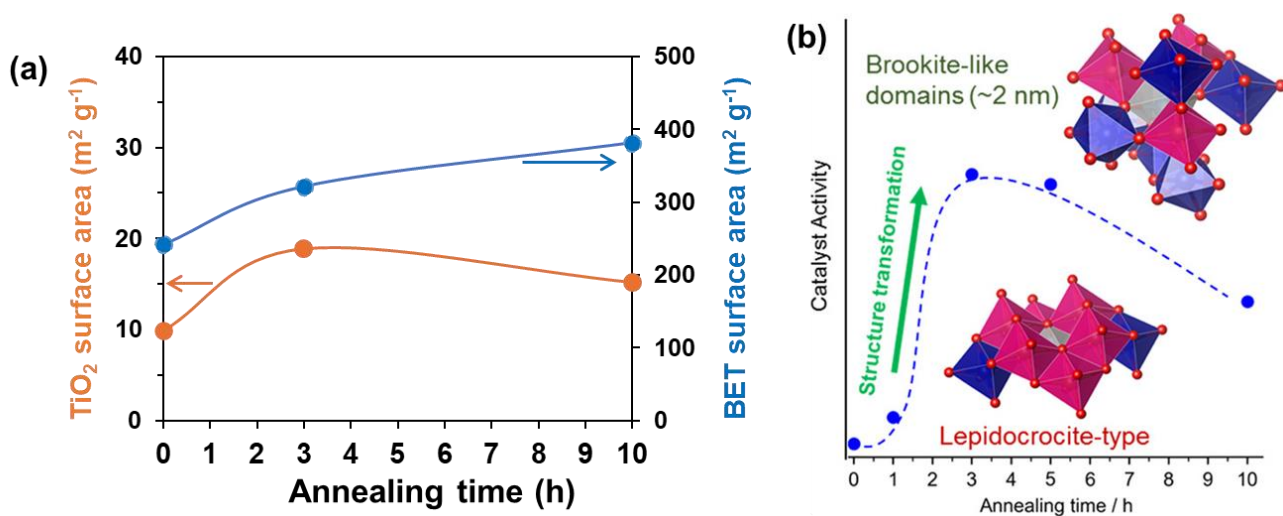


Figure 3.15. Dependence of annealing time on (a) TiO₂ surface area and BET surface area; (b) the catalytic activity of N-TiO₂/MWCNT catalysts [18d].

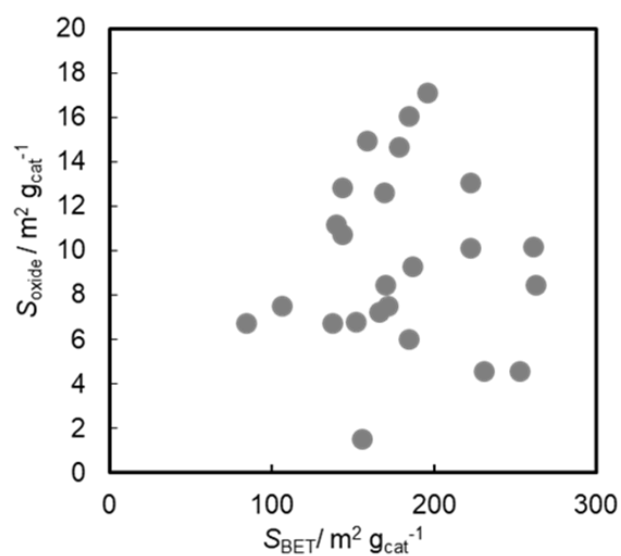


Figure 3.16. Relationship between TiO_2 surface area and BET surface area of N-Fe- TiO_2 /carbon catalysts [18].

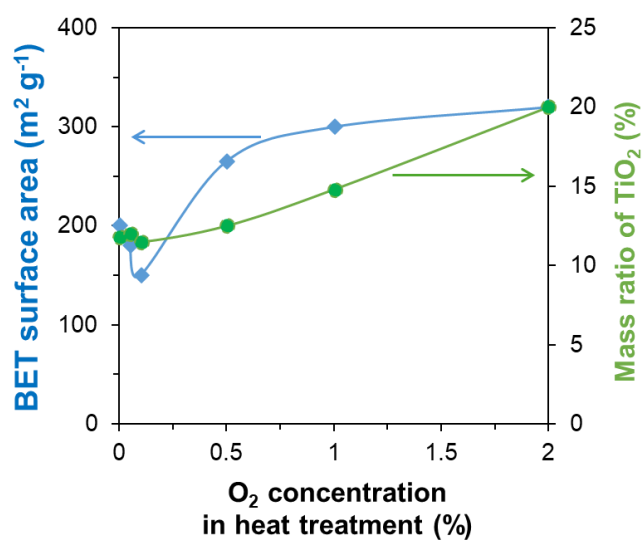
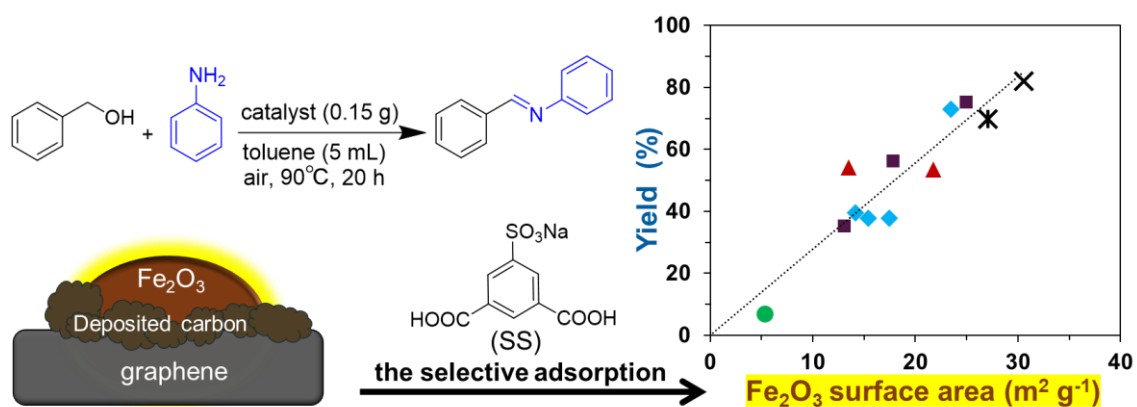


Figure 3.17. Dependence of O_2 concentration on the BET surface area and the TiO_2 loading amount of N- TiO_2 /MWCNT catalysts (data received from Ishihara group).

Chapter 4. Fe_2O_3 /graphene Catalysts for Imine Synthesis



4.1. Introduction: Iron oxide catalysts and imine synthesis

Iron (Fe), the second most abundant metal in the Earth's crust, has played a foundational role in the advancement of human civilization. The emergence of iron-making technologies marked a pivotal historical milestone, with the earliest known iron artifacts traced back to around 3500 BC in Central Asia. Iron's enduring significance spans from its critical roles in construction and machinery to its presence in the composition of rocky planets and human hemoglobin [20a].

In the field of catalysis, iron also occupies a central position. Applications range from traditional iron-based catalysts used in ammonia synthesis via the Haber–Bosch process (as noted in Chapter 1) to modern molecular iron catalysts for C–H bond activation [20b]. This chapter highlights the catalytic properties of iron oxides, which hold promise for a wide range of applications, including photocatalysis [20c], electrocatalytic hydrogen evolution [20d], and organic synthesis [20c].

Iron can exist in various oxidation states, including Fe_2O_3 , Fe_3O_4 , and FeO . Among them, Fe_2O_3 has demonstrated notable catalytic activity in a range of organic transformations, such as the direct borylation of aromatic compounds [20e], the Sonogashira–Hagihara cross-coupling reaction [20f], the Diels–Alder reaction [20f], and imine synthesis [20g]. The synthesis of imine from alcohols and amines is particularly attractive due to its high atom economy, generating only water as a byproduct. This reaction is both cost-effective and environmentally benign, as it employs inexpensive, readily available feedstock and proceeds under mild conditions. Moreover, imines with Schiff base structures, are widely found in biological systems and possess considerable pharmacological relevance due to their bioactivity. Representative examples of biologically active compounds and pharmaceuticals are shown in Figure 4.1 [21a-c]. In addition, imines serve as valuable intermediates in various synthetic pathways [21d, e].

Despite their potential, iron oxides face inherent limitations such as low electrical conductivity and a tendency to agglomerate under reaction conditions, which often leads to grain growth and reduced catalytic efficiency. One promising approach to mitigating these drawbacks is the use of supported iron oxide systems.

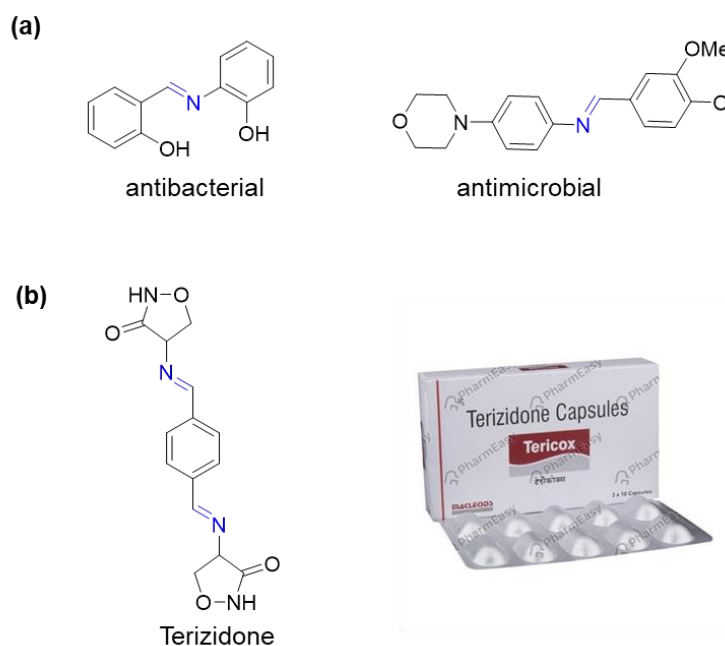


Figure 4.1. (a) Examples of biologically active compounds [21a, b]; (b) Tericox capsules (terizidone as the active ingredient), used for tuberculosis treatment [21c].

Carbon-based supports have been widely employed to enhance catalytic performance by improving the dispersion and conductivity of metal and metal oxide catalysts, as well as by modulating the local reaction environment. This strategy has proven effective in a variety of catalytic applications, including organic synthesis [6c, 22a], the Fischer–Tropsch reaction [6d, 22b, c], photodegradation of organic pollutants [6e], and the water–gas shift reaction [22d]. Among carbon materials, graphene has attracted particular interest due to its high specific surface area, two-dimensional structure, excellent electrical conductivity, and both thermal and chemical stability. These properties make graphene an ideal support for metal or metal oxide catalysts [22e, f]. Accordingly, this chapter explores graphene as a support for iron oxide catalysts.

While Fe_2O_3 catalysts have been studied for imine synthesis [20g], other graphene-based systems such as MnO_2 /graphene oxide [22g] and reduced graphene oxide composites [22h] have also been reported in previous research. In contrast, Fe_2O_3 /graphene catalysts remain relatively underexplored in imine synthesis. Further investigation of this system could help develop high-performance catalysts.

In this chapter, graphene-supported Fe_2O_3 catalysts were prepared using a modified method based on a previously reported protocol [23c] and applied to the synthesis of imines from alcohols and amines (Figure 4.2). The exposed Fe_2O_3 surfaces areas of the prepared catalysts were assessed via the selective adsorption of SS molecules, and the catalysts were characterized by XRD, TEM, and TG-DTA. By examining the relationship between the Fe_2O_3 surface area and catalytic activity in imine formation, this study aims to provide new insights into the rational design and optimization of efficient iron oxide catalysts.

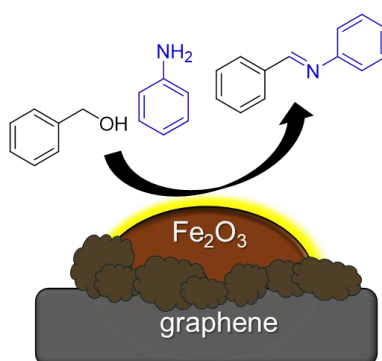


Figure 4.2. Fe_2O_3 /graphene catalysts used for imine synthesis.

4.2. Experimental

4.2.1. Preparation of supported Fe_2O_3 catalysts

Metal–organic gels (MOGs) are emerging as promising materials due to their large specific surface area, high porosity, and unique three-dimensional structures, offering potential applications in gas separation, catalysis, and drug delivery [23a]. Pyrolyzing MOGs to obtain metal oxide/carbon-supported catalysts has recently attracted attention as a versatile strategy for catalyst design and development [23b-d].

The standard synthesis procedure, adapted from a previously reported method [23c], is illustrated in Figure 4.3 and described as follows: Graphene (0.50 g) was first dispersed in a solution of isophthalic acid (0.10 mmol L^{-1} in ethanol) and stirred thoroughly at 70°C . Subsequently, an ethanolic solution of $\text{Fe}(\text{NO}_3)_3$ (0.20 mmol L^{-1}) was slowly added under continuous stirring at 70°C . The mixture became increasingly viscous upon the addition

of $\text{Fe}(\text{NO}_3)_3$, indicating the formation of Fe-based MOGs. After 30 min of stirring, the reaction mixture was cooled to room temperature (approximately 25°C) and further stirred for 12 h. The resulting solid was collected by centrifugation, washed three times with ethanol, and dried under reduced pressure.

For pyrolysis, the dried precursor was finely ground and heated in ambient air at a ramp rate of $10^\circ\text{C min}^{-1}$ to 350°C , then held at this temperature for 1 h. The resulting black magnetic powder was used directly as the catalyst for imine synthesis.

Theoretical Fe_2O_3 loadings, assuming complete conversion of Fe-MOGs to Fe_2O_3 and no loss of graphene and Fe during processing, were 12, 25, 40, and 57 wt%. Actual loading amounts were confirmed via thermogravimetric (TG) analysis. The same preparation method was employed for catalysts using other support materials. The catalyst prepared with a 25 wt% Fe_2O_3 loading on graphene, calcined at 350°C in air, is designated as the standard catalyst throughout this chapter and referred to as “25 wt% $\text{Fe}_2\text{O}_3/\text{graphene}$ (350°C)”. Other $\text{Fe}_2\text{O}_3/\text{graphene}$ catalysts were synthesized under varied conditions, including different MOG ligands (primarily isophthalic acid; trimesic acid for one variant), Fe_2O_3 loadings (12–57 wt%), supports (graphene, activated carbon, spherical silica, and mesoporous silica), calcination temperatures ($300\text{--}400^\circ\text{C}$), and atmospheres (air or N_2).

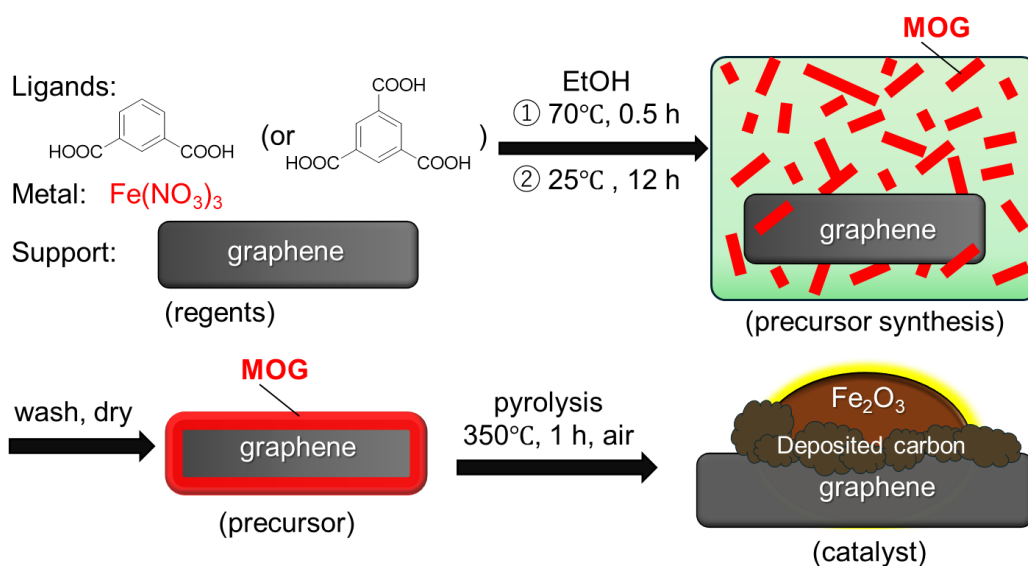


Figure 4.3. Preparation scheme of the $\text{Fe}_2\text{O}_3/\text{graphene}$ catalyst.

4.2.2. Catalyst characterization

The prepared supported Fe₂O₃ catalysts were characterized using various analytical techniques. The nitrogen (N₂) adsorption was employed to determine BET surface area, pore size, and pore volume. Fourier-transform infrared (FT-IR) spectra of the Fe₂O₃/graphene catalysts were recorded using the KBr pellet method. Transmission electron microscopy (TEM) was used to observe the morphology of the Fe₂O₃/graphene catalysts.

Thermogravimetric–differential thermal analysis (TG-DTA) was performed to analyze all supported Fe₂O₃ catalysts under the following conditions: heating from 40 °C at a rate of 10°C min⁻¹ to 800°C with a holding time of 0.5 h in an air atmosphere. TG analysis of the catalysts prepared on silica materials was conducted with the subtraction of the weight of absorbed water.

X-ray diffraction (XRD) analysis was conducted on all supported Fe₂O₃ catalysts using CuK α radiation ($\lambda = 1.5405 \text{ \AA}$) with a scan rate of 2° min⁻¹ and the prefocusing method. The crystallite size of Fe₂O₃ was estimated using the Scherrer equation. The mass ratio of α -Fe₂O₃ to γ -Fe₂O₃ phases was calculated based on XRD peak intensities using the simplified direct derivation method (DDM) (Formula 4.2), as described in literature [23e].

$$w_k = a_k S_k / \sum_{k'=1}^k a_{k'} S_{k'} \dots\dots\dots \textbf{(Formula 4.1)}$$

For Fe₂O₃ with α and γ crystal structures, the composition can be further simplified as follows:

$$w_k = S_k / \sum_{k'=1}^K S_{k'} \dots\dots\dots \textbf{(Formula 4.2)}$$

In these formulas 4.1 and 4.2, w_k is the weight fraction (α or γ -Fe₂O₃), a_k is a parameter determined by the chemical formula, and S_k is the integrated intensity of the peak.

For two phases containing only α - and γ -Fe₂O₃, the respective mass ratios α - and γ can be obtained by Formula 4.3. The weight can be further calculated by the volume and density of the α and γ -Fe₂O₃ spheres, and the number of particles α and γ can be further obtained by considering the loading amount. The total surface area of each α and γ phase can be obtained by the exposed ratio of the particles and the surface area of the sphere.

$$n_k = lw_k / \left[\frac{4}{3} \pi \left(\frac{d_k}{2} \right)^3 \rho_k \right] \dots \dots \dots \text{(Formula 4.3)}$$

$$S_k = f_k n_k \left[4\pi \left(\frac{d_k}{2} \right)^2 \right] \dots \dots \dots \text{(Formula 4.4)}$$

In these formulas 4.3 and 4.4, n_k is the number of particle, l is the loading amount determined by TG analysis, d_k is the particle size determined by XRD analysis (Scherrer Equation), ρ_k is density of α - (5.27 g·cm⁻³) [23f] or γ - (4.90 g·cm⁻³) [23g] phase of Fe₂O₃. S_k is the surface area of each phase (α or γ -Fe₂O₃), and f_k is the exposed ratio.

The surface area of each α and γ -Fe₂O₃ can be obtained from XRD by using Formulas 4.2–4.4.

4.2.3. Catalytic performance for imine synthesis

The standard reaction procedure was conducted as follows: catalyst (0.15 g), benzyl alcohol (0.50 mmol), aniline (1.0 mmol), and toluene (5.0 mL) were added into a 50 mL round-bottom flask. The reaction mixture was stirred magnetically at 90°C for 20 h in air. After completion, the catalyst was removed by centrifugation, followed by filtration, and the solvent (toluene) was evaporated under reduced pressure. The resulting crude product was analyzed either by ¹H NMR (using dimethyl sulfoxide as an internal standard) or by gas chromatography (GC) after adding toluene (5 mL) with naphthalene as an internal standard.

The selectivity (%) was calculated using the following formula:

$$\text{selectivity (\%)} = \frac{\text{yield (\%)} \text{ of imine}}{\text{conversion of alcohol (\%)}} \times 100 \dots \dots \dots \text{(Formula 4.5)}$$

The standard procedure for reuse of the catalyst is as follows: after the reaction, the spent catalyst was collected and washed with toluene 4–5 times. The washed catalyst was dried under reduced pressure, followed by thermal treatment at a heating rate of 10°C min⁻¹ in air, maintaining 315°C for 20 min. This regenerated catalyst was then directly utilized in the subsequent reaction.

4.2.4. Measurement of Fe₂O₃ surface area

In the typical procedure (similar to the method described in Chapter 3), the prepared supported Fe₂O₃ catalyst powder (10 mg) was added to an SS solution (5.0 mL) in DMF in a brown sealed vial. The mixture was shaken at 110°C for 1 h in air.

The adsorption ratios or amounts were calculated by UV-Vis analysis. It was assumed that the adsorption of SS in DMF on graphene, other supports (e.g., activated carbon, SiO₂), and any deposited carbon (formed during catalyst preparation) was negligible.

The Fe₂O₃ surface area was calculated based on the correlation shown in Figure 2.19a by using the formula below:

$$S = \frac{W}{W_s} \dots \dots \dots \text{(Formula 4.6)}$$

In this Formula 4.6, S is the Fe₂O₃ surface area (m² g⁻¹). W is the adsorption amount (mol) of organic compounds. W_s is the adsorption amount per unit surface area (mol m⁻²) in Figure 2.19a.

4.3. Results and discussion

4.3.1. Characterization of supported Fe₂O₃ catalysts

Figure 4.4 presents the XRD patterns of representative catalysts: (a) several typical supported Fe₂O₃ catalysts; (b) two Fe₂O₃/SiO₂ catalysts. The XRD patterns for all samples are provided in Figure 4.14 in Appendix. The standard catalyst exhibits diffraction peaks corresponding to both α and γ phases of Fe₂O₃. All Fe₂O₃/graphene catalysts calcined at 350°C in air showed these phases, regardless of the Fe₂O₃ loading amounts (Figure 4.14a). This observation aligns with a report on unsupported Fe₂O₃, where the coexistence of α and γ phases occurs when Fe(NO₃)₃ is pyrolyzed in air at 220–400°C [24a]. Notably, the variation in Fe₂O₃ loading did not affect the crystal structure observed. When the catalyst was prepared under a nitrogen (N₂) atmosphere, only the γ phase was detected. This may be because N₂ inhibits the transformation of the γ phase into the α phase, which is consistent with previous studies [24b]. Additionally, the Fe₂O₃/graphene catalyst prepared at 300°C showed no discernible Fe₂O₃ diffraction peaks. This absence could be attributed to the formation of ultrafine Fe₂O₃ crystallites or amorphous iron oxide on the graphene surface, which are below the detection limit of XRD. When the support material is

changed from graphene to activated carbon, the XRD pattern of Fe_2O_3 remains almost unchanged (Figure 4.14c in Appendix). On the other hand, for silica-supported catalysts, including spherical silica (SIO-10, particle size: 70–150 μm , pore size: 10 nm) and mesoporous silica (TMPS-2, pore size: 2 nm), only the α phase of Fe_2O_3 was observed. As shown in the magnified portion of Figure 4.4b (and Figure 4.14c in Appendix), the peak of the γ phase is less prominent. By using different precursor compounds (from isophthalic acid to trimesic acid), the corresponding peaks became relatively weak (Appendix Figure 4.14b); this may be due to insufficient pyrolysis of different precursors. The low Fe_2O_3 concentration, combined with the shielding effect of the support material, complicates the detection of small Fe_2O_3 crystallites by XRD, suggesting that further discussion of the XRD results is necessary.

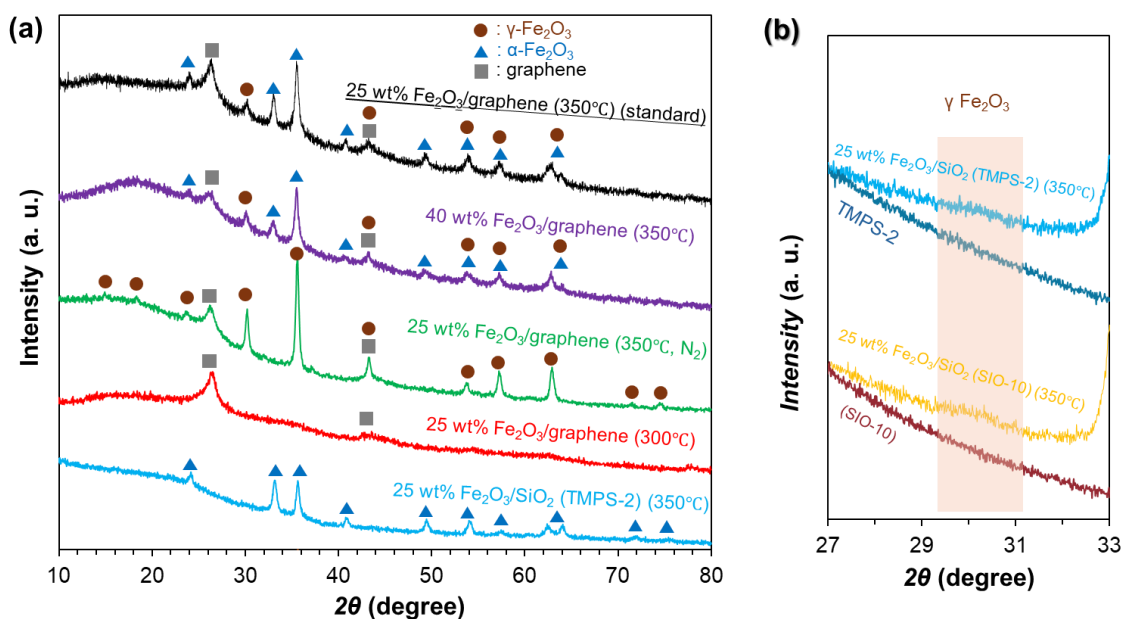


Figure 4.4. XRD patterns of (a) various supported Fe_2O_3 catalysts and (b) a magnified view of $\text{Fe}_2\text{O}_3/\text{SiO}_2$ catalysts.

Figure 4.5 presents the TEM images and particle size distribution of 25 wt% and 40 wt% $\text{Fe}_2\text{O}_3/\text{graphene}$ catalysts calcined at 350°C in air. The observed Fe_2O_3 particles have an average particle size of approximately 19 nm, consistent with the crystallite size of 16–17 nm determined by XRD. However, in certain observation areas, extremely small Fe_2O_3 particles, approximately 3 nm in size, were also identified (Figures 4.5c, d). These

tiny particles are embedded within the graphene layers and appear slightly blurred in the TEM images due to background noise from the graphene support and magnetic interference caused by Fe_2O_3 . Similar TEM observations have been reported for Fe/CNTs [24d] and Fe_2O_3 /graphene systems [24e], further confirming that the faint spots visible in the TEM images correspond to very small Fe_2O_3 particles. This finding supports the earlier assumption that ultra-small Fe_2O_3 particles, undetectable by XRD, are present. Additionally, support materials such as activated carbon and SiO_2 , which have highly porous structures, are also speculated to contain these small Fe_2O_3 particles.

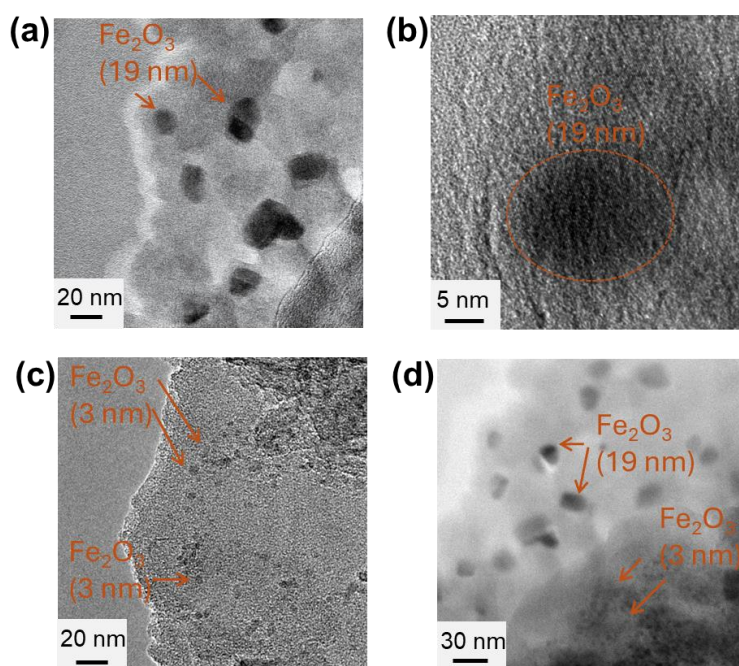


Figure 4.5. TEM images of (a, b, c) 25 wt% Fe_2O_3 /graphene (350°C) and (d) 40 wt% Fe_2O_3 /graphene (350°C) catalysts (original data by co-worker Naomiti Ando).

Due to the limited number of TEM images, a particle size distribution histogram was not generated.

Figure 4.6 shows the spectra of the 25% Fe_2O_3 /graphene (350°C) and 25% Fe_2O_3 / SiO_2 (TMPS-2) (350°C) catalysts. Both catalysts exhibit strong γ - Fe_2O_3 peaks, while α - Fe_2O_3 is less pronounced. Although FT-IR is rarely employed for analyzing the crystal structure of Fe_2O_3 , previous studies [24f, g] have demonstrated its capability to distinguish different crystalline phases effectively. The absorption intensity of the FT-IR peak is often proportional to the concentration. Therefore, regardless of whether the catalyst is

supported on graphene or SiO₂, γ -Fe₂O₃ is expected to be the predominant crystalline phase.

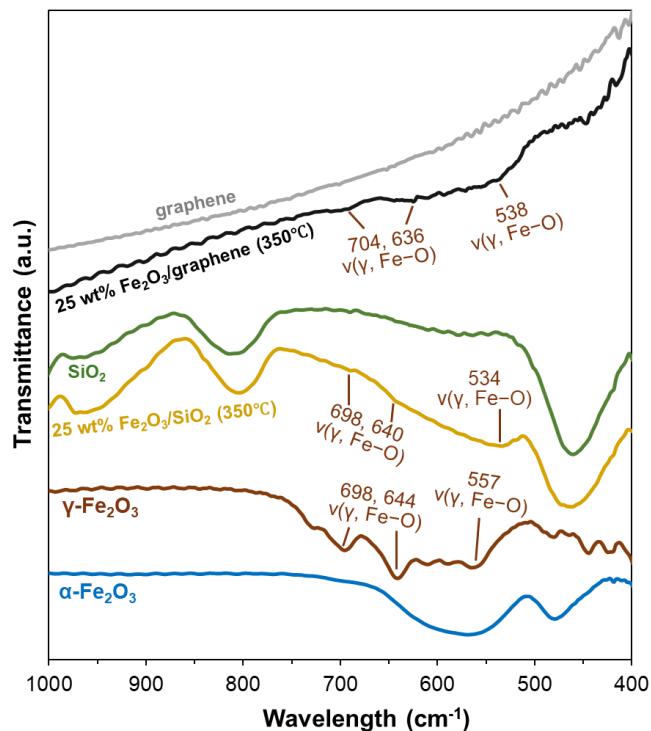


Figure 4.6. FT-IR (KBr) the 25% Fe₂O₃/graphene (350°C) and 25% Fe₂O₃/SiO₂ (TMPS-2) (350°C) catalysts.

Figure 4.7 presents the TG-DTA profiles of the 25 wt% and 40 wt% Fe₂O₃/graphene catalysts calcined at 350°C. A sharp peak was observed in the DTA spectrum at approximately 400°C, occurring significantly before the decomposition peak of the graphene support. This peak is likely attributed to the presence of deposited carbon [18a], which is derived from the pyrolysis of the Fe-MOG precursor during calcination. Consequently, the catalyst is inferred to contain two types of carbon: the supported graphene and deposited carbon formed from the thermal decomposition of the precursor. In addition, based on the TG analysis described above, the actual loading of Fe₂O₃ in the carbon-supported catalyst was determined (Table 4.3b in Appendix)

The BET surface area, average pore size, pore volume, α - and γ -Fe₂O₃ crystallite size, and iron oxide loading of the supported Fe₂O₃ catalyst samples were summarized in Table

4.3 in Appendix. Catalysts using graphene as a support ($S = 750 \text{ m}^2 \text{ g}^{-1}$) exhibited surface areas in the range of approximately $100\text{--}350 \text{ m}^2 \text{ g}^{-1}$, whereas those supported on activated carbons ($S = 975$ (RB3), 886 (1240W) $\text{m}^2 \text{ g}^{-1}$) or mesoporous silica (TMPS) ($S = 845 \text{ m}^2 \text{ g}^{-1}$) showed significantly higher specific surface areas exceeding $700 \text{ m}^2 \text{ g}^{-1}$. This observation suggests that the 2D planar structure of the graphene support may undergo partial stacking, leading to a substantial reduction in its accessible surface area, which is consistent with the TEM observation.

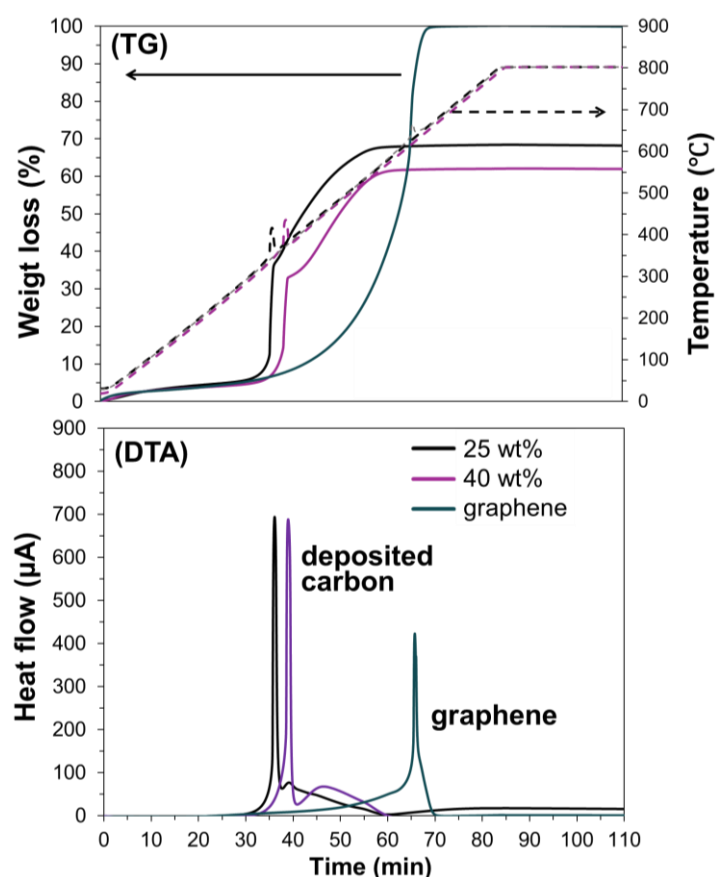


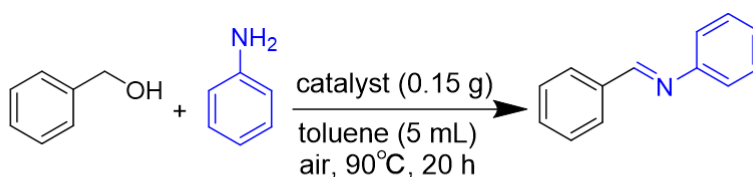
Figure 4.7. TG-DTA profiles (under air) of the 25 and 40 wt% $\text{Fe}_2\text{O}_3/\text{graphene}$ (350°C) catalysts (dotted lines are temperature).

Catalytic performance for imine synthesis

Catalytic performance of the various materials including the prepared supported Fe_2O_3 catalysts were preliminarily tested in the imine synthesis reaction (Table 4.1). Standard catalyst 25 wt% $\text{Fe}_2\text{O}_3/\text{graphene}$ (350°C) demonstrated over 80% yield, while the real loading amount was only 32% by TG analysis (Table 4.3b in Appendix). The $\gamma\text{-Fe}_2\text{O}_3$

exhibited the catalytic activities (entries 3 and 4), which are consistent with the previous reports [20g]. γ -Fe₂O₃ with higher surface areas led to high catalytic activities (entries 3 and 4). In addition, α -Fe₂O₃ and Fe₃O₄ with low surface area showed no or low activity (entries 5-9), which is also consistent with a report [20g]. Notably, Fe₂O₃ partially with γ phase exhibited apparently higher catalytic activity by comparison of entries 6 with 7. Fe powder, carbon and SiO₂ support (used in catalyst preparation) showed no catalytic activity (entries 10 and 11).

Table 4.1. Imine synthesis reactions catalyzed by various materials.



Entry	Catalyst (crystal structure, particle size)	BET S (m ² g ⁻¹)	Yield (%)	Selectivity (%)
1	25 wt% Fe ₂ O ₃ /graphene (350°C) (α and γ , 19 nm)	317	82	91
2	none	—	0	—
3	Fe ₂ O ₃ (γ , < 50 nm)	59	94	94
4	Fe ₂ O ₃ (γ , 20~40 nm)	41	38	75
5	Fe ₂ O ₃ (α , 0.3 μ m)	17	9	31
6	Fe ₂ O ₃ (α , < 5 μ m)	10	0	—
7	Fe ₂ O ₃ (α and γ)	10	4	13
8	Fe ₃ O ₄ (50~100 nm)	13	7	21
9	Fe ₃ O ₄ (1 μ m)	8	0	—
10	Fe (1 μ m)	5	0	—
11	support (5 carbon and SiO ₂)	300~900	< 0.1	—

Reaction conditions: benzyl alcohol (0.50 mmol) and aniline (1.0 mmol), catalyst (0.15 g), 5.0 mL toluene, air, 90°C, 20 h. Imine yield and selectivity were determined by GC analysis of crude product (naphthalene as an internal standard).

Table 4.2 summarizes the catalytic activities of all supported Fe₂O₃ catalysts for imine synthesis. Under standard preparation conditions, the iron oxide catalyst supported on graphene exhibited the highest catalytic activity, achieving a yield of approximately 80% (entry 2). Most catalysts demonstrated selectivity in the range of 60–85% for imine synthesis. In contrast, the yield of the 25 wt% Fe₂O₃/graphene (350°C, N₂) catalyst was

merely 7% (entry 7). Additionally, despite the high BET surface area of the Fe₂O₃, the catalytic activities of the catalysts supported on activated carbon were significantly low, with a yield of only about 40% (entries 9 and 10).

Table 4.2. Imine synthesis reaction catalyzed by supported Fe₂O₃ catalysts.

Entry	Catalyst	Yield (%)	Selectivity (%)
1	12 wt% Fe ₂ O ₃ /graphene (350°C)	75	85
2	25 wt% Fe ₂ O ₃ /graphene (350°C)	82	91
3	40 wt% Fe ₂ O ₃ /graphene (350°C)	56	91
4	57 wt% Fe ₂ O ₃ /graphene (350°C)	35	80
5	25 wt% Fe ₂ O ₃ /graphene (300°C)	53	78
6	25 wt% Fe ₂ O ₃ /graphene (400°C)	54	72
7	25 wt% Fe ₂ O ₃ /graphene (350°C, N ₂)	7	24
8	25 wt% Fe ₂ O ₃ /graphene (350°C, trimesic acid)	70	82
9	25 wt% Fe ₂ O ₃ /1240W (350°C)	38	70
10	25 wt% Fe ₂ O ₃ /RB3 (350°C)	40	75
11	25 wt% Fe ₂ O ₃ /SIO-10 (350°C)	38	62
12	25 wt% Fe ₂ O ₃ /TMPS-2 (350°C)	73	84
13*	12 wt% Fe ₂ O ₃ /graphene (350°C)	70	80
14*	25 wt% Fe ₂ O ₃ /graphene (350°C)	75	93

Reaction conditions: benzyl alcohol (0.50 mmol), aniline (1.0 mmol), catalyst (0.15 g), and toluene (5.0 mL), open to air, 90°C, 20 h. Selectivity and yield of imine were determined by GC analysis (naphthalene as an internal standard).

*Reaction for 16 h.

4.3.3. Fe₂O₃ surface area and catalytic activity

The surface area of the catalytically active γ -Fe₂O₃ phase is likely a key determinant of catalytic performance. This section describes the investigation of Fe₂O₃ surface area by using the previously established selective adsorption method in conjunction with XRD analysis.

To determine the surface area of Fe₂O₃, the author used the selective adsorption of SS,

as using TR for the other iron oxides/activated carbon (in other experiments not included in this thesis) resulted in additional peaks that interfered with the determination. Figure 4.8 illustrates the relationship between the Fe_2O_3 surface area and imine yield.

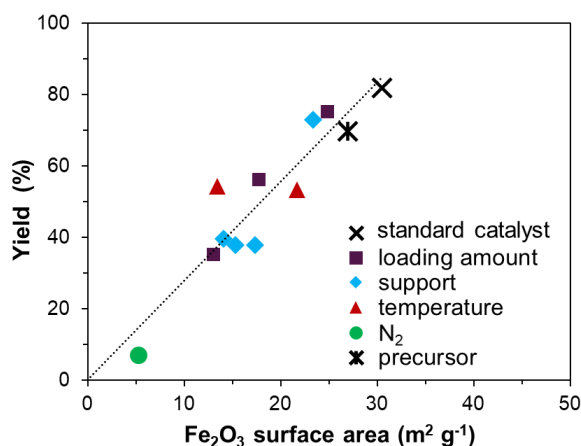


Figure 4.8 Relationship between the Fe_2O_3 surface area and yield in imine synthesis.

Adsorption condition of SS on the supported Fe_2O_3 catalysts for measuring Fe_2O_3 surface area: catalysts (10 mg) in DMF solution (5.0 mL) of organic molecule (0.20 mM), shaking, 110°C , 1 h. The adsorption amounts were determined by UV-Vis analysis. Reaction condition: benzyl alcohol (0.50 mmol), aniline (1.0 mmol), catalyst (0.15 g), and toluene (5.0 mL), in air, stirring, 90°C , 20 h. GC analysis (naphthalene as an internal standard). The standard catalyst: 25 wt% Fe_2O_3 /graphene (350°C , air). The other catalysts were prepared by changing the conditions of loading amount, support, pyrolysis temperature, atmosphere (N_2), or precursor.

Regardless of variations in preparation conditions, such as loading, support, calcination temperature, and atmosphere, the catalytic activity shows a positive correlation with the Fe_2O_3 surface area. Previous studies [20g], as well as the results of this work, indicate that only the $\gamma\text{-Fe}_2\text{O}_3$ phase is catalytically active, while the commonly observed $\alpha\text{-Fe}_2\text{O}_3$ and Fe_3O_4 phases exhibit lower catalytic activity. Additionally, it is reported that even amorphous Fe_2O_3 with a surface area larger than $200 \text{ m}^2 \text{g}^{-1}$ is almost inactive under conditions of 60°C , 3 h, and atmospheric pressure [25a, b]. Apparently, under the extended reaction time and elevated temperatures in this study, it is reasonable to conclude that the amorphous Fe_2O_3 would also have low catalytic activity.

However, XRD analysis revealed the prepared catalysts with mixed phases, including α and $\gamma\text{-Fe}_2\text{O}_3$, or the absence of clear Fe_2O_3 peaks, depending on the preparation conditions. This observation contradicts the positive correlation between Fe_2O_3 surface

area and imine yield, requiring further discussion.

Amorphous Fe_2O_3 generally crystallizes upon heating [25c-e], typically around at 300°C in both air and nitrogen atmospheres [25c, d]. Thus, it can be inferred that the catalysts prepared by thermal decomposition at 350°C contain negligible amorphous Fe_2O_3 , while those prepared at 300°C may retain small amounts.

α and $\gamma\text{-Fe}_2\text{O}_3$ phases are predominantly reported and studied [25f-h]. In contrast, other phases such as ε and β are typically formed only under specific conditions including high-energy deposition, sol-gel methods, or heating $\gamma\text{-Fe}_2\text{O}_3$ above 800°C [25g, h], which should not be the case in this study. The transition from γ - to $\alpha\text{-Fe}_2\text{O}_3$ is influenced by particle size, with a critical range of approximately 10–25 nm. Below this range, $\gamma\text{-Fe}_2\text{O}_3$ is more stable, while larger particles tend to adopt α phase more preferentially [25g]. The particle sizes of most Fe_2O_3 samples prepared in this study are around 18 nm, which would likely contain both α and γ phases during the phase transition. The extremely small Fe_2O_3 particles seen in TEM, but not detected by XRD, are more likely the catalytically active γ phase without amorphous or $\alpha\text{-Fe}_2\text{O}_3$.

On the other hand, analyzing each surface area of α - and $\gamma\text{-Fe}_2\text{O}_3$ phase in mixed-phase samples only by using the adsorption of SS is not feasible. Therefore, another method for estimating the surface area of each phase is also employed here. First, the ratio of α - and γ phases can be calculated by the direct derivation method (DDM) through the integrated peak area of XRD using Formulas 4.2 [23e] on the assumption that the crystallite size from XRD corresponds to the particle diameter (as supported by the previous TEM observations), and that the shape of the particles is an ideal, non-interacting and contacting sphere. If it is further assumed that the XRD peaks observed by XRD correspond to all α - and $\gamma\text{-Fe}_2\text{O}_3$ in a sample, considering that the presence of extremely small $\gamma\text{-Fe}_2\text{O}_3$ nanoparticles is ignored, an estimated portion of the γ -phase becomes a minimum. On the contrary, if it is assumed that the presence of extremely small $\alpha\text{-Fe}_2\text{O}_3$ nanoparticles is neglected, an estimated portion of the γ -phase becomes a maximum. Next, each surface area of α - and γ - phases can be estimated using Formulas 4.3-4 and Fe_2O_3 loading obtained by TG on the assumption that half of a Fe_2O_3 particle on the catalyst surface is exposed due to half coverage by deposited carbon.

The correlation between the calculated surface areas of $\gamma\text{-Fe}_2\text{O}_3$ (maximum, average and minimum values) and the yield is shown in Figure 4.9. The surface area of $\gamma\text{-Fe}_2\text{O}_3$ shows a strong positive correlation with catalytic activity. This relationship indicates that the γ phase dominates in the graphene-supported Fe_2O_3 catalyst.

The XRD patterns in Figures 4.4 and 4.14 indicate that α phase is more dominant in the catalysts supported on activated carbon or SiO_2 , probably because the particles on these support surfaces tend to aggregate into $\alpha\text{-Fe}_2\text{O}_3$ [25l]. At a lower calcination temperature of 300°C , no peaks were observed, likely because $\gamma\text{-Fe}_2\text{O}_3$ had not yet reached the temperature threshold for phase transition, and remained as smaller particles of $\gamma\text{-Fe}_2\text{O}_3$ [25f]. The presence of a small amount of inactive amorphous Fe_2O_3 , inferred by comparing the lower amount of $\alpha\text{-Fe}_2\text{O}_3$ in other catalysts, contributes to the overall positive correlation between the Fe_2O_3 surface area and catalytic activity (Figure 4.9).

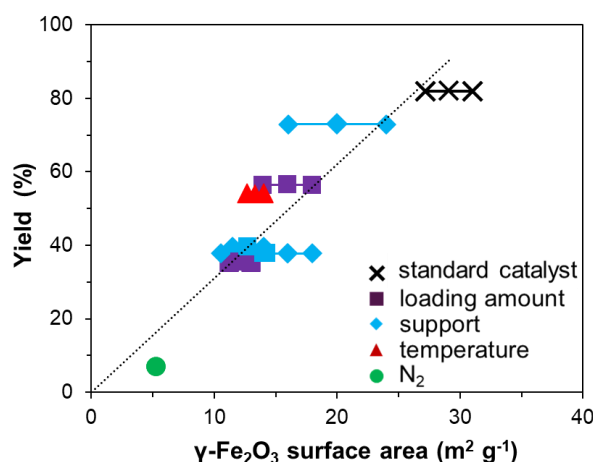


Figure 4.9. Relationship between $\gamma\text{-Fe}_2\text{O}_3$ surface area (maximum, average and minimum values from left to right) and yield in imine synthesis.

Due to the small XRD peaks, the $\gamma\text{-Fe}_2\text{O}_3$ surface areas of several supported Fe_2O_3 catalysts were not calculated.

For catalysts prepared at 400°C , the graphene support can help limit particle size growth due to agglomeration (graphene stacking), which prevents further formation of $\alpha\text{-Fe}_2\text{O}_3$. Although catalysts synthesized in an N_2 atmosphere consist solely of $\gamma\text{-Fe}_2\text{O}_3$, the carbon derived from Fe-MOG precursors under nitrogen can coat much of the $\gamma\text{-Fe}_2\text{O}_3$, reducing its surface area. Although the $\gamma\text{-Fe}_2\text{O}_3$ surface area of a catalyst from a different

precursor wasn't calculated due to weak XRD peaks, their γ -Fe₂O₃ surface areas are likely similar to that of the standard catalyst, considering the similar thermal decomposition conditions and catalytic activities.

On the other hand, the relationships between the catalytic activity and both the γ -Fe₂O₃ crystallite size (determined by XRD) and BET surface area were examined (Figure 4.10). No direct correlation between the catalytic activity and the γ -Fe₂O₃ crystallite size determined by XRD, probably because very small γ -phase particles could not be detected by XRD (Figure 4.10a). The correlation between catalytic activity and BET surface area appears weak (Figure 4.10b).

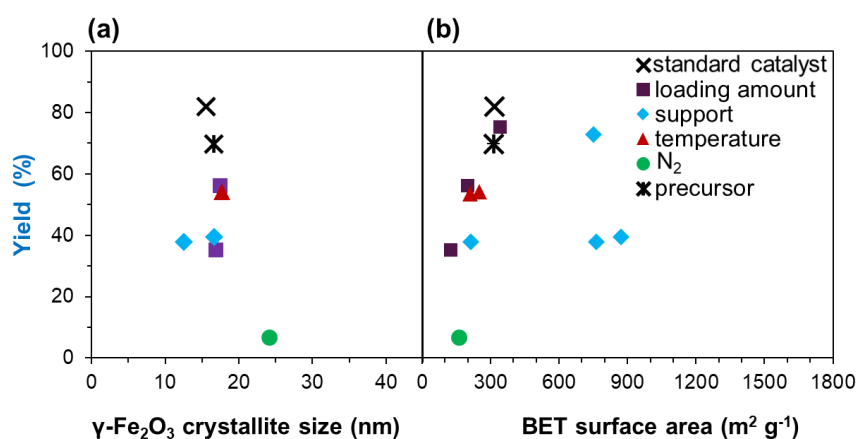


Figure 4.10. Relationships between (a) γ -Fe₂O₃ crystallite size and yield, (a) BET surface area and yield in imine synthesis for the prepared supported Fe₂O₃ catalysts (experimental condition was the same as that in Figure 4.9).

4.3.4. Substrate scope and reusability of Fe₂O₃/graphene catalyst

To confirm the versatility of the prepared supported Fe₂O₃ catalyst, synthesis of various imine derivatives by the standard catalyst, 25 wt% Fe₂O₃/graphene (350°C, air), was conducted (Figure 4.11). A variety of aromatic imines with different substituted groups including halogen (**3ab**, **3ac** and **3ba**), methyl (**3ad** and **3ca**), and carbomethoxy (**3ae** and **3da**) were obtained in high yields. However, the reactions with an amine having two carbomethoxy groups and alkyl amine resulted in low yields (**3af** and **3ah**).

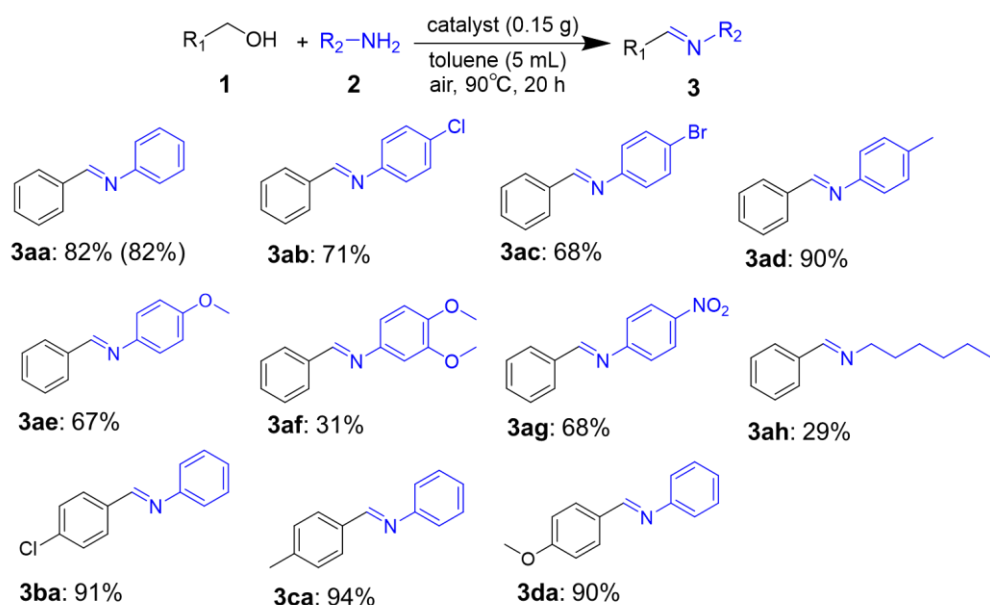


Figure 4.11. Imine synthesis catalyzed by the Fe₂O₃/graphene catalyst.

Reaction condition: alcohol (0.50 mmol), amine (1.0 mmol), catalyst: 25 wt% Fe₂O₃/graphene (350°C, air) (0.15 g), and toluene (5.0 mL), open to air, stirring, 90°C, 20 h. Yield was determined by ¹H NMR (Dimethyl sulfoxide as an internal standard) or (GC analysis (naphthalene as an internal standard).

In the ¹H NMR spectra, a peak corresponding to benzaldehyde (at 10.0 ppm) was identified (Figure 4.12). Benzyl alcohol adsorbs onto the γ-Fe₂O₃ surface of the catalyst [20g], where it undergoes dehydrogenation and oxidation to produce benzaldehyde. The resulting benzaldehyde then reacts with amines, forming imines through a subsequent dehydration process.

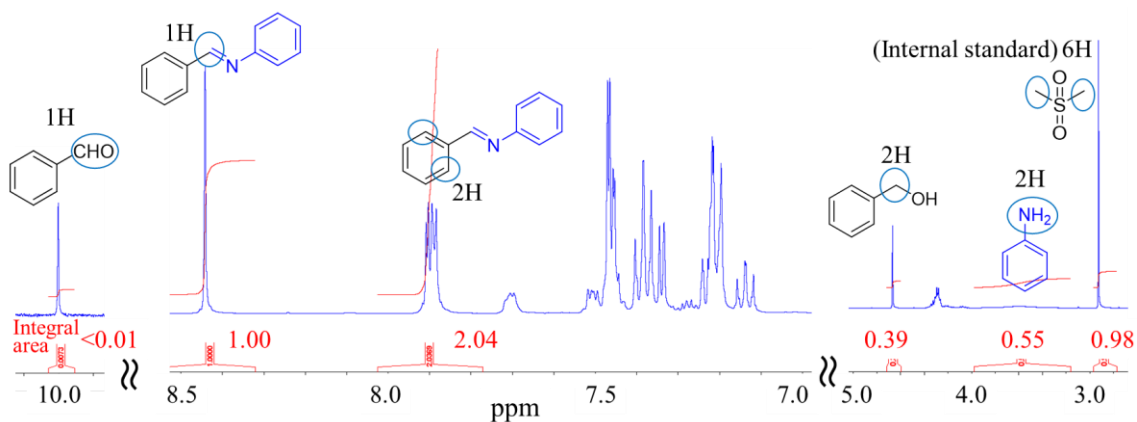


Figure 4.12. ¹H NMR spectra of crude imine product (**3aa** in Figure 4.11).

Since the reusability of heterogeneous catalysts is crucial, recycle experiments of the standard catalyst, 25 wt% Fe₂O₃/graphene (350°C, air), were conducted by 6 different procedures (Figure 4.13). In the first procedure, the catalyst was washed with toluene and dried under reduced pressure after use, demonstrating a gradual decline in catalytic activity (Figure 4.13a). A study in literature has also reported the similar activity losses [26b]. The FT-IR and XRD analyses of the spent catalyst were performed after 6 cycles of washing with toluene and reuse (Figures 4.15a, b in Appendix). The FT-IR spectrum shows a decrease in the absorption band attributed to the hydroxyl groups on the Fe₂O₃ surface, while the XRD peak intensity also diminished accordingly. These results suggest that the substrates adsorbed on the Fe₂O₃ surface cover the catalytic sites.

In the second procedure, the recovered catalyst was treated with extra heating at 315°C for 20 min in air, which afforded high recyclability (Figure 4.15b). Treating the catalyst at high temperatures in air can remove adsorbed substrates and regenerate the exposed Fe₂O₃ surface, which was confirmed by the FT-IR measurement showing an increase in peak intensity for surface hydroxyl groups (Figure 4.15a). XRD measurement showed that the crystallite size of Fe₂O₃ on the catalyst increased slightly from 16 nm of the fresh catalyst to 18 nm of the spent catalyst (Figure 4.15b). The exposed Fe₂O₃ surface area on the spent catalyst after its 6th use was determined by selective adsorption of SS to be approximately 27 m² g⁻¹, while the fresh catalyst has 31 m² g⁻¹. In addition, the weights of the catalyst over the recycling processes were measured as shown in Figure 4.15c. It was found that the weight of the catalyst gradually decreased.

In the third reuse method, compared to the second method, the heating temperature was changed to 215°C, resulting in almost complete loss of catalytic activity, probably due to surface coverage with the substrates and/or materials from their decomposition (Figure 4.13c).

Although a previous study has suggested that aqueous K₂CO₃ solution can effectively clean adsorbed substrates and enhance reusability [26b], no noticeable improvement in catalytic activities was obtained by washing with aqueous K₂CO₃ solution, and also with MeCN and MeOH (Figures 4.13d-f). This may be due to strong chemical adsorption of the substrate on the catalyst surface.

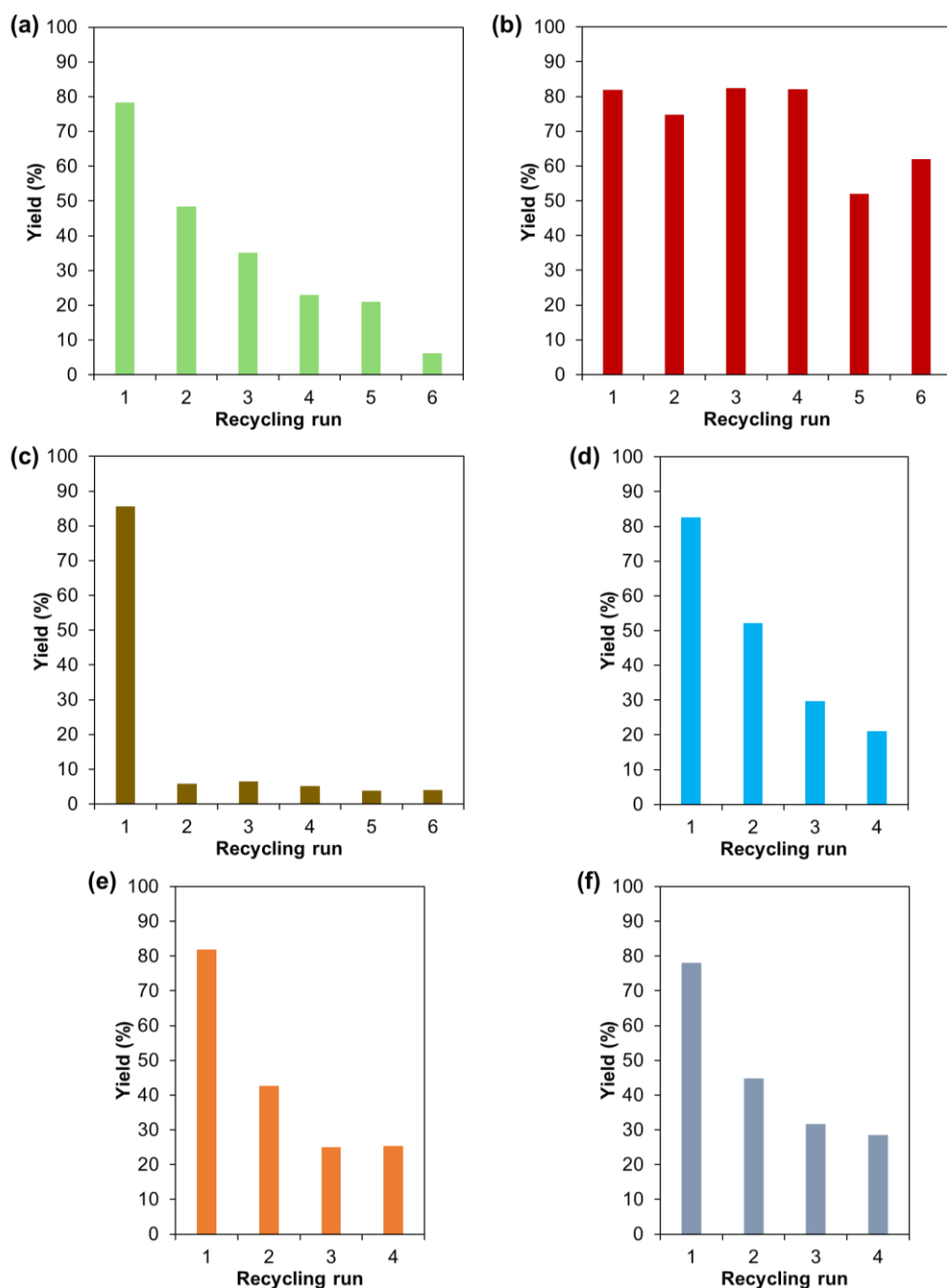


Figure 4.13. Reusability of Fe₂O₃/graphene for imine synthesis.

Reaction conditions: benzyl alcohol (0.50 mmol), aniline (1.0 mmol), catalyst: 25 wt% Fe₂O₃/graphene (350°C, air) (0.15 g), and toluene (5.0 mL), in air, stirring, 90°C, 20 h. Yield was determined by GC analysis (naphthalene as an internal standard). Catalyst reuse conditions: after use, the catalyst was washed with toluene and dried under reduced pressure; (a) no additional treatment; further heating at (b) 315°C or (c) 215°C for 20 min in air; further washing with (d) aqueous K₂CO₃ solution, (e) MeCN, or (f) MeOH, followed by drying.

4.4. Conclusions

A series of supported Fe₂O₃ catalysts was prepared by pyrolyzing mixtures of iron-based metal-organic gels (Fe-MOGs) with graphene, activated carbon, or SiO₂ under various conditions. These catalysts were subsequently applied to the synthesis of imines from alcohols and amines. The Fe₂O₃/graphene catalyst prepared under the standard conditions (pyrolysis at 350°C under ambient pressure for 1 h) exhibited both α - and γ -Fe₂O₃ crystalline phases and achieved an imine yield exceeding 80%. TEM analysis revealed the presence of both small γ -Fe₂O₃ particles and larger Fe₂O₃ particles. The Fe₂O₃ surface area was estimated using the selective adsorption of SS molecule, and the exposed surface area of γ -Fe₂O₃ was subsequently estimated based on XRD analysis and TG analysis. The results suggests that the exposed Fe₂O₃ surface predominantly consists of the catalytically active γ -Fe₂O₃ phase, which was also confirmed by FT-IR analysis. A positive correlation was observed between the surface area of the γ -Fe₂O₃ phase and the catalytic activity for imine synthesis.

The standard Fe₂O₃/graphene catalyst also demonstrated a wide range of substrate scope in the imine synthesis reactions. In addition, heating the spent catalyst to 315°C in air effectively restored its catalytic performance.

The successful application of the selective adsorption of SS molecule to estimate the Fe₂O₃ surface area further validated its utility and provided valuable guidance for catalyst design. The findings of this chapter are expected to promote the development of supported catalysts, advance the organic synthesis of pharmaceutical imines, and contribute to the improvement of characterization methods for solid composite materials.

4.5. Reference

[20] (a) Sheftel, A. D.; Mason, A. B.; Ponka, P. The long history of iron in the Universe and in health and disease. *Biochim Biophys Acta* **2012**, 1820 (3), 161-187. DOI: 10.1016/j.bbagen.2011.08.002. (b) Shang, R.; Ilies, L.; Nakamura, E. Iron-Catalyzed C–H Bond Activation. *Chem. Rev.* **2017**, 117 (13), 9086-9139. DOI: 10.1021/acs.chemrev.6b00772. (c) Chaudhari, D. S.; Upadhyay, R. P.; Shinde, G. Y.; Gawande, M. B.; Filip, J.; Varma, R. S.; Zboril,

R. A review on sustainable iron oxide nanoparticles: synthesis and application in organic catalysis and environmental remediation. *Green Chem.* **2024**. DOI: 10.1039/d4gc01870b. (d) Wang, H.; Su, R.; Liu, Y.; Kong, Y.; Ren, Z.; Jiang, B. Iron-group Metal Compound Electrocatalysts for Efficient Hydrogen Production: Recent Advances and Future Prospects. *ChemCatChem* **2024**, *16* (8), e202301241. DOI: 10.1002/cctc.202301241. (e) Yan, G.; Jiang, Y.; Kuang, C.; Wang, S.; Liu, H.; Zhang, Y.; Wang, J. Nano-Fe₂O₃-catalyzed direct borylation of arenes. *Chem. Commun.* **2010**, *46*, 3170–3172. DOI: 10.1039/B926945B. (f) Kataria, M.; Pramanik, S.; Kaur, N.; Kumar, M.; Bhalla, V. Ferromagnetic α -Fe₂O₃ NPs: a potential catalyst in Sonogashira–Hagihara cross coupling and hetero-Diels–Alder reactions. *Green Chem.* **2016**, *18*, 1495–1505. DOI: 10.1039/C5GC02337H. (g) Geng, L.; Jian, W.; Jing, P.; Zhang, W.; Yan, W.; Bai, F.-Q.; Liu, G. Crystal phase effect of iron oxides on the aerobic oxidative coupling of alcohols and amines under mild conditions: A combined experimental and theoretical study. *J. Catal.* **2019**, *377*, 145–152. DOI: 10.1016/j.jcat.2019.06.018.

[21] (a) Hodnett, E. M.; Mooney, P. D. Antitumor activities of some Schiff bases. *J. Med. Chem.* **1970**, *13* (4), 786–786. DOI: 10.1021/jm00298a065. (b) da Silva, C. M.; da Silva, D. L.; Modolo, L. V.; Alves, R. B.; de Resende, M. A.; Martins, C. V. B.; de Fátima, Â. Schiff bases: A short review of their antimicrobial activities. *J. Adv. Res.* **2011**, *2* (1), 1–8. DOI: 10.1016/j.jare.2010.05.004. (c) *Pharmeasy Home Page*. <https://pharmeasy.in/> (accessed 2024-10-10). (d) Gawronski, J.; Wascinska, N.; Gajewy, J. Recent Progress in Lewis Base Activation and Control of Stereoselectivity in the Additions of Trimethylsilyl Nucleophiles. *Chem. Rev.* **2008**, *108* (12), 5227–5252. DOI: 10.1021/cr800421c. (e) Adrio, J.; Carretero, J. C. Novel dipolarophiles and dipoles in the metal-catalyzed enantioselective 1,3-dipolar cycloaddition of azomethine ylides. *Chem. Commun.* **2011**, *47* (24), 6784–6794. DOI: 10.1039/C1CC10779H.

[22] (a) Wang, F.; Zhu, F.; Ren, E.; Zhu, G.; Lu, G.-P.; Lin, Y. Recent Advances in Carbon-Based Iron Catalysts for Organic Synthesis. *Nanomaterials* **2022**, *12* (19), 3462. DOI: 10.3390/nano12193462. (b) Cheng, Y.; Lin, J.; Xu, K.; Wang, H.; Yao, X.; Pei, Y.; Yan, S.; Qiao, M.; Zong, B. Fischer–Tropsch Synthesis to Lower Olefins over Potassium-Promoted Reduced Graphene Oxide Supported Iron Catalysts. *ACS Catal.* **2016**, *6* (1), 389–399. DOI: 10.1021/acscatal.5b02024. (c) Wei, Y.; Yan, L.; Ma, C.; Zhang, C.; Sun, S.; Wen, X.; Yang, Y.; Li, Y. Mesoporous Iron Oxide Nanoparticle-Decorated Graphene Oxide Catalysts for Fischer–Tropsch Synthesis. *ACS Appl. Nano Mater.* **2020**, *3* (7), 7182–7191. DOI: 10.1021/acsanm.0c01522. (d) Bychko, I. B.; Kosmambetova, G. R.; Kalishyn, Y. Y.; Khavrus, V. O.; Gritsenko, V. I.; Strizhak, P. E. Iron oxide nanoparticles supported on carbon nanotubes: an efficient catalyst for water–gas shift reaction. *React. Chem. Eng.* **2023**, *8* (11), 2841–2848,

10.1039/D3RE00301A. DOI: 10.1039/D3RE00301A. (e) Cheng, Y.; Fan, Y.; Pei, Y.; Qiao, M. Graphene-supported metal/metal oxide nanohybrids: synthesis and applications in heterogeneous catalysis. *Catal. Sci. Technol.* **2015**, *5* (8), 3903-3916. DOI: 10.1039/C5CY00630A. (f) Burkholder, M. B.; Rahman, F. B. A.; Chandler, E. H.; Regalbuto, J. R.; Gupton, B. F.; Tengco, J. M. Metal supported graphene catalysis: A review on the benefits of nanoparticulate supported specialty sp² carbon catalysts on enhancing the activities of multiple chemical transformations. *Carbon Trends* **2022**, *9*, 100196. DOI: 10.1016/j.cartre.2022.100196. (g) Cheng, S.; Ma, X.; Hu, Y.; Li, B. MnO₂/graphene oxide: A highly efficient catalyst for imine synthesis from alcohols and amines. *Appl. Organometal. Chem.* **2017**, *31* (8), e3659. DOI: 10.1002/aoc.3659. (h) He, H.; Li, Z.; Li, K.; Lei, G.; Guan, X.; Zhang, G.; Zhang, F.; Fan, X.; Peng, W.; Li, Y. Bifunctional Graphene-Based Metal-Free Catalysts for Oxidative Coupling of Amines. *ACS Appl. Mater. Interfaces* **2019**, *11* (35), 31844-31850. DOI: 10.1021/acsami.9b08741.

[23] (a) Liu, G.; Li, S.; Shi, C.; Huo, M.; Lin, Y. Progress in Research and Application of Metal–Organic Gels: A Review. *Nanomaterials* **2023**, *13* (7), 1178. DOI: 10.3390/nano13071178. (b) Ma, S.; Xu, J.; Sohrabi, S.; Zhang, J. Metal–organic gels and their derived materials for electrochemical applications. *J. Mater. Chem. A* **2023**, *11* (22), 11572-11606, DOI: 10.1039/D3TA01221B. (c) Tian, M.; Cui, X.; Yuan, M.; Yang, J.; Ma, J.; Dong, Z. Efficient chemoselective hydrogenation of halogenated nitrobenzenes over an easily prepared γ -Fe₂O₃-modified mesoporous carbon catalyst. *Green Chem.* **2017**, *19*, 1548–1554. DOI: 10.1039/C6GC03386E. (d) Wang, H.; Cheng, X.; Yin, F.; Chen, B.; Fan, T.; He, X. Metal-organic gel-derived Fe-Fe₂O₃@ nitrogen-doped-carbon nanoparticles anchored on nitrogen-doped carbon nanotubes as a highly effective catalyst for oxygen reduction reaction. *Electrochim. Acta* **2017**, *232*, 114-122. DOI: 10.1016/j.electacta.2017.02.144. (e) Toraya, H. Direct derivation (DD) of weight fractions of individual crystalline phases from observed intensities and chemical composition data: incorporation of the DD method into the whole-powder-pattern fitting procedure. *J. Appl. Crystallogr.* **2018**, *51* (2), 446-455. DOI: 10.1107/S1600576718001474. (f) *α -Fe₂O₃ hematite (Fe₂O₃ hem) Crystal Structure: Datasheet from "PAULING FILE Multinaries Edition–2022"* in Springer Materials. https://materials.springer.com/isp/crystallographic/docs/sd_1628103 (accessed 2024-10-13). (g) *γ Fe₂O₃ (Fe_{2.67}O₄ mag) Crystal Structure: Datasheet from "PAULING FILE Multinaries Edition–2022"* in Springer Materials. https://materials.springer.com/isp/crystallographic/docs/sd_0554674 (accessed 2024-10-13).

[24] (a) Cao, D.; Li, H.; Pan, L.; Li, J.; Wang, X.; Jing, P.; Cheng, X.; Wang, W.; Wang, J.; Liu, Q. High saturation magnetization of γ -Fe₂O₃ nano-particles by a facile one-step synthesis

approach. *Sci. Rep.* **2016**, *6* (1), 32360. DOI: 10.1038/srep32360. (b) Long, Z.; Yuan, L.; Shi, C.; Wu, C.; Qiao, H.; Wang, K. Porous Fe₂O₃ nanorod-decorated hollow carbon nanofibers for high-rate lithium storage. *Adv. Compos. Hybrid Mater.* **2022**, *5*, 370-382. DOI: 10.1007/s42114-021-00397-9. (c) Holder, C. F.; Schaak, R. E. Tutorial on Powder X-ray Diffraction for Characterizing Nanoscale Materials. *ACS Nano* **2019**, *13* (7), 7359-7365. DOI: 10.1021/acsnano.9b05157. (d) He, M.; Wang, Y.; Zhang, X.; Zhang, H.; Meng, Y.; Shang, D.; Xue, H.; Li, D.; Wu, Z. Stability of iron-containing nanoparticles for selectively growing single-walled carbon nanotubes. *Carbon* **2020**, *158*, 795-801. DOI: 10.1016/j.carbon.2019.11.056. (e) Priyavrat; Khan, A.; Kunal; Sadasivuni, K. K.; Singh, A. K.; Ansari, J. R. Fe₂O₃ decorated reduced graphene oxide sheets for enhanced sensing applications for dopamine. *emergent mater.* **2024**. DOI: 10.1007/s42247-024-00784-0. (f) Li, K.; Yan, J.; Luo, L.; He, Z.; Zhou, L.; Gao, F. Controlled synthesis of monodisperse core-shell γ -Fe₂O₃@SiO₂ nanoparticles with well-dispersed γ -Fe₂O₃ seeds. *Micro & Nano Lett.* **2020**, *15* (4), 255-257. DOI: 10.1049/mnl.2019.0626. (g) Zhou, C.; Wan, L.; Lou, Z.; Wu, S.; Baig, S. A.; Xu, X. Comparative Sb(V) removal efficacy of different iron oxides from textile wastewater: effects of co-existing anions and dye compounds. *Environ. Sci. Pollut. Res.* **2023**, *30* (57), 120030-120043. DOI: 10.1007/s11356-023-30771-7.

[25] (a) Qin, J.; Long, Y.; Wu, W.; Zhang, W.; Gao, Z.; Ma, J. Amorphous Fe₂O₃ improved [O] transfer cycle of Ce⁴⁺/Ce³⁺ in CeO₂ for atom economy synthesis of imines at low temperature. *J. Catal.* **2019**, *371*, 161-174. DOI: 10.1016/j.jcat.2019.01.032. (b) Qin, J.; Long, Y.; Gou, G.; Wu, W.; Luo, Y.; Cao, X.; Luo, S.; Wang, K.; Ma, J. Tuning effect of amorphous Fe₂O₃ on Mn₃O₄ for efficient atom-economic synthesis of imines at low temperature: improving [O] transfer cycle of Mn³⁺/Mn²⁺ in Mn₃O₄. *Catal. Sci. Technol.* **2020**, *10*, 5628-5640. DOI: 10.1039/D0CY01021A. (c) Cao, X.; Koltypin, Y.; Prozorov, R.; Kataby, G.; Gedanken, A. Preparation of amorphous Fe₂O₃ powder with different particle sizes. *J. Mater. Chem.* **1997**, *7* (12), 2447-2451. DOI: 10.1039/A704003B. (d) Mashlan, M.; Zboril, R.; Machala, L.; Vujtek, M.; Walla, J.; Nomura, K. Mössbauer spectroscopy in study of thermally induced crystallization of amorphous Fe₂O₃ nanoparticles. *J. Metastab. Nanocryst. Mater.* **2004**, *20*, 641-647. (e) Machala, L.; Zboril, R.; Gedanken, A. Amorphous Iron(III) Oxide—A Review. *J. Phys. Chem. B* **2007**, *111* (16), 4003-4018. DOI: 10.1021/jp064992s. (f) Belin, T.; Millot, N.; Bovet, N.; Gailhanou, M. In situ and time resolved study of the γ/α -Fe₂O₃ transition in nanometric particles. *J. Solid State Chem.* **2007**, *180* (8), 2377-2385. DOI: 10.1016/j.jssc.2007.06.013. (g) Machala, L.; Tuček, J.; Zbořil, R. Polymorphous Transformations of Nanometric Iron(III) Oxide: A Review. *Chem. Mater.* **2011**, *23* (14), 3255-3272. DOI: 10.1021/cm200397g. (h) Lee, S.; Xu, H. Size-Dependent Phase Map and Phase Transformation Kinetics for Nanometric Iron(III) Oxides ($\gamma \rightarrow \varepsilon \rightarrow \alpha$ Pathway). *J. Phys.*

Chem. C **2016**, *120* (24), 13316-13322. DOI: 10.1021/acs.jpcc.6b05287. (l) Masubuchi, Y.; Sato, Y.; Sawada, A.; Motohashi, T.; Kiyono, H.; Kikkawa, S. Crystallization and magnetic property of iron oxide nanoparticles precipitated in silica glass matrix. *J. Eur. Ceram. Soc.* **2011**, *31* (14), 2459-2462. DOI: 10.1016/j.jeurceramsoc.2011.02.016.

[26] (a) Xu, J.; Zhuang, R.; Bao, L.; Tang, G.; Zhao, Y. KOH-mediated transition metal-free synthesis of imines from alcohols and amines. *Green Chem.* **2012**, *14*, 2384–2387. DOI: 10.1039/C2GC35714C. (b) Bain, J.; Cho, P.; Voutchkova-Kostal, A. Recyclable hydrotalcite catalysts for alcohol imination via acceptorless dehydrogenation. *Green Chem.* **2015**, *17*, 2271–2280. DOI: 10.1039/C5GC00312A. (c) Sokoll, R.; Hobert, H. Thermal desorption and infrared studies of amines adsorbed on SiO₂, Al₂O₃, Fe₂O₃, MgO, and CaO III. Aniline and t-Butylamine. *J. Catal.* **1990**, *125* (2), 285-291. DOI: 10.1016/0021-9517(90)90304-3. (d) Marx, U.; Sokoll, R.; Hobert, H. Thermal desorption and infrared studies of primary aliphatic amines adsorbed on haematite (α -Fe₂O₃). *J. Chem. Soc., Faraday Trans. 1, Physical Chemistry in Condensed Phases* **1986**, *82* (8), 2505-2514. DOI: 10.1039/F19868202505.

4.6. Appendix

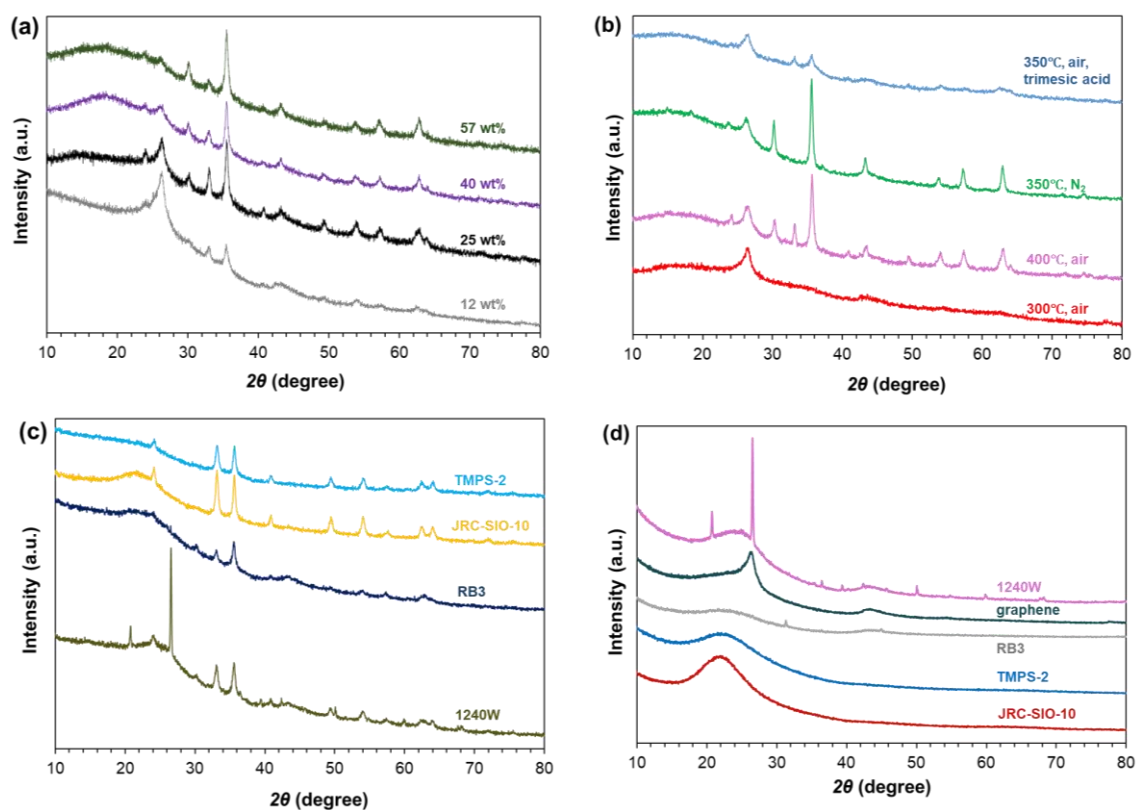


Figure 4.14. XRD patterns of (a) 12–57 wt% Fe_2O_3 /graphene (350°C, air); (b) 25 wt% Fe_2O_3 /graphene (different precursor and pyrolysis conditions in atmosphere or temperature); (c) 12–57 wt% Fe_2O_3 /different support (350°C, air); (d) various supports (graphene, activated carbon 1240W and RB3, SiO_2 namely JRC-SIO-10 and TMPS-2).

Table 4.3. Summary of characterization of all supported Fe₂O₃ catalysts.

(a)	Catalyst	BET S (m² g⁻¹)	Pore size (nm)	Pore volume (cm³ g⁻¹)
	12 wt% Fe ₂ O ₃ /graphene (350°C)	339	7.4	0.56
	25 wt% Fe ₂ O ₃ /graphene (350°C)	317	6.1	0.42
	40 wt% Fe ₂ O ₃ /graphene (350°C)	197	5.2	0.22
	57 wt% Fe ₂ O ₃ /graphene (350°C)	124	4.6	0.13
	25 wt% Fe ₂ O ₃ /graphene (300°C)	211	5.4	0.23
	25 wt% Fe ₂ O ₃ /graphene (400°C)	252	7.6	0.42
	25 wt% Fe ₂ O ₃ /graphene (350°C, N ₂)	160	7.3	0.27
	25 wt% Fe ₂ O ₃ /graphene (350°C, trimesic acid)	313	7.7	0.56
	25 wt% Fe ₂ O ₃ /1240W (350°C)	764	2.3	0.32
	25 wt% Fe ₂ O ₃ /RB3 (350°C)	872	2.1	0.26
	25 wt% Fe ₂ O ₃ /SiO ₂ (350°C)	214	14.7	0.79
	25 wt% Fe ₂ O ₃ /TMPS-2 (350°C)	753	3.7	0.77

(b)	Catalyst	Loading amount (wt%)	Crystallite size α (nm)	Crystallite size γ (nm)
	12 wt% Fe ₂ O ₃ /graphene (350°C)	19	17	n. d.
	25 wt% Fe ₂ O ₃ /graphene (350°C)	32	19	16
	40 wt% Fe ₂ O ₃ /graphene (350°C)	38	17	17
	57 wt% Fe ₂ O ₃ /graphene (350°C)	46	17	17
	25 wt% Fe ₂ O ₃ /graphene (300°C)	27	n. d.	n. d.
	25 wt% Fe ₂ O ₃ /graphene (400°C)	45	29	18
	25 wt% Fe ₂ O ₃ /graphene (350°C, N ₂)	19	n. d.	24
	25 wt% Fe ₂ O ₃ /graphene (350°C, trimesic acid)	33	18	n. d.
	25 wt% Fe ₂ O ₃ /1240W (350°C)	30	18	12
	25 wt% Fe ₂ O ₃ /RB3 (350°C)	23	20	17
	25 wt% Fe ₂ O ₃ /SiO ₂ (350°C)	n. d.	21	n. d.
	25 wt% Fe ₂ O ₃ /TMPS-2 (350°C)	n. d.	19	n. d.

The BET surface area, pore size (BJH method), and pore volume (BJH method) were determined using nitrogen adsorption analysis. The sizes of α and γ-Fe₂O₃ crystallite were obtained via XRD analysis. The loading amount was measured using TG analysis.

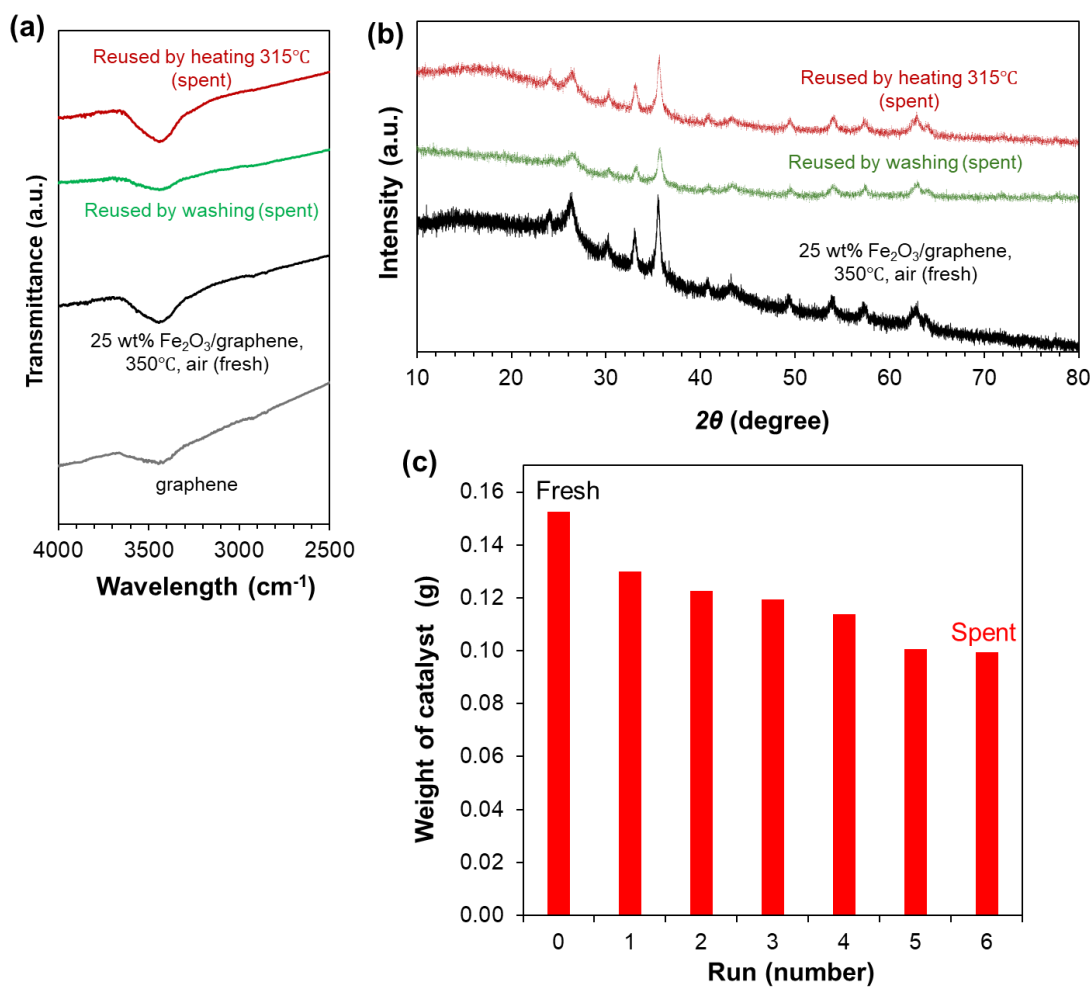
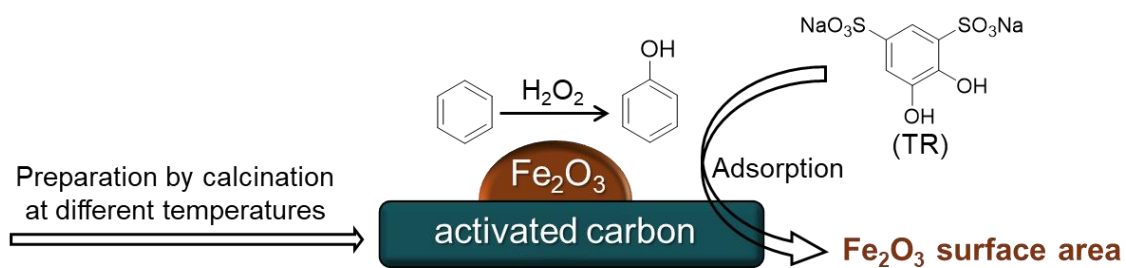


Figure 4.15. (a) FT-IR (KBr) spectra and (b) XRD pattern of fresh, spent catalyst (reused by washing and further heating at 315°C in Figure 4.13a, b); (c) weight changes with reuse (heating at 315°C in Figure 4.13b).

Chapter 5. Fe_2O_3 /Activated Carbon Catalysts for Oxidation of Benzene



5.1. Introduction: Carbon-supported Fe_2O_3 catalysts and direct oxidation of benzene to phenol

Activated carbon is a widely used porous material, distinguished by its highly developed pore structure and large specific surface area. These characteristics make it indispensable in various applications, including gas and liquid-phase adsorption, purification processes, and even medical treatments [27]. In catalysis, activated carbon serves extensively both as a catalyst [27d, e; 28a, b] and as a support material for catalysts [27d, e; 28c, d].

The direct conversion of benzene to phenol is a significant and challenging reaction in the chemical industry. Conventionally, phenol is produced via the three-step cumene (isopropylbenzene) process, commonly known as the Hock process, which also generates acetone as a by-product [29a, b]. Although economically viable, this method suffers from several inherent drawbacks, including low raw material efficiency, high energy consumption due to elevated reaction temperatures, and complex operational procedures [29c, d]. These limitations have motivated substantial efforts toward developing alternative routes, particularly those enabling the one-step synthesis of phenol from benzene under mild reaction conditions.

Carbon-supported Fe_2O_3 heterogeneous catalysts have emerged as promising candidates for the selective oxidation of benzene to phenol, drawing increasing attention in recent years [30]. While extensive research has been conducted on carbon-supported iron oxide materials, most studies have centered on a narrow range of catalysts [30]. In particular, the effect of preparation temperature, an important factor influencing catalytic performance, has not been investigated systematically.

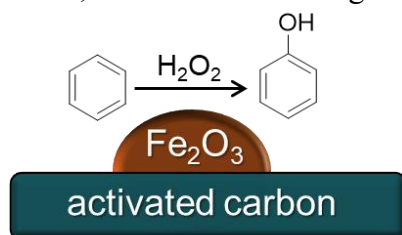


Figure 5.1. Fe_2O_3 /activated carbon catalyst for oxidation of benzene to phenol.

Chapter 4 presents a detailed investigation of supported Fe_2O_3 catalysts prepared at various temperatures, with particular emphasis on Fe_2O_3 catalyst supported on activated carbon for the oxidation of benzene to phenol. In addition to the synthesis and characterization of these catalysts, this chapter employs the selective adsorption method developed in Chapter 2 to quantify the Fe_2O_3 surface area dispersed on activated carbon.

5.2. Experimental

5.2.1. Preparation of Fe_2O_3 /activated carbon catalysts

The dried activated carbon (Norit GAC 1240W, hereafter referred to as AC, BET surface area = $917 \text{ m}^2 \text{ g}^{-1}$, Table 1.6 in Chapter 1) and ferric nitrate ($\text{Fe}(\text{NO}_3)_3$, purity > 99%) were purchased for catalyst preparation.

The catalysts were synthesized via the impregnation method as described in the literature [30a]. To modify the surface functional groups of the activated carbon, AC was treated with 5 M nitric acid at 90°C for 3 h, thoroughly rinsed with distilled water, dried under reduced pressure, and subsequently heated at 600°C for 3 h under a N_2 atmosphere. The nitric acid-treated activated carbon thus obtained is designated as AC-H.

The activated carbon-supported Fe_2O_3 catalyst was prepared by adding AC-H to an aqueous solution of $\text{Fe}(\text{NO}_3)_3$ (36 g L^{-1}) with an Fe : C weight ratio of 5 wt%. The mixture was stirred magnetically at 70°C for 30 min and dried under reduced pressure to remove residual moisture. The dried material, referred to as 5 wt% Fe/AC-H catalyst, was initially heated at 100°C in air and subsequently calcined at various temperatures (150, 350, 550, and 750°C) for 5 h under N_2 (example of Fe/AC-H-550 catalyst in Figure 5.2). These samples were labeled as 5 wt% Fe/AC-H-150, 5 wt% Fe/AC-H-350, 5 wt% Fe/AC-H-550, and 5 wt% Fe/AC-H-750, respectively.

For comparison, catalysts with 1 wt% and 10 wt% Fe loading were prepared using the same method, followed by calcination at 550°C under N_2 . These samples were designated as 1 wt% Fe/AC-H-550 and 10 wt% Fe/AC-H-550, respectively.

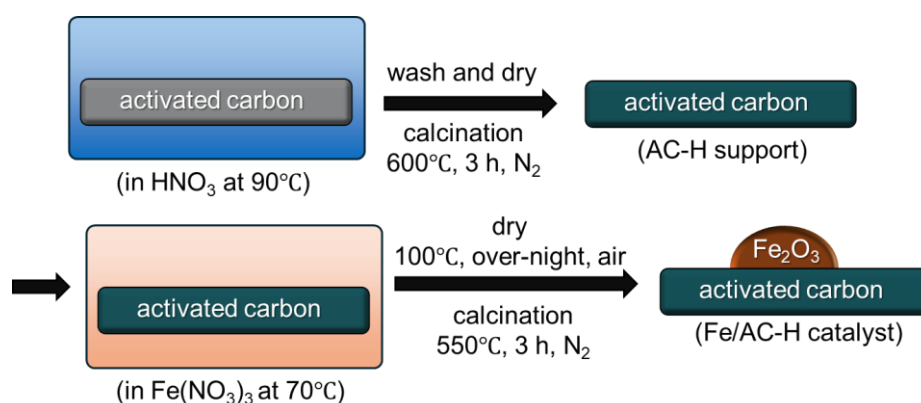


Figure 5.2. Preparation of the Fe₂O₃/activated carbon catalysts.

5.2.2. Catalyst characterization and measurement of Fe₂O₃ surface area

The BET surface area and the pore volume of the catalysts were measured using nitrogen adsorption-desorption isotherms. The crystallinity of the catalysts was analyzed using X-ray diffraction (XRD), while surface functional groups were characterized by Fourier-transform infrared spectroscopy with attenuated total reflectance FT-IR (ATR). The morphological features of the catalysts were examined using scanning electron microscopy (SEM).

Additionally, the surface areas of Fe₂O₃ on the prepared catalysts were determined through the selective adsorption of TR (see Chapter 4 for details of the methodology, and the adsorption on the activated carbon support (adsorption ratio as 3%, as discussed in Chapter 1) was subtracted.

5.2.3. Catalytic performance for oxidation of benzene

The oxidation of benzene to phenol was conducted in a 10 mL vial. Benzene (0.40 mL, 4.5 mmol) and the prepared catalyst (20 mg) were sequentially added to the vial, using acetonitrile (4.0 mL) as the solvent. Hydrogen peroxide (H₂O₂, 30 wt% aqueous solution, 1.0 mL, 10 mmol) was added in a single portion as the oxidant. The reaction was carried out at 25°C with shaking for 12 h in air.

After completion, the catalyst was separated from the reaction mixture by centrifugation. The resulting solution was sampled, mixed with *p*-xylene as an internal standard, and quantitatively analyzed using ¹H NMR spectroscopy in acetone-d (see Figure 5.9 in Appendix). Hydroquinone was identified as the sole byproduct. Based on the methodology outlined in the references [30b, 31a, b, d, f, g-l], the yield and selectivity of phenol were calculated using the formulas 5.1 and 5.2, respectively.

$$\text{yield (\%)} = \frac{\text{phenol (mol)}}{\text{initial benzene (mol)}} \times 100 \dots\dots\dots \text{(Formula 5.1)}$$

$$\text{selectivity (\%)} = \frac{\text{phenol (mol)}}{\text{phenol (mol)} + \text{hydroquinone (mol)}} \times 100 \dots\dots\dots \text{(Formula 5.2)}$$

The spent catalyst was washed alternately with water and acetonitrile several times, and then dried under reduced pressure. The catalyst was reused directly in subsequent catalytic reactions.

5.3. Results and Discussion

5.3.1. Characterization of Fe₂O₃/activated carbon catalysts

Figure 5.3 shows the XRD spectra of commercial activated carbon (AC), nitric acid-treated activated carbon (AC-H), and the 5 wt% Fe/AC-H catalysts calcined at various temperatures. No significant differences were observed between the XRD spectra of AC and AC-H, indicating that nitric acid treatment did not alter the crystal structure of the activated carbon.

For the 5 wt% Fe/AC-H catalyst, no peaks corresponding to Fe or its oxides were detected in either the uncalcined sample or the samples calcined at temperatures below 350°C. However, a weak peak near 36°, consistent with the reference spectrum of γ-Fe₂O₃ (PDF 039-1346), was observed in the sample calcined at 550°C. A distinct peak attributed to γ-Fe₂O₃ was clearly detected only in the sample calcined at 750°C. The precursor, Fe(NO₃)₃, typically begins to decompose in air to form Fe₂O₃ at temperatures above 80°C, and is fully converted to Fe₂O₃ at approximately 150°C [32a-c]. Therefore, it is expected that Fe₂O₃ should be present in all Fe/AC-H catalysts. Nevertheless, the absence of discernible Fe₂O₃ peaks in the XRD patterns of samples calcined below 550°C suggests

the formation of amorphous or fine crystalline Fe_2O_3 particles on the activated carbon surface [32d], whose crystallite size is below the detection limit of XRD [24c]. Using the Scherrer equation, the crystallite size of $\gamma\text{-Fe}_2\text{O}_3$ in the 5 wt% Fe/AC-H-750 catalyst was estimated to be approximately 16 nm.

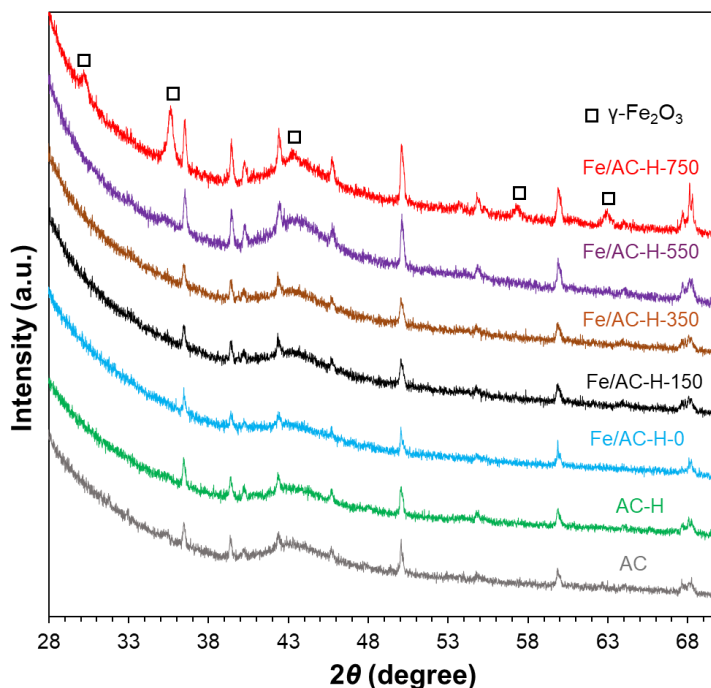


Figure 5.3. XRD patterns of the Fe_2O_3 /activated carbon catalysts.

Figure 5.4 illustrates the BET surface area and the average pore volume of AC, AC-H, and Fe/AC-H catalysts. The surface area and the pore volume of activated carbon remain almost unchanged after nitric acid treatment, indicating that the treatment does not significantly affect the physical properties of the support. In contrast, the surface area and the pore volume of the catalyst decrease sharply after Fe loading, suggesting that Fe deposition occurs primarily on the surface of the activated carbon. As the calcination temperature increases, the surface area and pore volume of the Fe/AC-H catalyst gradually increase. Notably, at a calcination temperature of 750°C, the surface area and the pore volume of the Fe/AC-H catalyst exceed those of the original AC support. This phenomenon can be attributed to the slight decomposition of the activated carbon support at high temperatures, which likely results in the enlargement of pores. Additionally, some

Fe_2O_3 particles may migrate from micropores to the outer surface, as inferred from the XRD analysis.

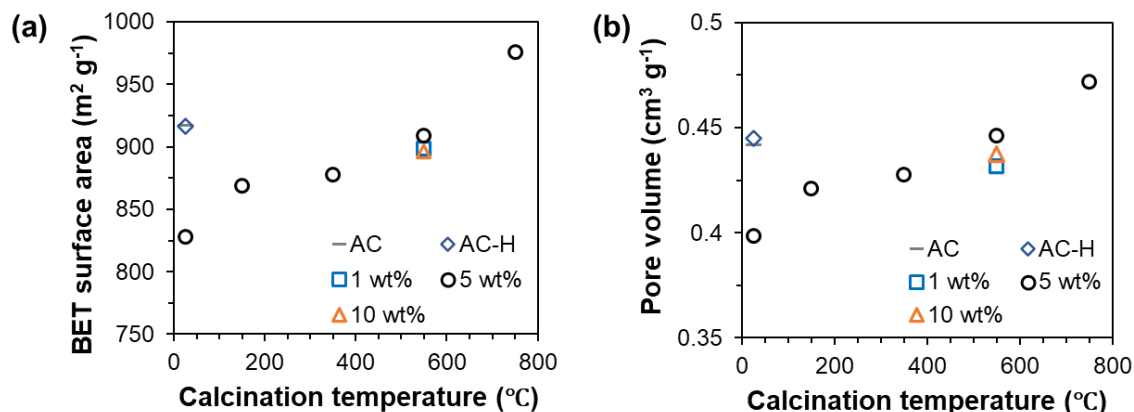


Figure 5.4. (a) BET surface area and (b) average pore volume of Fe/AC-H catalysts.

Figure 5.5 presents the SEM images of the carbon support (AC-H) and the Fe_2O_3 -supported catalyst (Fe/AC-H-550). The images reveal that, although the Fe_2O_3 -supported catalyst consists of smaller particles compared to the original carbon support, the flat surface characteristic of the carbon support is largely preserved. XRD analysis suggests that these smaller particles are not directly attributed to the deposited Fe_2O_3 . On the other hand, the reduction in particle size of the catalyst may result from Fe loading and the grinding process involved in catalyst preparation.

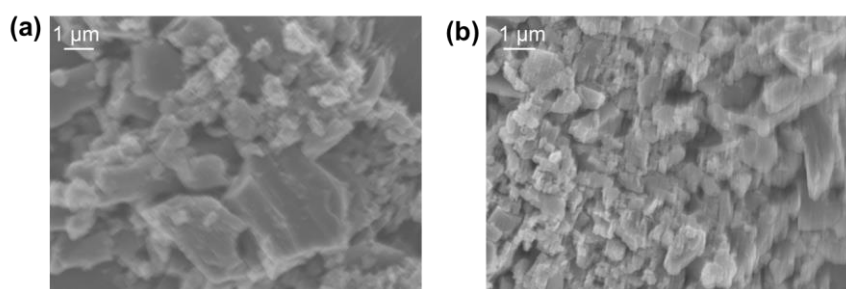


Figure 5.5. SEM images of (a) support AC-H and (b) Fe/AC-H-550 catalyst.

Figure 5.6 shows the FT-IR spectra of GAC, GAC-H, and 5 wt% Fe/GAC-H catalysts, with peak assignments based on a previous report [33]. After nitric acid treatment, the GAC-H catalyst exhibits a distinct $\nu(\text{C}=\text{O})$ stretching vibration band at 1730 cm^{-1} , attributed to the oxidation of the activated carbon surface. In the 5 wt% Fe/GAC-H

catalyst, the $\nu(\text{C}=\text{O})$ stretching vibration band at 1730 cm^{-1} and the $\nu(\text{C}-\text{O}-\text{C}$ in lactones or ester etc.) stretching vibration band at 1215 cm^{-1} (which is very weak or possibly absent for activated carbon) disappear. This disappearance can be attributed to the adsorption of the $\text{Fe}(\text{NO}_3)_3$ precursor onto these functional groups during catalyst preparation. Subsequently, the formation of Fe_2O_3 likely masks these functional groups, a phenomenon consistent with reports on graphene-supported Fe catalysts [33a-c].

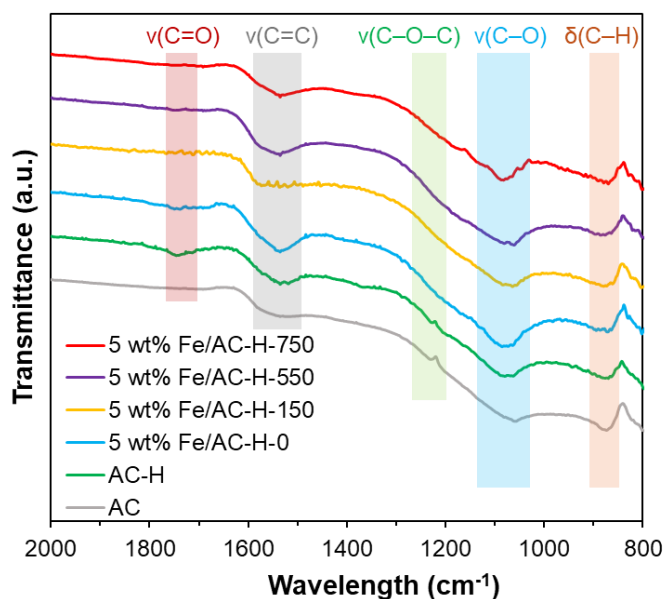


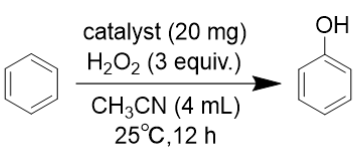
Figure 5.6. FT-IR (ATR) spectra of support activated carbon and Fe/AC-H catalysts.

5.3.2. Catalytic performance and Fe_2O_3 surface area

Table 5.1 summarizes the catalytic activities of the prepared catalysts for the direct oxidation of benzene to phenol. As shown in entry 1, the untreated activated carbon exhibited low catalytic activity. However, as indicated in entry 2, the catalytic activity significantly improved after nitric acid treatment (AC-H), likely due to the oxidation of functional groups on the activated carbon surface [30a-c, 31a]. Nonetheless, as shown in Figure 5.6, the disappearance of oxygen-containing functional groups ($\nu(\text{C}=\text{O})$ and $\nu(\text{C}-\text{O}-\text{C})$ stretching vibration bands) suggests that the contribution of the support material (AC-H) to the catalytic performance of the Fe/AC-H catalyst is minimal. In entries 3–6 and 9, the catalytic activity decreased as the calcination temperature increased during catalyst preparation, highlighting the strong influence of calcination temperature on

catalytic performance. This trend will be discussed further later. Additionally, entries 6–8 demonstrate that increasing the Fe loading for Fe/AC-H-550 significantly enhanced catalytic activity, confirming that Fe species (primarily Fe_2O_3) serve as the main active component. Entry 10 shows that no catalytic activity was observed in the absence of a catalyst. Meanwhile, entries 11–14 reveal that catalytic activity increased as the reaction temperature was raised from 25°C to 65°C, with trace amounts of phenol detected even without a catalyst. The highest phenol yield (14.4%) was achieved using the 5 wt% Fe/AC-H-550 catalyst, as shown in entry 13. However, increasing the reaction temperature also promoted the formation of byproducts due to the overoxidation of phenol, consistent with previous reports [30c, 31b-e].

Table 5.1. Catalytic performance of the various catalysts for phenol synthesis.^[a]



Entry	Catalysts	Yield (%)	Selectivity (%)
1	AC	0.4	100
2	AC-H	2.6	100
3	5 wt% Fe/AC-H	6.9	99
4	5 wt% Fe/AC-H-150	5.5	98
5	5 wt% Fe/AC-H-350	5.3	100
6	5 wt% Fe/AC-H-550	5.2	100
7	1 wt% Fe/AC-H-550	4.0	100
8	10 wt% Fe/AC-H-550	9.5	100
9	5 wt% Fe/AC-H-750	4.4	100
10	none	0	–
11 ^[b]	AC	7.5	100
12 ^[b]	AC-H	8.8	99
13 ^[b]	5 wt% Fe/AC-H-550	14.4	81
14 ^[b]	none	0.3	100

^[a]Reaction condition: benzene (0.40 mL, 4.5 mmol), catalyst (20 mg) and H_2O_2 (1.0 mL, 10 mmol) in CH_3CN (4.0 mL), 25°C, 12 h. Yield and selectivity of phenol were determined by ^1H NMR analysis, *p*-xylene as an internal standard. ^[b]Temperature at 65°C.

The Fe_2O_3 surface areas on the Fe/AC-H catalysts were determined using the selective adsorption of TR. For the uncalcined Fe/AC-H samples, the $\text{Fe}(\text{NO}_3)_3$ precursor had not been fully converted to Fe_2O_3 [32], and a significant amount of residual species, such as $\text{Fe}(\text{NO}_3)_3$ or FeOOH , may remain. These residual precursors can dissolve in DMF or partially interact with TR, thereby interfering with the UV spectroscopy measurements. Moreover, due to the considerable retention of these precursors, the selective adsorption of SS molecules may fail to assess the Fe_2O_3 surface area accurately. Fortunately, after calcination, the Fe_2O_3 surface area of the Fe/AC-H catalysts could be successfully measured by TR selective adsorption.

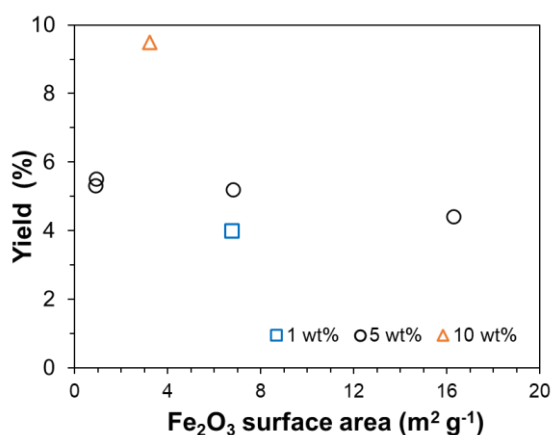


Figure 5.7. Relationship between the Fe_2O_3 surface area and yield in oxidation of benzene.

It was found that the Fe_2O_3 surface area on the Fe/AC-H catalyst is slightly inversely proportional to its catalytic activity (Figure 5.7). As shown in Figure 5.10 (Appendix), the Fe_2O_3 surface area increases with the calcination temperature, which is not a general trend that higher temperatures promote the aggregation and growth of metal oxide particles and reduce their surface area. The unique phenomenon found in this work can be explained by the presence of ultrafine Fe_2O_3 particles dispersed within the micropores of the activated carbon and the inaccessibility of TR probe molecule inside the micropore. The Fe_2O_3 particles can remain very small below 550°C due to confinement within the micropores, the anchoring effect of surface functional groups, and the protective environment of nitrogen gas during calcination (consistent with XRD analysis) [25c, e, g, h]. The relatively large TR probe molecules (>1 nm, estimated by ChemDraw 3D) may

not access these small micropores. Additionally, extremely small Fe_2O_3 particles embedded between the surface functional groups of the activated carbon might be shielded by neighboring groups, making them less accessible for binding with TR. For Fe/AC-H catalysts with higher Fe loadings (e.g., 10 wt%), the Fe_2O_3 surface area measured by TR decreased significantly, likely because TR molecules could not access the pores blocked by excessive Fe deposits.

In this work, H_2O_2 , used as the oxidant, generates reactive oxygen species on the surface of Fe_2O_3 particles, which oxidize benzene to phenol [30, 31]. While the reactants and products might adsorb onto the activated carbon surface [30, 31], they do not directly participate in surface reactions on the Fe_2O_3 particles. The smaller H_2O_2 molecules are less affected by pore size variations, allowing efficient utilization of Fe_2O_3 particles within even the smallest pores. However, as Fe_2O_3 particles grow and become detectable by TR, the actual surface area accessible to H_2O_2 decreases, leading to reduced catalytic activity. For uncalcined Fe/AC-H, significant amounts of $\text{Fe}(\text{NO}_3)_3$ or FeOOH may exist on the catalyst surface [32], and these compounds could also exhibit catalytic activity [34a, b].

Moreover, as a side reaction, H_2O_2 decomposes on the surface of Fe_2O_3 particles to produce O_2 [34c-e]. The generation of O_2 was suggested by the observation of pressure when opening a sealed reaction vial. With increasing calcination temperatures, Fe_2O_3 particles grow larger, reducing their dispersion on the carbon support and altering the local hydrophilic/hydrophobic microenvironment of the catalyst surface. In addition, the larger Fe_2O_3 particles are distributed within larger pores or on the outer surface, facilitating efficient substance transfer. On these particles, H_2O_2 is activated to generate reactive oxygen species, which subsequently decompose rapidly to produce O_2 . This process occurs instead of the reactive oxygen species interacting with benzene adsorbed on the adjacent carbon support. This hypothesis is further supported by the observation of the higher pressure upon opening the sealed reaction vials with the higher calcination temperature, indicating the more O_2 generation on Fe_2O_3 /activated carbon catalysts calcined at the higher temperature.

5.3.3. Reusability and comparison with literature

The reusability of heterogeneous catalysts is critically important for industrial applications. As shown in Figure 5.8, the catalytic reusability of three Fe/AC-H catalysts was evaluated. All three catalysts exhibited high reusability. However, while the 5 wt% Fe/AC-H-0 catalyst (uncalcined) demonstrated high initial catalytic activity, its reusability was inferior to those of the 5 wt% Fe/AC-H-350 and 5 wt% Fe/AC-H-550 catalysts. This difference can be attributed to the detachment of the Fe_2O_3 precursor, $\text{Fe}(\text{NO}_3)_3$, from the catalyst surface. Without calcination, this precursor contributed partially to the catalytic activity but lacked the stability needed for sustained reuse.

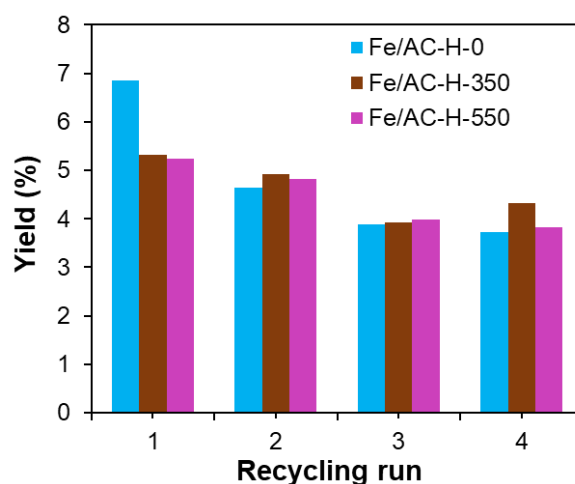


Figure 5.8. Reusability of several Fe/AC-H catalysts for oxidation of benzene.

Reaction condition: benzene (0.40 mL, 4.5 mmol), catalyst (20 mg) and H_2O_2 (1.0 mL, 10 mmol) in acetonitrile (4.0 mL), 25°C, 12 h.

Table 5.2 compares the catalytic performance of the Fe/AC-H-550 catalyst in this work with those of reported Fe-based catalysts. Although the Fe/AC-H-550 catalyst was not optimized under ideal conditions (e.g., oxidant dosage, Fe loading, or catalyst amount), its catalytic activity with 10 wt%Fe loading at room temperature is comparable to those reported in the literature under heated reaction conditions. The direct catalytic oxidation of benzene to phenol remains a highly challenging reaction [29c, d, 30, 31, 34b]. For instance, while a high phenol yield of 78.4% has been reported [31], it required a 13-fold excess of H_2O_2 . In contrast, this work offers a cost-effective catalyst that does not require a high excess of H_2O_2 , highlighting its potential for industrial applications.

Table 5.2. Comparison with recent reports on Fe-based catalysts.^[a]

Catalysts	Fe loading (wt%)	W_{catalyst} (mg)	n_{benzene} (mmol)	$n_{\text{H}_2\text{O}_2}$ (mmol)	T (°C)	t (h)	Yield (%)	Reference
Fe/AC-H-550	5	20	4.5	10	25	12	5.2	this study
Fe/AC-H-550	10	20	4.5	10	25	12	9.5	this study
Fe/AC-H-550	5	20	4.5	10	65	12	14.4	this study
Fe ₃ O ₄ /CMK-3	5.5	40	11.2	20	63	5	12.8	[31e]
Fe/GO ^[b]	12.5	40	11.2	35	65	3	15.0	[31f]
Fe/MWCNTs	5	50	11.3	13.5	60	3.5	14.4	[30c]
Fe-oxide CNC	27.1	1	3.9	4.6	60	48	16.1	[30e]
Fe ₂ O ₃ -TiO ₂	5	50	10	30	70	10	30.8	[31d]
Fe/SBA-16 ^[c]	10	100	11.2	48.5	65	8	11.7	[31b]
Fe@NC ^[c, d]	10.7	30	2.5	20	60	4	16.0	[31c]
FSD15 ^[c]	4	50	5.0	10	60	6	5.7	[31g]
FeN ₄ /GN-2.7 ^[c]	2.7	50	4.5	60	25	24	18.7	[31h]
Fe-N ₂ C ₂ SAs/N-C ^[c]	3.1	50	4.5	60	30	24	78.4	[31i]

^[a]Reaction condition: iron oxide catalyst (Fe/support wt%), acetonitrile as a solvent, H₂O₂ as an oxidant. ^[b]Acetic acid as a solvent. ^[c]Iron atom catalyst. ^[d]Acetonitrile / water (1:1) as a solvent.

5.4. Conclusions

A series of Fe₂O₃ catalysts supported on nitric acid-treated activated carbon (Fe/AC-H) were prepared by a simple impregnation method and subsequent calcination at various temperatures. These catalysts were applied for the direct oxidation of benzene to phenol using H₂O₂ as the oxidant.

The prepared Fe/AC-H catalysts were characterized by various techniques, including XRD, N₂ adsorption, and FT-IR analysis, which suggested that Fe₂O₃ particles were dispersed within the micropores of the activated carbon support and grew in size with increasing calcination temperature. The AC-H support treated with nitric acid contains abundant oxygen-containing functional groups that may contribute to catalytic activity, whereas these groups are largely absent in the Fe₂O₃-loaded Fe/AC-H catalysts.

A slightly negative correlation was observed between the Fe₂O₃ surface area measured by TR adsorption and the catalytic activity, which may be attributed to the fact that larger

Fe₂O₃ surface areas promote the side reaction of H₂O₂ decomposition to oxygen and that the Fe₂O₃ surface areas are underestimated due to the inaccessibility of the TR molecules into small Fe₂O₃ particles within the micropores. The small Fe₂O₃ particles confined within the micropores of the activated carbon could promote the generation of reactive oxygen species from H₂O₂, leading to more selective phenol formation.

In addition, the relationship among the sizes of H₂O₂, benzene, and TR molecules, the distribution of Fe₂O₃ particles, and the pore structure of the activated carbon is highly complex, which may also affect the catalytic activity from another perspective.

Although the catalysts and synthesis conditions have not yet been fully optimized, a maximum phenol yield of 14.4% was achieved, which is comparable to recently reported Fe-based catalysts. Furthermore, the catalysts demonstrated good reusability and showed potential for industrial application. The work in this chapter is expected to promote the development of supported iron catalysts and their application in the direct oxidation of benzene to phenol.

5.5. Reference

- [27] (a) Hassen, J. H.; Abdulkadir, H. K. Recent Developments in the Use of Activated Charcoal in Medicine. *JMS* **2022**, 91 (2), e647. DOI: 10.20883/medical.e647. (b) Lewoyehu, M. Comprehensive review on synthesis and application of activated carbon from agricultural residues for the remediation of venomous pollutants in wastewater. *J. Anal. Appl. Pyrolysis* **2021**, 159, 105279. DOI: 10.1016/j.jaap.2021.105279. (c) Malini, K.; Selvakumar, D.; Kumar, N. S. Activated carbon from biomass: Preparation, factors improving basicity and surface properties for enhanced CO₂ capture capacity – A review. *J. CO₂ Util.* **2023**, 67, 102318. DOI: 10.1016/j.jcou.2022.102318. (d) Chew, T. W.; H'Ng, P. S.; Luqman Chuah Abdullah, B. C. T. G.; Chin, K. L.; Lee, C. L.; Mohd Nor Hafizuddin, B. M. S.; TaungMai, L. A Review of Bio-Based Activated Carbon Properties Produced from Different Activating Chemicals during Chemicals Activation Process on Biomass and Its Potential for Malaysia. *Materials* **2023**, 16 (23), 7365. DOI: 10.3390/ma16237365. (e) Zhao, C.; Ge, L.; Mai, L.; Li, X.; Chen, S.; Li, Q.; Li, S.; Yao, L.; Wang, Y.; Xu, C. Review on Coal-Based Activated Carbon: Preparation, Modification, Application, Regeneration, and Perspectives. *Energy & Fuels* **2023**, 37 (16), 11622-11642. DOI: 10.1021/acs.energyfuels.3c01866.

[28] (a) Song, K. H.; Jeong, S. K.; Jeong, B. H.; Lee, K.-Y.; Kim, H. J. Acid/Base-Treated Activated Carbon Catalysts for the Low-Temperature Endothermic Cracking of N-Dodecane with Applications in Hypersonic Vehicle Heat Management Systems. *Catalysts* **2020**, *10* (10), 1149. DOI: 10.3390/catal10101149. (b) Yang, J.; Fu, L.; Wu, F.; Chen, X.; Wu, C.; Wang, Q. Recent Developments in Activated Carbon Catalysts Based on Pore Size Regulation in the Application of Catalytic Ozonation. *Catalysts* **2022**, *12* (10), 1085. DOI: 10.3390/catal12101085. (c) Iwanow, M.; Gärtner, T.; Sieber, V.; König, B. Activated carbon as catalyst support: precursors, preparation, modification and characterization. *Beilstein J. Org. Chem.* **2020**, *16*, 1188-1202. DOI: 10.3762/bjoc.16.104. (d) Gamal, A.; Jlassi, K.; Ahmad, Y. H.; Tang, M.; Al-Qaradawi, S. Y.; Chehimi, M. M.; Ozoemena, K. I.; Abdullah, A. M. Carbon-supported catalysts for carbon dioxide methanation: A review. *J. CO₂ Util.* **2024**, *85*, 102881. DOI: 10.1016/j.jcou.2024.102881.

[29] (a) Schmidt, R. J. Industrial catalytic processes—phenol production. *Appl. Catal. A Gen.* **2005**, *280* (1), 89-103. DOI: 10.1016/j.apcata.2004.08.030. (b) Zakoshansky, V. M. The cumene process for phenol-acetone production. *Pet. Chem.* **2007**, *47* (4), 273-284. DOI: 10.1134/S096554410704007X. (c) Mancuso, A.; Sacco, O.; Sannino, D.; Venditto, V.; Vaiano, V. One-Step Catalytic or Photocatalytic Oxidation of Benzene to Phenol: Possible Alternative Routes for Phenol Synthesis? *Catalysts* **2020**, *10* (12), 1424. DOI: 10.3390/catal10121424. (d) Rahmani, N.; Amiri, A.; Ziarani, G. M.; Badiei, A. Review of some transition metal-based mesoporous catalysts for the direct hydroxylation of benzene to phenol (DHBP). *Mol. Catal.* **2021**, *515*, 111873. DOI: 10.1016/j.mcat.2021.111873.

[30] (a) Choi, J.-S.; Kim, T.-H.; Choo, K.-Y.; Sung, J.-S.; Saidutta, M. B.; Ryu, S.-O.; Song, S.-D.; Ramachandra, B.; Rhee, Y.-W. Direct synthesis of phenol from benzene on iron-impregnated activated carbon catalysts. *Appl. Catal. A Gen.* **2005**, *290* (1), 1-8. DOI: 10.1016/j.apcata.2005.04.060. (b) Zhong, Y.; Li, G.; Zhu, L.; Yan, Y.; Wu, G.; Hu, C. Low temperature hydroxylation of benzene to phenol by hydrogen peroxide over Fe/activated carbon catalyst. *J. Mol. Catal. A Chem.* **2007**, *272* (1), 169-173. DOI: 10.1016/j.molcata.2007.03.015. (c) Song, S.; Yang, H.; Rao, R.; Liu, H.; Zhang, A. High catalytic activity and selectivity for hydroxylation of benzene to phenol over multi-walled carbon nanotubes supported Fe₃O₄ catalyst. *Appl. Catal. A Gen.* **2010**, *375* (2), 265-271. DOI: 10.1016/j.apcata.2010.01.008. (d) Qin, Q.; Liu, Y.; Shan, W.; Hou, W.; Wang, K.; Ling, X.; Zhou, Y.; Wang, J. Synergistic Catalysis of Fe₂O₃ Nanoparticles on Mesoporous Poly(ionic liquid)-Derived Carbon for Benzene Hydroxylation with Dioxygen. *Ind. Eng. Chem. Res.* **2017**, *56* (43), 12289-12296. DOI: 10.1021/acs.iecr.7b02566. (e) Abay, T. A.; Wanna, W. H.; Natarajan, T.; Tsai, Y.-F.; Janmanchi, D.; Jiang, J.-C.; Abu-Reziq, R.; Yu, S. S. F. Selective oxidation of benzene by an iron oxide

carbonaceous nanocatalyst prepared from iron perchlorate salts and hydrogen peroxide in benzene and acetonitrile. *Mol. Catal.* **2022**, 526, 112397. DOI: 10.1016/j.mcat.2022.112397.

[31] (a) Wen, G.; Wu, S.; Li, B.; Dai, C.; Su, D. S. Active Sites and Mechanisms for Direct Oxidation of Benzene to Phenol over Carbon Catalysts. *Angew. Chem. Int. Ed.* **2015**, 54 (13), 4105-4109. DOI: 10.1002/anie.201410093. (b) Jourshabani, M.; Badiei, A.; Shariatnia, Z.; Lashgari, N.; Mohammadi Ziarani, G. Fe-Supported SBA-16 Type Cage-like Mesoporous Silica with Enhanced Catalytic Activity for Direct Hydroxylation of Benzene to Phenol. *Ind. Eng. Chem. Res.* **2016**, 55 (14), 3900-3908. DOI: 10.1021/acs.iecr.5b04976. (c) Lu, E.; Wu, J.; Yang, B.; Yu, D.; Yu, Z.; Hou, Y.; Zhang, J. Selective Hydroxylation of Benzene to Phenol over Fe Nanoparticles Encapsulated within N-Doped Carbon Shells. *ACS Appl. Nano Mater.* **2020**, 3 (9), 9192-9199. DOI: 10.1021/acsanm.0c01824. (d) Singha, A.; Bhaduri, K.; Kothari, A. C.; Chowdhury, B. Selective hydroxylation of benzene to phenol via CH activation over mesoporous Fe₂O₃-TiO₂ using H₂O₂. *Mol. Catal.* **2022**, 533, 112800. DOI: 10.1016/j.mcat.2022.112800. (e) Arab, P.; Badiei, A.; Koolivand, A.; Mohammadi Ziarani, G. Direct Hydroxylation of Benzene to Phenol over Fe₃O₄ Supported on Nanoporous Carbon. *Chin. J. Catal.* **2011**, 32 (1), 258-263. DOI: 10.1016/S1872-2067(10)60173-8. (f) Wang, C.; Hu, L.; Hu, Y.; Ren, Y.; Chen, X.; Yue, B.; He, H. Direct hydroxylation of benzene to phenol over metal oxide supported graphene oxide catalysts. *Catal. Commun.* **2015**, 68, 1-5. DOI: 10.1016/j.catcom.2015.04.014. (g) Xiao, P.; Wang, Y.; Kondo, J. N.; Yokoi, T. Consequences of Fe speciation in MFI zeolites for hydroxylation of benzene to phenol with H₂O₂. *Appl. Catal. A Gen.* **2019**, 579, 159-167. DOI: 10.1016/j.apcata.2019.04.025. (h) Deng, D.; Chen, X.; Yu, L.; Wu, X.; Liu, Q.; Liu, Y.; Yang, H.; Tian, H.; Hu, Y.; Du, P.; et al. A single iron site confined in a graphene matrix for the catalytic oxidation of benzene at room temperature. *Sci. Adv.* **2015**, 1 (11), e1500462. DOI: 10.1126/sciadv.1500462. (i) Pan, Y.; Chen, Y.; Wu, K.; Chen, Z.; Liu, S.; Cao, X.; Cheong, W.-C.; Meng, T.; Luo, J.; Zheng, L.; et al. Regulating the coordination structure of single-atom Fe-N_xC_y catalytic sites for benzene oxidation. *Nat. Commun.* **2019**, 10 (1), 4290. DOI: 10.1038/s41467-019-12362-8.

[32] (a) Wiecezorek-Ciurowa, K.; Kozak, A. J. The Thermal Decomposition of Fe(NO₃)₃·9H₂O. *J. Therm. Anal. Calorim.* **1999**, 58 (3), 647-651. DOI: 10.1023/A:1010112814013. (b) Melnikov, P.; Nascimento, V. A.; Arkhangelsky, I. V.; Zaroni Consolo, L. Z.; de Oliveira, L. C. S. Thermal decomposition mechanism of iron(III) nitrate and characterization of intermediate products by the technique of computerized modeling. *J. Therm. Anal. Calorim.* **2014**, 115 (1), 145-151. DOI: 10.1007/s10973-013-3339-1. (c) Zhang, X.; Li, Y.; Li, G.; Hu, C. Preparation of Fe/activated carbon directly from rice husk pyrolytic carbon and its application in catalytic hydroxylation of

phenol. *RSC Adv.* **2015**, *5* (7), 4984-4992. DOI: 10.1039/C4RA13248C. (d) Kadirova, Z. C.; Hojamberdiev, M.; Katsumata, K.-I.; Isobe, T.; Matsushita, N.; Nakajima, A.; Okada, K. Fe₂O₃-loaded activated carbon fiber/polymer materials and their photocatalytic activity for methylene blue mineralization by combined heterogeneous-homogeneous photocatalytic processes. *Appl. Surf. Sci.* **2017**, *402*, 444-455. DOI: 10.1016/j.apsusc.2017.01.131.

[33] (a) Jia, X.; Lian, D.; Shi, B.; Dai, R.; Li, C.; Wu, X. Facile synthesis of α -Fe₂O₃@graphene oxide nanocomposites for enhanced gas-sensing performance to ethanol. *J Mater Sci: Mater Electron* **2017**, *28* (16), 12070-12079. DOI: 10.1007/s10854-017-7019-y. (b) Abdel-Aal, S. K.; Ionov, A.; Mozhechil, R. N.; Naqvi, A. H. Simple synthesis of graphene nanocomposites MgO-rGO and Fe₂O₃-rGO for multifunctional applications. *Appl. Phys. A* **2018**, *124* (5), 365. DOI: 10.1007/s00339-018-1748-5. (c) Ghamsari, M.; Madrakian, T. Highly Fast and Efficient Removal of some Cationic Dyes from Aqueous Solutions Using Sulfonated-oxidized Activated Carbon. *Anal. Bioanal. Chem. Res.* **2019**, *6* (1), 157-169. DOI: 10.22036/abcr.2018.145499.1242. (d) Mopoung, S.; Dejang, N. Activated carbon preparation from eucalyptus wood chips using continuous carbonization–steam activation process in a batch intermittent rotary kiln. *Sci. Rep.* **2021**, *11* (1), 13948. DOI: 10.1038/s41598-021-93249-x. (e) Jahan, M.; Feni, F. Environmentally friendly bifunctional catalyst for ORR and OER from coconut shell particles. *Adv. Chem. Phys. Mater.* **2022**, *12* (05), 106-123. DOI: 10.4236/ampc.2022.125008.

[34] (a) Bianchi, D.; Bortolo, R.; Tassinari, R.; Ricci, M.; Vignola, R. A Novel Iron-Based Catalyst for the Biphasic Oxidation of Benzene to Phenol with Hydrogen Peroxide. *Angew. Chem. Int. Ed.* **2000**, *39* (23), 4321-4323. DOI: 10.1002/1521-3773(20001201)39:23<4321::AID-ANIE4321>3.0.CO;2-5. (b) Wang, Y.; Wang, J.; Wei, J.; Wang, C.; Wang, H.; Yang, X. Catalytic Mechanisms and Active Species of Benzene Hydroxylation Reaction System Based on Fe-Based Enzyme-Mimetic Structure. *Catal. Letters* **2023**, *153* (11), 3311-3332. DOI: 10.1007/s10562-022-04238-2. (c) Huang, H.-H.; Lu, M.-C.; Chen, J.-N. Catalytic Decomposition of Hydrogen Peroxide and 2-chlorophenol with iron oxides. *Wat. Res.* **2001**, *35* (9), 2291-2299. DOI: 10.1016/S0043-1354(00)00496-6. (d) Lin, S.-S.; Gurol, M. D. Catalytic Decomposition of Hydrogen Peroxide on Iron Oxide: Kinetics, Mechanism, and Implications. *Environ. Sci. Technol.* **1998**, *32* (10), 1417-1423. DOI: 10.1021/es970648k. (e) Lousada, C. M.; Johansson, A. J.; Brinck, T.; Jonsson, M. Mechanism of H₂O₂ Decomposition on Transition Metal Oxide Surfaces. *J. Phys. Chem. C* **2012**, *116* (17), 9533-9543. DOI: 10.1021/jp300255h.

5.6. Appendix

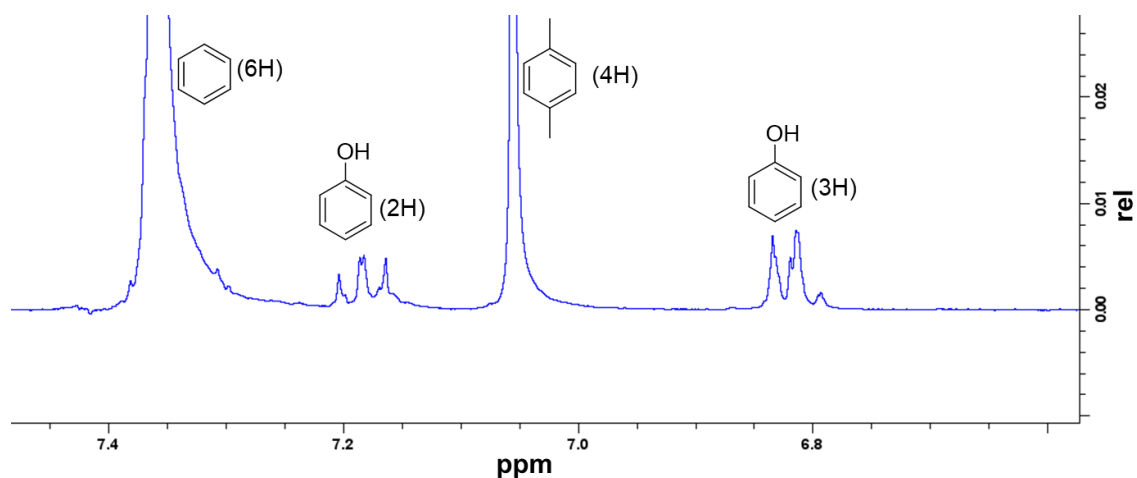


Figure 5.9. ^1H NMR spectra of the crude product in acetone- d_6 , over the 5 wt% Fe/AC-H-550 catalyst under reaction conditions at 25°C (see entry 6 in Table 5.1).

The peak assignments in ^1H NMR (400 MHz, acetone- d_6) analysis of the reaction mixtures was conducted as follows: benzene: δ 7.36 (s, 6H); phenol: δ 8.23 (or 8.13 with water) (s, 1H), 7.16–7.20 (m, 2H), 6.79–6.84 (m, 3H); *p*-xylene (an internal standard): δ 7.05 (s, 4H), 2.26 (s, 6H).

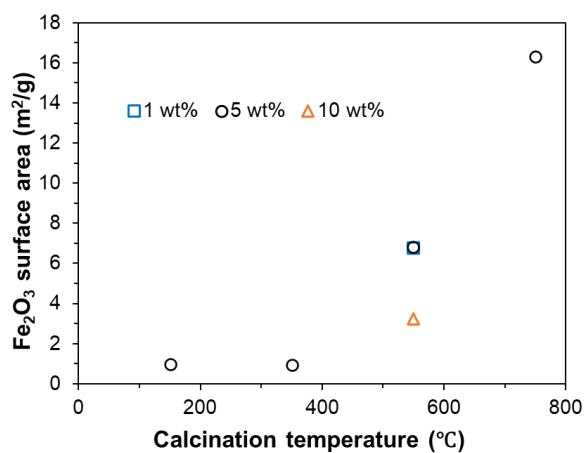
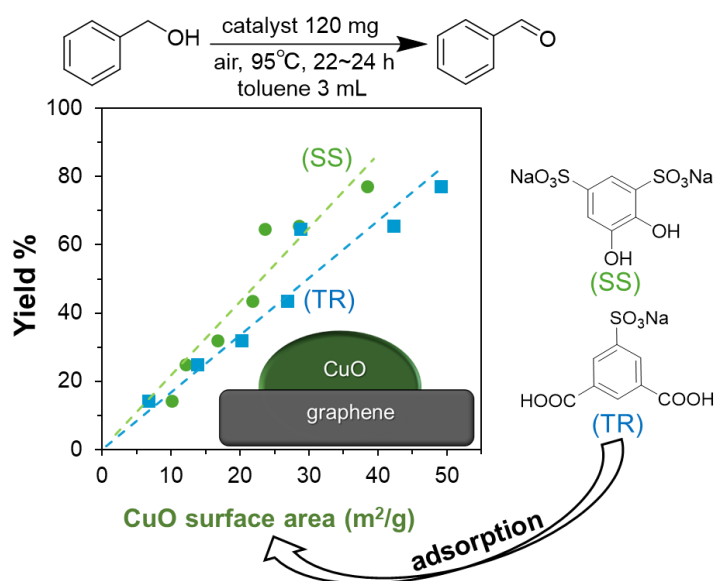


Figure 5.10. Relationship between Fe₂O₃ surface area of Fe/AC-H catalysts and calcination temperature.

Chapter 6. CuO/graphene Catalysts for Oxidative Dehydrogenation of Alcohols



6.1. Introduction: Copper oxide catalysts and oxidative dehydrogenation of alcohols

Historically, copper (Cu) was one of the first metals utilized by humans, playing a crucial role in the development of human society. Before the widespread use of iron, copper was the primary metal in use. Even today, due to its abundant reserves, copper remains an essential metal, with applications ranging from electrical wiring, machines and electronic components to currency production [35a].

In catalysis, copper-based catalysts are similarly significant in the chemical industry. For example, Cu/ZnO catalysts are widely utilized for hydrogen production via reforming processes [35b], Cu/SiO₂ catalysts facilitate the conversion of esters to alcohols [35c], and molecular copper catalysts are employed in alcohol oxidation [35d]. Recent studies have also explored various Cu-based catalysts [36a], such as homogeneous molecular catalysts for organic transformations such as aerobic Csp³-H oxidation [36b], asymmetric synthesis [36c], and C-N and C-O bond formation [36d]. Heterogeneous copper catalysts have also been investigated, such as CuO for CO₂ electroreduction [37a], CuS for nonaqueous rechargeable lithium-oxygen batteries [37b], and Cu/C or SiO₂ for the hydrogenation of 1,3-butadiene [37c] and other organic transformations [37d].

Among the various copper-based catalysts discussed earlier, CuO stands out due to its stability, low cost, and high catalytic potential. However, its catalytic performance is significantly limited by its low dispersibility and the lack of uniformity in its catalytic environment. To address these challenges, this chapter focuses on the development of CuO/graphene catalysts, utilizing graphene as a support material (as discussed in Chapter 4). This strategy aims to enhance the dispersibility of CuO and diversify its catalytic environment, thereby improving its overall catalytic activity.

CuO/graphene catalysts have been applied in various reactions, including lithium-oxygen (Li-O₂) batteries [38a], nitrogen reduction for ammonia synthesis [38b], photocatalytic degradation of organic pollutants [38c], and alcohol oxidation [38d]. Among these, the catalytic oxidation of alcohols using heterogeneous catalysts is a cornerstone reaction in the chemical industry [35d]. CuO-based catalysts exhibit substantial promise in alcohol oxidation, with notable examples including nano-CuO

[38e], CuO/graphene oxide [38d], Au/CuO-ZnO [38f], and CuO/SiO₂ [38g] catalysts. However, most of these systems face severe limitations. For example, while nano-CuO exhibits high catalytic activity, its synthesis is complex, and the particles tend to agglomerate [38e]; the reported CuO/graphene oxide catalyst requires high concentrations of oxygen as a reaction condition [38d]. Similarly, other catalysts often rely on oxygen or expensive noble metals such as gold (Au) to achieve high performance. To overcome these drawbacks, there is a need to develop environmentally friendly, supported CuO catalysts that maintain high activity without requiring noble metals or additional oxidants.

In this chapter, preparation of CuO/graphene catalysts and evaluation of their performance in the oxidation of benzyl alcohol to synthesize benzaldehyde are described (Figure 6.1). The incorporation of graphene was expected to enhance the catalytic activity of the CuO catalyst. Additionally, the CuO surface area on the supported catalyst was measured using the previously developed selective adsorption method described in Chapter 2, allowing for further exploration of the correlation between the catalytic activity and the CuO surface area.

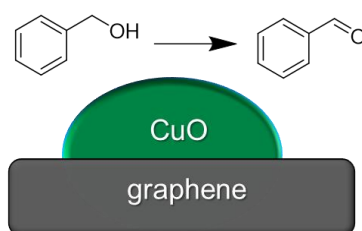


Figure 6.1. CuO/graphene catalyst for oxidation of benzyl alcohol.

6.2. Experimental

6.2.1. Preparation of CuO/graphene catalysts

CuO/graphene catalysts were prepared by the impregnation method, as shown in Figure 6.2. Graphene and Cu(NO₃)₂ were dispersed in water with a CuO/carbon ratio of 30 wt% and stirred at room temperature for 20 h. The resulting mixtures were centrifuged to remove the supernatant and then dried under reduced pressure overnight to obtain the precursor. The catalysts were then prepared by pyrolyzing the precursor at 200–400°C for

1 h in air. The resulting black solids (catalysts) were designated as "CuO/graphene-temperature (200–400)". Additionally, another catalyst was prepared using EtOH as the impregnation solvent and pyrolyzed at 250°C for 1 h in air, labeled as "CuO/graphene-250-EtOH".

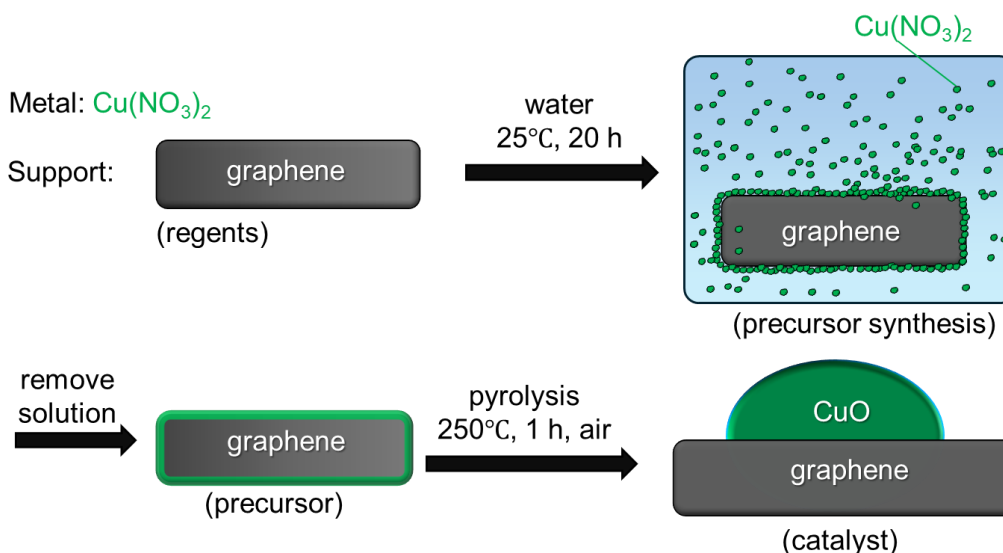


Figure 6.2. Preparation of CuO/graphene catalysts.

6.2.2. Catalyst characterization and measurement of CuO surface area

First, the prepared CuO/graphene catalyst was characterized using standard techniques, including XRD, TEM, TG, and BET surface area analysis (by N_2 adsorption). The CuO surface area on the graphene support was then determined by the selective adsorption of TR and SS, following the procedure described in Chapter 2. It was assumed that the selective adsorption of TR and SS on graphene in DMF was negligible. The CuO surface area was calculated based on the calibration curve shown in Figure 2.19b (Chapter 2).

6.2.3. Catalytic performance for oxidation of benzyl alcohols

In a typical reaction procedure, a 50 mL flask was charged with the catalyst (0.12 g), benzyl alcohol (0.50 mmol), and toluene (3.0 mL). The reaction mixture was magnetically

stirred at 95°C for 22–24 h under air. After the reaction, the catalyst mixture was washed with toluene, and the crude product solution was collected. The crude product was then analyzed by gas chromatography (GC) using naphthalene as an internal standard.

For the oxidation of various alcohols, the crude products were analyzed by ^1H NMR, using dimethyl sulfoxide as the internal standard. In the standard reuse procedure, the spent catalyst, was reused in the next cycle after washing with toluene, and drying under reduced pressure.

6.3. Results and discussion

6.3.1. Characterization of CuO/graphene catalysts

Typically, copper nitrate decomposes into CuO at around 180°C [39a], as indicated by the reaction formula: $2 \text{Cu}(\text{NO}_3)_2 \rightarrow 2 \text{CuO} + 4 \text{NO}_2 + \text{O}_2$. Similar conditions have been reported for the preparation of CuO catalysts [39b]. In this work, CuO/graphene catalysts were prepared by impregnating graphene with copper nitrate, followed by pyrolysis.

Several typical CuO/graphene catalysts prepared in this study, along with commercially available CuO (particle size: 10–50 nm, crystallite size: 14 nm, $S = 26 \text{ m}^2 \text{ g}^{-1}$) were analyzed by XRD measurements (Figure 6.3). The CuO/graphene-250, CuO/graphene-400, and CuO/graphene-250-EtOH catalysts exhibit the characteristic crystal structure of CuO. The crystallite sizes were calculated using the Scherrer formula from the XRD patterns (Figure 6.9a in Appendix). Notably, the diffraction patterns of CuO/graphene-200 and CuO/graphene-250 catalysts were extremely weak, falling below the XRD detection limit [24c]. This observation suggests that CuO/graphene catalysts prepared in this study achieved significantly reduced crystallite sizes, likely due to enhanced dispersion of CuO on the graphene support.

Furthermore, a comparison between the CuO/graphene-250 and CuO/graphene-400 catalysts revealed that lower calcination temperatures favored the formation of smaller CuO crystals. Differences in the adsorption behavior of the copper nitrate precursor on the graphene support, depending on the choice of ethanol or water as the impregnation

solvent, may also influence the resulting crystallite sizes. CuO/graphene-250 catalysts prepared using ethanol (EtOH) exhibited slightly larger CuO crystals compared to those prepared with water. These results highlight the critical roles of both the calcination temperature and the solvent choice in controlling the crystallite size of the CuO/graphene catalysts.

Although copper oxides include CuO, Cu₂O and Cu₄O₃, the latter two are metastable phases and are typically not formed during pyrolysis of copper nitrate in air [31a]. Consistently, no peaks corresponding to Cu₂O or Cu₄O₃ were observed in the XRD patterns (Figure 6.3).

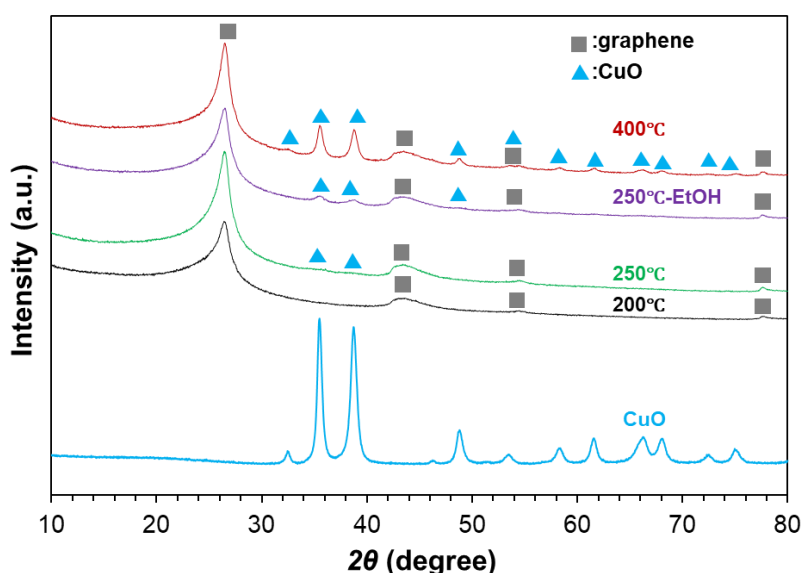


Figure 6.3. XRD patterns of several CuO/graphene catalysts and a commercial CuO (particles size: 10–50 nm).

Figure 6.4 shows the TEM images of CuO/graphene-250 and CuO/graphene-400 catalysts. Consistent with the results from the XRD analysis, CuO/graphene-250 catalyst exhibited smaller CuO particles, with an average size of approximately 3.9 nm. In contrast, increasing the calcination temperature led to significant particle growth in CuO/graphene-400 catalyst, where the average CuO particle size reached 16.7 nm.

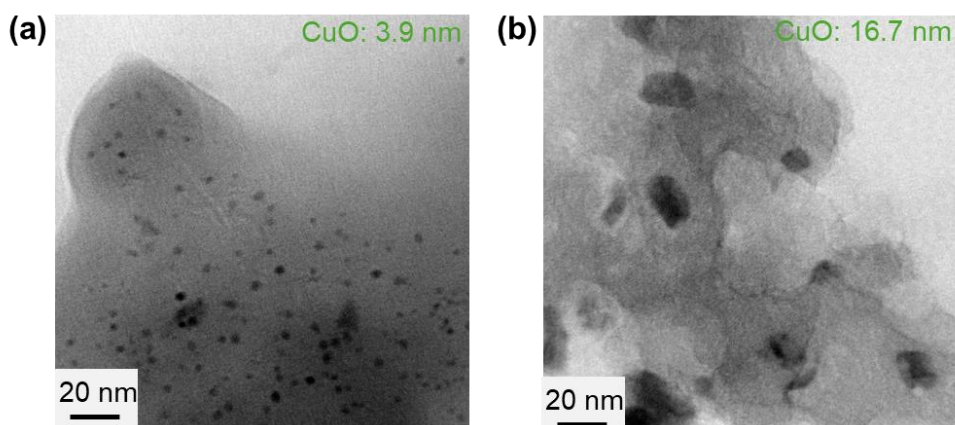


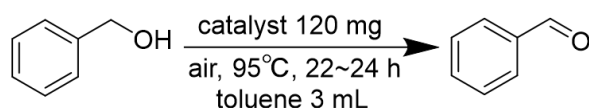
Figure 6.4. TEM images of (a) CuO/graphene-250, (b) CuO/graphene-400 catalysts (original data by co-worker Naomiti Ando).

6.3.2. Catalytic performance and CuO surface area

Table 6.1 summarizes the catalytic performance of commercially available CuO materials and the prepared CuO/graphene catalysts for benzyl alcohol oxidation, along with their corresponding BET surface areas. In general, commercial CuO with smaller grain sizes exhibits a larger BET surface area, which enhances its catalytic activity for benzyl alcohol oxidation. The inconsistencies between catalytic activity and BET surface area (e.g., entries 2 and 3) may be attributed to potential differences in the preparation methods of commercial CuO.

Among the commercial CuO samples, the highest yield was approximately 30%. In contrast, the CuO/graphene catalysts prepared in this study exhibited substantially increased surface areas compared to commercial CuO. Notably, the maximum yield reached nearly 80% (entry 7), representing a remarkable enhancement in catalytic activity compared to the commercial CuO samples. CuO/graphene-250 catalyst, which achieved the highest yield, contained only around 12 wt% CuO (Figure 6.10 in Appendix), underscoring the superior catalytic performance of the materials prepared in this work.

Table 6.1. Oxidation of benzyl alcohol catalyzed by commercial CuO and CuO/graphene catalysts.



Entry	Catalyst (BET S m ² g ⁻¹)	Yield (%)	Conversion (%)
1	CuO (26)	27 (24*)	41 (32*)
2	CuO (24)	20 (20*)	31 (22*)
3	CuO (24)	12 (14*)	17 (15*)
4	CuO (14)	8	9
5	CuO (5)	0.4	2
6	CuO/graphene-200 (552)	66	93
7	CuO/graphene-250 (467)	77	83
8	CuO/graphene-300 (383)	44	45
9	CuO/graphene-350 (347)	32	45
10	CuO/graphene-400 (496)	25	27
11	CuO/graphene-250-EtOH (500)	65	80
12	graphene (750)	< 1	—

Reaction conditions: benzyl alcohol (0.50 mmol), catalyst (0.12 g), and toluene (3.0 mL), in air, 95°C, 22~24 h. *Double experimental scales. Conversion and yield of benzaldehyde were determined by GC analysis (naphthalene as an internal standard). BET surface area was determined by N₂ adsorption.

Figure 6.5 illustrates the relationship between the CuO surface area determined via the selective adsorption of TR and SS, and the yield of benzaldehyde using the CuO/graphene catalysts. In contrast to the behavior observed in Chapters 3–5, TR (tiron) may not, or only weakly, interacted with copper ions, thereby allowing for the successful determination of the CuO surface area. On the other hand, the surface areas measured using TR and SS are not consistent, with TR giving relatively higher values. This can be attributed to the slightly stronger adsorption equilibrium and higher affinity of TR toward carbon materials compared to SS, as observed for titanium oxide (see Section 2.3.1 and 2.3.2, Chapter 2). Furthermore, under the standard adsorption conditions used in this study, SS exhibited slightly better selectivity than TR for carbon-supported metal oxides (refer to Chapter 2). As a result, the adsorption of TR may underestimate the surface area of CuO.

Despite these differences, the CuO surface areas determined by both TR and SS show a positive correlation with catalytic activity, indicating that the catalytic active sites are

located on the CuO surface. This finding emphasizes the effectiveness of the selective adsorption method used in this study for accurately determining the surface area of supported metal oxides. Moreover, the observed differences in surface area measured by TR and SS do not affect the analysis of catalytic activity.

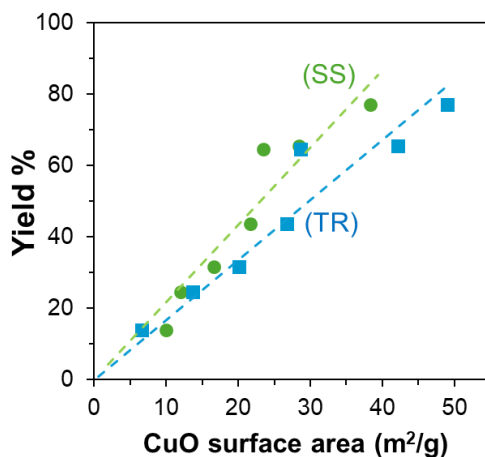


Figure 6.5. The relationship between CuO surface area (by adsorption of SS and TR) and yield in oxidations of benzyl alcohol (yield based on Table 6.1).

Previous studies suggest that the CuO {001} plane is likely the primary catalytically active crystal plane [38e, g]. While the specific crystal planes were not identified in this chapter, all the prepared CuO/graphene catalysts were synthesized under comparable conditions, suggesting the formation of similar crystal plane structures. The observed correlation between catalytic activity and CuO surface area further supports the hypothesis that analogous crystal plane structures are present in CuO/graphene catalysts examined in this work.

Figure 6.6 shows the dependence of the yield of benzaldehyde on the CuO crystallite size and BET surface area. While the yield is inversely proportional to the CuO crystallite size, it is noteworthy that smaller crystals fall below the detection limit of XRD. Additionally, no discernible correlation between the BET surface area and the benzaldehyde yield was observed.

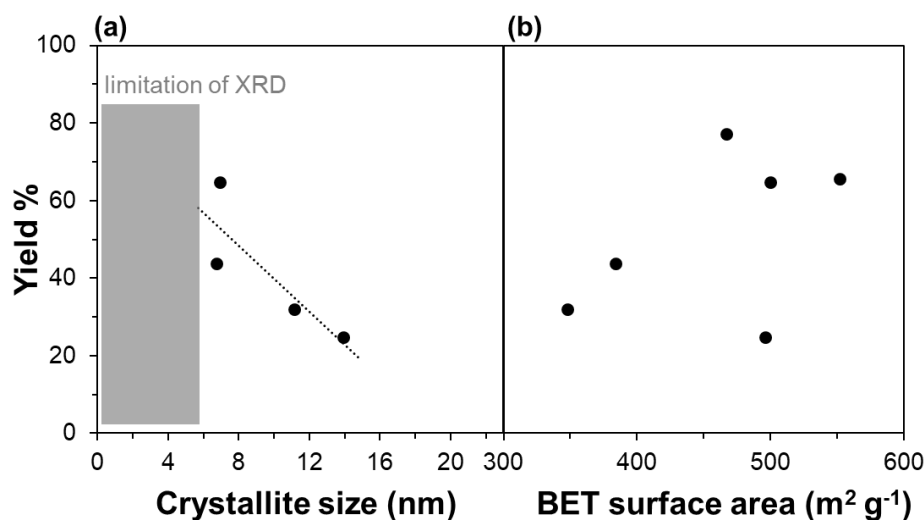


Figure 6.6. Dependence of the yield on (a) CuO crystallite size and (a) BET surface area in oxidation of benzyl alcohol.

6.3.3. Substrate scope and reusability of CuO/graphene catalyst

The catalytic versatility of the catalyst toward various derivatives is a critical aspect of its performance. Accordingly, CuO/graphene-250 was evaluated for the oxidation of different alcohols under standard experimental conditions (Figure 6.7). The yields of products **2b–d** were similar or slightly lower than that of **2a**, likely due to steric hindrance or electronic effects. Similarly, the lower yields observed for **2e** and **2f** can be attributed to the higher activation energies required for aliphatic alcohols. In the oxidation of substrates leading to **2g** and **2h**, several unidentified by-products were detected, which affected the overall yields of the desired products. Despite these challenges with certain substrates, CuO/graphene-250 catalyst exhibited significant versatility in the oxidation of a range of alcohols.

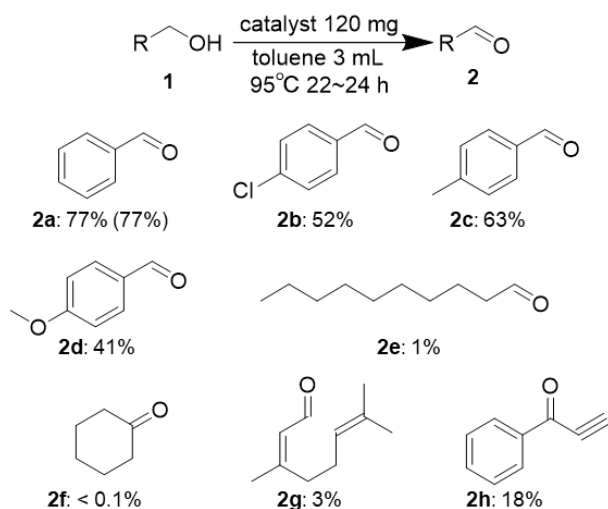


Figure 6.7. Oxidation of alcohol catalyzed by CuO/graphene catalyst.

Reaction conditions: alcohol (0.50 mmol), catalyst (CuO/graphene-250, 0.12 g), and toluene (3.0 mL), in air, 95°C, 22–24 h.

To evaluate the reusability of the catalyst, the spent CuO/graphene-250 catalyst was washed exclusively with toluene and dried under reduced pressure before being used in subsequent reaction cycles. The catalyst treated by this method demonstrated excellent reusability and sustained the catalytic activity (Figure 6.8). With the iron oxide catalysts described in the previous chapter, it was noted that washing with solvent alone was insufficient to remove adsorbed substrates effectively. However, the spent CuO catalyst retained high activity by simply washing with toluene. This discrepancy may arise from weaker adsorption of benzyl alcohol compared to stronger adsorption of aniline. The crystallite size of the spent catalyst remained nearly unchanged after four reaction cycles as shown in Figure 6.12 (Appendix). These findings highlight the potential of the CuO/graphene catalyst developed in this work for industrial applications.

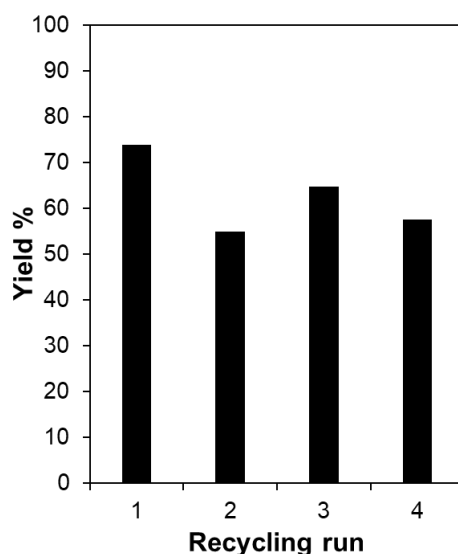


Figure 6.8. Reusability of the CuO/graphene-250 catalyst for oxidation of benzyl alcohol.

Reaction condition: benzyl alcohol (0.50 mmol), catalyst (0.12 g), and toluene (3.0 mL), in air, 95°C, 22–24 h. Catalyst reuse condition: the spent catalyst was washed with toluene and dried using reduced pressure for next run.

6.4. Conclusions

In this chapter, a series of CuO/graphene catalysts were synthesized by the impregnation using copper nitrate and graphene, followed by pyrolysis at various temperatures. The prepared catalysts were characterized by several techniques including XRD, TEM, and N₂ adsorption analysis, and evaluated for the oxidation of alcohols to aldehydes.

It was found that increasing the pyrolysis temperature led to the growth of CuO particles, which correspondingly resulted in a decrease in catalytic activity. Compared to commercial CuO, the synthesized CuO/graphene catalysts exhibited significantly enhanced catalytic performance.

The selective adsorption of TR and SS revealed a strong positive correlation between the catalytic activity for benzyl alcohol oxidation and the CuO surface area. Moreover, the CuO/graphene catalysts demonstrated excellent activity across various alcohol oxidation reactions and could be reused after simple washing and drying.

These findings validate the feasibility of using selective adsorption-based surface area measurements of metal oxides as reliable predictors of catalytic performance.

Furthermore, the development of CuO/graphene catalysts offers valuable insights and approaches for the design of Cu-based catalysts and their application in alcohol oxidation reactions.

6.5. Reference

- [35] (a) Singer, D. A. Future copper resources. *Ore Geol. Rev.* **2017**, *86*, 271-279. DOI: 10.1016/j.oregeorev.2017.02.022. (b) Xu, X.; Shuai, K.; Xu, B. Review on Copper and Palladium Based Catalysts for Methanol Steam Reforming to Produce Hydrogen. *Catalysts* **2017**, *7* (6), 183. DOI: 10.3390/catal7060183. (c) Strekalova, A. A.; Shesterkina, A. A.; Kustov, L. M. Recent progress in hydrogenation of esters on heterogeneous bimetallic catalysts. *Catal. Sci. Tech.* **2021**, *11* (22), 7229-7238. DOI: 10.1039/d1cy01603b. (d) Silva, T. F. S.; Martins, L. M. D. R. S. Recent Advances in Copper Catalyzed Alcohol Oxidation in Homogeneous Medium. *Molecules* **2020**, *25* (3), 748. DOI: 10.3390/molecules25030748.
- [36] (a) Trammell, R.; Rajabimoghadam, K.; Garcia-Bosch, I. Copper-Promoted Functionalization of Organic Molecules: from Biologically Relevant Cu/O₂ Model Systems to Organometallic Transformations. *Chem. Rev.* **2019**, *119* (4), 2954-3031. DOI: 10.1021/acs.chemrev.8b00368. (b) Kim, H. Y.; Oh, K. Recent advances in the copper-catalyzed aerobic C_{sp3}-H oxidation strategy. *Org. Biomol. Chem.* **2021**, *19* (16), 3569-3583. DOI: 10.1039/d1ob00081k. (c) Ahmad, H.; Bilal, M.; Maqbool, T.; Rasool, N.; Adnan Ali Shah, S.; Amiruddin Zakaria, Z. Recent advances on copper-catalyzed asymmetric synthesis and their potential biological applications. *J. Saudi Chem. Soc.* **2023**, *27* (4), 101658. DOI: 10.1016/j.jscs.2023.101658. (d) Jena, S.; Chanda, K. Copper Catalyzed Synthesis of Heterocyclic Molecules via C-N and C-O Bond Formation under Microwaves: A Mini-Review. *ACS Omega* **2023**, *8* (26), 23240-23256. DOI: 10.1021/acsomega.3c02041.
- [37] (a) Wang, X.; Klingan, K.; Klingenhof, M.; Möller, T.; Ferreira de Araújo, J.; Martens, I.; Bagger, A.; Jiang, S.; Rossmeisl, J.; Dau, H.; et al. Morphology and mechanism of highly selective Cu(II) oxide nanosheet catalysts for carbon dioxide electroreduction. *Nat. Commun.* **2021**, *12* (1), 794. DOI: 10.1038/s41467-021-20961-7. (b) Ding, S.; Liu, S.; Li, J.; Wu, L.; Ma, Z.-F.; Yuan, X. Multifunctional Catalyst CuS for Nonaqueous Rechargeable Lithium-Oxygen Batteries. *ACS Appl. Mater. Interfaces* **2021**, *13* (42), 50065-50075. DOI: 10.1021/acsami.1c16231. (c) Totarella, G.; Beerthuis, R.; Masoud, N.; Louis, C.; Delannoy, L.; de Jongh, P. E. Supported Cu Nanoparticles as Selective and Stable Catalysts for the Gas Phase Hydrogenation of 1,3-

Butadiene in Alkene-Rich Feeds. *J. Phys. Chem. C* **2021**, *125* (1), 366-375. DOI: 10.1021/acs.jpcc.0c08077. (d) Zhang, R.; Chen, Y.; Ding, M.; Zhao, J. Heterogeneous Cu catalyst in organic transformations. *Nano Res.* **2022**, *15* (4), 2810-2833. DOI: 10.1007/s12274-021-3935-5.

[38] (a) Kim, D.-S.; Lee, G.-H.; Lee, S.; Kim, J.-C.; Lee, H. J.; Kim, B.-K.; Kim, D.-W. Electrocatalytic performance of CuO/graphene nanocomposites for Li–O₂ batteries. *J. Alloy. Compd.* **2017**, *707*, 275-280. DOI: 10.1016/j.jallcom.2016.11.317. (b) Wang, F.; Liu, Y.-p.; Zhang, H.; Chu, K. CuO/Graphene Nanocomposite for Nitrogen Reduction Reaction. *ChemCatChem* **2019**, *11* (5), 1441-1447. DOI: 10.1002/cctc.201900041. (c) Anjum, F.; Shaban, M.; Ismail, M.; Gul, S.; Bakhsh, E. M.; Khan, M. A.; Sharafat, U.; Khan, S. B.; Khan, M. I. Novel Synthesis of CuO/GO Nanocomposites and Their Photocatalytic Potential in the Degradation of Hazardous Industrial Effluents. *ACS Omega* **2023**, *8* (20), 17667-17681. DOI: 10.1021/acsomega.3c00129. (d) Malik, M. A.; Surepally, R.; Akula, N.; Cheedarala, R. K.; Alshehri, A. A.; Alzahrani, K. A. Oxidation of Alcohols into Carbonyl Compounds Using a CuO@GO Nano Catalyst in Oxygen Atmospheres. *Catalysts* **2023**, *13* (1), 55. DOI: 10.3390/catal13010055. (e) Poreddy, R.; Engelbrekt, C.; Riisager, A. Copper oxide as efficient catalyst for oxidative dehydrogenation of alcohols with air. *Catal. Sci. Technol.* **2015**, *5*, 2467–2477. DOI: 10.1039/C4CY01622J. (f) Albadi, J.; Alihoseinzadeh, A.; Razeghi, A. Novel metal oxide nanocomposite of Au/CuO–ZnO for recyclable catalytic aerobic oxidation of alcohols in water. *Catal. Commun.* **2014**, *49*, 1-5. DOI: 10.1016/j.catcom.2014.01.030. (g) Ji, R.; Li, N.; Xu, J.; Huang, R.; Yan, X.; Li, X.; Sun, Y.; Li, C. Regulating the dispersion of CuO over SiO₂ surface for selective oxidation of isobutane to tert-butanol. *J. Colloid Interface Sci.* **2025**, *681*, 215-228. DOI: 10.1016/j.jcis.2024.11.119.

[39] (a) Zhang, J.; Richardson, H. W. Copper Compounds. In *Ullmann's Encyclopedia of Industrial Chemistry*, pp 1-31. DOI: 10.1002/14356007.a07_567.pub2. (b) K, R.; N, P.; C.P, V.; Khan, T. S.; Gupta, S.; Haider, M. A.; Jagadeesan, D. CuO as a reactive and reusable reagent for the hydrogenation of nitroarenes. *Appl. Catal. B: Environ.* **2021**, *297*, 120417. DOI: 10.1016/j.apcatb.2021.120417. (c) Zhang, Q.; Zhang, K.; Xu, D.; Yang, G.; Huang, H.; Nie, F.; Liu, C.; Yang, S. CuO nanostructures: Synthesis, characterization, growth mechanisms, fundamental properties, and applications. *Prog. Mater. Sci.* **2014**, *60*, 208-337. DOI: 10.1016/j.pmatsci.2013.09.003.

[40] (a) Bhat, N.; Ukkund, S. J.; Ashraf, M.; Acharya, K.; J. Ramegouda, N.; Puthiyillam, P.; Hasan, M. A.; Islam, S.; Koradoor, V. B.; Praveen, A. D.; et al. GO/CuO Nanohybrid-Based Carbon Dioxide Gas Sensors with an Arduino Detection Unit. *ACS Omega* **2023**, *8* (36), 32512-

32519. DOI: 10.1021/acsomega.3c02598. (b) Kesse, X.; Adam, A.; Begin-Colin, S.; Mertz, D.; Larquet, E.; Gacoin, T.; Maurin, I.; Vichery, C.; Nedelec, J.-M. Elaboration of Superparamagnetic and Bioactive Multicore–Shell Nanoparticles (γ -Fe₂O₃@SiO₂-CaO): A Promising Material for Bone Cancer Treatment. *ACS Appl. Mater. Interfaces* **2020**, *12* (42), 47820-47830. DOI: 10.1021/acsami.0c12769.

6.6. Appendix

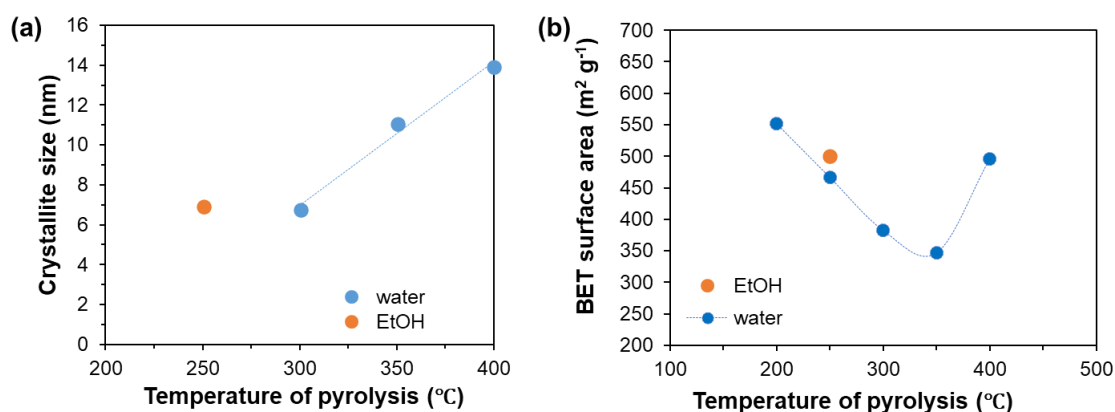


Figure 6.9. Dependence of (a) crystallite size (by XRD analysis) and (b) BET surface area on the pyrolysis temperature of the CuO/graphene catalysts.

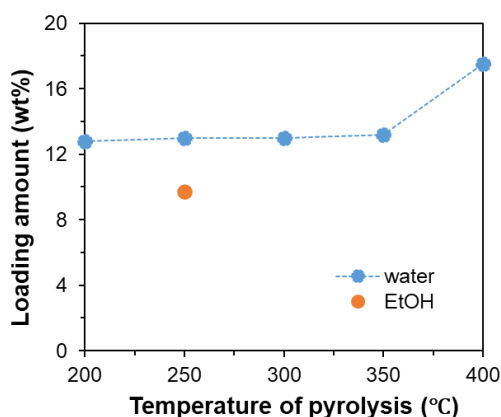


Figure 6.10. Relationship between loading amount (by TG analysis in air) of CuO and pyrolysis temperature for the CuO/graphene catalysts.

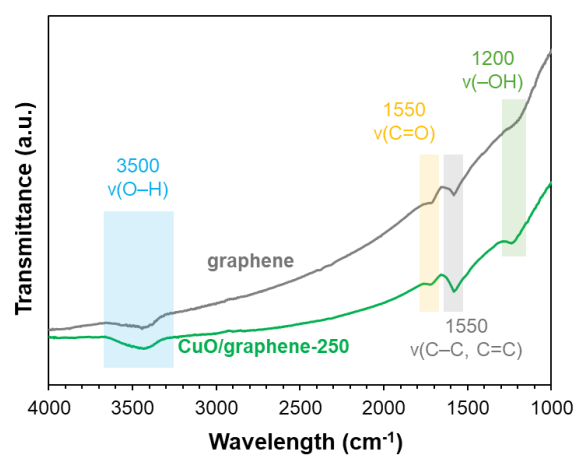


Figure 6.11. FT-IR (KBr) spectra of the CuO/graphene-250 catalysts and graphene.

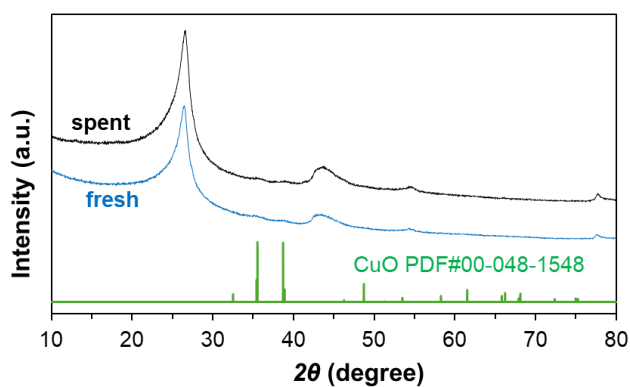


Figure 6.12. XRD patterns of the fresh and spent CuO/graphene-250 catalysts (based on Figure 6.7).

Chapter 7. Conclusions and Challenges

In this thesis, a method for determining the surface area of supported metal oxides was developed using the selective adsorption of organic molecules in solution. This approach was subsequently applied to the several supported metal oxide catalysts.

In Chapter 1, the importance of catalyst development in the chemical industry is highlighted with focus on supported metal oxide catalysts due to their practical application and promising potential. Conventional methods for evaluating surface area often struggle with accurate measurement of the surface area of metal oxides in supported catalysts (e.g., TiO_2 surface area on $\text{TiO}_2/\text{MWCNT}$ catalysts). Thus, this study was aimed to develop a method for determining the metal oxide surface area using molecular adsorption in solution, which is applicable specifically to supported metal oxide catalysts. This work included widely used carbon and SiO_2 supports, focusing on titanium, iron, and copper oxide catalysts.

Chapter 2 describes the development of a method to evaluate the surface area of various metal oxide catalysts on carbon and silica supports. It was observed that Tiron (TR) and Monosodium 5-Sulfoisophthalate (SS) molecules selectively adsorbed onto metal oxides in DMF solution, while adsorption on carbon and silica supports was minimal. This selectivity was attributed to differences in hydrophilicity, hydrophobicity, and surface acidity or basicity. The selective adsorption of TR and SS was applied to determine the surface area of metal oxides in the subsequent chapters. The adsorption experiments under various conditions, using different molecules and structures, and examined microscopic adsorption models were conducted to understand the adsorption behaviors of TR and SS. Besides developing methods for evaluating the surface area of metal oxide catalysts, these findings can also contribute to the broader understanding of adsorption theory.

Chapter 3 shows a series of examinations of the surface areas of various carbon-supported titanium oxide ($\text{TiO}_2/\text{carbon}$) catalysts for hydrogen fuel by using the newly developed TR and SS selective adsorption methods. For N-doped TiO_2 catalysts, a positive correlation was observed between the surface area of titania and catalytic activity when parameters such as trace metal content, annealing time, and oxygen concentration during pyrolysis or annealing were varied. In contrast, Nb-doped TiO_2 exhibited an

inverse correlation between surface area and catalytic activity with changes in preparation temperature. This indicates that nitrogen doping significantly improves electrical conductivity, while the effect of niobium doping, which results in lower conductivity, is more dependent on structural changes that influence conductivity and thus catalytic performance. These findings offer important insights into the development of titania-based catalysts for hydrogen fuel cell applications.

Chapter 4 focused on a series of iron oxide catalysts supported by graphene ($\text{Fe}_2\text{O}_3/\text{graphene}$), prepared by pyrolysis of the precursors of Fe-MOG with graphene supports. These catalysts were characterized using several measurements including XRD, TEM, and TG. The $\text{Fe}_2\text{O}_3/\text{graphene}$ catalysts were applied for the synthesis of imines, and demonstrated high catalytic performance, with yields exceeding 80%. The surface area of iron oxide on the supported catalysts was determined through the selective adsorption of SS, revealing a positive correlation between Fe_2O_3 surface area and catalytic activity. This work also investigated and estimated the surface area of $\gamma\text{-Fe}_2\text{O}_3$ using XRD analysis, revealing that $\gamma\text{-Fe}_2\text{O}_3$ predominates in these catalysts and is responsible for the catalytic activity. The catalysts were also tested for their versatility and reusability in synthesizing various imines. These findings contribute to advancements in iron oxide catalysts and imine synthesis.

Chapter 5 deals with a series of $\text{Fe}_2\text{O}_3/\text{activated carbon}$ catalysts synthesized via an impregnation method, followed by calcination under an N_2 atmosphere. These catalysts were characterized by various techniques and applied in the direct oxidation of benzene to synthesize phenol using H_2O_2 as the oxidant. The catalytic activity and recyclability were comparable to those reported in the literature. The Fe_2O_3 surface area measured by TR selective adsorption exhibited a slight inverse correlation with catalytic activity, possibly due to inaccessibility of the probe molecules (e.g., TR) into the small micropores of activated carbon. These results contribute to the development of supported iron catalysts and provide valuable insights for advancing the one-step synthesis of phenol from benzene.

In Chapter 6, the focus shifted toward $\text{CuO}/\text{graphene}$ catalysts. A series of $\text{CuO}/\text{graphene}$ catalysts were synthesized using an impregnation method, followed by

calcination at various temperatures in air. These catalysts were characterized by various techniques and evaluated for their performance in the oxidation of benzyl alcohol to benzaldehyde. The synthesized catalysts demonstrated significantly higher catalytic activity compared to commercial copper oxide powder. A positive correlation between the CuO surface area (measured via selective adsorption of SS) and catalytic activity was observed. Furthermore, the CuO/graphene catalysts exhibited excellent reusability, maintaining activity after simple washing. These findings not only enhance our understanding of copper oxide-based catalytic systems but also provide valuable insights into alcohol oxidation reactions, with potential implications for industrial applications.

This work established a method for measuring the surface area of supported metal oxides through adsorption of probe organic molecules, and applied this method to titanium oxide, iron oxide, and copper oxide catalysts. The positive correlation between catalytic activity and surface area validated the method's effectiveness. This approach could be extended to evaluate the surface area of various carbon and silica-supported metal oxides, aiding in the understanding of surface and catalytic processes for supported metal oxides.

The method developed in this study may also be applicable to other materials like polymers or zeolites. For instance, in alumina-supported gold catalysts, the probe molecule could adsorb on alumina (oxide) instead of gold (metal), allowing the measurement of the support's surface area, with subsequent calculations for the gold surface area. This approach can enable the determination of surface areas in metal oxide/metal catalysts, offering a simpler alternative to the method based on the adsorption of hydrogen or CO.

The development of this specific surface area evaluation method fosters innovative approaches for supported catalysts and has potential applications across various industries. By enhancing the understanding of hydrogen fuel cells, imine synthesis, and alcohol oxidation reactions, this research contributes to advancements in these fields. Furthermore, the adsorption phenomena and the established metal oxide surface area measurement method explored in this study could support applications in other sectors, such as electronic sensors [40a] and medical applications [40b], where composite metal

oxide materials are essential. Based on these findings and their potential applications, this work aims to contribute to the development of a sustainable society.

Publications

Papers

1. **Lei Shang**, Kenji Hara, Adsorption of Aromatic Carboxylic Acids and Phenolic Compounds on Titanium Oxide, *The 2nd International Conference on Advanced Technology and Sustainable Development – ICATSD 2022*, **2022.11.25**, Ho Chi Minh City, Vietnam (Conference paper, **Chapter 2**).
2. **Lei Shang**, Kenji Hara, Surface Area Measurement of Metal Oxides by Selective Adsorption of Organic Molecules, *The 18th International Conference on Catalysis – ICC 2024*, **2023.07.15**, Lyon, France (Conference paper, **Chapter 2**).
3. **Lei Shang**, Kenji Hara, Adsorption of Aromatic Carboxylic Acid and Phenolic Compounds on Titanium Oxide: A Study of Adsorptions Amount and Structures, *Journal of Science and Technology – IUH* (in press, accepted on 2024.09.20, **Chapter 2**).
4. Momo Obata, Koich Matsyzawa, Yuu Takeuchi, **Lei Shang**, Kenji Hara, Shinji Ishihara Takaaki Nagai, Ryuji Monden, Akimitsu Ishihara, Improvement of Oxygen Reduction Activity by Addition of Fe and Zn to Titanium oxide-based Catalysts in Acid Electrolytes, *The journal of fuel cell technology*, **2024**, 23 (3),83-94 (in Japanese, **Chapter 3**).
5. **Lei Shang**, Kenji Hara, Effect of Calcination Temperature on the Catalytic Activity of Iron Oxide/Activated Carbon in Benzene Oxidation (in manuscript, **Chapter 2**, 5).
6. **Lei Shang**, Akimitsu Isihara, Hideo Watanabe, Toru Hashimoto, Kenji Hara, A method for measuring the surface area of TiO₂ on carbon supports via selective adsorption of the probe organic molecule tiron (in manuscript, **Chapter 2**, 3).
7. **Lei Shang**, Takaaki Nagai, Akimitsu Isihara, Toru Hashimoto, Kenji Hara, Determination of TiO₂ Surface Area on Carbon Supports Using Selective Adsorption of Monosodium 5-Sulfoisophthalate as a Probe Molecule (in manuscript, **Chapter 2**, 3).
8. **Lei Shang**, Naomichi Ando, Toru Hashimoto, Akimitsu Ishihara, Kenji Hara, Measurement of Fe₂O₃ Surface Area by Selective Adsorption of Organic Molecule and Application for Imine Synthesis (in manuscript, **Chapter 2**, 4).

9. **Lei Shang**, Naomichi Ando... CuO Surface Area on Support and Catalytic Activity in Oxidation of Alcohol (in manuscript, **Chapter 2, 6**).

Presentations

1. **Lei Shang**, Kenji Hara, Development of Method for Quantitatively Evaluating the Surface Area of Titanium Oxide, *12th Catalysis Science Research Presentation, Catalysis Society of Japan (West Japan Branch)*, **2021.06.04**, Poster, Japan, Online.
2. **Lei Shang**, Kenji Hara, Development of Quantitative Analysis Method to Determine TiO₂ Surface Area for Hydrogen Fuel Cell Catalyst, *Green Chemistry and Engineering towards Sustainable Development—An Industrial Perspective*, **2021.06.17**, Oral presentation, India, Online.
3. **Lei Shang**, Kenji Hara, Development of Method for Quantitatively Evaluating the Surface Area of Titanium Oxide, *41st Summer Training Session, Young Researchers Association, Catalysis Society of Japan*, **2021.08.05**, Poster, Japan, Online.
4. **Lei Shang**, Kenji Hara, Development of a quantitative evaluation method for titanium oxide surface area by adsorption of organic molecules, *11ed CSJ Chemistry Festival 2021, Chemical Society of Japan*, **2021.10.20**, Poster, Japan, Online.
5. **Lei Shang**, Akimitsu Isihara, Kenji Hara, Development of a quantitative evaluation method for titanium oxide surface area by adsorption of organic molecules, *102nd Spring Annual Meeting, Chemical Society of Japan*, **2022.03.25**, Poster, Japan, Online.
6. **Lei Shang**, Kenji Hara, Adsorption of Aromatic Carboxylic Acids and Phenolic Compounds on Titanium Oxide, *The 2ed International Conference on Advanced Technology and Sustainable Development – ICATSD 2022, International Symposium for Green Solutions (ISGS 2022)*, **2022.11.25**, Oral presentation, Ho Chi Minh City University of Industrial – IUH, Ho Chi Minh City, Vietnam, (peer reviewed).

7. Momo Obata, Koichi Matsuzawa, Yuu Takeuchi, Yushi Tamaki, Yuta Uetake, Satoshi Seino, **Lei Shang**, Kenji Hara, Takaaki Nagai, Ryuji Monden, Akimitsu Ishihara, Factors affecting oxygen reduction activity of Ti oxide-based catalysts, *2023 Electrochemical Fall Meeting, Electrochemical Society of Japan*, **2023.09.11**, Oral presentation, Kyushu University, Japan.
8. **Lei Shang**, Akimitsu Ishihara, Kenji Hara, Adsorption of Organic Compounds on Titanium Oxide in Solution for Quantitative Measurement of Surface Area, *132nd Catalysis Symposium, Catalysis Society of Japan*, **2023.09.13**, Oral presentation, Hokkaido University, Japan.
9. **Lei Shang**, Kenji Hara, Surface Area Measurement of Metal Oxides by Selective Adsorption of Organic Molecules, *18th ICC– The 18th International Conference on Catalysis, Roots and Wings for a Better World*, **2023.07.15**, Post presentation, Lyon, France, (peer reviewed).
10. **Lei Shang**, Akimitsu Ishihara, Toru Hashimoto, Kenji Hara, Measurement of Fe₂O₃ surface area by selective adsorption of organic molecule and application for imine synthesis, *134th Catalysis Symposium, Catalysis Society of Japan*, **2024.09.18**, Oral presentation, Nagoya University, Japan.
11. **Lei Shang**, Naomichi Ando, Akimitsu Ishihara, Toru Hashimoto, Kenji Hara, Surface Area Measurement of Metal Oxides via Selective Adsorption of Organic Molecule and Its Catalytic Applications, *135th Catalysis Symposium, Catalysis Society of Japan*, **2025.03.18**, Oral presentation, Osaka University, Japan, (peer reviewed).

Acknowledgements

First and foremost, I would like to express my deepest gratitude to my supervisor, Prof. Dr. Kenji Hara, for his invaluable guidance and unwavering support throughout my doctoral studies (2020–2025). His mentorship extended far beyond scientific research and professional development, encompassing language acquisition in both Japanese and English, Japanese culture, and many aspects of daily life.

I am sincerely grateful to the members of my PhD Examination Committee: Prof. Dr. Kazuyuki Nishio, Prof. Dr. Yasuyuki Egashira, Prof. Dr. Jun Sumaoka, and Assistant Prof. Dr. Toru Hashimoto, for their insightful comments and constructive suggestions, which were instrumental in improving the quality of this dissertation.

A special acknowledgment goes to Assistant Prof. Dr. Toru Hashimoto for his generous support in scientific research, including experimental work and manuscript preparation, during our time together from 2024 to 2025.

I would also like to extend my sincere appreciation to Prof. Dr. Akimitsu Ishihara, Assistant Prof. Dr. Takaaki Nagai, and Ms. Momo Kobata at Yokohama National University for their invaluable assistance during our joint research (2020–2025), as well as to Dr. Hideo Watanabe, Part-time Lecturer at Tokyo University of Technology, for his kind support from 2021 to 2022.

I am grateful to my colleague Mr. Naomiti Ando for her help with the TEM analysis of supported catalysts.

My heartfelt thanks go to all members of the Catalysis Chemistry (Hara) Laboratory, especially Mr. Hiroshi Mizukoshi, Mr. Mamori Konndo, Mr. Masaya Kimura, and Mr. Tomohiro Ichii, for their continuous support and camaraderie from 2020 to 2025.

I am also deeply thankful to the Hasegawa International Scholarship Foundation and the Heiwa Nakajima Foundation for their generous financial support during my graduate studies.

This work was supported in part by the New Energy and Industrial Technology Development Organization (NEDO) and by the Japan Society for the Promotion of Science (JSPS) KAKENHI Grant Number JP24K08163.

Additionally, I would like to express my sincere gratitude to the faculty, staff, and students at Tokyo University of Technology, especially Lecturer Dr. Kohei Iritani from the Faculty of Engineering and Dr. Ryoma Amanuma from the Advanced Lignin Materials Research Center, for their generous support throughout my academic journey.

Finally, I would like to express my heartfelt gratitude to my parents in China for their financial and emotional support, and to my relatives in China, as well as my friends in both China and Japan, for their unwavering encouragement throughout my studies in Japan.